Analytical Developments for Measuring Atmospheric Peroxy Radicals

Ahmad Lahib

N° d'ordre:

INDIANA UNIVERSITY **IMT LILLE DOUAI** **UNIVERSITE DE LILLE**

THESE

présentée en vue
d'obtenir le grade de

DOCTEUR

en

Discipline : Sciences de la Terre et de l'Univers
Spécialité : Optique et Lasers, Physico-Chimie, Atmosphère

Par

Ahmad LAHIB

DOCTORAT DE L'UNIVERSITE DE LILLE DELIVRE PAR IMT LILLE DOUAI

Titre de la thèse :

Analytical Developments for Measuring Atmospheric Peroxy Radicals

Date de soutenance prévue le 16 décembre 2019 devant le jury d'examen :

Rapporteur	Lisa WHALLEY	Senior Scientist, NCAS, Leeds (UK)
Rapporteur	Christopher CANTRELL	Professeur, LISA, Université de Paris
Examinatrice	Manuela CIRTOG	Maître de conférences, LISA, Université de Paris
Examinatrice	Christa FITTSCHEN	Directrice de Recherche CNRS, PC2A, Université de Lille
Examinatrice	Gisèle EL DIB	Maître de conférences, Institut de Physique de Rennes
Examinateur	Philip STEVENS	Professeur, Indiana University (USA)
Examinateur	Sébastien DUSANTER	Maître Assistant, IMT Lille Douai
Directeur de thèse	Alexandre TOMAS	Professeur, IMT Lille Douai

Laboratoires d'accueil : Sciences de l'Atmosphère & Génie de l'Environnement, IMT Lille Douai

O'Neill School of Public and Environmental Affairs, Indiana University (USA)

Ecole Doctorale SMRE 104 (ULille, ULCO, UVHC, Centrale Lille, Chimie Lille, IMT Lille Douai)

Acknowledgments

This project was in fulfillment of obtaining a doctoral degree at University of Lille. Apart from the efforts of myself, the success of any project depends largely on the encouragements and guidelines of many others.

First of all, I would like to thank my committee members: Lisa Whalley, Christopher Cantrell, Christa Fittschen, Manuela Cirtog and Gisèle EL Dib for accepting to be part of my defense and to review my work.

I take this opportunity to express my gratitude to the people who have been instrumental in the successful completion of this project. I would like to show my greatest appreciation to Sebastien Dusanter and Philip Stevens, Alexandre Tomas for their support and supervision throughout the duration of this project. I cannot say thank you enough for their tremendous support and help. I feel motivated and encouraged every time I attended their meeting and without their encouragement and guidance, this project would not have materialized.

I would like also to express my deepest appreciation to Sebastien Dusanter, he provided me the possibility to complete this project even stimulating the suggestions, encouragement and coordinate writing this manuscript as well.

I thank all my labmates, especially Marius Duncianu for his unyielding patience and helps with PERCA technique, Colleen Rosales for offering her time and help using the FAGE technique and Vinay Kumar for experiences and the time we worked together on VOC measurements and Zachary Payne, Brandon Bottorff and Emily Reidy for the interesting conversions we shared. I want to thank also all members at IMT LILLE DOUAI and Indiana University who indirectly contributed to this project.

Last, but not least, I thank my family, especially my lovely wife Douaa Hamad, for their never-ending support and constant encouragement. You have been the ultimate person motivation behind this work. Love You.

"There are no secrets to success. It is the result of preparation, hard work, and learning from failure." -- Colin Powel

Table of contents

List of Figures

CHAPTER 1

CHAPTER 2

CHAPTER 3

CHAPTER 4

List of Tables

CHAPTER 1

CHAPTER 2

CHAPTER 3

CHAPTER 4

GENERAL INTRODUCTION

General Introduction

The troposphere is the region of the Earth's atmosphere in which we live and into which many chemical compounds are emitted as a result of biogenic processes and human activities. These compounds, emitted from both natural and anthropogenic sources (Atkinson, 2000; Koppmann, 2007), undergo physicochemical transformations that affect both air quality and climate. Indeed, these emissions contribute to smog and acid rain formation, stratospheric ozone depletion, and global warming (Kerr, 1991; Madronich et al., 2015). The discovery of these environmental issues has increased the worldwide interest to investigate atmospheric chemistry during recent decades, with the goal to develop efficient strategies to mitigate their consequences.

Large amounts of volatile organic compounds (VOCs) are emitted into the troposphere with an estimated flux of 1250 Tg $year^{-1}$ (10^{12} g) (Atkinson and Arey, 2003), approximately 140 Tg $year^{-1}$ due to anthropogenic activities(Goldstein and Galbally, 2007) and the rest from biogenic emissions (Guenther et al., 1995, 2012; Sindelarova et al., 2014). Our atmosphere has the ability to remove most of these pollutants through oxidation processes initiated by several oxidants such as the hydroxyl (OH) and nitrate (NO_3) radicals, chlorine atoms (Cl) and ozone (O_3) (Monks, 2005). Among these species, OH plays a key role in the self-cleaning capacity of the atmosphere (Montzka et al., 2011) due to its high reactivity with both organic and inorganic species (lifetime lower than a second), and drives the lifetime of most VOCs. Although atmospheric concentrations of OH are usually small, ranging from a few 10^5 cm^{-3} at night up to 2×10^7 cm^{-3} during the day (Heard and Pilling, 2003; Monks, 2005), its important role in atmospheric oxidation is due to a radical reaction cycle initiated when OH reacts with VOCs, which leads to the production of organic peroxy (RO_2) and hydroperoxy (HO_2) radicals, which can then recycle back to OH through reactions with nitrogen monoxide (NO).

Peroxy radicals (HO_2 + RO_2) are also short-lived species (lifetime of a few tens seconds) playing an essential role in the formation of ozone (Atkinson, 2000) and secondary organic aerosols (Kroll and Seinfeld, 2008a), with both of these secondary pollutants being formed in smog episodes. The oxidizing capacity of the global atmosphere of the Earth is mainly controlled by OH, and as a consequence peroxy radicals due to their propagation to OH, whose spatial distribution has a major impact on the concentration and distribution of greenhouse gases. Thus, understanding the variability of these radicals, along with their souces and sinks is crucial to

evaluate future changes of the chemical composition of the atmosphere, with implications for both air quality and climate change.

Measurements of atmospheric peroxy radicals, which are present at low concentrations (10^6-10^9 cm^{-3}) and that exhibiting short lifetimes require sensitive and selective techniques. Various instruments using different experimental approaches have been developed over the last few decades to measure peroxy radicals, including Matrix Isolation Electron Spin Resonance spectroscopy (MIESR) (Mihelcic et al., 2003, 1985), Laser-Induced Fluorescence-Fluorescent Assay by Gas Expansion (LIF-FAGE) (Stevens et al., 1994a; Hendrik Fuchs et al., 2008; Dusanter et al., 2009b; Faloona et al., 2004; Heard, 2006) and the ROxLIF variant(Hendrik Fuchs et al., 2008; Whalley et al., 2018a) , Chemical Ionization Mass Spectrometry (CIMS) (Albrecht et al., 2019; Edwards et al., 2003; Hornbrook et al., 2011; Kukui et al., 2008a) and Chemical Amplification (CA, PERCA: PEroxy Radical Chemical Amplifier, ECHAMP: Ethane-Based Chemical Amplification) (Cantrell et al., 1984; Hernández et al., 2001; Kartal et al., 2010; Liu et al., 2009; Wood and Charest, 2014). However, it was recently highlighted that some of these techniques may suffer from interferences (Fuchs et al., 2011; Stone et al., 2012) and it is therefore important to improve our technological understanding of peroxy radical measurements. This is a prerequisite for accurate field measurements as well as for kinetic studies of atmospheric reactions in the laboratory.

The main objective of this work is to improve our knowledge on two measurements techniques: Chemical Amplification and ROxLIF. CA is an indirect technique for measuring the sum of peroxy radicals (HO_2+RO_2) whose simplicity and low cost make it attractive for intensive field measurements. This technique involves the chemical conversion of all peroxy radicals into nitrogen dioxide (NO_2) and its subsequent quantification using an NO_2 analyzer. The ROxLIF technique allows measuring both HO_2 and the sum of organic peroxy radicals (RO_2) separately through a selective conversion of these radicals into OH, which is then quantified by laser induced fluorescence at low pressure (Fuchs et al., 2010, 2008). During this work, a CA instrument was built, characterized and tested for field measurements at IMT Lille Douai, France, while the RO_xLIF technique was implemented on an existing FAGE instrument and tested in the field at Indiana University, United States.

The first chapter of this manuscript describes the tropospheric chemistry involving initiation, propagation and termination reactions of RO_x radicals (OH, HO_2, RO and RO_2) and

provides a brief overview of field measurements for these species. The instruments developed for RO_x measurements in ambient air are also described. This chapter ends by introducing the objectives of the work reported manuscript herein.

Chapter 2 describes the development of a dual channel CA at IMT Lille Douai. This chapter reports the characterization of two different amplification chemistries based on the PERCA (PEroxy Radical Chemical Amplifier) and ECHAMP (Ethane-Based Chemical Amplification) approaches. This characterization work consisted in the optimization of reagent gases, the quantification of radical wall losses inside the instrument, and the calibration of the instrument's response (and its humidity dependence) to different peroxy radicals. Both laboratory experiments and model simulations were used to provide a detailed description of the two amplification chemistries. Finally, the instrument was tested by performing ambient measurements.

Chapter 3 describes the construction and characterization of the ROxLIF conversion flow-tube that was coupled to the existing Indiana University-FAGE instrument. Similar to the CA apparatus, a combination of laboratory experiments and model simulations were used to characterize optimum conditions for the addition of reagent gases, to assess radical wall losses in the conversion flow-tube and to calibrate the instrument's sensitivity to both HO_2 and RO_2 radicals. This chapter also reports the first deployment of the Indiana University-ROxLIF for outdoor and indoor measurements of peroxy radicals.

Chapter 4 reports an intercomparison of the CA developed in this study with a RO_xLIF instrument developed at the University of Lille (PC2A laboratory) and a CIMS instrument from the LPC2E laboratory (University of Orleans). This intercomparison exercise was conducted at the HELIOS chamber (ICARE, Orleans) where different pools of peroxy radicals were generated in the chamber under dark and irradiated conditions using different chemical systems. This chapter describes the agreement between the different instruments and shows how the measurements compare to preliminary box model simulations.

CHAPTER 1: BIBLIOGRAPHICAL CONTEXT

Chapter 1. Bibliographical Context

This chapter provides a detailed description of the chemistry of peroxy radicals in the atmosphere and highlights their initiation, propagation and termination pathways. The different techniques used for measuring RO_x (OH, HO_2, RO_2) radicals in the atmosphere and their suitability for field measurements are also discussed. Finally, a brief overview of their measurements in the field is presented.

1.1 Tropospheric Chemistry of ROx radicals

The fate of volatile organic compounds (VOCs) in the troposphere depends on physical processes such as wet and dry depositions (Chen et al., 2019; Mellouki et al., 2015) as well as chemical processes, including direct photolysis and chemical reactions with oxidants such as OH (hydroxyl radical), NO_3 (nitrate radical) and O_3 (ozone). Table 1 reports rate constants of a few selected anthropogenic and biogenic VOCs with these different oxidants and their associated lifetimes. Oxidation reactions initiated by OH are thought to be the most important during daytime due to its high reactivity (bimolecular rate constants usually ranging from 10^{-13} up to 10^{-10} cm^3 $molecule^{-1}$ s^{-1}). While O_3 only reacts with unsaturated VOCs with bimolecular rate constants that are several orders of magnitude lower than for OH, its larger concentration can balances its lower reactivity and this oxidant is also important during daytime. For instance, sesquiterpenes (β-carryophylene in Table 1.1) exhibits a lifetime with respect to O_3 oxidation that is smaller than for OH oxidation. Interestingly, NO_3 oxidation is not important during the day due to its efficient photolysis its reaction with NO, however, its build-up in the dark conditions can lead to a significant impact of this oxidant on VOC oxidation rates at night such as seen for α-pinene.

Table 1-1 Rate constants and Lifetimes of selected VOCs with OH, O_3 and NO_3 during daytime and nighttime.

VOC	Rate constant (298 K) (cm^3 $molecule^{-1}$ s^{-1})			Lifetime (days)			
	OH	O_3	NO_3	Daytime		Nighttime	
				OH^a	O_3^b	O_3^c	NO_3^d
Methane	6.4×10^{-15}*	-	1.0×10^{-18} ∞	3.6×10^{3}			2.3×10^{6}
Hexane	5.2×10^{-12}**	-	1.1×10^{-16}ϯ	4.5			2.0×10^{4}
Toluene	6.1×10^{-12}***	-	7.0×10^{-17}ϯ	3.8			3.3×10^{4}
Isoprene	1.0×10^{-10}*	1.3×10^{-17}ϯ	7.0×10^{-13}ϯ	0.2	2.6	6	3.3
α-pinene	5.3×10^{-11}*	8.4×10^{-17}≈	6.2×10^{-12}ϯ	0.4	0.4	0.9	0.4
β-carryophylene	2.0×10^{-10}≈	1.2×10^{-14}≈		0.1	2.8×10^{-3}	6.6×10^{-3}	

*Atkinson et al., 2006; **Atkinson, 2003; ∞Atkinson et al., 1997; ***Atkinson, 2007; ≈(R. Atkinson, 1997); ϯ(Atkinson and Arey, 2003), [a]Assuming the day time (6am- 6pm) [OH] = 10^6 molecules cm^{-3}, [b] Assuming the day time (6am- 6pm) [O_3] = 7×10^{11} molecules cm^{-3}, [c] Assuming the night time (6pm-6am) [O_3] = 3×10^{11} molecules cm^{-3}, [d] Assuming the night time (6pm-6am), [NO_3] = 10^7 molecules cm^{-3}

The reaction of a VOC with OH will lead to the formation of an organic peroxy radical (RO_2) through the addition of OH to an unsaturated carbon or the abstraction of an hydrogen. RO_2 will then react with NO (NO > approx. 100 ppt) to form an alkoxyl radical (RO), which will further react with O_2, isomerize or decompose to produce the hydroperoxyl (HO_2) radical. HO_2 is known as a temporary reservoir of OH since it subsequently react with NO (or O_3) to reform OH (Finlayson-Pitts and Jr, 2000). It is interesting to note that the oxidation of VOCs initiated by either O_3 or NO_3 will also lead to the formation of peroxy radicals and OH, which will then increase the pool of RO_x (OH, HO_2, RO_2) radicals involved in the cycling chemistry shown in Figure 1.1.

This fast cycling of radicals controls many aspects of atmospheric chemistry such as the formation of ozone, through the conversion of NO into NO_2 when peroxy radicals react with NO, and the formation of secondary organic aerosols (Finlayson-Pitts and Jr, 2000). This radical cycling also controls the removal of the most abundant atmospheric VOCs such as methane and other greenhouse gases that affect the radiative balance of the atmosphere (Monks, 2005). Because of

the important role played by both OH and peroxy radicals in the atmosphere, their sources and sinks have been the subject of intensive research as summarized in recent reviews (Clemitshaw, 2004; Heard and Pilling, 2003; Monks, 2005; Stone et al., 2012).

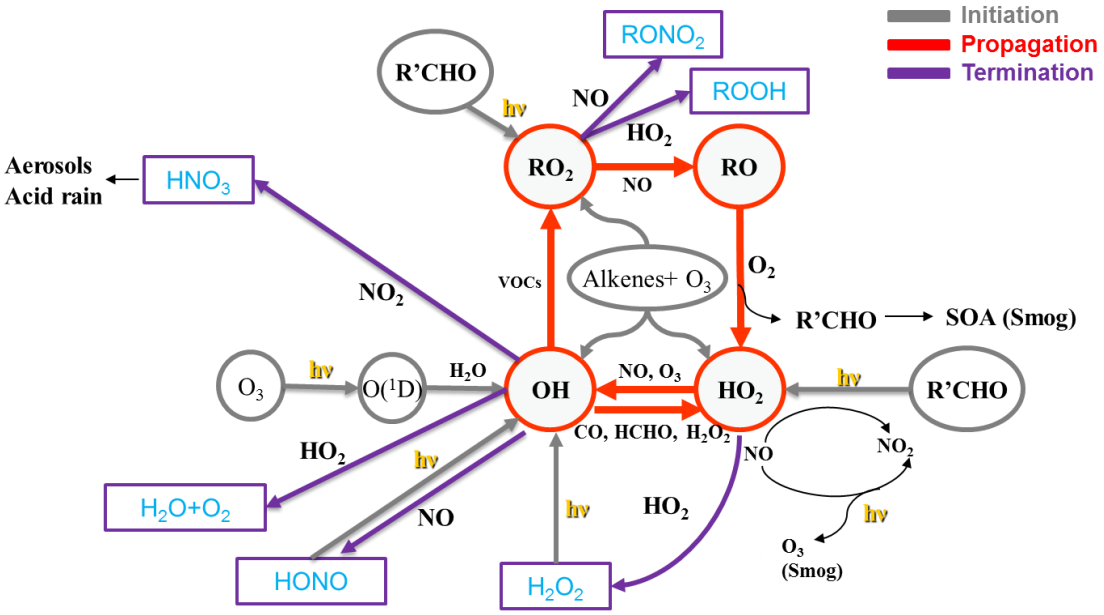

Figure 1.1 Simplified schematic of tropospheric photochemistry (adapted from Ren et al., 2009)

The reactions shown in Figure 1.1 can be grouped in 3 categories to characterize the RO_x chemistry: initiation (grey), propagation (red), and termination (purple):

- Initiation reactions (radical sources) lead to radical production from closed-shell molecules. For instance, HONO photolysis leads to the formation of OH.
- Propagation reactions lead to the conversion of one radical species into another one. For instance, HO_2 propagates to OH by reaction with NO.
- Termination reactions (radical sinks) occur when two radical species react with each other to form a closed-shell molecule. For instance, OH is terminated through its reaction with NO_2 to form nitric acid (HNO_3).

1.1.1 This chemistry is discussed in more details in the following sections.

1.1.2 Radical Initiation

1.1.2.1 Initiation pathways

On a global scale, OH is primarily initiated as a result of ozone photolysis at wavelengths less than 310 nm, resulting in the formation of an excited oxygen atom, $O(^1D)$, as shown in R1. Collisions of $O(^1D)$ with ambient oxygen or nitrogen molecules (M in R2) quench it back to its ground atomic state, $O(^3P)$, which subsequently reacts with molecular oxygen to reproduce O_3. However, the large abundance of water vapor in the troposphere opens a path for collisions of $O(^1D)$ with H_2O towards the formation of hydroxyl radicals, as shown in R3.

R1 $$O_3 + h\nu \rightarrow O_2 + O(^1D) \qquad \lambda < 310\ nm$$

R2 $$O(^1D) + M \rightarrow O(^3P) + M$$

R3 $$O(^1D) + H_2O \rightarrow 2\ OH$$

The fraction of $O(^1D)$ atoms that forms OH depends on the water-vapor concentration. In the lower troposphere where the water concentration is fairly high (mixing ratios ranging from 1-3%), approximately 10% of $O(^1D)$ reacts with H_2O leading to form OH (Monks, 2005).

While R1 and R3 are the main contributors to the formation of OH in the global troposphere (Monks, 2005), there are additional sources (see Figure 1.1) involving the photolysis of OH-precursors such as nitrous acid (HONO) (R4) and hydrogen peroxide (H_2O_2) (R5).

R4 $$HONO + h\nu \rightarrow OH + NO \quad \lambda < 400nm$$

R5 $$H_2O_2 + h\nu \rightarrow 2OH \quad \lambda < 366\ nm$$

The photolysis of HONO (R4) at short wavelengths (300-400 nm) acts as an important source of OH radicals in ozone-deficient polluted air masses (Finlayson-Pitts and Jr, 2000). HONO usually

accumulates during nighttime and provides an early morning pulse of radical formation shortly after sunrise, before O_3 photolysis becomes important since HONO is photolyzed at longer wavelengths than O_3 (Spataro and Ianniello, 2014) .

Another initiation route of OH that has received a lot of attention is the reaction of ozone with unsaturated VOCs such as alkenes (Paulson and Orlando, 1996; Johnson and Marston, 2008). This type of reactions does not require photons and can also operating at night in contrast to the photolytic sources (R1-R5). The exact mechanism for ozonolysis reactions differ between the various alkenes, but a large fraction of the products are radicals. For instance, the reaction of the simplest alkene (ethene, C_2H_4) is believed to proceed by the formation of a biradical species, CH_2OO (R6), also known as a Criegee intermediate, whose subsequent decomposition produces HO_x (OH, HO_2) radicals.

R6 $$O_3 + C_2H_4 \rightarrow\rightarrow CH_2OO + CH_2O$$

A more general mechanism for the ozonolysis of alkenes is thought to proceed through the reaction of ozone with alkene to produce an energy-rich primary ozonide (Path 1 in Figure 1.2). The decomposition (Path 2) of this ozonide produces a carbonyl and a Criegee intermediate (red box) (Baker et al., 2002; Kroll et al., 2001). The Criegee intermediate can be formed in either syn or anti configuration. The Criegee intermediate maintains an excess of energy of the excited ozonide, and can decompose (Path 3a-3b) or become stabilized (Path 4) through collisions with the bath gas by transferring its energy. The OH generated during alkene ozonolysis is typically the result of syn-Criegee intermediate decomposition, but anti-Criegees have shown to contribute up to one third of the OH yield (Kroll et al., 2001).

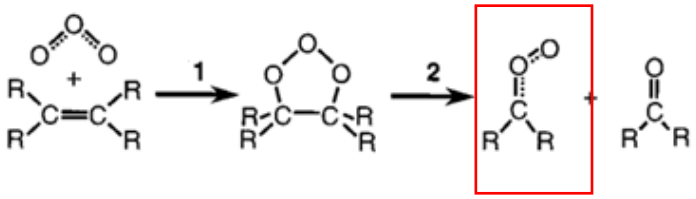

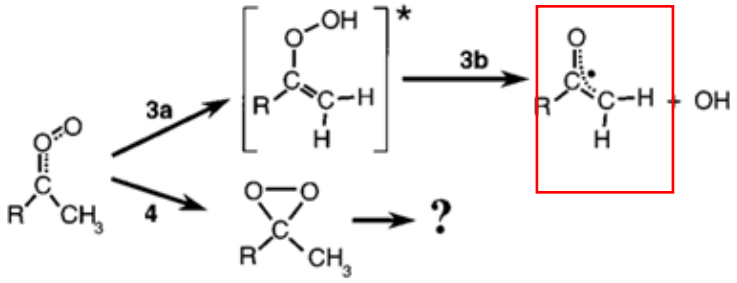

Figure 1.2: Reaction schematic of the ozonolysis of an alkene (Kroll et al., 2001).

The photolysis of Oxygenated VOCs (OVOCs) that are of primary origin, i.e. emitted in the atmosphere by natural or anthropogenic sources, or secondary origin, i.e. produced during the oxidation of primary VOCs, can also act as an important source of RO_x radicals. For instance, formaldehyde (HCHO), glyoxal (CHOCHO), and other dicarbonyls such as methyl glyoxal ($CH_3C(O)CHO$) can easily be photolyzed to produce two radical species. The photolysis of HCHO at short wavelengths ($\lambda < 334$ nm), an important HO_x radical source in the remote atmosphere (Fleming et al., 2006), can produce two HO_2 radicals as shown in reactions R7-R9 (Monks, 2005).

R7 $$HCHO + h\nu \rightarrow H + HCO \quad \lambda < 334\, nm$$

R8 $$HCO + O_2 \rightarrow HO_2 + CO$$

R9 $$H + O_2 + M \rightarrow HO_2 + M$$

The thermal decomposition of Peroxyacyl Nitrates ($RC(O)O_2NO_2$) which only formed from the peroxyacetyl radicals and NO_2, known as PAN species, is an additional source of organic peroxy radicals in the lower troposphere. Peroxy acetyl nitrate ($CH_3C(O)O_2NO_2$) is the most abundant PAN species in the troposphere, with typical atmospheric mixing ratios ranging from a few ppt in the remote marine boundary layer to several ppbv in heavily polluted urban regions. Its decomposition into peroxy acetyl radicals ($CH_3C(O)O_2$) as shown in R10 is very sensitive to temperature (Zheng et al., 2011), with a PAN lifetime ranging from about 30 minutes at 298 K to 8 h at 273 K. This behavior makes PAN species important sources of peroxy radicals and NO_x when their decomposition rate is larger than their formation rate (back reaction of R10). In contrast,

if the decomposition rate is lower than the formation rate, PAN formation becomes a net sink of peroxy radical

R10 $$CH_3C(O)O_2NO_2 \rightarrow CH_3C(O)O_2 + NO_2$$

1.1.2.2 Comparison of initiation rates between different types of environments

The importance of each type of initiation reactions has been studied in environments characterized by different VOC emissions and NOx levels such as forested areas (Wolfe et al., 2011; Whalley et al., 2012; Griffith et al., 2013a; Heard and Pilling, 2003; Stone et al., 2012), urban areas (Heard and Pilling, 2003; Dusanter et al., 2009b; Volkamer et al., 2010; Stone et al., 2012), and the remote marine boundary layer (Berresheim et al., 2002; Creasey et al., 2003; Heard and Pilling, 2003; Stone et al., 2012). For instance, an investigation of the RO_x radical budget in a low-NO_x/high-isoprene forested environment (Griffith et al., 2016) revealed that photolytic processes (R1-R3, R4, R5 and R7) are the main sources of radicals as shown in Figure 1.3 (73% of the total initiation rate on average). For the campaign average, photolysis of O_3, HCHO and HONO contributed to 22%, 23% and 14% of the total initiation rate, respectively. The contribution of ozonolysis reactions was also significant and account for 23% of the total initiation rate.

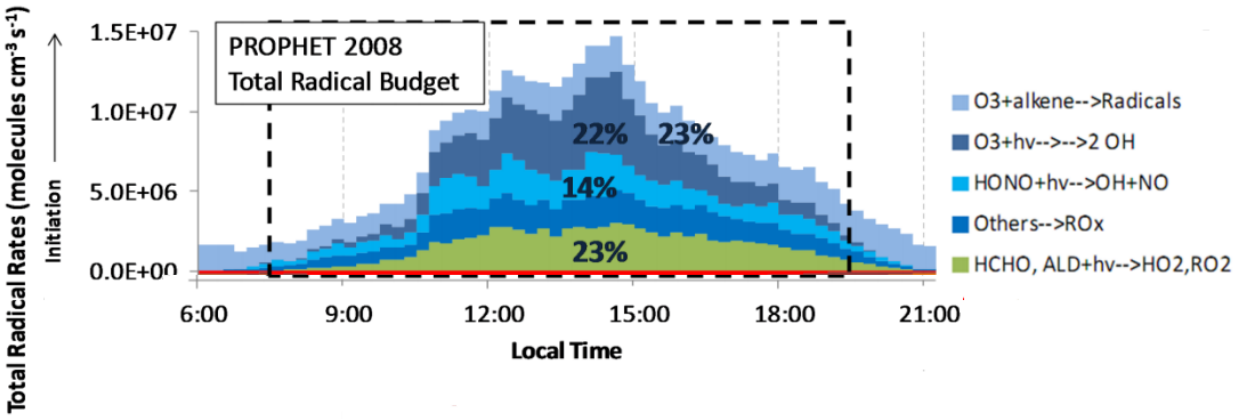

Figure 1.3: Contributions of initiation processes to the total initiation rate of RO_x radicals in a forested area (Griffith et al., 2013a).

For urban areas as shown in Figure 1.4, which are characterized by high emissions of anthropogenic species (VOCs and NO_x), the photolysis of HONO is the main contributors for radical initiation, usually overpassing ozone photolysis. For example, a radical budget analysis performed in Mexico City during the 2006 MILAGRO campaign (Dusanter et al., 2009b) shows

that HONO photolysis accounted for 35% of the total RO_x initiation rate, which is approximately 6 times larger than O_3 photolysis in this environment. The impact of O_3-alkene reactions and HCHO photolysis was also significant with contributions in the range of 19-25 % to the total RO_x initiation rate.

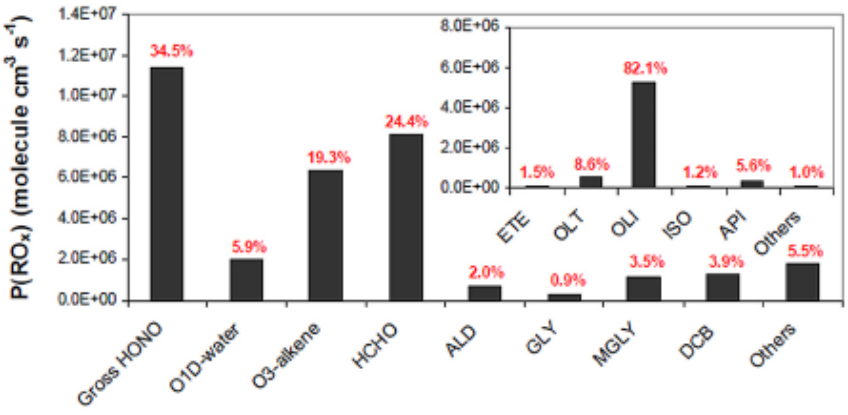

Figure 1.4: Contributions of individual processes to the total production rate of RO_x radicals in Mexico City during MILAGRO 2006. The insert in the upper right panel displays a breakdown of the O_3-alkene contribution. (Dusanter et al., 2009b).

Marine environments are characterized by low concentrations of reactive VOCs (NMHCs and OVOCs) and little or no influence from anthropogenic activities. Figure 1.5 shows the calculated OH and HO_2 production rates during the Observations at a Remote Island of Okinawa intensive field campaign (ORION99) in the northern part Okinawa Island, a subtropical island in Japan (Kanaya et al., 2001a). The major initiation pathways for OH and HO_2 are the photolysis of ozone and formaldehyde, respectively.

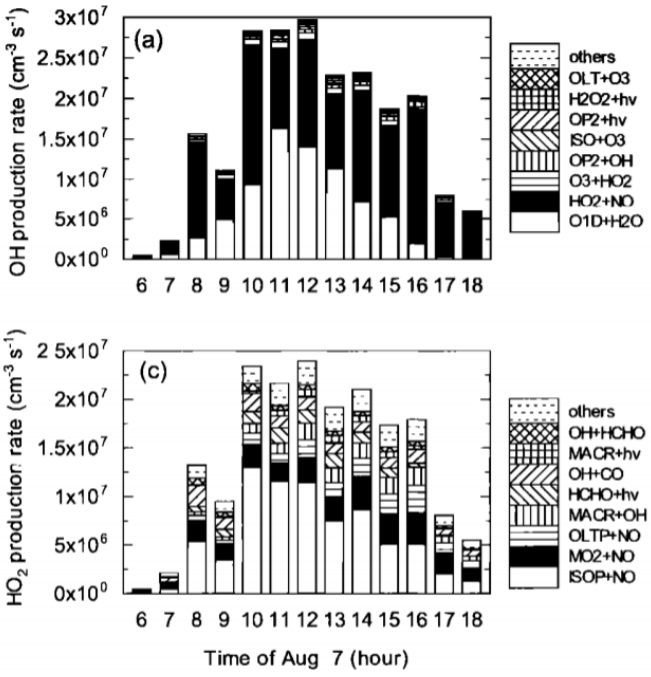

Figure 1.5: OH and HO_2 production rates during the ORION99 campaign (Kanaya et al., 2001a).

Photolysis processes are the main contributors to the radical budget in the three different environments discussed above. However, the most important photolysis process depends on the environment. For instance, the photolysis of O_3 plays a significant role in the production of radicals in environments characterized by low NO_x emissions such as forested and marine environments. The photolysis of HONO and formaldehyde are a common sources of radicals in the 3 environments. High daytime HONO concentrations observed in a number of field studies in urban(Acker et al., 2006; Elshorbany et al., 2010; Villena et al., 2011) and rural areas (Kleffmann et al., 2003; He et al., 2006; Zhou et al., 2011) makes it most important source of radicals in these environments.

of non-photolytic processes, the O_3-alkene reactions make a dominant contribution for the radical budget in urbanized areas and forests where the emissions of anthropogenic or biogenic unsaturated VOCs are important.

1.1.3 Radical Propagation

As shown in Figure 1, there are various reactions leading to the propagation of RO_x radicals. For the sake of clarity, below we present 4 groups of reactions leading to (1) the propagation of OH (but also NO_3 and Cl) to peroxy radicals, (2) the propagation of RO_2 to HO_2, (3) the propagation of peroxy radicals to OH, and finally (4) the interconversion between OH and HO_2.

1.1.3.1 Propagation from oxidants (OH, NO_3, Cl) to peroxy radicals (RO_2, HO_2)

In the remote troposphere, OH predominantly reacts with CO (R11) and CH_4 (R12), the second most efficient anthropogenic climate-forcing gas after carbon dioxide, to form HO_2 (R9) and the methyl peroxy (CH_3O_2) radical (R13).

R11 $OH + CO \rightarrow CO_2 + H$

R9 $H + O_2 + M \rightarrow HO_2 + M$

R12 $OH + CH_4 \rightarrow H_2O + CH_3$

R13 $CH_3 + O_2 + M \rightarrow CH_3O_2 + M$

OH can also react with formaldehyde (R14 and R8) and hydrogen peroxide (H_2O_2) (R15) to form HO_2:

R14 $OH + HCHO \rightarrow CHO + H_2O$

R8 $HCO + O_2 \rightarrow HO_2 + CO$

R15 $H_2O_2 + OH \rightarrow HO_2 + H_2O$

In areas impacted by biogenic or anthropogenic emissions, reactions of OH with larger VOCs lead to its propagation to organic peroxy radicals (RO_2), which in turn react further to form closed-shell oxygenated compounds such as carbonyls, organic peroxides, alcohols and carboxylic acids

(Atkinson and Arey, 2003). It is interesting that the reaction of, the initial reaction for the oxidation of alkanes (R14) proceeds through a hydrogen abstraction:

R14 $$RH + OH \rightarrow R + H_2O$$

R15 $$R + O_2 + M \rightarrow RO_2 + M$$

Reaction R14 leads to the formation of an alkyl radical (R), which then quickly reacts with ambient oxygen to form an organic peroxy radical (R15).

As mentioned previously, NO_3 oxidation also plays an important role in atmospheric chemistry (Jenkin and Clemitshaw, 2000). Since most initiation routes of OH are photolytic (R1-R5), NO_3 becomes the most important alternative to OH oxidation at night, where it rapidly reacts with VOCs to propagate to peroxy radicals (R16 and R15) (Geyer et al., 2001). It is interesting to note that the reaction of NO_3 with HO_2 provides a night-time source of OH radicals (R17).

R16 $$NO_3 + RH \rightarrow HNO_3 + R$$

R17 $$NO_3 + HO_2 \rightarrow OH + NO_2 + O_2$$

In the marine boundary layer, the chlorine (Cl) radical chemistry can also enhance the tropospheric hydrocarbon oxidation. The photolysis of chlorine (Cl_2) R18 and nitryl chloride ($ClNO_2$) provides a daytime sources of Cl atoms (Hossaini et al., 2016). The chlorine radical quickly abstracts hydrogen from hydrocarbons through reactions similar to that of OH radicals, producing alkyl (R19) and alkylperoxy (R15) radicals.

R18 $$Cl_2 + hv \rightarrow Cl + Cl$$

R19 $$Cl + RH \rightarrow R + HCl$$

1.1.3.2 Propagation from RO_2 to HO_2

Organic peroxy radicals can either (i) react with peroxy radicals from the same type or other types or (ii) with NO_x species (NO and NO_2). Reactions of peroxy radicals with closed-shell molecules are sufficiently slow to be negligible at tropospheric temperatures. Under sufficiently high NO (NO > approx.. 100 ppt), reactions of peroxy radicals with NO will dominate leading to radical propagation (R20a) through the formation of an alkoxyl radical (RO). It is worth noting that this implies the oxidation of NO into NO_2, which in turn can be photolyzed to form ozone.

R20a $$RO_2 + NO \rightarrow RO + NO_2$$

For instance, the methyl peroxy radical (CH_3O_2), the most abundant RO_2 in the atmosphere, reacts with NO to form the methoxy radical (CH_3O) (R21), which then reacts with oxygen to form HCHO and to form HO_2 (R22).

R21 $$CH_3O_2 + NO \rightarrow CH_3O + NO_2$$

R22 $$CH_3O + O_2 \rightarrow HCHO + HO_2$$

Under low NO conditions (NO < approx. 100 ppt), self- and cross-reactions of peroxy radicals are significant and can also form alkoxy radicals (R23a):

R23a $$RO_2 + RO_2 \rightarrow 2RO + O_2$$

RO radicals will either react with oxygen as shown above for CH_3O above (R22), isomerize or decompose (Orlando et al., 2003) to form the HO_2.

Additional propagation pathways of large organic peroxy radicals have also been recently proposed in the literature. In isoprene-rich environments, HO_2 (and OH) can be produced from the isomerization and decomposition of isoprene-based peroxy radicals (Figure 1.6). For instance, the 1,6-H-shift isomerization of the Z-conformers of the δ-hydroxyperoxy radicals produced from OH

addition to the 1 and 4 carbons of isoprene can lead to the production of HO_2 radicals and a C5-hydroperoxy aldehyde (HPALD) (Peeters et al., 2009; Peeters and Müller, 2010).

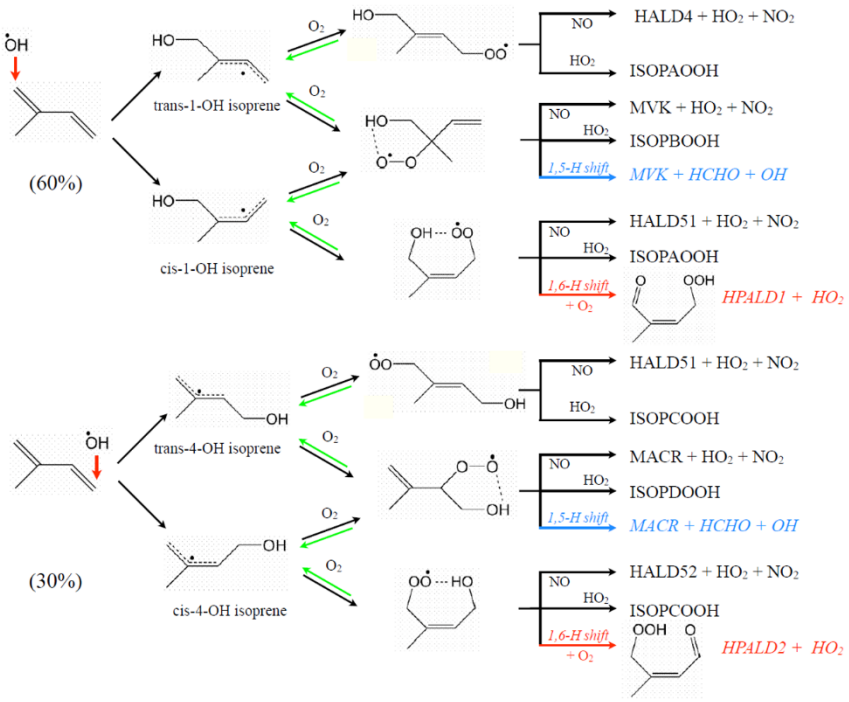

Figure 1.6 Reaction mechanism of isoprene oxidation (Stavrakou et al., 2010)

In monoterpene-rich environments, the autoxidation of monoterpene-based peroxy radicals have been recently proposed to explain the formation of extremely low volatile organic compounds (ELVOC) (Ehn et al., 2014; Mentel et al., 2015; Zhang et al., 2017). This process is an intramolecular hydrogen shift producing a hydroperoxyalkyl radical represented as QOOH in figure 1.7 for the oxidation of n-hexane (Praske et al., 2018). As shown on this figure, the autoxidation process ultimately leads to the generation of low-volatility molecules and HO_2.

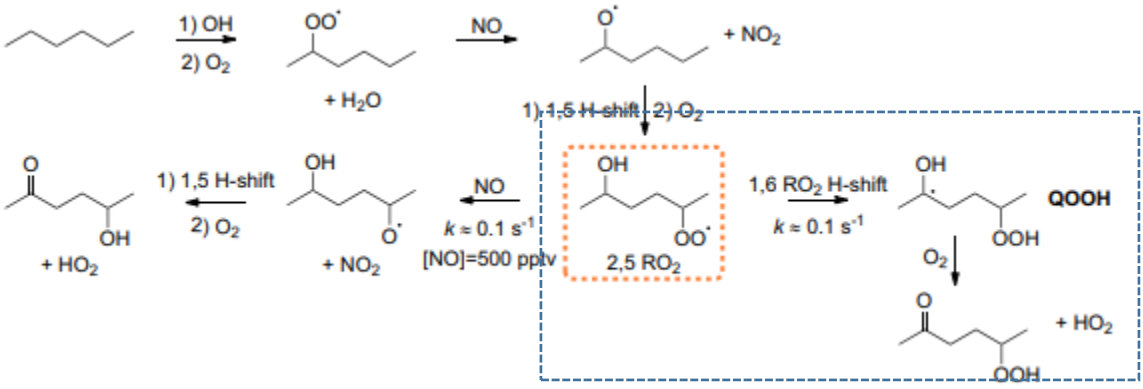

Figure 1.7 Schematic mechanism of autoxidation (dashed blue box) of the 2,5 RO_2 radical (orange box) issuing from OH + n-hexane (Praske et al., 2018).

1.1.3.3 Propagation from HO_2 (and other peroxy radicals) to OH

Once HO_2 is formed,reaction with NO will produce OH:

R24a $$HO_2 + NO \rightarrow OH + NO_2$$

Additional pathways exist in the atmosphere to propagate other peroxy radicals to OH. The reaction of RO_2 radicals with HO_2 can lead to the formation of OH. For instance, the reaction of acetyl peroxy ($CH_3C(O)O_2$) with HO_2 (Hasson et al., 2004) shown in R26 has been shown to form OH with a yield of (0.61 ± 0.09) (Groß et al., 2014).

R25 $$RO_2 + HO_2 \rightarrow RO + OH + O_2$$

R26 $$CH_3C(O)O_2 + HO_2 \rightarrow CH_3C(O)O + OH + O_2$$

1.1.3.4 Interconversion between OH and HO_2

As shown above, the reaction of OH with CO (R11) will convert OH to HO_2 and the reaction of HO_2 with NO (R24a) or NO_2 will convert it back to OH. In the atmosphere there are other reactions that can lead to an interconversion between these two radicals. In low NO_x areas, additional

propagation reactions involve reactions of OH and HO_2 with ozone (R27-R28). HO_2 reacts with ozone with a rate constant of 2.0×10^{-15} cm^3 $molecule^{-1}$ s^{-1} (Atkinson et al., 2004) to form OH:

$$\text{R27} \qquad HO_2 + O_3 \rightarrow OH + 2\,O_2$$

OH also reacts with O_3 with a rate constant of 7.30×10^{-14} cm^3 $molecule^{-1}$ s^{-1} (Atkinson et al., 2004) to produce HO_2:

$$\text{R28} \qquad OH + O_3 \rightarrow HO_2 + O_2$$

The rate constant for OH + O_3 is approximately 37 times larger than for HO_2 + O_3 which will favor partitioning towards HO_2.

1.1.3.5 Comparison of propagation rates between different types of environments

The radical propagation rates are mainly dependent on the environment as illustrated in Figure 1.8 for a forested area (green numbers) and an urban area (blue numbers). Under high NO_x concentrations typical of urban environments, organic peroxy radicals quickly react with NO to propagate to HO_2 and then OH. The RO_2-to-HO_2, HO_2-to-OH, and OH-to-RO_2 propagation rates are 10-45 times larger for the urban atmosphere of Mexico City compared to the atmosphere of a forested environment as shown in figure 1.8. The lower propagation rates observed in forested areas will lead to lower oxidation rates of VOCs. It is interesting that in the low NO_x forested environments, there is still significant cycling between radicals due to the presence of only 20-100 ppt of NO, whose rates are the same order of magnitude as that observed for HO_2 + O_3 (R27). The latter becomes important and starts to compete with the reaction HO_2 + NO (R24a).

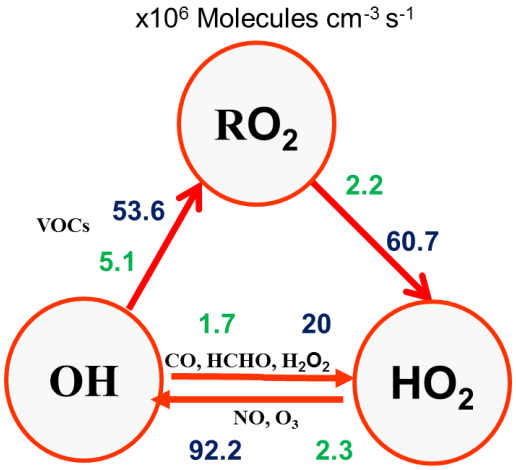

Figure 1.8 Propagation rates of OH, HO_2 and RO_2 radicals in a forested (green) and urban (dark blue) environments. (Adapted from (Dusanter et al., 2009b; Griffith et al., 2013a))

1.1.4 Radical Termination

1.1.4.1 Termination pathways

The atmospheric cycling of RO_x radicals shown in Fig. 1.8 can be terminated by radical-NO_x reactions, which are predominant in urbanized areas where large concentrations of NO_x are present, and by radical recombination reactions in low NO_x areas such as remote forested environments and the marine boundary layer.

In areas characterized by elevated NO_x levels, OH reacts with NO_2 and produces nitric acid (HNO_3), which will mainly be lost through wet deposition:

R29 $$OH + NO_2 + M \rightarrow HNO_3 + M$$

NO can also react with OH and HO_2, leading to the formation of HONO (R30) and HNO_3 (R24b). However, HONO has a lifetime of less than 1 h during the day due to its efficient photolysis (R4) and should be seen as a temporary reservoir of radicals. R24b is a minor pathway of the HO_2 + NO reaction, with 0.5-4% of the reaction flux leading to the formation of HNO_3 (Butkovskaya et al., 2007, 2009).

R30 $OH + NO + M \rightarrow HONO + M$

R24b $HO_2 + NO + M \rightarrow HNO_3 + M$

The reaction between alkyl peroxy radicals and NO can also act as a significant terminating channel through the formation of organic nitrates ($RONO_2$) as shown in R20b. This reaction is negligible for short chain organic radicals (C < 4), but becomes increasingly important for radicals with longer chains (Lightfoot et al., 1992). The branching ratio R20b/R20a is as large at 25% for C10 and larger alkyl peroxy radicals (Orlando and Tyndall, 2012).

R20a $RO_2 + NO \rightarrow RO + NO_2$

R20b $RO_2 + NO + M \rightarrow RONO_2$

Reaction R20b is of importance for ozone production since it does not lead to the conversion of NO into NO_2 and by sequestering both RO_2 and NO_2, organic nitrate formation reduces ozone production rates. The association reaction between alkoxy radicals and NO (R31) is not important in the atmosphere but can be important in laboratory experiments, especially where high NO concentrations are used to quantify peroxy radicals as described in chapter 2.

R31 $RO + NO \rightarrow RONO$

In areas characterized by low NO_x concentrations, RO_x radicals significantly react through cross- and self-reactions to form peroxide species such as H_2O_2, ROOR and ROOH (R32, 23b & 33) (Penkett et al., 1997).

R32 $HO_2 + HO_2 \rightarrow H_2O_2 + O_2$

R23b $RO_2 + RO_2 \rightarrow ROOR + O_2$

R33 $HO_2 + RO_2 \rightarrow ROOH + O_2$

R34 $OH + HO_2 \rightarrow H_2O + O_2$

R35 $OH + RO_2 \rightarrow products$

Interestingly, R35 has been neglected until recently when the rate constants between OH and RO_2 radicals have been measured experimentally (Assaf et al., 2017; Bossolasco et al., 2014; Faragó et al., 2015). It has been shown that this type of reactions is extremely fast and can be of importance at remote locations and for the marine boundary layer (Fittschen et al., 2014).

1.1.4.2 Comparison of termination rates between different types of environments

As shown in Figure 1.9 (Dusanter et al., 2009b), OH + NO_2 (R29) is the dominant sink for RO_x radicals in urbanized areas such as Mexico City where NO_x concentrations are elevated, with a contribution of approximately 60% to the total loss rate. Other important pathways for radical termination are OH + NO (R30) and RO_2 + NO (R20b) accounting for approximately 20 and 14% of the total loss rate, respectively. However, as mentioned previously, HONO formation has to be seen as a temporary reservoir for OH since its photolysis will reform OH.

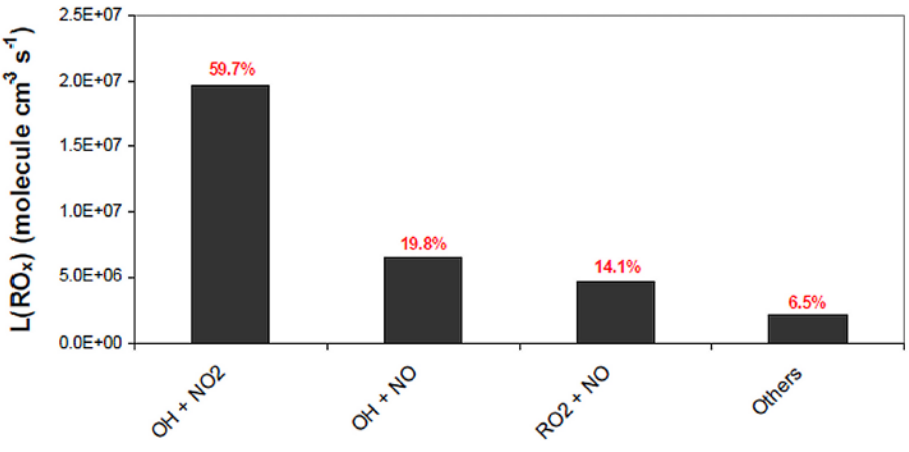

Figure 1.9 Contributions of termination reactions to the total termination rate of RO_x radicals in the urban environment of Mexico City (Dusanter et al., 2009b).

In contrast, RO_2 radical self- and cross-reactions are the dominant loss processes when NO is low (< approx. 100 ppt) as shown in Figure 1.10 for a forested environment in Michigan (US). It can be seen that $RO_2 + HO_2$ termination reactions contribute up to 79% of the total loss of RO_x radicals, with an additional 10-15 % loss due to $HO_2 + HO_2$ (R32) (Griffith et al., 2013a). Under typical ambient HO_2 and RO_2 concentrations observed in forested areas (< 80 pptv, HO_2/RO_2 close to unity), the $HO_2 + HO_2$ reaction rate is slow compared to $RO_2 + HO_2$ (Boyd et al., 2003)

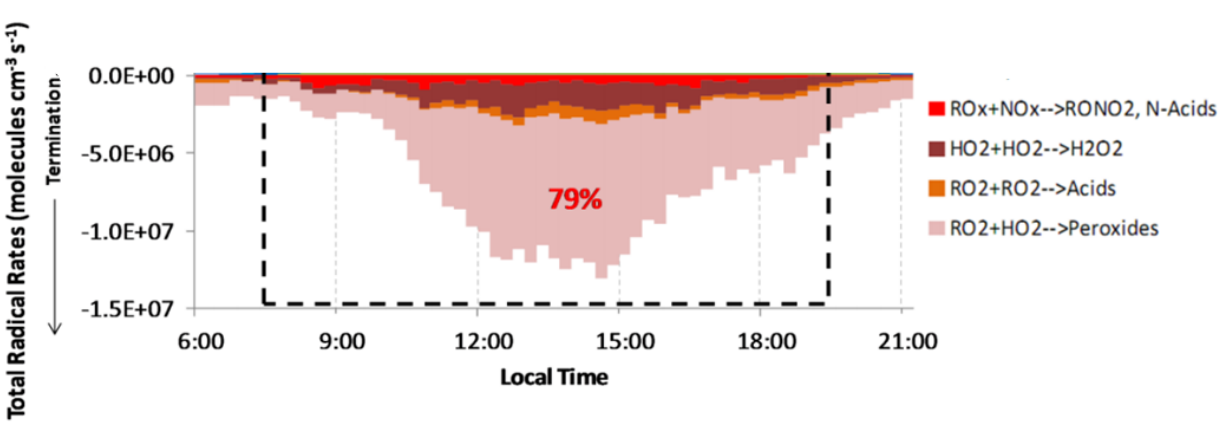

Figure 1.10 Contributions of termination reactions to the total loss rate of RO_x radicals in a forested area (Griffith et al., 2013a). The negative sign indicates a loss.

The reaction between RO_2 and OH can be significant under typical marine boundary layer conditions (Fittschen et al., 2014). As mentioned above, the determination of rate constant for several organic peroxy radical with OH have been found to be fast and should be included in models describing the chemistry in low NO_x environments (Fittschen et al., 2014). These authors showed that the reaction of CH_3O_2 with OH represents approximately 25% of the CH_3O_2 loss rate using data from a field campaign performed at Cape Verde.

1.1.5 Ozone production and destruction

Besides their role in the oxidation of ambient trace gases, peroxy radicals are involved in the production of ozone. Tropospheric ozone is mainly produced and destroyed by photochemistry involving both NO and NO_2:

R36 $NO + O_3 \rightarrow NO_2 + O_2$

R37 $NO_2 + h\nu\ (\lambda < 420\ \text{nm}) \rightarrow NO + O(3P)$

R38 $O\ (3P) + O_2 \rightarrow O_3$

The NO and NO_2 concentrations are usually in a quasi-stationary equilibrium during daytime due to the fast cycling occurring between the species. This group of reactions (R36-R38) is known as the O_3-NO_x photostationary state.

This cycle does not lead to net production of ozone since O_3 is both produced and consumed. Since NO_x are mainly emitted in the form of NO through anthropogenic and natural emissions (Finlayson-Pitts and Pitts Jr, 2000), net ozone production requires additional routes to convert NO into NO_2. In polluted areas where NO_x concentrations are relatively high, the propagation reactions of peroxy radicals discussed above can promote the production of O_3:

R20a $RO_2 + NO \rightarrow RO + NO_2$

R24a $HO_2 + NO \rightarrow OH + NO_2$

The conversion of NO into NO_2 (R20a, R24a) due to the presence of peroxy radicals in the atmosphere leads to the formation of NO_2 without consumption of O_3, which in turn leads to the formation of additional molecules of O_3 from NO_2 photolysis.

In contrast, the reaction between HO_x radicals and ozone can lead to the net destruction of O_3 in very low-NO_x areas (R27& R28):

R27 $HO_2 + O_3 \rightarrow OH + 2\ O_2$

R28 $OH + O_3 \rightarrow HO_2 + O_2$

It is worthwhile to note that anthropogenic activities lead to concomitant emissions of NO, CO and VOCs, favoring ozone production. This is a self-energizing process since a higher ozone

concentration will lead to an increasing in OH concentration and therefore a faster oxidation rate of VOCs.

1.2 Measuring peroxy radicals in the atmosphere

Measurements of ambient radicals are extremely challenging since their concentrations are extremely low, less than 1 pptv for OH and ranging from the sub pptv to a few tens of pptv for peroxy radicals, due to their high reactivity and short lifetimes (less than a second for OH and up to tens of seconds for peroxy radicals). In addition, radicals can easily be lost on surfaces during sampling into instruments. Several techniques have been developed for measuring RO_x radicals in the atmosphere and below we focus on techniques used to measure peroxy radicals, including Matrix Isolation Electron Spin Resonance spectroscopy (MIESR) (Mihelcic et al., 2003, 1985) , Chemical Ionization Mass Spectrometry (CIMS) (Albrecht et al., 2019; Edwards et al., 2003; Hanke et al., 2002; Hornbrook et al., 2011; Kukui et al., 2008a), Chemical Amplification (CA, PERCA: PEroxy Radical Chemical Amplifier, ECHAMP: Ethane-Based Chemical Amplification) (Cantrell et al., 1984; Clemitshaw et al., 1997; Hernández et al., 2001; Kartal et al., 2010; Liu et al., 2009; Wood et al., 2017; Wood and Charest, 2014), and Laser-Induced Fluorescence (LIF) (Stevens et al., 1994a; Dusanter et al., 2009b; Faloona et al., 2004; Hard et al., 1984; Holland et al., 1995; Matsumi Yutaka et al., 2002; Heal et al., 1995; Amedro et al., 2012a; Whalley et al., 2018a; Chan et al., 1990; Martinez et al., 2010), including RO_x-LIF(Hendrik Fuchs et al., 2008; Whalley et al., 2018a). These techniques are briefly presented below for MIESR and CIMS, highlighting some of the known limitations, but are discussed in more details for PERCA and RO_x-LIF, which represent the core of this Ph.D work. Techniques used to calibrate these instruments are also discussed in this section.

1.2.1 Matrix Isolation and Electron Spin Resonance Spectroscopy (MIESR)

Measurements of atmospheric peroxy radicals using Matrix Isolation and Electron Spin Resonance Spectroscopy was reported by Mihelcic et al. (Mihelcic et al., 1985, 1990, 2003). So far, only one instrument of this kind exists in the world at the Forschungszentrum Jülich, Germany

(Fuchs et al., 2010). To the best of our knowledge, this instrument was lastly used in 2010 on the SAPHIR atmospheric chamber (Fuchs et al., 2010) and is no longer employed.

This is the only technique that allows measurements of speciated peroxy radicals in one sample: HO_2, some RO_2, $CH_3C(O)O_2$. MIESR is very selective, being only sensitive to radicals, and exhibits a low detection limit of 2 pptv at a time resolution of 30 min (Mihelcic et al., 2003). This technique consists of trapping ambient air samples in a D_2O matrix at 77 K for 30 min. The energy difference between the two principal spin states of the unpaired electron in a radical species is then probed by Electron Spin Resonance (Fuchs et al., 2010). The radical concentrations are computed from the resulting microwave spectra by fitting reference spectra for the targeted radicals.

The main disadvantages of this method are (i) its cost, (ii) the necessity to trap an air sample before its analysis in the laboratory, (iii) the difficulty of maintaining the sample under vacuum at 77 K until it is analyzed (Mihelcic et al., 2003), (iv) long analysis time (8 hours per sample). However, this technique exhibits several advantages such as (i) its ability to distinguish between HO_2 and organic peroxy radicals, (ii) the measurement of individual RO_2 radicals.

1.2.2 Chemical Ionization Mass Spectrometry (CIMS)

The CIMS technique (Albrecht et al., 2019; Edwards et al., 2003; Hanke et al., 2002; Hornbrook et al., 2011; Kukui et al., 2008a) is based on the chemical conversion of RO_x radicals to sulphuric acid (H_2SO_4) and its subsequent detection by chemical ionization mass spectrometry, which is an established method for indirect measurements of OH (Berresheim et al., 2000).

As shown in Figure 1.11, ambient air is continuously sampled through an orifice into an inlet held at reduced pressure. Both SO_2 and NO are added in the front injector to convert RO_2 into HO_2 (R20a) and HO_2 (R24a) into OH. In the meantime, OH reacts with SO_2, resulting in the formation of sulfuric acid (H_2SO_4) and its propagation to HO_2 (R39-R41).

R39 $$OH + SO_2 + M \rightarrow HSO_3 + M$$

R40 $$HSO_3 + O_2 \rightarrow SO_3 + HO_2$$

R41 $SO_3 + 2H_2O \rightarrow H_2SO_4 + H_2O$

The reformation of HO_2 leads to an amplification chemistry since several molecules of H_2SO_4 will be produced for each sampled RO_x radical (R24a, R39-R41). The chain length reported for this type of instruments, i.e. the number of H_2SO_4 molecules produced per sampled RO_x radical, is in the range of 10-15 (Edwards et al., 2003; Hanke et al., 2002).

R24a $HO_2 + NO \rightarrow OH + NO_2$

The amount of H_2SO_4 produced in the inlet is quantified by mass spectrometry using NO_3^- as reagent ion. The concentration of RO_x radicals is derived from the measured H_2SO_4 concentration, taking into account the background H_2SO_4 concentration in the atmosphere, and the calibrated chain length. Since atmospheric concentrations of OH (10^5-10^7 cm^{-3}) and RO (<10^5 cm^{-3}) are negligible compared to concentrations of HO_2 and RO_2 (10^8-10^9 cm^{-3}), the CIMS measurement is considered as the sum of peroxy radicals (HO_2+RO_2).

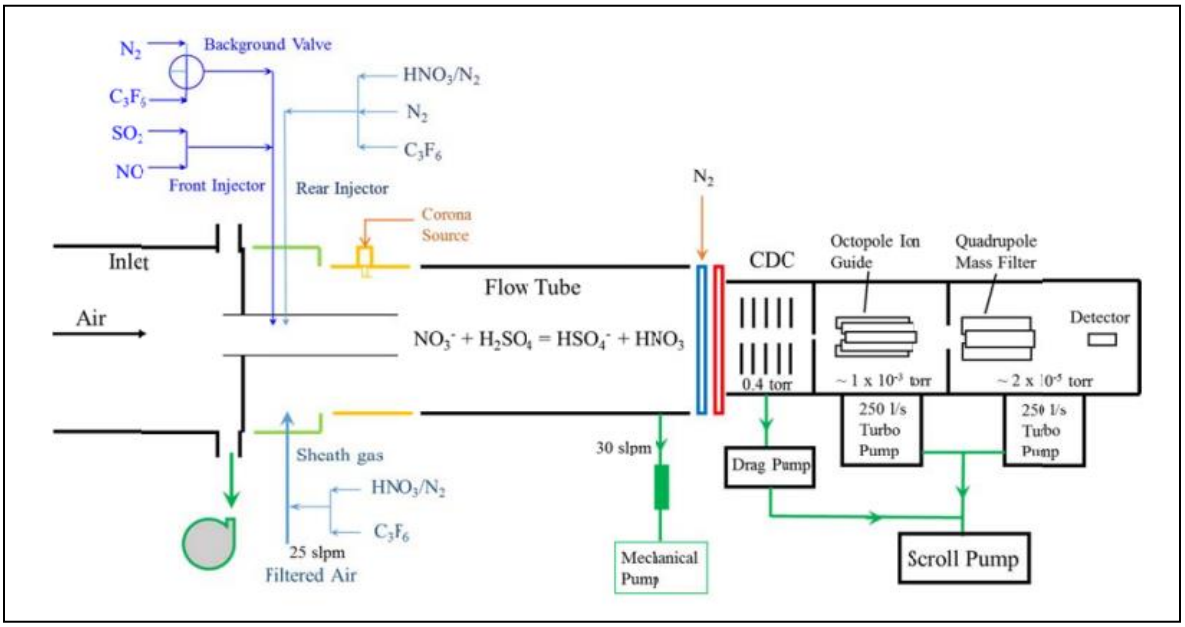

Figure 1.11 Schematic of the RO_x-CIMS instrument (Hofzumahaus and Heard, 2015)

This allows the selective observation of peroxy radicals at a time resolution of about 10 s and a detection limit lower than 3×10^6 cm^{-3} thanks to the low background level of sulphuric acid in ambient air (Hofzumahaus and Heard, 2015). However, the RO_2 + NO reaction leads to an incomplete propagation of RO_2 radicals to HO_2 since organic nitrates (R20b) and nitrites (R31) are also produced during the propagation steps. Thus, it necessarily involves an incomplete conversion of RO_x radicals to sulphuric acid and the measurements will be a lower limit of ambient RO_x. Hornbrook et al. reported a method to speciate HO_2 and the sum of RO_2 radical on CIMS instruments at a time resolution of 1 min (Hornbrook et al., 2011). This was achieved by varying both [NO] and [O_2] simultaneously in the chemical conversion region of the inlet. The idea of this method is based on a change of the conversion efficiency of RO_2 into HO_2 under different inlet [NO]/[O_2] ratios. This allows to selectively observe either HO_2 or the sum of HO_2 and RO_2. To measure HO_2 + RO_2, ambient air is diluted by half with O_2, whereas for HO_2 measurements, ambient air is diluted by half with N_2. In both cases, the first step is to convert RO_2 into RO in the presence of NO while the difference is in the second step when O_2 or N_2 is added. In the case of an addition of O_2, most RO will convert into HO_2 (R22) and HO_2 + RO_2 will be quantified. In case of an addition of N_2, less chemical conversions of RO into HO_2 will occur. Thus, only HO_2 will be quantified.

1.2.3 Chemical Amplification (PERCA & ECHAMP)

The PERCA technique is an indirect measurement method pioneered by Cantrell and Stedman (Cantrell et al., 1984) to measure the sum of RO_x radicals. In this technique, RO_x radicals are converted into NO_2 via an amplification chemistry to produce several molecules of NO_2 per sampled RO_x radical.

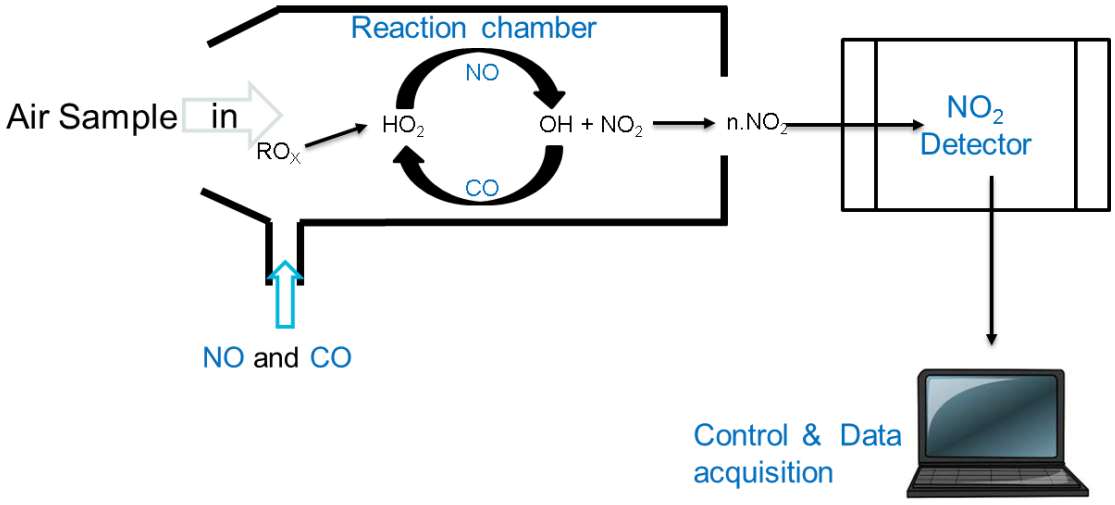

Figure 1.12 Schematic representation of the PEroxy Radical Chemical Amplification system
The sampling inlet is usually made of Pyrex or PFA (PerFluoroAlkoxy) materials.

The amplification chemistry takes place close to the sampling point by adding two reagent gases (NO and CO). The number of NO_2 molecules produced per sampled RO_x radical can easily be calibrated and is called the chain length (CL). The distance between the sampling point and the addition of the reagent gases is kept as short as possible to minimize potential wall-losses of the radical species (OH, HO_2 and RO_2). NO_2 is then transported to a suitable detector based on luminol chemiluminescence (Clemitshaw et al., 1997), LIF (Sadanaga et al., 2004), cavity ring-down spectroscopy (CRDS) (Liu et al., 2009) or cavity attenuated phase-shift spectroscopy (CAPS) (Wood and Charest, 2014). The principle of PERCA measurements is based on a chain reaction cycle involving both OH and HO_2 by adding NO and CO to the sampled air (Figure 1.13).

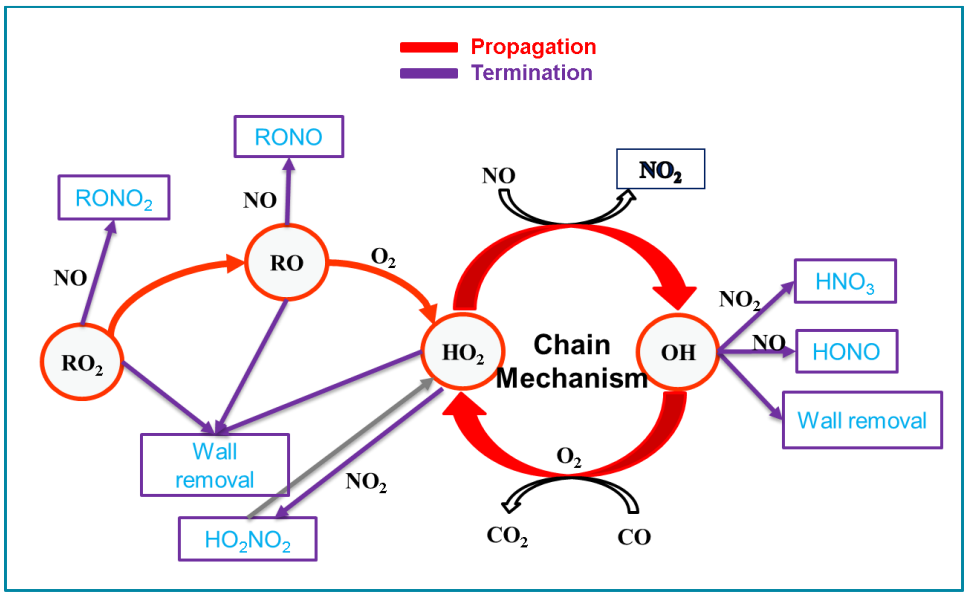

Figure 1.13 Amplification chemistry of a PERCA system.

NO converts ambient RO_2 radicals into HO_2 (R20a and R22) and the resulting HO_2, together with the ambient HO_2, are converted into OH (R24a). CO converts OH back to HO_2 as shown in R11 and R9, and as a consequence, the suite of reactions R11/R 9/R24a acts as an amplification system where several NO_2 molecules are produced for each radical entering in the cycle. The CL is a finite number because the reaction cycle ends due to termination reactions for both OH (R29, R30, R34 &R36) and HO_2 (R24b, R44). Termination reactions due to cross- and self-reactions of RO_x radicals are not included since R35 and R36 together with wall losses of radicals are the most important radical sinks under the high NO conditions in the inlet (Cantrell et al., 1984).

R20a $RO_2 + NO \rightarrow RO + NO_2$

R20b $RO_2 + NO \rightarrow RONO_2$

R22 $RO + O_2 \rightarrow R_{-H}O + HO_2$

R31 $RO + NO \rightarrow RONO$

R24a $HO_2 + NO \rightarrow OH + NO_2$

R24b $HO_2 + NO + M \rightarrow HNO_3 + M$

R11 $OH + CO \rightarrow CO_2 + H$

R9 $H + O_2 + M \rightarrow HO_2 + M$

R32 $HO_2 + HO_2 \rightarrow H_2O_2 + O_2$

R33 $HO_2 + RO_2 \rightarrow ROOH + O_2$

R29 $OH + NO_2 + M \rightarrow HNO_3 + M$

R30 $OH + NO + M \rightarrow HONO + M$

R34 $OH + HO_2 \rightarrow H_2O + O_2$

R35 $RO_2 + Wall \rightarrow non - radical\ products$

R36 $OH + Wall \rightarrow non - radical\ products$

R44 $HO_2 + NO_2 \rightarrow HO_2NO_2$

A PERCA instrument therefore amplifies all the radicals that can cycle to HO_2, such as OH, HO_2, RO and RO_2, and measures the sum of RO_x. However, as already mentioned above for the CIMS apparatus, atmospheric concentrations of OH are negligible compared HO_2 and RO_2 and the PERCA measurements can therefore be seen as the sum of HO_2 and RO_2.The following aspects, which can influence the chain length (amplification factor) and the PERCA response are briefly discussed below:

- Concentrations of reagent gases (CO and NO): drive the competition between radical propagation and termination,
- Relative humidity: water molecules adsorbed at the reactor surface can enhance the heterogeneous loss of peroxy radicals and elevated water concentrations can lead to the formation of $HO_2.H_2O$ adducts whose chemistry may differ from HO_2,
- Propagation efficiency of RO_2 into HO_2: may depend on the RO_2 species.

The CL, calculated as the number of NO_2 molecules produced per sampled peroxy radical, depends on reagent gases as shown in Figure 1.14. This figure illustrates the dependence of CL on both NO and CO reagents for an instrument developed at the University of East Anglia (UEA) (Clemitshaw et al., 1997). This PERCA system employed consisted of a Pyrex inlet equipped with two ports for the addition of the reagent gases. The exit of the inlet was connected to a NO_2 chemiluminescence detector. Figure 1.14 shows that the CL increases with [CO] up to 7-8% and then levels off at a value of approximately 180 when NO is kept constant at 3 ppm. Other studies have shown similar results with a plateau reached at 10% CO (Kartal et al., 2010; Sadanaga et al., 2004) and 2.3% CO (Wood et al., 2017) for NO mixing ratios of 3 and 1 ppm, respectively. The increase of the CL with CO is due to an increase of the OH + CO reaction rate (R11) with respect to the OH + NO termination rate (R30), until the OH+NO rate becomes negligible compared to the total termination rate of radicals in the PERCA reactor. Figure 1.14 also shows that the CL strongly depends on NO. For a CO mixing ratio of 7%, the CL reaches a maximum value of approximately 200 at 5 ppm NO. Other studies have found maximum CL values at NO mixing ratios ranging from 2-4 ppm for different CO mixing ratios. The CL increases with NO below 5 ppm due to a larger enhancement of the HO_2-to-OH propagation rate (R24a) compared to the OH + NO termination rate (R30) and decreases for higher mixing ratios due to the opposite behavior.

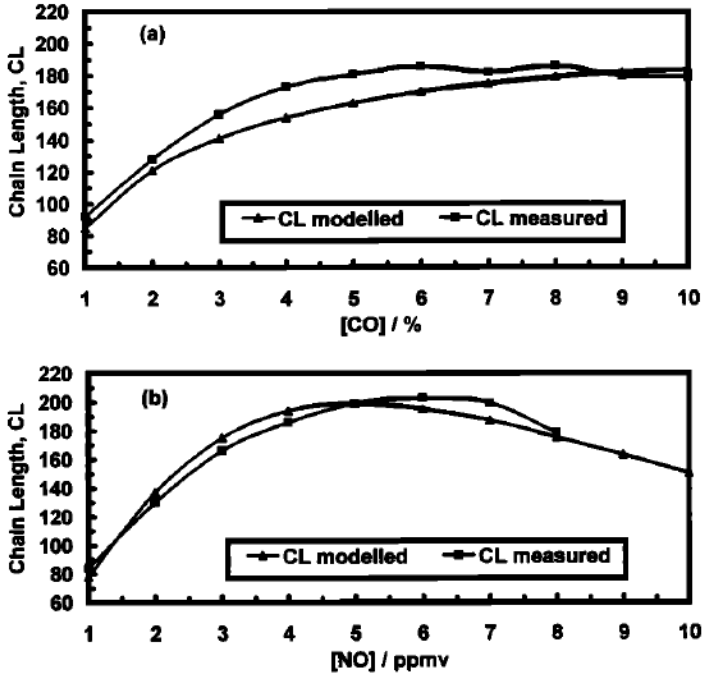

Figure 1.14 Dependence of the PERCA CL on both CO (a) and NO (b) (Clemitshaw et al., 1997).

The most problematic issue concerning PERCA is the dependence of the CL, and therefore the sensitivity of the instrument, on ambient humidity. Figure 1.15 shows that the CL, normalized to dry conditions, decreases significantly with relative humidity (RH), with a drop of approximately 65% at 80% RH. This was first reported by Mihele and Hastie (Mihele et al., 1999a) and confirmed by other groups using PERCA instruments (Burkert et al., 2001; Sadanaga et al., 2004; Wood et al., 2017). Due to the high variability of relative humidity in ambient air, an accurate determination of the water dependence is therefore necessary to perform reliable measurements of peroxy radicals with PERCA.

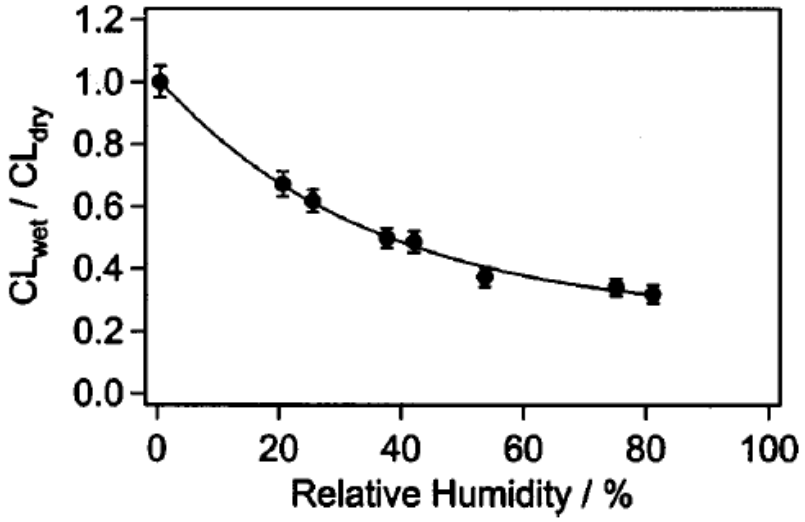

Figure 1.15 Dependence of the PERCA CL on relative humidity (T=20°C) (Sadanaga et al., 2004).

While the processes leading to the water dependence are still poorly understood, it is speculated that wet surfaces enhance the heterogeneous loss of radicals and, as a consequence, lead to higher termination rates when ambient water increases (Mihele et al., 1999; Miyazaki et al., 2010; Reichert et al., 2003). However, other possible explanations may involve the impact of H_2O dimers or $HO_2.H_2O$ adducts on gas-phase reactions, also leading to enhanced termination rates (Reichert et al., 2003):

R45 $OH + CO \ \ (presence\ of\ nH_2O) \ \rightarrow \ \text{non} - \text{radical products}$

R46 $CO + HO_2 \ \ (presence\ of\ nH_2O) \rightarrow \ CO_2 + OH$

R47 $HO_2.H_2O + NO + M \ \rightarrow HNO_3 + \ (faster\ rate\ than\ for\ HO_2)$

The effect of water-vapor on the HO_2+NO reaction pathway leading to HNO_3 formation was recently investigated and was found to favor the formation of HNO_3 (Butkovskaya et al., 2009), reaching an enhancement factor of about 8 at 50% relative humidity (T=25°C). It was therefore concluded that water vapor enhances the termination rate of R47 and may play a major role in the reduction of the chain length. Wood et al. (Wood et al., 2017) recently reported a new improvement to minimize the CL dependence on water by replacing CO by ethane (C_2H_6). This

different approach is now referred to as Ethane CHemical AMPlifier (ECHAMP) in the literature. The amplification chemistry for ECHAMP is shown below (R20a, R22, R24a, R48-R52).

R20a $RO_2 + NO \rightarrow RO + NO_2$

R22 $RO + O_2 \rightarrow R_{-H}O + HO_2$

R24a $HO_2 + NO \rightarrow OH + NO_2$

R48 $OH + C_2H_6 \rightarrow H_2O + C_2H_5$

R49 $C_2H_5 + O_2 + M \rightarrow C_2H_5O_2 + M$

R50a $C_2H_5O_2 + NO \rightarrow C_2H_5O + NO_2$

R50b $C_2H_5O_2 + NO + M \rightarrow C_2H_5ONO_2 + M$

R51 $C_2H_5O + O_2 \rightarrow CH_3CHO + HO_2$

R52 $C_2H_5O + NO + M \rightarrow C_2H_5ONO + M$

The first step for the propagation of sampled RO_2 radicals to HO_2 is similar to the PERCA approach (R20a, R22). Once HO_2 is formed, it propagates to OH through R24a, which then quickly reacts with ethane (R48) to form an ethyl peroxy radical ($C_2H_5O_2$). This peroxy radical propagates to the ethoxyl radical (C_2H_5O) through R50a, which further reacts with O_2 to reform HO_2. This propagation cycle is more complex than for CO and involves several addition steps where radicals can be lost (R50b, R52). For instance, when $C_2H_5O_2$ reacts with NO, a fraction of the reaction flux is channeled towards the formation of small yield of $C_2H_5ONO_2$. Similarly, C_2H_5O will also react with NO to form C_2H_5ONO. These two reactions lead to additional loss of radicals during the amplification chemistry and, as a consequence, to a lower CL. Indeed, Wood et al. (2017) reported a CL of 20 at 50% RH for ECHAMP, which is 4-6 times lower than the CL observed for PERCA

on the same apparatus (Figure 1.16). A close inspection of Figure 1.16 shows that ECHAMP is less sensitive to changes in water (factor 2 compared to factor 3 for PERCA) when relative humidity increases from 0 to 50% (Wood et al., 2017).

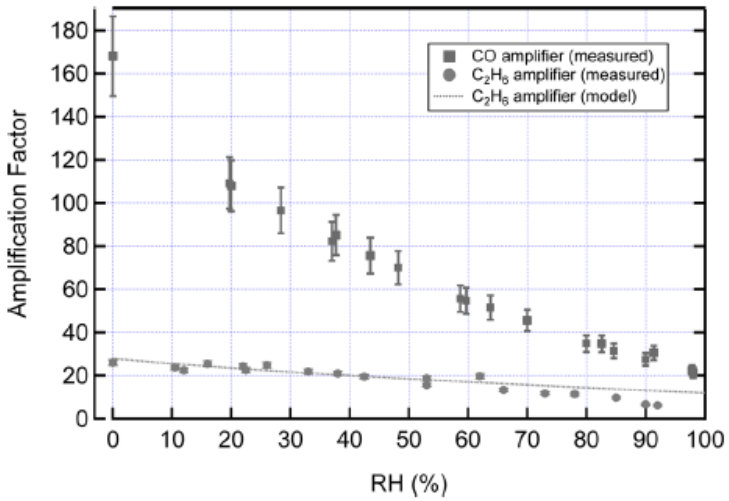

Figure 1.16 RH-dependence of the CL for both PERCA and ECHAMP (Wood et al., 2017).

For the field deployment, recent instruments using the PERCA or ECHAMP approaches are based on a dual-inlet system that allows concomitant measurements of NO_2 with and without amplification chemistry. The latter is called "background" and is achieved by replacing CO or ethane by an equivalent volumetric flow of N_2. This dual approach was first proposed by Cantrell et al. (Cantrell et al., 1996) to efficiently distinguish the NO_2 resulting from radical amplification from ambient NO_2 (and the conversion of ambient O_3 in the CA inlet). This approach, compared to intermittently shutting down the amplification chemistry for small periods of time in only one inlet, allows a more precise determination of the background NO_2. The difference in NO_2 between "amplification" and "background" measurements (ΔNO_2) represents the amount of NO_2 produced by chemical amplification of the sampled peroxy radicals and is used to compute the radical concentration from equation 1.1 using the known chain length determined from calibration.

$$[HO_2] + \sum[RO_2] = \frac{\Delta NO_2}{CL} \qquad (1.1)$$

In order to derive the sum of peroxy radicals from Equation 1.1, the chemical amplifier CL must be calibrated as a function of relative humidity. Also, calibration of NO_2 sensitivity are needed. To do so, it is necessary to generate a known concentration of HO_2, or another peroxy radical, that can be used to determine the CL from Equation 1.2.

$$CL = \frac{\Delta NO_2}{[HO_2 \text{or } RO_2]} \qquad (1.2)$$

PERCA instruments have been widely used in the field at a variety of sites over the past two decades (Cantrell et al., 1984; Green et al., 2003; Hernández et al., 2001; Kartal et al., 2010; Kundu et al., 2019; Liu et al., 2009; Wood and Charest, 2014) due to its portability, its low cost, and its low level of complexity. However, only a few groups are currently using this technique due to the chain length dependence on water vapor and the availability of other techniques.

1.2.4 Laser Induced Fluorescence-Fluorescence Assay by Gas Expansion (LIF-FAGE) & RO_x Laser Induced Fluorescence (RO_x-LIF)

The LIF-FAGE technique is based on direct and indirect LIF detection of OH and HO_2, respectively, after conversion of the latter into OH. This approach was first pioneered by Hard et al. (1984) and Stevens et al. (Stevens et al., 1994a) for tropospheric measurements of HO_x radicals. This technique was then used by several groups at ground level (Stevens et al., 1994a; Dusanter et al., 2009b; Faloona et al., 2004; Hard et al., 1984; Holland et al., 1995; Matsumi et al., 2002; Heal et al., 1995; Amedro et al., 2012a; Whalley et al., 2018a; Chan et al., 1990; Martinez et al., 2010) and in research airplanes (Commane et al., 2010; Faloona et al., 2004).

The LIF detection of OH requires the expansion of ambient air at low pressure (few Torr) and the excitation of OH using the $A^2\Sigma^+$ υ'=0 ← $X^2\Pi$ υ"= 0 transition band near 308 nm (Stevens et al., 1994b). The excited radicals emit radiation by fluorescene at the same wavelength (on-resonance), which is detected perpendicular to the excitation beam using a photodetector, either a photomultiplier tube or a micro channel plate. Short laser pulses at high repetition rates (typ. 10-20 ns at 1-10 kHz) allow the separation of the slowly decaying OH fluorescence signal from the quickly decaying scattered light using temporal filtering. A schematic of the University of Lille

FAGE instrument is shown in figure 1.17. This instrument is based on the Penn State design (2 white cells, an HO_2 cell downstream of an OH cell, P=1.5 Torr). Ambient air is pumped at approximately 9 L/min through a 1 mm pinhole. OH excitation at about 308 nm is accomplished using a 5 kHz rate pulsed laser (Spectra Physics Navigator + Sirah dye laser).

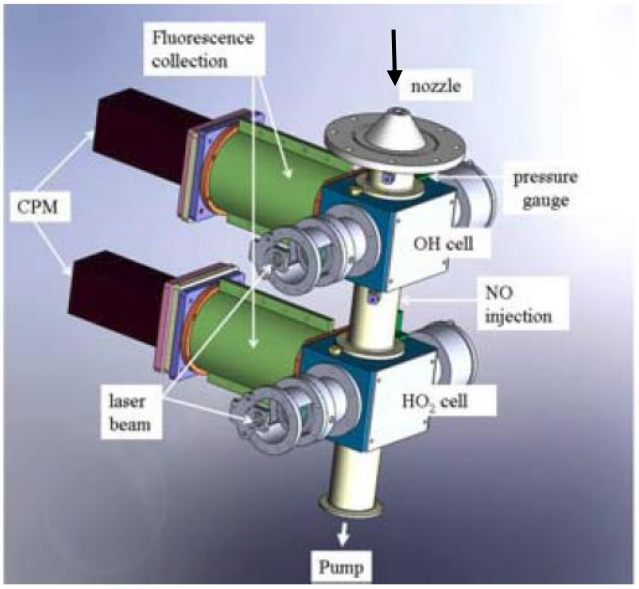

Figure 1.17: University of Lille-FAGE instrument (Amedro et al., 2012a).

This technique requires the generation of a known OH concentration at the FAGE nozzle to calibrate the fluorescence signal. The sensitivity in OH (C_{OH}) in cps ($cm^{-3}\,mW^{-1}$) is derived from the concentration OH generated in the radical generator ([OH]), the fraction of OH exiting the calibrator (L_{OH}), the laser power (P_W), and the measured fluorescence signal (S_{OH}) as shown in Equation 1.3

$$C_{OH} = \frac{S_{OH}}{[OH] \times L_{OH} \times Pw} \qquad (1.3)$$

The OH sensitivity depends on the lifetime of the OH excited state, which in turn depends on the probability of collisional deactivation. A higher pressure will lead to a higher probability for collisional deactivation (quenching) and thus a lower sensitivity. In addition to N_2 and O_2, OH is efficiently quenched by H_2O in ambient air. While N_2 and O_2 are present at constant mixing ratios

in the atmosphere, H_2O is highly variable (ranging from 1-3% near the earth's surface), and thus must be considered in calibrating the dependence of the OH response on water concentration (Dusanter et al., 2008a).

For HO_2 measurements, NO is added to the ambient airflow between the two detection cells, which converts HO_2 to OH (24a):

R24a $$HO_2 + NO \rightarrow OH + NO_2$$

The subsequent quantification of OH as previously described allows quantifying HO_2 if the HO_2-to-OH conversion efficiency is known. The later has to be determined by generating a known concentration of HO_2 at the FAGE nozzle. Similarly to OH (Eq. 1.3), the instrument sensitivity towards HO_2 can be calibrated.

A significant interference in HO_2 measurements was recently identified (Fuchs et al., 2011; Lew et al., 2018; Whalley et al., 2013), where some RO_2 radicals can be detected together with HO_2. This interference results from the fast conversion of large RO_2 and β-hydroxy-RO_2 radicals into alkoxyl radicals through their reaction with NO (R20a). These alkoxyl radicals then quickly react with ambient oxygen to generate HO_2 (R22).

R20a $$RO_2 + NO \rightarrow RO + NO_2$$

R22 $$RO + O_2 \rightarrow R_HO + HO_2$$

The disturbed HO_2 measurement is now referred to as HO_2^* since it corresponds to HO_2 plus a certain fraction of RO_2 radicals. However, it has been shown that this interference can be efficiently reduced by adjusting the chemical conversion conditions, i.e. by reducing the NO concentration in the sampling cell (Fuchs et al., 2008; Lew et al., 2018; Whalley et al., 2013). The conversion efficiency of HO_2 into OH mainly depends on the concentration of NO added into the detection cell. Lew et al. (2018) reported that using a low NO concentration (9×10^{11} cm^{-3}) for minimizing the interference from RO_2 radicals results in a conversion efficiency of approximately ~17% for HO_2 and a conversion efficiency of β-hydroxy-RO_2 radicals (isoprene-based) into OH lower than

1.7%. On the other hand, HO_2^* (HO_2 + alkene-based peroxy radicals) can be measured by introducing a higher NO concentration. In this case, the HO_2 conversion efficiency is approximately 80% and the β-hydroxy-RO_2 radicals (isoprene-based) conversion into HO_2 is close to 90% (Lew et al., 2018). Whalley et al. (2018) have shown that switching between low and high NO during ambient measurements allows measuring both HO_2 and the sum of alkene and aromatic-based RO_2 (called RO_2^i).

Both OH and HO_2 (or HO_2^*) are detected in the second detection axis (figure 1.17) after conversion of HO_2 (or HO_2 + alkene-based peroxy radicals) into OH, leading to the measurement of the sum of ambient OH and HO_2 (or HO_2^*). Subtracting the measured OH leads to HO_2 (or HO_2^*). Measurements are done with time resolution of a few seconds to a few minutes, with typical detection limits of ~10^5-10^6 molecule cm^{-3} for both OH and HO_2 (Heard and Pilling, 2003).

The FAGE technique was recently expanded to the measurement of HO_2 + RO_2 by the Forschungszentrum Julich group (Fuchs et al., 2008). This technique requires coupling a RO_2-to-HO_2 conversion flow-tube on top of the FAGE nozzle (only one detection cell required) and is now referred to as RO_x-LIF. A schematic diagram of the flow tube and the entrance to the LIF instrument is shown in Figure 1.18. In this technique, RO_2 radicals are converted into OH in a two-step process, involving the conversion of RO_2 into HO_2 in the flow-tube, and the conversion of HO_2 into OH in the FAGE detection cell. Two pumping systems are needed to independently adjust the pressure and other operating conditions in the RO_2-to-HO_2 conversion flow-tube and in the detection cell.

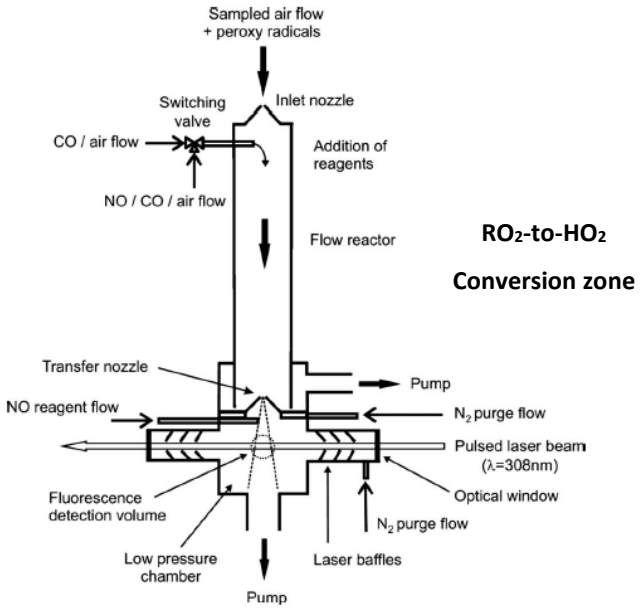

Figure 1.18 Schematic of the RO_x-LIF instrument (Fuchs et al., 2008) with sampling flow of 7 l min^{-1} at pressure of 19 torr.

Ambient air is sampled into the low pressure RO_2-to-HO_2 conversion flow-tube through a small pinhole. In this flow-tube, RO_2, RO and OH are converted into HO_2 as shown in R20a, R22, R11 and R9 by adding NO and CO after the sampling pinhole (Figure 1.18). This measurement mode is called "RO_x mode" since all RO_x radicals are then quantified in the FAGE detection cell as OH. When only CO is added as a reagent (no NO), only OH is converted into HO_2 (R11-12), leading to the quantification of OH+HO_2 in the detection cell. This measurement mode is called "HO_x mode".

R20a $$RO_2 + NO \rightarrow RO + NO_2$$

R22 $$RO + O_2 \rightarrow R_HO + HO_2$$

R11 $$OH + CO \rightarrow CO_2 + H$$

R9 $$H + O_2 + M \rightarrow HO_2 + M$$

The RO_x-LIF chamber shown in Figure 1.18 (Fuchs et al., 2008) is made of an aluminum tube (length: 830 mm, ID: 66mm), which is internally coated by Teflon. Ambient air is sampled at 7 L min^{-1} and is expanded through a conically shaped nozzle (orifice diameter; 1 mm) from ambient pressure to a reduced pressure of 19 Torr. The reagent gases are added at mixing ratios of 0.7 ppm and 0.17% for NO and CO, respectively, 20 mm downstream of the sampling nozzle. At the end of the conversion flow-tube, 3.5 L min^{-1} of air is sampled by another conically inlet nozzle (orifice diameter: 4 mm) into the FAGE detection cell where HO_2 is converted into OH by reaction with NO, as in regular FAGE instruments. OH is then quantified as described above for the FAGE technique. The optimum residence time to reach the highest sensitivity for the detection of RO_2 radicals is shown in figure 1.19 where experimental (symbols) and modelled (lines) sensitivities for the methyl peroxy radical (CH_3O_2) and HO_2 are displayed. The experimental sensitivity for ambient CH_3O_2 (solid square symbols) increases with the residence time to reach a maximum at a time of 0.61 s of residence time in the conversion flow-tube. In contrast, the ambient HO_2 sensitivity decreases continuously with increasing residence time due to wall losses inside the flow-tube.

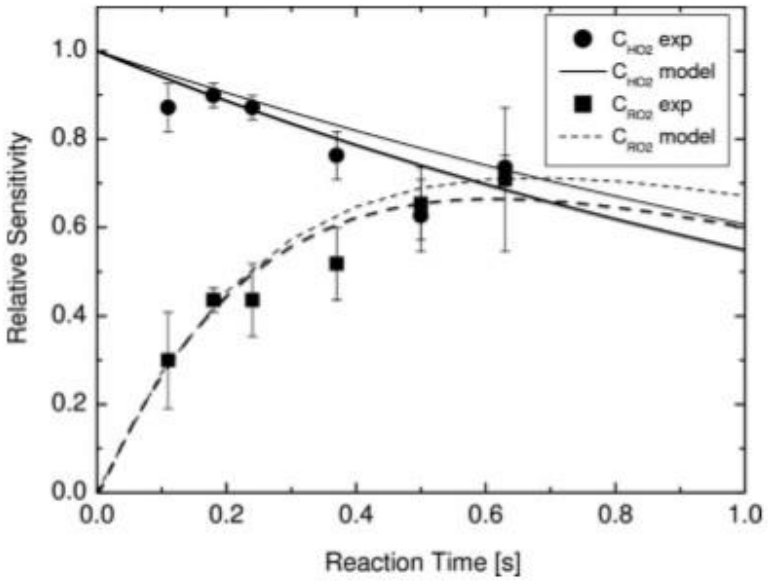

Figure 1.19 RO_x-LIF - Relative detection sensitivity for HO_2 and CH_3O_2 as a function of the gas residence time in the conversion flow-tube (Fuchs et al., 2008).

An investigation to determine optimum conditions for the NO and CO reagent gases was also performed as shown in figure 1.20 for NO (CO mixing ratio of 0.17%, 0.6 s of residence time

in the flow-tube). The modeled and experimental sensitivities for RO_2 increase with NO and reach maxima around 0.7 ppm of NO. For HO_2, the sensitivity decreases by approximately 8% when NO is increased from 0 to 0.7 ppm. The dependence of HO_2 and RO_2 sensitivities on ambient water was also investigated showing a decrease of approximately 10% of the sensitivity when the water mixing ratio is increased by 1%. This decrease in sensitivity is attributes to the OH fluorescence quenching by H_2O in the LIF detection cell.

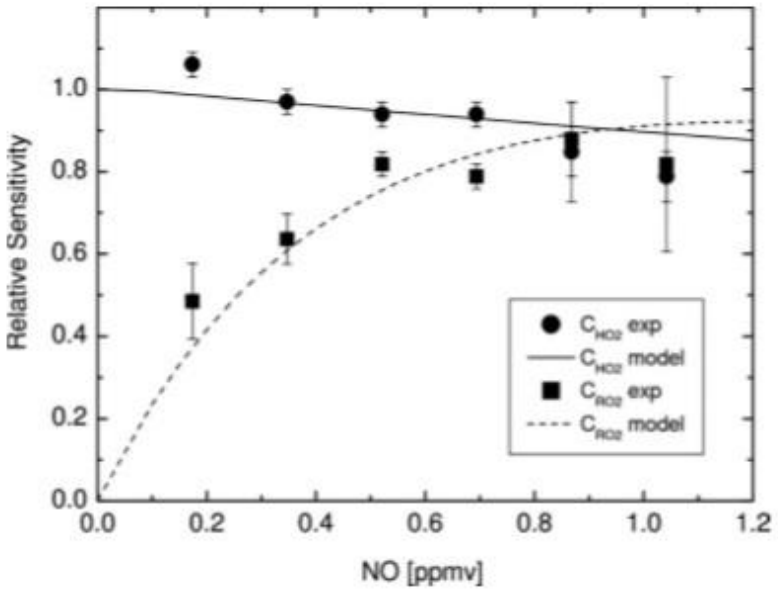

Figure 1.20 RO_x-LIF - Relative sensitivity for HO_2 and CH_3O_2 as a function of NO in the conversion flow-tube (Fuchs et al., 2008)

The detection sensitivity for different peroxy radicals was also measured and results are shown in table 1.3. This type of experiment is important to determine whether the instrumental response is similar for different RO_2. The sensitivity for most peroxy radicals, normalized to the CH_3O_2 sensitivity, was found to be within 10% of that observed for CH_3O_2. However, the sensitivity for isobutene-based RO_2 is lower by 40% and the sensitivity for isoprene-based RO_2 is higher by 20% than the CH_3O_2 sensitivity. The difference for isobutene-based RO_2 was attributed to a complex conversion chemistry of $(CH_3)_3CO_2$ into HO_2 requiring a longer residence time than 0.6 s to be completed. The discrepancy for isoprene-based RO_2 can be explained by experimental uncertainty which is 20% estimated from applied calibration method.

Table 1-2 RO_x-LIF - Experimental relative sensitivity for different RO_2 radicals (Fuchs et al., 2008)

Peroxy radicals	**Relative sensitivity (RO_2 sensitivity/ CH_3O_2 sensitivity)**
CH_3O_2	1
$CH_3CH_2O_2$	0.91
$C_2H_5CH_2O_2$, $(CH_3)2CHO_2$	0.96
$(CH_3)_3CO_2$, $(CH_3)_2CHCH_2O_2$	0.59
$CH_2(OH)CH_2O_2$	0.98
$C_5H_8(OH)O_2$	1.21

The LIF-FAGE and RO_x-LIF techniques exhibit several advantages: (i) Sampling at low pressure reduces the concentration of both O_3 and H_2O in the sampled air, as well as other trace gases, reducing interferences from the production of laser-generated OH as well as unwanted secondary chemistry (Stevens et al., 1994a); (ii) The fluorescence lifetime of the excited OH radical is extended to hundreds of nanoseconds due to lower quenching rates, allowing temporal filtering of the weak OH fluorescence from the scattered laser light (Stevens et al., 1994a). However, note that in contrast to MIESR, LIF-FAGE and RO_x-LIF can only measure the sum of RO_2 and cannot provide speciated measurements, with the exception of the alkene-based RO_2. This technique is relatively costly and requires highly specialized operators.

1.2.5 ROx calibration techniques

1.2.5.1 Water-photolysis technique

This source of radicals is based on photolysing water-vapor at about 185 nm in a flow of humid air (Schultz et al., 1995). An example of a calibration cell is shown in figure 1.21(Dusanter

et al., 2008a). This calibrator consists of a rectangular flow reactor made of aluminum and equipped with a suprasil window on two sides. The light source is a low-pressure mercury lamp housed in an aluminum cartridge that is continuously purged with dry nitrogen to avoid photolysis of oxygen in the lamp housing that would produce ozone, which in turn could filter the lamp emission. The irradiated region inside the calibration cell is the photolysis zone where the photolysis reactions take place. The lamp housing location along the calibrator can be adjusted to characterize the loss of radicals by changing the residence time in the calibrator. Both water and oxygen are photolyzed by the 185 nm radiation (R53):

R53 $H_2O + h\nu(\lambda = 185\ \text{nm}) \rightarrow \text{OH} + \text{H}$

R9 $H + O_2 + M \rightarrow HO_2 + M$

R54 $O_2 + h\nu \rightarrow O(^3P) + O(^3P)$

R38 $O\ ^3P + O_2 \rightarrow O_3$

The concentrations of OH and HO_2 can be calculated from Equation 1.4 where the product (F×t) is determined by O_2 actinometry (Eqs. 1.5 and 1.6).

$$[HO_2] = [OH] = [H_2O] \times \sigma_{water} \times \Phi_{OH+H} \times (F \times t) \quad (1.4)$$

$$[O_3] = [O_2] \times \sigma_{O_2} \times \Phi_{O_3} \times (F \times t) \quad (1.5)$$

$$(F \times t) = \frac{[O_3]}{2 \times [O_2] \times \sigma_{O_2}} \quad (1.6)$$

Where, [X] denotes the concentration of a species X, σ_x the absorption cross-section of a species X at about 185 nm, Φ_{OH+H} the photo-dissociation quantum yield of water into OH+H, F the photon flux, t is the photolysis time t, and Φ_{O3} the photo-dissociation quantum yield of oxygen.

The absorption cross section for H_2O at 185 nm reported in several studies is 7.14×10^{-20} cm^2 $molecule^{-1}$ (Cantrell et al., 1997; Creasey et al., 2000). The quantum yield reported for the production of OH and H is unity (Sander et al., 2006). The effective O_2 absorption cross section at

185 nm is close to $\sigma_{O2} = 1.2\times10^{-20}$ cm^{-2} as measured by Dusanter et al. (Dusanter et al., 2008a) and is setup dependent.

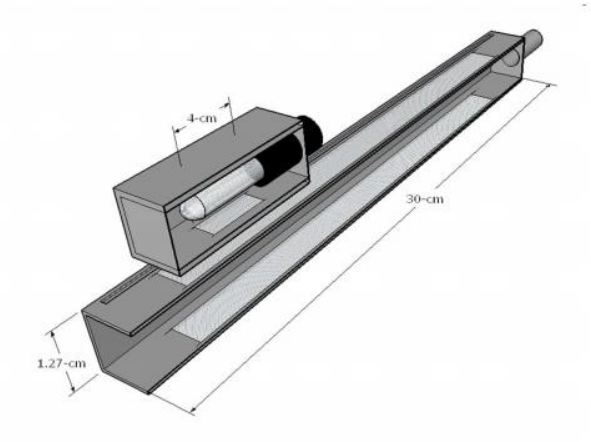

Figure 1.21 Cross-section view of the calibrator based on the water-vapor UV-photolysis technique (Dusanter et al., 2008a)

This type of calibrator can also be used to generate organic peroxy radicals by adding a VOC to the calibrator to convert the OH radicals before any wall loss occurs (Lew et al., 2018). For instance Lew et al. generated peroxy radicals from the OH oxidation of various alkenes (isoprene; ethene; trans-2-butene; tetramethylethylene), alkanes (propane, butane, octane), aromatic compounds (toluene) and oxygenated VOCs (methyl vinyl ketone, methacrolein, methyl ethyl ketone).

1.2.5.2 Other calibration sources of radicals

- Photolysis of methyl iodide (CH_3I)

The production of known concentrations of the methyl peroxy radical (CH_3O_2) can be achieved from the photolysis of methyl iodide (CH_3I) at 253.7 nm using a low-pressure mercury lamp (R55) (Clemitshaw et al., 1997; Green et al., 2006; Miyazaki et al., 2010) in air:

R55 $$CH_3I + hv(\lambda = 253.7\text{nm}) \rightarrow CH_3 + I$$

R13 $CH_3 + O_2 + M \rightarrow CH_3O_2 + M$

The reaction of CH_3O_2 with iodine atoms rapidly produces an adduct CH_3O_2I (R56). However, even at the highest radical concentration of 100 pptv generated with calibrators based on CH_3I photolysis, the adduct is estimated to be less than 10% of CH_3O_2 owing to its decomposition (R57) and its rapid reaction with iodine atoms which regenerates CH_3O_2. At lower concentrations of CH_3O_2 and I, the rate of R56 is negligible.

R56 $CH_3O_2 + I + M \rightarrow CH_3O_2I + M$

R57 $CH_3O_2I \rightarrow CH_3O_2 + I$

This source of radicals was used to calibrate PERCA instruments (Clemitshaw et al., 1997). The generated CH_3O_2 concentration is derived from the folowing equation:

$$[CH_3O_2] = J_{(CH_3I)} \times [CH_3I] \times t_{res}$$

Where the $J_{(CH_3I)}$ is the first-order photodissociation rate coefficient for CH_3I in the photolysis cell and t_{res} is its residence time within the photolysis zone.

- Photolysis of acetone $(CH_3)_2CO$

Known concentrations of CH_3O_2 and $CH_3C(O)O_2$ radicals can be generated by the photolysis of acetone at 253.7 nm using a low-pressure mercury lamp (R58) (Miyazaki et al., 2010; Wood and Charest, 2014):

R58 $(CH_3)_2CO + h\nu(\lambda = 253.7\text{nm}) \rightarrow CH_3 + CH_3CO$

R13 $CH_3 + O_2 + M \rightarrow CH_3O_2 + M$

R59 $CH_3CO + O_2 + M \rightarrow CH_3C(O)O_2 + M$

The calibration setup (Wood and Charest, 2014) is illustrated in Figure 1.22. A small flow of zero air (5 cm^3 min^{-1}) goes over the vapor headspace of acetone stored in a flask placed in ice water (0°C). This flow is diluted twice before entering the UV photolysis chamber. A second dilution occurrs after exiting from the photolysis chamber. The final acetone concentration is calculated based on its vapor pressure and the subsequent dilutions.

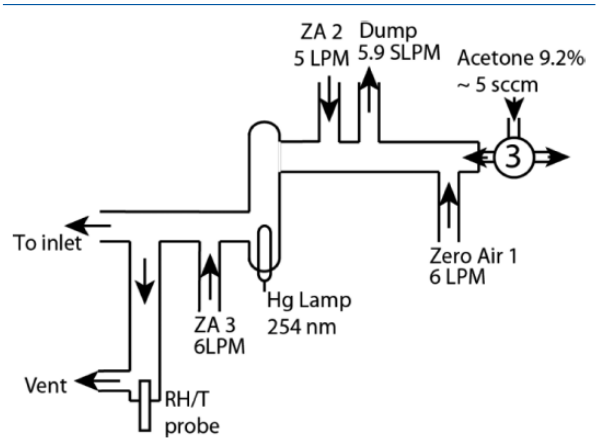

Figure 1.22 Schematic diagram of a radical calibration source based on acetone photolysis (Wood and Charest, 2014).

1.2.5.3 Summary of the measurement techniques

Amongst the four measurement techniques described above, three are currently used for atmospheric measurements of RO_x radicals, with the most widely used being CIMS and FAGE. To our knowledge, only three groups are still using a chemical amplifier (PERCA or ECHAMP) (Bremen's group from Germany, Leicester's group from UK, Ezra Wood's group from USA) worldwide. Table 1.4 below provides the figures of merit for these different techniques, including time resolution, detection limits and accuracy, and provides a qualitative summary of the advantages and drawbacks of each approach, highlighting some of the known limitations.

Table 1-3 Summary of established RO_x measurement techniques

Technique	Temporal Resolution	Limit of Detection (SNR=2) for OH and HO_2 (molecule cm^{-3})	2 σ Accuracy (%)	Advantages	Drawbacks
MIESR **HO_2, speciated RO_2**	**30 min**[**]	**5×10^7** [**]	**5**[**]	**Speciation of RO_2** **Good sensitivity**	**Offline technique, cryogenic** **Sample storage** **Sampling time of 30 mins** **Not in use anymore**
LIF-FAGE **HO_2, HO_2***	**few s - min**	**2×10^5 (OH)** **5×10^7 (HO_2)**	**20-40**	**Direct OH measurements** **Online technique** **Fast response**	**Indirect HO_2 measurements** **Interferences from RO_2 species during HO_2 measurements** **Cumbersome & expensive**
RO_x-LIF extension of FAGE **ΣHO_2+RO_2**	**1 min** [≠]	**2×10^6** [≠]	**±20** [≠]**(HO_2)**	**Same as LIF-FAGE** **Speciation HO_2 and $\sum RO_2$**	**Same as LIF-FAGE** **No speciation of RO_2 radicals**
CIMS ***HO_2, ΣHO_2+RO_2***	**10s - min**	**3×10^5-5×10^6**	**20-80**	**Online technique** **Fast response** **Possibility of speciation between HO_2 and $\sum RO_2$**	**Indirect measurements** **No speciation of RO_2 radicals** **Varying sensitivity between RO_2**
PERCA **ΣHO_2+RO_2**	**20s**	**2.5-7.5 $\times10^7$**	**25-45**	**Online technique** **Fast response** **Portable, cheap** **Easy to use**	**Indirect measurements** **Use of CO (PERCA) / not an issue for ECHAMP** **No speciation of peroxy radicals** **Water-dependent sensitivity**

HO_2* concentration in ambient air plus contributions from RO_2 interferences (Fuchs et al., 2011), [**](Mihelcic et al., 2003), [≠](Fuchs et al., 2008). References for the table: Report of the international HO_x workshop at Julich (Hofzumahaus and Heard, 2015).

1.3 Field measurements of RO_x radicals in the troposphere

Tropospheric measurements of OH, HO_2 and the sum of peroxy radicals have been performed in the atmosphere by a growing number of groups since the development of appropriate measurement techniques (Heard and Pilling, 2003; Stone et al., 2012; Dusanter and Stevens, 2017).

Research efforts have been devoted to better understand the photochemical oxidation of VOCs in the troposphere by comparing ambient measurements of RO_x radicals to zero-dimensional (0-D) simulations based on the most advanced chemical mechanisms published in the literature, including the Master Chemical Mechanism (MCM), the Regional Atmospheric Chemistry Mechanism 1 & 2 (RACM) (Goliff et al., 2013), the Leuven Isoprene Mechanism (LIM1) (Peeters, et al., 2009) and others. The 0-D models are constrained by measured long lived species and assume that the transport of radicals is unimportant. This assumption is based on the short lifetimes of the radicals, which are equal or less than 1, 60, and 100 s for OH, HO_2 and RO_2. The majority of published tropospheric radical measurements have been made at ground stations under a wide range of various atmospheric conditions, including clean air (marine boundary layer), continental low-NO_x regions influenced by biogenic emissions, polluted urban areas, and polar regions. Some of these studies have highlighted large differences between measured and modeled radicals at different sites and under different conditions. Differences between field measurements and model outputs suggest either either measurement artifacts or incomplete understanding of radical chemistry. A brief summary of the current understanding of both (i) measurement interferences and (ii) the radical chemistry in the above-mentioned enviroments are given below.

However, it is worth noting that a good agreement between measured and modeled OH concentrations may occur fortuitously if the rate of production from missing OH sources counterbalances the rate of destruction from missing OH sinks. Indeed, large missing OH sinks have been reported for forested areas (Edwards et al., 2013; Nölscher et al., 2016, 2012; Sinha et al., 2010) and significant missing OH reactivity was also reported for urban areas (Chen et al., 2010; Griffith et al., 2016; Dolgorouky et al., 2012) and in a marine area (Lee et al., 2009).

1.3.1 Interferences for OH and HO_2 measurements in FAGE and CIMS

FAGE and CIMS techniques are used by several groups around the world. FAGE is currently used by the National Centre for Atmospheric Science (NCAS)-Leeds (UK) (Heal et al., 1995; Ingham et al., 2009), the department of meteorology from Pennsylvania State University (US) (Stevens et al., 1994a, lew et al., 2018), the School of Public & Environmental Affairs from Indiana University (US) (Dusanter et al., 2009a), the PC2A laboratory from the University of Lille

(France) (Amedro et al., 2012a), the Forschungszentrum Jülich (Germany) (Holland et al., 1995), the Max Planck Institute (Germany) (Martinez et al., 2010), Peking University (China) (Tan et al., 2017) and the Japan Agency for Marine-Earth Science and Technology (Japan)(Kanaya et al., 2001b). The CIMS technique is used by the National Center for Atmospheric Research (US) (Edwards et al., 2003; Hornbrook et al., 2011), the LPC2E laboratory from the University of Orleans (France) (Kukui et al., 2008a), and the National University of Ireland Galway (Berresheim et al., 2000). As discussed above, these two techniques can measure tropospheric radicals with high sensitivity and appropriate limits of detection. Recently, the RO_x-LIF method developed by Fuchs et al. (Fuchs et al., 2008) was deployed in the field by the Jülich and Leeds groups (Fuchs et al., 2008; Tan et al., 2017, 2018b, 2019; Whalley et al., 2018a).

A. FAGE

As discussed previously, RO_2 species produced during the oxidation of VOCs, especially alkenes and aromatics, can interfere in the HO_2 measurements due to their conversion into HO_2 when NO is added in the FAGE detection cell (Fuchs et al., 2011; Lew et al., 2018; Whalley et al., 2013). However, the conversion efficiency of RO_2 is influenced by a number of operating conditions which vary considerably between different field instruments. (Fuchs et al., 2011) demonstrated that by changing the configuration of the FAGE cell or using lower concentrations of NO, the interference can changed considerably. Laboratory characterizations of this interference and the controlling parameters led the FAGE group to adjust operating conditions of their sampling systems and fluorescence cells to either minimize interferences for measuring HO_2 or to optimize the conversion of RO_2 into HO_2 to measure HO_2^*. As mentioned previously, Whalley et al. (2013) proposed to alternatively measure HO_2 and HO_2^* in order to derive the fraction of interfering RO_2, which are mainly alkene- and aromatic-based peroxy radicals. This is of particular interest since there is no field measurement of speciated RO_2.

In addition, OH interferences using FAGE have also been recently reported in the literature (Mao et al., 2010; Novelli et al., 2014; Fittschen et al., 2019; Lew et al., 2019), which seem to be related to the oxidation of biogenic VOCs or the reaction of OH with RO_2 species under pristine conditions. These studies have shown that a significant ambient interference was observed on both the Pennsylvania State(Mao et al., 2010) and Max Planck Institute (Novelli et al., 2014) instruments

during field measurements performed in forested areas. More recently, Lew et al. (2018) also observed an unknown source of interferences in the IU-FAGE during the 2015 IRRONIC campaign, which was found to increase with both ozone and temperature. Recently, Fuchs et al. (2016) have shown that under typical ambient concentrations of ozone and several biogenic compounds, their FAGE instrument does not detect any instrumental interferences. However, when high concentrations of ozone are reacted with high concentrations of α-pinene, limonene, or isoprene, a measurable OH interference is detected. The observed interference is strongly correlated with the ozonolysis rate coefficient and their results suggest that at atmospherically relevant rates, the interference is negligible. Rickly and Stevens (2018) also observed an interference using the IU-FAGE during ozonolysis experiments of BVOCs (α-pinene, β-pinene, ocimene, isoprene, and 2-methyl-3-buten-2-ol) when large concentrations of both ozone and BVOCs were used. This interference was found to be independent of the reaction time and the addition of acetic acid in the reactor eliminated it. This interference was attributed to the decomposition of stabilized Crieege intermediates inside the FAGE, which should be below detection limit in ambient air.

Recently, Fittschen et al. revealed a possible OH interference for FAGE instruments under low NO_x conditions (Fittschen et al., 2019). This OH interference results from the decomposition of a trioxide species (ROOOH) during the expansion within the FAGE detection cell. It was shown that this species is formed when RO_2 reacts with OH, requiring pristine atmospheric conditions to sufficiently extend the lifetime of RO_2 in the atmosphere. Box model simulations showed that ROOOH concentrations could be high enough in the atmosphere to generate the ambient interference that has been observed in several field studies. This study also highlighted that the intensity of this interference may be different between FAGE instruments due to the use of different designs and operating conditions.

OH interferences are now quantified on most FAGE instruments using a chemical modulation method of ambient OH (Lew et al., 2019; Mao et al., 2010; Novelli et al., 2014) , i.e. by scrubbing ambient OH and recording the remaining background signal as an interference that needs to be subtracted from ambient OH measurements.

B. CIMS

Interferences for CIMS instruments are linked to any species, such as Criegee intermediates (CH_2OO for instance), that have the capability to oxidize SO_2 into SO_3, which will then be detected as H_2SO_4, causing a positive bias in the OH measurements. This interference is quantified through chemical modulation by scrubbing ambient OH through the addition of propane in the inlet of the instrument. The assumption here is that propane will quickly react with OH but will not react with the interfering species. The interference, which is measured as a background signal, is then subtracted from ambient measurements of OH. A negative bias in OH measurements could also be due to losses of OH in the CIMS inlet once the air has been sampled but before the SO_2 injection point (for instance from the reaction of OH with trace gases). To the best of our knowledge, no interferences were reported for peroxy radical measurements.

C. Conclusions

With these kinds of difficulties, measuring radical species in the atmosphere is still considered challenging and the techniques need to continue used to be tested and improved. The development of other techniques would also help to fully assess the reliability of current instruments and to characterize the range of potentially interfering species.

1.3.2 Model-measurement comparisons of RO_x radicals

This section provides a brief description of measurement-model discrepancies observed in different environments and the suggestions reported in the literature to help solve some of the remaining uncertainties are given. This discussion is based on recent reviews published in the literature (Dusanter and Stevens, 2017.; Heard and Pilling, 2003; Stone et al., 2012; Whalley et al., 2013) and is mainly focused on HO_x radicals.

A. Marine boundary layer (MBL)

The MBL environment is characterized by clean air with low concentrations of reactive VOCs (NMHCs and OVOCs) and little or no influence from anthropogenic activities. Series of ground based field measurements of OH and HO_2 were performed in the MBL at Mace Head (Ireland), Cape Grim (Tasmania) and Cape Verde (Atlantic Ocean) (Heard et al., 2003; Stone et al., 2012 and references therein). These field campaigns suffered from a lack of supporting measurements and incomplete chemical mechanisms used to analyze the radical measurements often resulted in model overestimation of both OH and HO_2. Recently, it was shown that the chemistry of halogen oxide species has to be included in the models due to their large impact on speciated concentrations of RO_x. Indeed, it was shown that IO and BrO can lead to interconversions between OH and HO_2 (Lee et al., 2010). Future field measurements should improve the coverage of observations of NMHCs and OVOCs to better characterize OH sinks in model simulations and should include measurements of halogen oxide species to constrain the models.

There are also uncertainties related to HO_2 uptake coefficients onto aerosols and the heterogeneous loss of HO_2 still remains a significant source of uncertainty in determining its budget in this region. Further laboratory studies are needed to measure uptake coefficients of HO_2 onto real submicron particles (Stone et al., 2012).

B. Forested areas characterized by low NOx mixing ratios

The highest biogenic VOC emitted by the biosphere on a global scale is isoprene (~500 Tg C $year^{-1}$) (Guenther et al., 2012). Other biogenic compounds are also highly emitted in the atmosphere, including monoterpenes, sesquiterpenes and OVOCs. However, only a few studies have been performed in monoterpene and sesquiterpene rich-areas, such as pine forests (Mao et al., 2010; Novelli et al., 2014).

In the NO_x-poor isoprene-rich environments, the modeled OH concentrations are usually underestimated by a factor of 3-10 (Tan et al., 2001; Lelieveld et al., 2008; Pugh et al., 2010; Kubistin et al., 2010; Whalley et al., 2011; Kim et al., 2013). These studies suggest that the mechanisms for VOC oxidation are less well understood when reactions between peroxy radicals and NO do not dominate. These campaigns instigated new developments in the laboratory and

molecular dynamics and ab-initio calculations to investigate potential recycling pathways of radicals in the oxidation mechanism of isoprene and other BVOCs. Several new pathways of radical recycling were discovered, highlighting for example that reaction of OH with isoprene was not a large sink for OH as previously thought. This includes radical cycling in HO_2 + RO_2 reactions (Hasson et al., 2012), peroxy radical isomerization reactions (Peeters and Müller, 2010), and the reformation of OH during the oxidation of isoprene-based hydroperoxides (ISOPOOH) leading to the formation of epoxides (Paulot et al., 2009). However, while the implementation of these recycling mechanisms in models helped to get better agreement between simulated and measured OH concentrations, large differences remain.

As mentioned above, OH measurements using FAGE (employed during the above-studies) can be prone to interferences for FAGE instruments. It is likely that interferences impacted some of the OH measurements performed in forested areas and additional campaigns with improved versions of OH instruments are needed to test our current understanding of BVOC oxidation.

C. Polluted urban environments

Polluted urban regions are characterized by high levels of NO_x and anthropogenic VOCs. Models usually succeed at simulating the measured HO_x concentrations, with the exception of high NO_x conditions (> 5-15 ppb). Indeed, several studies (Martinez et al., 2003; Dusanter et al., 2009b; Whalley et al., 2018a; Ren et al., 2013; Brune et al., 2016) highlighted that disagreements of factors 2-10 between measured and modelled HO_2 concentrations when NO_x was higher than 5 ppb. Measurements were usually performed with the FAGE technique. Although potential interferences for HO_2 FAGE measurements from alkene- and aromatic-based RO_2 species need to be taken into account to confirm the conclusion of some of these studies, it seems unlikely that interferences alone could account for the disagreement. Indeed, these types of interferences were shown to account for 10-30% of the measured HO_2 under different operating conditions of the IU-FAGE instrument (Griffith et al., 2016; Lew et al., 2018), while the disagreement observed between HO_2 measurements and model simulations is significantly larger. These results seem to imply an incomplete understanding of the VOC oxidation chemistry under high NO_x conditions.

D. Polar environments

These remote locations are typically characterized by pristine conditions. The concentrations of both OH and HO_2 in these regions are usually elevated at high solar zenith angle and low concentrations of water vapor. The measured OH and HO_2 concentrations are usually overestimated by a factor of 2 by the models (Stone et al., 2012). Important precursors of HO_x radicals (HCHO and H_2O_2) are emitted from the snowpack (Honrath et al., 2002). However, there is a lack of high quality measurements of these precursors to constrain the box models. Moreover, some polar studies suggested that aerosols could act as a significant radical sink in this region but this suggestion is not well demonstrated yet due to the lack of reported data on reactive uptake coefficient of radicals on different types of aerosols under appropriate low temperature conditions.

1.4 Outline of Dissertation

Peroxy radicals are key species in the atmosphere due to their role in propagating OH during the oxidation of trace gases and their measurement is therefore essential to well understand the chemical processes driving atmospheric composition. For instance, peroxy radicals convert NO into NO_2 in areas characterized by high NO_x concentrations. This NO_2 is then photolyzed with the consequence of producing tropospheric ozone, which is harmful to humans and ecosytems and, which disturb the radiative balance of the earth's atmosphere. Thus, improving model simulations of HO_2 and RO_2 is essential to forecast the effects of the changing composition of the atmosphere on air quality and climate change.

The short lifetime of peroxy radicals due to their inherent high reactivity makes them ideal targets to test the chemistry implemented in atmospheric models. As discussed above, several techniques have been developed and used to quantify ambient concentrations of these radicals, including LIF-FAGE, RO_x-LIF, CIMS and Chemical Amplifiers. Field measurements of peroxy radicals have suffered from limitations related to interferences and the inability to distinguish different peroxy radicals. The use of improved instrumentation and potentially new measurement techniques can help improving our understanding of both radical measurements and atmospheric chemistry.

The PERCA technique was proposed more than 25 years ago, its development was put on hold when it was shown that its sensitivity was strongly dependent on ambient humidity. However, the

identification of a new amplification chemistry that is less sensitive to ambient humidity and the development of new NO_2 detectors suitable for chemical amplifiers provide a renewed interest in this technique. In addition, the recently proposed RO_x-LIF technique has the potential to speciate HO_2 and organic peroxy radicals.

The main objectives of this work is to improve our technological understanding of peroxy radicals in the troposphere. It consist of the following activities

1. Assemble and characterize two apparatus: a chemical amplifier using both the PERCA and ECHAMP approaches, and a RO_x-LIF system using an existing LIF-FAGE instrument,
2. Perform an intercomparison of the PERCA technique with a LIF-FAGE instrument from the University of Lille (France) and a CIMS instrument from the University of Orléans (France) at the HELIOS atmospheric chamber.

The methodology followed in this work is divided into 2 parts:

1. **First part: 18 months at IMT-Lille-Douai, SAGE, Douai (France)**
   - Construction of a dual channel amplifier,
   - Characterization and optimization of operating conditions for both the PERCA and ECHAMP approaches,
   - Field testing,
   - Intercomparison of the peroxy radical instruments at HELIOS.

2. **Second part: 18 months at Indiana University, School of Public and Environmental Affairs (SPEA) , Bloomington (US)**
   - Development of the RO_x-LIF conversion flow-tube and coupling to LIF-FAGE
   - Characterization and optimization of the operating conditions of the RO_x-LIF apparatus (operating conditions),
   - Indoor and outdoor field testing at the Research and Teaching Preserve (RTP), Bloomington, Indiana.

1.5 References

Acker, K., Möller, D., Wieprecht, W., Meixner, F.X., Bohn, B., Gilge, S., Plass-Dülmer, C., Berresheim, H., 2006. Strong daytime production of OH from HNO2 at a rural mountain site. Geophys. Res. Lett. 33. https://doi.org/10.1029/2005GL024643

Ahmed, M., Blunt, D., Chen, D., Suits, A.G., 1997. UV photodissociation of oxalyl chloride yields four fragments from one photon absorption. J. Chem. Phys. 106, 7617–7624.

Albrecht, S.R., Novelli, A., Hofzumahaus, A., Kang, S., Baker, Y., Mentel, T., Wahner, A., Fuchs, H., 2019. Measurements of hydroperoxy radicals (HO2) at atmospheric concentrations using bromide chemical ionisation mass spectrometry. Atmos Meas Tech 12, 891–902. https://doi.org/10.5194/amt-12-891-2019

Amedro, D., Miyazaki, K., Parker, A., Schoemaecker, C., Fittschen, C., 2012a. Atmospheric and kinetic studies of OH and HO2 by the FAGE technique. J. Environ. Sci. 24, 78–86. http://dx.doi.org/10.1016/S1001-0742(11)60723-7

Archibald, A.T., Levine, J.G., Abraham, N.L., Cooke, M.C., Edwards, P.M., Heard, D.E., Jenkin, M.E., Karunaharan, A., Pike, R.C., Monks, P.S., Shallcross, D.E., Telford, P.J., Whalley, L.K., Pyle, J.A., 2011. Impacts of HOx regeneration and recycling in the oxidation of isoprene: Consequences for the composition of past, present and future atmospheres. Geophys. Res. Lett. 38, n/a-n/a. https://doi.org/10.1029/2010GL046520

Ashbourn, S.F.M., Jenkin, M.E., Clemitshaw, K.C., 1998. Laboratory Studies of the Response of a Peroxy Radical Chemical Amplifier to HO2 and a Series of Organic Peroxy Radicals. J. Atmospheric Chem. 29, 233–266. https://doi.org/10.1023/a:1005992316512

Assaf, E., Tanaka, S., Kajii, Y., Schoemaecker, C., Fittschen, C., 2017. Rate constants of the reaction of C2–C4 peroxy radicals with OH radicals. Chem. Phys. Lett. 684, 245–249. https://doi.org/10.1016/j.cplett.2017.06.062

Atkinson, R., 2003. Kinetics of the gas-phase reactions of OH radicals with alkanes and cycloalkanes. Atmos Chem Phys 3, 2233–2307. https://doi.org/10.5194/acp-3-2233-2003

Atkinson, R., 2000. Atmospheric chemistry of VOCs and NOx. Atmos. Environ. 34, 2063–2101. http://dx.doi.org/10.1016/S1352-2310(99)00460-4

Atkinson, R., 1986. Kinetics and mechanisms of the gas-phase reactions of the hydroxyl radical with organic compounds under atmospheric conditions. Chem. Rev. 86, 69–201. https://doi.org/10.1021/cr00071a004

Atkinson, R., Arey, J., 2003. Atmospheric Degradation of Volatile Organic Compounds. Chem. Rev. 103, 4605–4638. https://doi.org/10.1021/cr0206420

Atkinson, R., Baulch, D.L., Cox, R.A., Crowley, J.N., Hampson, R.F., Hynes, R.G., Jenkin, M.E., Rossi, M.J., Troe, J., 2007. Evaluated kinetic and photochemical data for atmospheric chemistry: Volume III – gas phase reactions of inorganic halogens. Atmos Chem Phys 7, 981–1191. https://doi.org/10.5194/acp-7-981-2007

Atkinson, R., Baulch, D.L., Cox, R.A., Crowley, J.N., Hampson, R.F., Hynes, R.G., Jenkin, M.E., Rossi, M.J., Troe, J., 2004. Evaluated kinetic and photochemical data for atmospheric chemistry: Volume I - gas phase reactions of O_x, HO_x, NO_x and SO_x species. Atmos Chem Phys 4, 1461–1738. https://doi.org/10.5194/acp-4-1461-2004

Atkinson, R., Baulch, D.L., Cox, R.A., Crowley, J.N., Hampson, R.F., Hynes, R.G., Jenkin, M.E., Rossi, M.J., Troe, J., IUPAC Subcommittee, 2006. Evaluated kinetic and photochemical data for atmospheric

chemistry: Volume II – gas phase reactions of organic species. Atmos Chem Phys 6, 3625–4055. https://doi.org/10.5194/acp-6-3625-2006

Atkinson, R., Baulch, D.L., Cox, R.A., Hampson, R.F., Kerr, J.A., Rossi, M.J., Troe, J., 1997a. Evaluated Kinetic, Photochemical and Heterogeneous Data for Atmospheric Chemistry: Supplement V. IUPAC Subcommittee on Gas Kinetic Data Evaluation for Atmospheric Chemistry. J. Phys. Chem. Ref. Data 26, 521–1011. https://doi.org/10.1063/1.556011

Atkinson, Roger., Tuazon, E.C., Aschmann, S.M., 1995. Products of the Gas-Phase Reactions of O3 with Alkenes. Environ. Sci. Technol. 29, 1860–1866. https://doi.org/10.1021/es00007a025

Avzianova, E.V., Ariya, P.A., 2002. Temperature-dependent kinetic study for ozonolysis of selected tropospheric alkenes. Int. J. Chem. Kinet. 34, 678–684. https://doi.org/10.1002/kin.10093

Bailey, A.E., Heard, D.E., Paul, P.H., Pilling, M.J., 1997. Collisional quenching of OH (A 2Σ+, v′ = 0) by N2, O2 and CO2 between 204 and 294 K. Implications for atmospheric measurements of OH by laser-induced fluorescence. J Chem Soc Faraday Trans 93, 2915–2920. https://doi.org/10.1039/A701582H

Baker, J., Aschmann, S.M., Arey, J., Atkinson, R., 2002. Reactions of stabilized criegee intermediates from the gas-phase reactions of O3 with selected alkenes. Int. J. Chem. Kinet. 34, 73–85. https://doi.org/10.1002/kin.10022

Baklanov, A.V., Krasnoperov, L.N., 2001. Oxalyl Chloride A Clean Source of Chlorine Atoms for Kinetic Studies. J. Phys. Chem. A 105, 97–103.

Berresheim, H., Elste, T., Plass-Dülmer, C., Eiseleb, F.L., Tannerb, D.J., 2000. Chemical ionization mass spectrometer for long-term measurements of atmospheric OH and H2SO4. Int. J. Mass Spectrom. 202, 91–109. http://dx.doi.org/10.1016/S1387-3806(00)00233-5

Berresheim, H., Elste, T., Tremmel, H.G., Allen, A.G., Hansson, H.C., Rosman, K., Dal Maso, M., Mäkelä, J.M., Kulmala, M., O'Dowd, C.D., 2002. Gas-aerosol relationships of H2SO4, MSA, and OH: Observations in the coastal marine boundary layer at Mace Head, Ireland. J. Geophys. Res. Atmospheres 107, PAR 5-1-PAR 5-12. https://doi.org/10.1029/2000JD000229

Bossolasco, A., Faragó, E.P., Schoemaecker, C., Fittschen, C., 2014. Rate constant of the reaction between CH3O2 and OH radicals. Chem. Phys. Lett. 593, 7–13. https://doi.org/10.1016/j.cplett.2013.12.052

Boyd, A.A., Flaud, P.-M., Daugey, N., Lesclaux, R., 2003. Rate Constants for RO2 + HO2 Reactions Measured under a Large Excess of HO2. J. Phys. Chem. A 107, 818–821. https://doi.org/10.1021/jp026581r

Braure, T., Bedjanian, Y., Romanias, M.N., Morin, J., Riffault, V., Tomas, A., Coddeville, P., 2014. Experimental Study of the Reactions of Limonene with OH and OD Radicals: Kinetics and Products. J. Phys. Chem. A 118, 9482–9490. https://doi.org/10.1021/jp507180g

Brune, W.H., Baier, B.C., Thomas, J., Ren, X., Cohen, R.C., Pusede, S.E., Browne, E.C., Goldstein, A.H., Gentner, D.R., Keutsch, F.N., Thornton, J.A., Harrold, S., Lopez-Hilfiker, F.D., Wennberg, P.O., 2016. Ozone production chemistry in the presence of urban plumes. Faraday Discuss. 189, 169–189. https://doi.org/10.1039/C5FD00204D

Burkert, J., Behmann, T., Andrés Hernández, M.D., Stöbener, D., Weißenmayer, M., Perner, D., Burrows, J.P., 2001. Measurements of peroxy radicals in a forested area of Portugal. Field Stud. Atmospheric Chem. Volatile Org. Compd. Emit. Eucalyptus For. FIELDVOC94 3, 327–338. https://doi.org/10.1016/S1465-9972(01)00014-9

Butkovskaya, N., Kukui, A., Le Bras, G., 2007. HNO3 Forming Channel of the HO2 + NO Reaction as a Function of Pressure and Temperature in the Ranges of 72−600 Torr and 223−323 K. J. Phys. Chem. A 111, 9047–9053. https://doi.org/10.1021/jp074117m

Butkovskaya, N., Rayez, M.-T., Rayez, J.-C., Kukui, A., Le Bras, G., 2009. Water Vapor Effect on the HNO3 Yield in the HO2 + NO Reaction: Experimental and Theoretical Evidence. J. Phys. Chem. A 113, 11327–11342. https://doi.org/10.1021/jp811428p

Calvert, J., Mellouki, A., Orlando, J., 2011. Mechanisms of atmospheric oxidation of the oxygenates. OUP USA.

Cantrell, C.A., Shetter, R.E., Calvert, J.G., 1996. Dual-Inlet Chemical Amplifier for Atmospheric Peroxy Radical Measurements. Anal. Chem. 68, 4194–4199. https://doi.org/10.1021/ac960639e

Cantrell, C.A., Stedman, D.H., Wendel, G.J., 1984. Measurement of atmospheric peroxy radicals by chemical amplification. Anal. Chem. 56, 1496–1502. https://doi.org/10.1021/ac00272a065

Cantrell, C.A., Zimmer, A., Tyndall, G.S., 1997. Absorption cross sections for water vapor from 183 to 193 nm. Geophys. Res. Lett. 24, 2195–2198. https://doi.org/10.1029/97GL02100

Chan, C.Y., Hard, T.M., Mehrabzadeh, A.A., George, L.A., O'Brien, R.J., 1990. Third-generation FAGE instrument for tropospheric hydroxyl radical measurement. J. Geophys. Res. Atmospheres 95, 18569–18576. https://doi.org/10.1029/JD095iD11p18569

Chen, S., Ren, X., Mao, J., Chen, Z., Brune, W.H., Lefer, B., Rappenglück, B., Flynn, J., Olson, J., Crawford, J.H., 2010. A comparison of chemical mechanisms based on TRAMP-2006 field data. Atmos. Environ. 44, 4116–4125. http://dx.doi.org/10.1016/j.atmosenv.2009.05.027

Chen, X., Millet, D.B., Singh, H.B., Wisthaler, A., Apel, E.C., Atlas, E.L., Blake, D.R., Bourgeois, I., Brown, S.S., Crounse, J.D., de Gouw, J.A., Flocke, F.M., Fried, A., Heikes, B.G., Hornbrook, R.S., Mikoviny, T., Min, K.-E., Müller, M., Neuman, J.A., O'Sullivan, D.W., Peischl, J., Pfister, G.G., Richter, D., Roberts, J.M., Ryerson, T.B., Shertz, S.R., Thompson, C.R., Treadaway, V., Veres, P.R., Walega, J., Warneke, C., Washenfelder, R.A., Weibring, P., Yuan, B., 2019. On the sources and sinks of atmospheric VOCs: an integrated analysis of recent aircraft campaigns over North America. Atmos Chem Phys 19, 9097–9123. https://doi.org/10.5194/acp-19-9097-2019

Clemitshaw, K., 2004. A Review of Instrumentation and Measurement Techniques for Ground-Based and Airborne Field Studies of Gas-Phase Tropospheric Chemistry. Crit. Rev. Environ. Sci. Technol. 34, 1–108. https://doi.org/10.1080/10643380490265117

Clemitshaw, K.C., Carpenter, L.J., Penkett, S.A., Jenkin, M.E., 1997. A calibrated peroxy radical chemical amplifier for ground-based tropospheric measurements. J. Geophys. Res. Atmospheres 102, 25405–25416. https://doi.org/10.1029/97JD01902

Commane, R., Floquet, C.F.A., Ingham, T., Stone, D., Evans, M.J., Heard, D.E., 2010. Observations of OH and HO2 radicals over West Africa. Atmos Chem Phys 10, 8783–8801. https://doi.org/10.5194/acp-10-8783-2010

Creasey, D.J., Evans, G.E., Heard, D.E., Lee, J.D., 2003. Measurements of OH and HO2 concentrations in the Southern Ocean marine boundary layer. J. Geophys. Res. Atmospheres 108, n/a-n/a. https://doi.org/10.1029/2002JD003206

Creasey, D.J., Heard, D.E., Lee, J.D., 2000. Absorption cross-section measurements of water vapour and oxygen at 185 nm. Implications for the calibration of field instruments to measure OH, HO2 and RO2 radicals. Geophys. Res. Lett. 27, 1651–1654. https://doi.org/10.1029/1999GL011014

Dolgorouky, C., Gros, V., Sarda-Esteve, R., Sinha, V., Williams, J., Marchand, N., Sauvage, S., Poulain, L., Sciare, J., Bonsang, B., 2012. Total OH reactivity measurements in Paris during the 2010 MEGAPOLI winter campaign. Atmos Chem Phys 12, 9593–9612. https://doi.org/10.5194/acp-12-9593-2012

Dusanter, S., Stevens, P.S., 2017. Recent Advances in the Chemistry of OH and HO^2 Radicals in the Atmosphere: Field and Laboratory Measurements, in: Advances in Atmospheric Chemistry. pp. 493–579. https://doi.org/10.1142/9789813147355_0007

Dusanter, S., Vimal, D., Stevens, P.S., 2008a. Technical note: Measuring tropospheric OH and HO_2 by laser-induced fluorescence at low pressure. A comparison of calibration techniques. Atmos Chem Phys 8, 321–340. https://doi.org/10.5194/acp-8-321-2008

Dusanter, S., Vimal, D., Stevens, P.S., Volkamer, R., Molina, L.T., 2009a. Measurements of OH and HO_2 concentrations during the MCMA-2006 field campaign – Part 1: Deployment of the Indiana University laser-induced fluorescence instrument. Atmos Chem Phys 9, 1665–1685. https://doi.org/10.5194/acp-9-1665-2009

Dusanter, S., Vimal, D., Stevens, P.S., Volkamer, R., Molina, L.T., Baker, A., Meinardi, S., Blake, D., Sheehy, P., Merten, A., Zhang, R., Zheng, J., Fortner, E.C., Junkermann, W., Dubey, M., Rahn, T., Eichinger, B., Lewandowski, P., Prueger, J., Holder, H., 2009b. Measurements of OH and HO_2 concentrations during the MCMA-2006 field campaign – Part 2: Model comparison and radical budget. Atmos Chem Phys 9, 6655–6675. https://doi.org/10.5194/acp-9-6655-2009

Edwards, G.D., Cantrell, C.A., Stephens, S., Hill, B., Goyea, O., Shetter, R.E., Mauldin, R.L., Kosciuch, E., Tanner, D.J., Eisele, F.L., 2003. Chemical Ionization Mass Spectrometer Instrument for the Measurement of Tropospheric HO2 and RO2. Anal. Chem. 75, 5317–5327. https://doi.org/10.1021/ac034402b

Edwards, P.M., Evans, M.J., Furneaux, K.L., Hopkins, J., Ingham, T., Jones, C., Lee, J.D., Lewis, A.C., Moller, S.J., Stone, D., Whalley, L.K., Heard, D.E., 2013. OH reactivity in a South East Asian tropical rainforest during the Oxidant and Particle Photochemical Processes (OP3) project. Atmos Chem Phys 13, 9497–9514. https://doi.org/10.5194/acp-13-9497-2013

Ehn, M., Thornton, J.A., Kleist, E., Sipilä, M., Junninen, H., Pullinen, I., Springer, M., Rubach, F., Tillmann, R., Lee, B., 2014. A large source of low-volatility secondary organic aerosol. Nature 506, 476.

Elshorbany, Y.F., Kleffmann, J., Kurtenbach, R., Lissi, E., Rubio, M., Villena, G., Gramsch, E., Rickard, A.R., Pilling, M.J., Wiesen, P., 2010. Seasonal dependence of the oxidation capacity of the city of Santiago de Chile. Atmospheric Chem. Mech. Sel. Pap. 2008 Conf. 44, 5383–5394. https://doi.org/10.1016/j.atmosenv.2009.08.036

Faloona, I.C., Tan, D., Lesher, R.L., Hazen, N.L., Frame, C.L., Simpas, J.B., Harder, H., Martinez, M., Di Carlo, P., Ren, X., 2004. A laser-induced fluorescence instrument for detecting tropospheric OH and HO2: Characteristics and calibration. J. Atmospheric Chem. 47, 139–167.

Faragó, E.P., Schoemaecker, C., Viskolcz, B., Fittschen, C., 2015. Experimental determination of the rate constant of the reaction between C2H5O2 and OH radicals. Chem. Phys. Lett. 619, 196–200. https://doi.org/10.1016/j.cplett.2014.11.069

Finlayson-Pitts, B.J., Jr, J.N.P., 2000. {CHAPTER} 5 - Kinetics and Atmospheric Chemistry, in: Finlayson-Pitts, B.J., Pitts, J.N. (Eds.), Chemistry of the Upper and Lower Atmosphere. Academic Press, San Diego, pp. 130–178. https://doi.org/10.1016/B978-012257060-5/50007-1

Finlayson-Pitts, B.J., Pitts, J.N. (Eds.), 2000. Acknowledgments, in: Chemistry of the Upper and Lower Atmosphere. Academic Press, San Diego, pp. xxi–xxii. https://doi.org/10.1016/B978-012257060-5/50002-2

Finlayson-Pitts, B.J., Pitts Jr, J.N., 2000. CHAPTER 6 - Rates and Mechanisms of Gas-Phase Reactions in Irradiated Organic – NOx – Air Mixtures, in: Chemistry of the Upper and Lower Atmosphere. Academic Press, San Diego, pp. 179–263.

Fittschen, C., Al Ajami, M., Batut, S., Ferracci, V., Archer-Nicholls, S., Archibald, A.T., Schoemaecker, C., 2019. ROOOH: a missing piece of the puzzle for OH measurements in low-NO environments? Atmos Chem Phys 19, 349–362. https://doi.org/10.5194/acp-19-349-2019

Fittschen, C., Whalley, L.K., Heard, D.E., 2014. The Reaction of CH3O2 Radicals with OH Radicals: A Neglected Sink for CH3O2 in the Remote Atmosphere. Environ. Sci. Technol. 48, 7700–7701. https://doi.org/10.1021/es502481q

Fleming, Z.L., Monks, P.S., Rickard, A.R., Heard, D.E., Bloss, W.J., Seakins, P.W., Still, T.J., Sommariva, R., Pilling, M.J., Morgan, R., Green, T.J., Brough, N., Mills, G.P., Penkett, S.A., Lewis, A.C., Lee, J.D., Saiz-Lopez, A., Plane, J.M.C., 2006. Peroxy radical chemistry and the control of ozone photochemistry at Mace Head, Ireland during the summer of 2002. Atmos Chem Phys 6, 2193–2214. https://doi.org/10.5194/acp-6-2193-2006

Fuchs, H., Bohn, B., Hofzumahaus, A., Holland, F., Lu, K.D., Nehr, S., Rohrer, F., Wahner, A., 2011. Detection of HO_2 by laser-induced fluorescence: calibration and interferences from RO_2 radicals. Atmos Meas Tech 4, 1209–1225. https://doi.org/10.5194/amt-4-1209-2011

Fuchs, H., Brauers, T., Dorn, H.P., Harder, H., Häseler, R., Hofzumahaus, A., Holland, F., Kanaya, Y., Kajii, Y., Kubistin, D., Lou, S., Martinez, M., Miyamoto, K., Nishida, S., Rudolf, M., Schlosser, E., Wahner, A., Yoshino, A., Schurath, U., 2010. Technical Note: Formal blind intercomparison of HO_2 measurements in the atmosphere simulation chamber SAPHIR during the HOxComp campaign. Atmos Chem Phys 10, 12233–12250. https://doi.org/10.5194/acp-10-12233-2010

Fuchs, H., Holland, F., Hofzumahaus, A., 2008. Measurement of tropospheric RO2 and HO2 radicals by a laser-induced fluorescence instrument. Rev. Sci. Instrum. 79, 084104. https://doi.org/10.1063/1.2968712

Fuchs, H., Tan, Z., Hofzumahaus, A., Broch, S., Dorn, H.P., Holland, F., Künstler, C., Gomm, S., Rohrer, F., Schrade, S., Tillmann, R., Wahner, A., 2016. Investigation of potential interferences in the detection of atmospheric ROx radicals by laser-induced fluorescence under dark conditions. Atmos Meas Tech 9, 1431–1447. https://doi.org/10.5194/amt-9-1431-2016

Geyer, A., Alicke, B., Konrad, S., Schmitz, T., Stutz, J., Platt, U., 2001. Chemistry and oxidation capacity of the nitrate radical in the continental boundary layer near Berlin. J. Geophys. Res. Atmospheres 106, 8013–8025. https://doi.org/10.1029/2000JD900681

Goldstein, A.H., Galbally, I.E., 2007. Known and Unexplored Organic Constituents in the Earth's Atmosphere. Environ. Sci. Technol. 41, 1514–1521. https://doi.org/10.1021/es072476p

Green, T.J., Reeves, C.E., Brough, N., Edwards, G.D., Monks, P.S., Penkett, S.A., 2003. Airborne measurements of peroxy radicals using the PERCA technique. J Env. Monit 5, 75–83.

Green, T.J., Reeves, C.E., Fleming, Z.L., Brough, N., Rickard, A.R., Bandy, B.J., Monks, P.S., Penkett, S.A., 2006. An improved dual channel PERCA instrument for atmospheric measurements of peroxy radicals. J. Environ. Monit. 8, 530–536. https://doi.org/10.1039/B514630E

Griffith, S.M., Hansen, R.F., Dusanter, S., Michoud, V., Gilman, J.B., Kuster, W.C., Veres, P.R., Graus, M., de Gouw, J.A., Roberts, J., Young, C., Washenfelder, R., Brown, S.S., Thalman, R., Waxman, E., Volkamer, R., Tsai, C., Stutz, J., Flynn, J.H., Grossberg, N., Lefer, B., Alvarez, S.L., Rappenglueck, B., Mielke, L.H., Osthoff, H.D., Stevens, P.S., 2016. Measurements of hydroxyl and hydroperoxy radicals during CalNex-LA: Model comparisons and radical budgets. J. Geophys. Res. Atmospheres 121, 4211–4232. https://doi.org/10.1002/2015JD024358

Griffith, S.M., Hansen, R.F., Dusanter, S., Stevens, P.S., Alaghmand, M., Bertman, S.B., Carroll, M.A., Erickson, M., Galloway, M., Grossberg, N., Hottle, J., Hou, J., Jobson, B.T., Kammrath, A., Keutsch, F.N., Lefer, B.L., Mielke, L.H., O'Brien, A., Shepson, P.B., Thurlow, M., Wallace, W., Zhang, N., Zhou, X.L., 2013a. OH and HO_2 radical chemistry during PROPHET 2008 and CABINEX 2009 – Part 1: Measurements and model comparison. Atmos Chem Phys 13, 5403–5423. https://doi.org/10.5194/acp-13-5403-2013

Groß, C., Dillon, T., Schuster, G., Lelieveld, J., Crowley, J., 2014. Direct kinetic study of OH and O3 formation in the reaction of CH3C (O) O2 with HO2. J. Phys. Chem. A 118, 974–985.

Guenther, A., Hewitt, C.N., Erickson, D., Fall, R., Geron, C., Graedel, T., Harley, P., Klinger, L., Lerdau, M., McKay, W.A., Pierce, T., Scholes, B., Steinbrecher, R., Tallamraju, R., Taylor, J., Zimmerman, P., 1995. A global model of natural volatile organic compound emissions. J. Geophys. Res. Atmospheres 100, 8873–8892. https://doi.org/10.1029/94JD02950

Guenther, A.B., Jiang, X., Heald, C.L., Sakulyanontvittaya, T., Duhl, T., Emmons, L.K., Wang, X., 2012. The Model of Emissions of Gases and Aerosols from Nature version 2.1 (MEGAN2.1): an extended and updated framework for modeling biogenic emissions. Geosci Model Dev 5, 1471–1492. https://doi.org/10.5194/gmd-5-1471-2012

Hanke, M., Uecker, J., Reiner, T., Arnold, F., 2002. Atmospheric peroxy radicals: ROXMAS, a new mass-spectrometric methodology for speciated measurements of HO2 and ∑RO2 and first results. Int. J. Mass Spectrom. 213, 91–99. http://dx.doi.org/10.1016/S1387-3806(01)00548-6

Hard, T.M., O'Brien, R.J., Chan, C.Y., Mehrabzadeh, A.A., 1984. Tropospheric free radical determination by fluorescence assay with gas expansion. Environ. Sci. Technol. 18, 768–777. https://doi.org/10.1021/es00128a009

Hasson, A.S., Tyndall, G.S., Orlando, J.J., 2004. A Product Yield Study of the Reaction of HO2 Radicals with Ethyl Peroxy (C2H5O2), Acetyl Peroxy (CH3C(O)O2), and Acetonyl Peroxy (CH3C(O)CH2O2) Radicals. J. Phys. Chem. A 108, 5979–5989. https://doi.org/10.1021/jp048873t

Hasson, A.S., Tyndall, G.S., Orlando, J.J., Singh, S., Hernandez, S.Q., Campbell, S., Ibarra, Y., 2012. Branching Ratios for the Reaction of Selected Carbonyl-Containing Peroxy Radicals with Hydroperoxy Radicals. J. Phys. Chem. A 116, 6264–6281. https://doi.org/10.1021/jp211799c

He, Y., Zhou, X., Hou, J., Gao, H., Bertman, S.B., 2006. Importance of dew in controlling the air-surface exchange of HONO in rural forested environments. Geophys. Res. Lett. 33. https://doi.org/10.1029/2005GL024348

Heal, M.R., Heard, D.E., Pilling, M.J., Whitaker, B.J., 1995. On the Development and Validation of FAGE for Local Measurement of Tropospheric OH and H02. J. Atmospheric Sci. 52, 3428–3441. https://doi.org/10.1175/1520-0469(1995)052<3428:OTDAVO>2.0.CO;2

Heard, D.E., 2006. Atmospheric field measurements of the hydroxyl radical using laser-induced fluorescence spectroscopy. Annu. Rev. Phys. Chem. 57, 191–216. https://doi.org/10.1146/annurev.physchem.57.032905.104516

Heard, D.E., Pilling, M.J., 2003. Measurement of OH and HO_2 in the Troposphere. Chem. Rev. 103, 5163–5198. https://doi.org/10.1021/cr020522s

Hemmi, N., Suits, A.G., 1997. Photodissociation of oxalyl chloride at 193 nm probed via synchrotron radiation. J. Phys. Chem. A 101, 6633–6637.

Hendrik Fuchs, Frank Holland, Andreas Hofzumahaus, 2008. Measurement of tropospheric RO2 and HO2 radicals by a laser-induced fluorescence instrument. Rev. Sci. Instrum. 79, 084104. https://doi.org/10.1063/1.2968712

Hernández, M.D.A., Burkert, J., Reichert, L., Stöbener, D., Meyer-Arnek, J., Burrows, J.P., Dickerson, R.R., Doddridge, B.G., 2001. Marine boundary layer peroxy radical chemistry during the AEROSOLS99 campaign: Measurements and analysis. J. Geophys. Res. Atmospheres 106, 20833–20846. https://doi.org/10.1029/2001JD900113

Hewitt, C.N., Lee, J.D., MacKenzie, A.R., Barkley, M.P., Carslaw, N., Carver, G.D., Chappell, N.A., Coe, H., Collier, C., Commane, R., Davies, F., Davison, B., DiCarlo, P., Di Marco, C.F., Dorsey, J.R., Edwards, P.M., Evans, M.J., Fowler, D., Furneaux, K.L., Gallagher, M., Guenther, A., Heard, D.E., Helfter, C.,

Hopkins, J., Ingham, T., Irwin, M., Jones, C., Karunaharan, A., Langford, B., Lewis, A.C., Lim, S.F., MacDonald, S.M., Mahajan, A.S., Malpass, S., McFiggans, G., Mills, G., Misztal, P., Moller, S., Monks, P.S., Nemitz, E., Nicolas-Perea, V., Oetjen, H., Oram, D.E., Palmer, P.I., Phillips, G.J., Pike, R., Plane, J.M.C., Pugh, T., Pyle, J.A., Reeves, C.E., Robinson, N.H., Stewart, D., Stone, D., Whalley, L.K., Yin, X., 2010. Overview: oxidant and particle photochemical processes above a south-east Asian tropical rainforest (the OP3 project): introduction, rationale, location characteristics and tools. Atmos Chem Phys 10, 169–199. https://doi.org/10.5194/acp-10-169-2010

Hofzumahaus, A., Heard, D. (Eds.), 2015. Assessment of local HOx and ROx Measurement Techniques: Achievements, Challenges, and Fututre Directions.

Holland, F., Hessling, M., Hofzumahaus, A., 1995. In Situ Measurement of Tropospheric OH Radicals by Laser-Induced Fluorescence—A Description of the KFA Instrument. J. Atmospheric Sci. 52, 3393–3401. https://doi.org/10.1175/1520-0469(1995)052<3393:ISMOTO>2.0.CO;2

Honrath, R.E., Lu, Y., Peterson, M.C., Dibb, J.E., Arsenault, M.A., Cullen, N.J., Steffen, K., 2002. Vertical fluxes of NOx, HONO, and HNO3 above the snowpack at Summit, Greenland. Atmos. Environ. 36, 2629–2640. http://dx.doi.org/10.1016/S1352-2310(02)00132-2

Horie, O., Moortgat, G.K., 1991. Decomposition pathways of the excited Criegee intermediates in the ozonolysis of simple alkenes. Int. Conf. Gener. Oxid. Reg. Glob. Scales 25, 1881–1896. https://doi.org/10.1016/0960-1686(91)90271-8

Hornbrook, R.S., Crawford, J.H., Edwards, G.D., Goyea, O., Mauldin Iii, R.L., Olson, J.S., Cantrell, C.A., 2011. Measurements of tropospheric HO_2 and RO_2 by oxygen dilution modulation and chemical ionization mass spectrometry. Atmos Meas Tech 4, 735–756. https://doi.org/10.5194/amt-4-735-2011

Horstjann, M., Andrés Hernández, M.D., Nenakhov, V., Chrobry, A., Burrows, J.P., 2014. Peroxy radical detection for airborne atmospheric measurements using absorption spectroscopy of NO_2. Atmos Meas Tech 7, 1245–1257. https://doi.org/10.5194/amt-7-1245-2014

Hossaini, R., Chipperfield, M.P., Saiz-Lopez, A., Fernandez, R., Monks, S., Feng, W., Brauer, P., von Glasow, R., 2016. A global model of tropospheric chlorine chemistry: Organic versus inorganic sources and impact on methane oxidation. J. Geophys. Res. Atmospheres 121, 14,271-14,297. https://doi.org/10.1002/2016JD025756

Howard, C.J., 1979. Kinetic measurements using flow tubes. J. Phys. Chem. 83, 3–9. https://doi.org/10.1021/j100464a001

Ingham, T., Goddard, A., Whalley, L.K., Furneaux, K.L., Edwards, P.M., Seal, C.P., Self, D.E., Johnson, G.P., Read, K.A., Lee, J.D., Heard, D.E., 2009. A flow-tube based laser-induced fluorescence instrument to measure OH reactivity in the troposphere. Atmos Meas Tech 2, 465–477. https://doi.org/10.5194/amt-2-465-2009

Japar, S., Wu, C., Nikl, H., 1974. Rate constants for the reaction of ozone with olefins in the gas phase. J. Phys. Chem. 78, 2318–2320.

Jenkin, M.E., Clemitshaw, K.C., 2000. Ozone and other secondary photochemical pollutants: chemical processes governing their formation in the planetary boundary layer. Atmos. Environ. 34, 2499–2527. http://dx.doi.org/10.1016/S1352-2310(99)00478-1

Johnson, D., Marston, G., 2008. The gas-phase ozonolysis of unsaturated volatile organic compounds in the troposphere. Chem. Soc. Rev. 37, 699–716. https://doi.org/10.1039/B704260B

Kanaya, Y., Matsumoto, J., Kato, S., Akimoto, H., 2001a. Behavior of OH and HO2 radicals during the Observations at a Remote Island of Okinawa (ORION99) field campaign: 2. Comparison between observations and calculations. J. Geophys. Res. Atmospheres 106, 24209–24223.

Kanaya, Y., Sadanaga, Y., Hirokawa, J., Kajii, Y., Akimoto, H., 2001b. Development of a Ground-Based LIF Instrument for Measuring HOx Radicals: Instrumentation and Calibrations. J. Atmospheric Chem. 38, 73–110. https://doi.org/10.1023/A:1026559321911

Kartal, D., Andrés-Hernández, M.D., Reichert, L., Schlager, H., Burrows, J.P., 2010. Technical Note: Characterisation of a DUALER instrument for the airborne measurement of peroxy radicals during AMMA 2006. Atmos Chem Phys 10, 3047–3062. https://doi.org/10.5194/acp-10-3047-2010

Kerr, R.A., 1991. Hydroxyl, the cleanser that thrives on dirt. Science 253, 1210. https://doi.org/10.1126/science.253.5025.1210

Kim, S., Wolfe, G.M., Mauldin, L., Cantrell, C., Guenther, A., Karl, T., Turnipseed, A., Greenberg, J., Hall, S.R., Ullmann, K., Apel, E., Hornbrook, R., Kajii, Y., Nakashima, Y., Keutsch, F.N., DiGangi, J.P., Henry, S.B., Kaser, L., Schnitzhofer, R., Graus, M., Hansel, A., Zheng, W., Flocke, F.F., 2013. Evaluation of HOx sources and cycling using measurement-constrained model calculations in a 2-methyl-3-butene-2-ol (MBO) and monoterpene (MT) dominated ecosystem. Atmos Chem Phys 13, 2031–2044. https://doi.org/10.5194/acp-13-2031-2013

Kleffmann, J., Kurtenbach, R., Lörzer, J., Wiesen, P., Kalthoff, N., Vogel, B., Vogel, H., 2003. Measured and simulated vertical profiles of nitrous acid—Part I: Field measurements. Atmos. Environ. 37, 2949–2955. https://doi.org/10.1016/S1352-2310(03)00242-5

Koppmann, R., 2007. Volatile organic compounds in the atmosphere. Wiley Online Library.

Kroll, J.H., Clarke, J.S., Donahue, N.M., Anderson, J.G., 2001. Mechanism of HOx Formation in the Gas-Phase Ozone−Alkene Reaction. 1. Direct, Pressure-Dependent Measurements of Prompt OH Yields. J. Phys. Chem. A 105, 1554–1560. https://doi.org/10.1021/jp002121r

Kroll, J.H., Seinfeld, J.H., 2008a. Chemistry of secondary organic aerosol: Formation and evolution of low-volatility organics in the atmosphere. Atmos. Environ. 42, 3593–3624. http://dx.doi.org/10.1016/j.atmosenv.2008.01.003

Kubistin, D., Harder, H., Martinez, M., Rudolf, M., Sander, R., Bozem, H., Eerdekens, G., Fischer, H., Gurk, C., Klüpfel, T., Königstedt, R., Parchatka, U., Schiller, C.L., Stickler, A., Taraborrelli, D., Williams, J., Lelieveld, J., 2010. Hydroxyl radicals in the tropical troposphere over the Suriname rainforest: comparison of measurements with the box model MECCA. Atmos Chem Phys 10, 9705–9728. https://doi.org/10.5194/acp-10-9705-2010

Kukui, A., Ancellet, G., Le Bras, G., 2008a. Chemical ionisation mass spectrometer for measurements of OH and Peroxy radical concentrations in moderately polluted atmospheres. J. Atmospheric Chem. 61, 133–154. https://doi.org/10.1007/s10874-009-9130-9

Kundu, S., Deming, B.L., Lew, M.M., Bottorff, B.P., Rickly, P., Stevens, P.S., Dusanter, S., Sklaveniti, S., Leonardis, T., Locoge, N., Wood, E.C., 2019. Peroxy Radical Measurements by Ethane – Nitric Oxide Chemical Amplification and Laser-Induced Fluorescence/Fluorescence Assay by Gas Expansion during the IRRONIC field campaign in a Forest in Indiana. Atmos Chem Phys Discuss 2019, 1–31. https://doi.org/10.5194/acp-2018-1359

Lee, J.D., McFiggans, G., Allan, J.D., Baker, A.R., Ball, S.M., Benton, A.K., Carpenter, L.J., Commane, R., Finley, B.D., Evans, M., Fuentes, E., Furneaux, K., Goddard, A., Good, N., Hamilton, J.F., Heard, D.E., Herrmann, H., Hollingsworth, A., Hopkins, J.R., Ingham, T., Irwin, M., Jones, C.E., Jones, R.L., Keene, W.C., Lawler, M.J., Lehmann, S., Lewis, A.C., Long, M.S., Mahajan, A., Methven, J., Moller, S.J., Müller, K., Müller, T., Niedermeier, N., O'Doherty, S., Oetjen, H., Plane, J.M.C., Pszenny, A.A.P., Read, K.A., Saiz-Lopez, A., Saltzman, E.S., Sander, R., von Glasow, R., Whalley, L., Wiedensohler, A., Young, D., 2010. Reactive Halogens in the Marine Boundary Layer (RHaMBLe): the tropical North

Atlantic experiments. Atmos Chem Phys 10, 1031–1055. https://doi.org/10.5194/acp-10-1031-2010

Lee, J.D., Young, J.C., Read, K.A., Hamilton, J.F., Hopkins, J.R., Lewis, A.C., Bandy, B.J., Davey, J., Edwards, P., Ingham, T., Self, D.E., Smith, S.C., Pilling, M.J., Heard, D.E., 2009. Measurement and calculation of OH reactivity at a United Kingdom coastal site. J. Atmospheric Chem. 64, 53–76. https://doi.org/10.1007/s10874-010-9171-0

Lelieveld, J., Butler, T.M., Crowley, J.N., Dillon, T.J., Fischer, H., Ganzeveld, L., Harder, H., Lawrence, M.G., Martinez, M., Taraborrelli, D., Williams, J., 2008. Atmospheric oxidation capacity sustained by a tropical forest. Nature 452, 737.

Lew, M.L., Rickly, P.S., Bottorff, B.P., Sklaveniti, S., Léonardis, T., Locoge, N., Dusanter, S., Kundu, S., Wood, E., Stevens, P.S., 2019. OH and HO2 radical chemistry in a midlatitude forest: Measurements and model comparisons. Atmos Chem Phys Discuss 2019, 1–35. https://doi.org/10.5194/acp-2019-726

Lew, M.L., Dusanter, S., Stevens, P.S., 2018. Measurement of interferences associated with the detection of the hydroperoxy radical in the atmosphere using laser-induced fluorescence. Atmos Meas Tech 11, 95–109. https://doi.org/10.5194/amt-11-95-2018

Lightfoot, P.D., Cox, R.A., Crowley, J.N., Destriau, M., Hayman, G.D., Jenkin, M.E., Moortgat, G.K., Zabel, F., 1992. Organic peroxy radicals: Kinetics, spectroscopy and tropospheric chemistry. Atmospheric Environ. Part Gen. Top. 26, 1805–1961. http://dx.doi.org/10.1016/0960-1686(92)90423-I

Liu, Y., Morales-Cueto, R., Hargrove, J., Medina, D., Zhang, J., 2009. Measurements of Peroxy Radicals Using Chemical Amplification−Cavity Ringdown Spectroscopy. Environ. Sci. Technol. 43, 7791–7796. https://doi.org/10.1021/es901146t

Liu, Y., Zhang, J., 2014. Atmospheric Peroxy Radical Measurements Using Dual-Channel Chemical Amplification Cavity Ringdown Spectroscopy. Anal. Chem. 86, 5391–5398. https://doi.org/10.1021/ac5004689

Madronich, S., Shao, M., Wilson, S.R., Solomon, K.R., Longstreth, J.D., Tang, X.Y., 2015. Changes in air quality and tropospheric composition due to depletion of stratospheric ozone and interactions with changing climate: implications for human and environmental health. Photochem Photobiol Sci 14, 149–169. https://doi.org/10.1039/C4PP90037E

Mao, J., Jacob, D.J., Evans, M.J., Olson, J.R., Ren, X., Brune, W.H., Clair, J.M.S., Crounse, J.D., Spencer, K.M., Beaver, M.R., Wennberg, P.O., Cubison, M.J., Jimenez, J.L., Fried, A., Weibring, P., Walega, J.G., Hall, S.R., Weinheimer, A.J., Cohen, R.C., Chen, G., Crawford, J.H., McNaughton, C., Clarke, A.D., Jaeglé, L., Fisher, J.A., Yantosca, R.M., Le Sager, P., Carouge, C., 2010. Chemistry of hydrogen oxide radicals (HO_x) in the Arctic troposphere in spring. Atmos Chem Phys 10, 5823–5838. https://doi.org/10.5194/acp-10-5823-2010

Martinez, M., Harder, H., Kovacs, T.A., Simpas, J.B., Bassis, J., Lesher, R., Brune, W.H., Frost, G.J., Williams, E.J., Stroud, C.A., Jobson, B.T., Roberts, J.M., Hall, S.R., Shetter, R.E., Wert, B., Fried, A., Alicke, B., Stutz, J., Young, V.L., White, A.B., Zamora, R.J., 2003. OH and HO2 concentrations, sources, and loss rates during the Southern Oxidants Study in Nashville, Tennessee, summer 1999. J. Geophys. Res. Atmospheres 108, n/a-n/a. https://doi.org/10.1029/2003JD003551

Martinez, M., Harder, H., Kubistin, D., Rudolf, M., Bozem, H., Eerdekens, G., Fischer, H., Klüpfel, T., Gurk, C., Königstedt, R., Parchatka, U., Schiller, C.L., Stickler, A., Williams, J., Lelieveld, J., 2010. Hydroxyl radicals in the tropical troposphere over the Suriname rainforest: airborne measurements. Atmos Chem Phys 10, 3759–3773. https://doi.org/10.5194/acp-10-3759-2010

Martinez, M., Harder, H., Ren, X., Lesher, R.L., Brune, W.H., 2004. Measuring atmospheric naphthalene with laser-induced fluorescence. Atmos Chem Phys 4, 563–569. https://doi.org/10.5194/acp-4-563-2004

Matsumi, M., Kono, M., Ichikawa, T., Takahashi, K., Kondo, Y., 2002. Laser-Induced Fluorescence Instrument for the Detection of Tropospheric OH Radicals. Bull. Chem. Soc. Jpn. 75, 711–717. https://doi.org/doi:10.1246/bcsj.75.711

Mellouki, A., Wallington, T.J., Chen, J., 2015. Atmospheric Chemistry of Oxygenated Volatile Organic Compounds: Impacts on Air Quality and Climate. Chem. Rev. 115, 3984–4014. https://doi.org/10.1021/cr500549n

Mentel, T.F., Springer, M., Ehn, M., Kleist, E., Pullinen, I., Kurtén, T., Rissanen, M., Wahner, A., Wildt, J., 2015. Formation of highly oxidized multifunctional compounds: autoxidation of peroxy radicals formed in the ozonolysis of alkenes – deduced from structure–product relationships. Atmos Chem Phys 15, 6745–6765. https://doi.org/10.5194/acp-15-6745-2015

Mihelcic, D., Holland, F., Hofzumahaus, A., Hoppe, L., Konrad, S., Müsgen, P., Pätz, H.W., Schäfer, H.J., Schmitz, T., Volz-Thomas, A., Bächmann, K., Schlomski, S., Platt, U., Geyer, A., Alicke, B., Moortgat, G.K., 2003. Peroxy radicals during BERLIOZ at Pabstthum: Measurements, radical budgets and ozone production. J. Geophys. Res. Atmospheres 108, n/a-n/a. https://doi.org/10.1029/2001JD001014

Mihelcic, D., Müsgen, P., Ehhalt, D.H., 1985. An improved method of measuring tropospheric NO2 and RO2 by matrix isolation and electron spin resonance. J. Atmospheric Chem. 3, 341–361. https://doi.org/10.1007/bf00122523

Mihelcic, D., Volz-Thomas, A., Pätz, H.W., Kley, D., Mihelcic, M., 1990. Numerical analysis of ESR spectra from atmospheric samples. J. Atmospheric Chem. 11, 271–297. https://doi.org/10.1007/bf00118353

Mihele, C.M., Hastie, D.R., 2003. Radical chemistry at a forested continental site: Results from the PROPHET 1997 campaign. J. Geophys. Res. Atmospheres 108. https://doi.org/10.1029/2002JD002888

Mihele, C.M., Hastie, D.R., 2000. Optimized Operation and Calibration Procedures for Radical Amplifier-Type Detectors. J. Atmospheric Ocean. Technol. 17, 788–794. https://doi.org/10.1175/1520-0426(2000)017<0788:OOACPF>2.0.CO;2

Mihele, C.M., Hastie, D.R., 1998. The sensitivity of the radical amplifier to ambient water vapour. Geophys. Res. Lett. 25, 1911–1913. https://doi.org/10.1029/98GL01432

Mihele, C.M., Mozurkewich, M., Hastie, D.R., 1999a. Radical loss in a chain reaction of CO and NO in the presence of water: Implications for the radical amplifier and atmospheric chemistry. Int. J. Chem. Kinet. 31, 145–152. https://doi.org/10.1002/(SICI)1097-4601(1999)31:2<145::AID-KIN7>3.0.CO;2-M

Miyazaki, K., Parker, A.E., Fittschen, C., Monks, P.S., Kajii, Y., 2010. A new technique for the selective measurement of atmospheric peroxy radical concentrations of HO_2 and RO_2 using a denuding method. Atmos Meas Tech 3, 1547–1554. https://doi.org/10.5194/amt-3-1547-2010

Monks, P.S., 2005. Gas-phase radical chemistry in the troposphere. Chem. Soc. Rev. 34, 376–395. https://doi.org/10.1039/B307982C

Montzka, S.A., Krol, M., Dlugokencky, E., Hall, B., Jöckel, P., Lelieveld, J., 2011. Small Interannual Variability of Global Atmospheric Hydroxyl. Science 331, 67–69. https://doi.org/10.1126/science.1197640

Müller, M., Mikoviny, T., Jud, W., D'Anna, B., Wisthaler, A., 2013. A new software tool for the analysis of high resolution PTR-TOF mass spectra. Chemom. Intell. Lab. Syst. 127, 158–165.

Nguyen, T.B., Tyndall, G.S., Crounse, J.D., Teng, A.P., Bates, K.H., Schwantes, R.H., Coggon, M.M., Zhang, L., Feiner, P., Millller, D.O., Skog, K.M., Rivera-Rios, J.C., Dorris, M., Olson, K.F., Koss, A., Wild, R.J., Brown, S.S., Goldstein, A.H., de Gouw, J.A., Brune, W.H., Keutsch, F.N., Seinfeld, J.H., Wennberg, P.O., 2016. Atmospheric fates of Criegee intermediates in the ozonolysis of isoprene. Phys Chem Chem Phys 18, 10241–10254. https://doi.org/10.1039/C6CP00053C

Nölscher, A.C., Williams, J., Sinha, V., Custer, T., Song, W., Johnson, A.M., Axinte, R., Bozem, H., Fischer, H., Pouvesle, N., Phillips, G., Crowley, J.N., Rantala, P., Rinne, J., Kulmala, M., Gonzales, D., Valverde-Canossa, J., Vogel, A., Hoffmann, T., Ouwersloot, H.G., Vilà-Guerau de Arellano, J., Lelieveld, J., 2012. Summertime total OH reactivity measurements from boreal forest during HUMPPA-COPEC 2010. Atmos Chem Phys 12, 8257–8270. https://doi.org/10.5194/acp-12-8257-2012

Nölscher, A.C., Yañez-Serrano, A.M., Wolff, S., de Araujo, A.C., Lavrič, J.V., Kesselmeier, J., Williams, J., 2016. Unexpected seasonality in quantity and composition of Amazon rainforest air reactivity. Nat. Commun. 7, 10383. https://doi.org/10.1038/ncomms10383

Novelli, A., Hens, K., Tatum Ernest, C., Kubistin, D., Regelin, E., Elste, T., Plass-Dülmer, C., Martinez, M., Lelieveld, J., Harder, H., 2014. Characterisation of an inlet pre-injector laser-induced fluorescence instrument for the measurement of atmospheric hydroxyl radicals. Atmos Meas Tech 7, 3413–3430. https://doi.org/10.5194/amt-7-3413-2014

Orlando, J.J., Tyndall, G.S., 2012. Laboratory studies of organic peroxy radical chemistry: an overview with emphasis on recent issues of atmospheric significance. Chem Soc Rev 41, 6294–6317. https://doi.org/10.1039/C2CS35166H

Orlando, J.J., Tyndall, G.S., Wallington, T.J., 2003. The Atmospheric Chemistry of Alkoxy Radicals. Chem. Rev. 103, 4657–4690. https://doi.org/10.1021/cr020527p

Parker, A.E., Amédro, D., Schoemaecker, C., Fittschen, C., 2011. OH RADICAL REACTIVITY MEASUREMENTS BY FAGE. Environ. Eng. Manag. J. EEMJ 10.

Paulot, F., Crounse, J.D., Kjaergaard, H.G., Kürten, A., St. Clair, J.M., Seinfeld, J.H., Wennberg, P.O., 2009. Unexpected Epoxide Formation in the Gas-Phase Photooxidation of Isoprene. Science 325, 730–733. https://doi.org/10.1126/science.1172910

Paulson, S.E., Orlando, J.J., 1996. The reactions of ozone with alkenes: An important source of HOx in the boundary layer. Geophys. Res. Lett. 23, 3727–3730. https://doi.org/10.1029/96GL03477

Peeters, J., Müller, J.-F., 2010. HOx radical regeneration in isoprene oxidation via peroxy radical isomerisations. II: experimental evidence and global impact. Phys. Chem. Chem. Phys. 12, 14227–14235.

Peeters, J., Nguyen, T.L., Vereecken, L., 2009. HO x radical regeneration in the oxidation of isoprene. Phys. Chem. Chem. Phys. 11, 5935–5939.

Penkett, S.A., Monks, P.S., Carpenter, L.J., Clemitshaw, K.C., Ayers, G.P., Gillett, R.W., Galbally, I.E., Meyer, C.P., 1997. Relationships between ozone photolysis rates and peroxy radical concentrations in clean marine air over the Southern Ocean. J. Geophys. Res. Atmospheres 102, 12805–12817. https://doi.org/10.1029/97JD00765

Perring, A.E., Pusede, S.E., Cohen, R.C., 2013. An Observational Perspective on the Atmospheric Impacts of Alkyl and Multifunctional Nitrates on Ozone and Secondary Organic Aerosol. Chem. Rev. 113, 5848–5870. https://doi.org/10.1021/cr300520x

Praske, E., Otkj\a er, R.V., Crounse, J.D., Hethcox, J.C., Stoltz, B.M., Kjaergaard, H.G., Wennberg, P.O., 2018. Atmospheric autoxidation is increasingly important in urban and suburban North America. Proc. Natl. Acad. Sci. 115, 64–69. https://doi.org/10.1073/pnas.1715540115

Pugh, T.A.M., MacKenzie, A.R., Hewitt, C.N., Langford, B., Edwards, P.M., Furneaux, K.L., Heard, D.E., Hopkins, J.R., Jones, C.E., Karunaharan, A., Lee, J., Mills, G., Misztal, P., Moller, S., Monks, P.S., Whalley, L.K., 2010. Simulating atmospheric composition over a South-East Asian tropical rainforest: performance of a chemistry box model. Atmos Chem Phys 10, 279–298. https://doi.org/10.5194/acp-10-279-2010

Read, K.A., Lewis, A.C., Bauguitte, S., Rankin, A.M., Salmon, R.A., Wolff, E.W., Saiz-Lopez, A., Bloss, W.J., Heard, D.E., Lee, J.D., Plane, J.M.C., 2008. DMS and MSA measurements in the Antarctic Boundary Layer: impact of BrO on MSA production. Atmos Chem Phys 8, 2985–2997. https://doi.org/10.5194/acp-8-2985-2008

Reichert, L., Andrés Hernández, M.D., Stöbener, D., Burkert, J., Burrows, J.P., 2003. Investigation of the effect of water complexes in the determination of peroxy radical ambient concentrations: Implications for the atmosphere. J. Geophys. Res. Atmospheres 108, ACH 4-1-ACH 4-16. https://doi.org/10.1029/2002JD002152

Ren, X., Edwards, G.D., Cantrell, C.A., Lesher, R.L., Metcalf, A.R., Shirley, T., Brune, W.H., 2003. Intercomparison of peroxy radical measurements at a rural site using laser-induced fluorescence and Peroxy Radical Chemical Ionization Mass Spectrometer (PerCIMS) techniques. J. Geophys. Res. Atmospheres 108. https://doi.org/10.1029/2003JD003644

Ren, X., van Duin, D., Cazorla, M., Chen, S., Mao, J., Zhang, L., Brune, W.H., Flynn, J.H., Grossberg, N., Lefer, B.L., Rappenglück, B., Wong, K.W., Tsai, C., Stutz, J., Dibb, J.E., Thomas Jobson, B., Luke, W.T., Kelley, P., 2013. Atmospheric oxidation chemistry and ozone production: Results from SHARP 2009 in Houston, Texas. J. Geophys. Res. Atmospheres 118, 5770–5780. https://doi.org/10.1002/jgrd.50342

Ren, Y., Grosselin, B., Daële, V., Mellouki, A., 2017. Investigation of the reaction of ozone with isoprene, methacrolein and methyl vinyl ketone using the HELIOS chamber. Faraday Discuss 200, 289–311. https://doi.org/10.1039/C7FD00014F

Rickly, P., Stevens, P.S., 2018. Measurements of a potential interference with laser-induced fluorescence measurements of ambient OH from the ozonolysis of biogenic alkenes. Atmos Meas Tech 11, 1–16. https://doi.org/10.5194/amt-11-1-2018

Sadanaga, Y., Matsumoto, J., Sakurai, K., Isozaki, R., Kato, S., Nomaguchi, T., Bandow, H., Kajii, Y., 2004. Development of a measurement system of peroxy radicals using a chemical amplification/laser-induced fluorescence technique. Rev. Sci. Instrum. 75, 864–872. https://doi.org/doi:http://dx.doi.org/10.1063/1.1666985

Sanchez, J., Tanner, D.J., Chen, D., Huey, L.G., Ng, N.L., 2016. A new technique for the direct detection of HO2 radicals using bromide chemical ionization mass spectrometry (Br-CIMS): initial characterization. Atmos Meas Tech 9, 3851–3861. https://doi.org/10.5194/amt-9-3851-2016

Sander, S., Friedl, R., Golden, D., Kurylo, M., Huie, R., Orkin, V., Moortgat, G., Ravishankara, A., Kolb, C., Molina, M., 2003. NASA/JPL Data Evaluation, JPL Publication 02-25 Evaluation No 14. Jet Propuls. Lab. Pasadena CA.

Sander, S., Golden, D., Kurylo, M., Moortgat, G., Wine, P., Ravishankara, A., Kolb, C., Molina, M., Finlayson-Pitts, B., Huie, R., 2006. Chemical kinetics and photochemical data for use in atmospheric studies evaluation number 15. Pasadena, CA: Jet Propulsion Laboratory, National Aeronautics and Space ….

Schultz, M., Heitlinger, M., Mihelcic, D., Volz-Thomas, A., 1995. Calibration source for peroxy radicals with built-in actinometry using H2O and O2 photolysis at 185 nm. J. Geophys. Res. Atmospheres 100, 18811–18816. https://doi.org/10.1029/95JD01642

Sindelarova, K., Granier, C., Bouarar, I., Guenther, A., Tilmes, S., Stavrakou, T., Müller, J.-F., Kuhn, U., Stefani, P., Knorr, W., 2014. Global data set of biogenic VOC emissions calculated by the MEGAN model over the last 30 years. Atmos Chem Phys 14, 9317–9341. https://doi.org/10.5194/acp-14-9317-2014

Sinha, V., Williams, J., Lelieveld, J., Ruuskanen, T.M., Kajos, M.K., Patokoski, J., Hellen, H., Hakola, H., Mogensen, D., Boy, M., Rinne, J., Kulmala, M., 2010. OH Reactivity Measurements within a Boreal Forest: Evidence for Unknown Reactive Emissions. Environ. Sci. Technol. 44, 6614–6620. https://doi.org/10.1021/es101780b

Sklaveniti, S., Locoge, N., Stevens, P.S., Wood, E., Kundu, S., Dusanter, S., 2018. Development of an instrument for direct ozone production rate measurements: measurement reliability and current limitations. Atmos Meas Tech 11, 741–761. https://doi.org/10.5194/amt-11-741-2018

Sneep, M., Ubachs, W., 2005. Direct measurement of the Rayleigh scattering cross section in various gases. J. Quant. Spectrosc. Radiat. Transf. 92, 293–310. https://doi.org/10.1016/j.jqsrt.2004.07.025

Spataro, F., Ianniello, A., 2014. Sources of atmospheric nitrous acid: State of the science, current research needs, and future prospects. J. Air Waste Manag. Assoc. 64, 1232–1250. https://doi.org/10.1080/10962247.2014.952846

Stavrakou, T., Peeters, J., Müller, J.-F., 2010. Improved global modelling of HO x recycling in isoprene oxidation: evaluation against the GABRIEL and INTEX-A aircraft campaign measurements. Atmospheric Chem. Phys. 10, 9863–9878.

Stevens, P.S., Mather, J.H., Brune, W.H., 1994a. Measurement of tropospheric OH and HO2 by laser-induced fluorescence at low pressure. J. Geophys. Res. Atmospheres 99, 3543–3557. https://doi.org/10.1029/93JD03342

Stone, D., Whalley, L.K., Heard, D.E., 2012. Tropospheric OH and HO2 radicals: field measurements and model comparisons. Chem. Soc. Rev. 41, 6348–6404. https://doi.org/10.1039/C2CS35140D

Sutton, J.A., Driscoll, J.F., 2004. Rayleigh scattering cross sections of combustion species at 266, 355, and 532 nm for thermometry applications. Opt Lett 29, 2620–2622. https://doi.org/10.1364/OL.29.002620

Tan, D., Faloona, I., Simpas, J.B., Brune, W., Shepson, P.B., Couch, T.L., Sumner, A.L., Carroll, M.A., Thornberry, T., Apel, E., Riemer, D., Stockwell, W., 2001. HO x budgets in a deciduous forest: Results from the PROPHET summer 1998 campaign. J. Geophys. Res. Atmospheres 106, 24407–24427. https://doi.org/10.1029/2001JD900016

Tan, Z., Fuchs, H., Lu, K., Hofzumahaus, A., Bohn, B., Broch, S., Dong, H., Gomm, S., Häseler, R., He, L., Holland, F., Li, X., Liu, Y., Lu, S., Rohrer, F., Shao, M., Wang, B., Wang, M., Wu, Y., Zeng, L., Zhang, Y., Wahner, A., Zhang, Y., 2017. Radical chemistry at a rural site (Wangdu) in the North China Plain: observation and model calculations of OH, HO2 and RO2 radicals. Atmos Chem Phys 17, 663–690. https://doi.org/10.5194/acp-17-663-2017

Tan, Z., Lu, K., Hofzumahaus, A., Fuchs, H., Bohn, B., Holland, F., Liu, Y., Rohrer, F., Shao, M., Sun, K., Wu, Y., Zeng, L., Zhang, Y., Zou, Q., Kiendler-Scharr, A., Wahner, A., Zhang, Y., 2019. Experimental budgets of OH, HO2, and RO2 radicals and implications for ozone formation in the Pearl River Delta in China 2014. Atmos Chem Phys 19, 7129–7150. https://doi.org/10.5194/acp-19-7129-2019

Tan, Z., Rohrer, F., Lu, K., Ma, X., Bohn, B., Broch, S., Dong, H., Fuchs, H., Gkatzelis, G.I., Hofzumahaus, A., Holland, F., Li, X., Liu, Y., Liu, Y., Novelli, A., Shao, M., Wang, H., Wu, Y., Zeng, L., Hu, M., Kiendler-Scharr, A., Wahner, A., Zhang, Y., 2018b. Wintertime photochemistry in Beijing: observations of ROx radical concentrations in the North China Plain during the BEST-ONE campaign. Atmos Chem Phys 18, 12391–12411. https://doi.org/10.5194/acp-18-12391-2018

Teruel, M.A., Lane, S.I., Mellouki, A., Solignac, G., Le Bras, G., 2006. OH reaction rate constants and UV absorption cross-sections of unsaturated esters. Atmos. Environ. 40, 3764–3772. https://doi.org/10.1016/j.atmosenv.2006.03.003

Vaughan, S., Ingham, T., Whalley, L.K., Stone, D., Evans, M.J., Read, K.A., Lee, J.D., Moller, S.J., Carpenter, L.J., Lewis, A.C., Fleming, Z.L., Heard, D.E., 2012. Seasonal observations of OH and HO_2 in the remote tropical marine boundary layer. Atmospheric Chem. Phys. 12, 2149–2172. https://doi.org/10.5194/acp-12-2149-2012

Villena, G., Kleffmann, J., Kurtenbach, R., Wiesen, P., Lissi, E., Rubio, M.A., Croxatto, G., Rappenglück, B., 2011. Vertical gradients of HONO, NOx and O3 in Santiago de Chile. Atmos. Environ. 45, 3867–3873. https://doi.org/10.1016/j.atmosenv.2011.01.073

Volkamer, R., Sheehy, P., Molina, L.T., Molina, M.J., 2010. Oxidative capacity of the Mexico City atmosphere – Part 1: A radical source perspective. Atmos Chem Phys 10, 6969–6991. https://doi.org/10.5194/acp-10-6969-2010

Whalley, L., Stone, D., Heard, D., 2012. New insights into the tropospheric oxidation of isoprene: combining field measurements, laboratory studies, chemical modelling and quantum theory, in: Atmospheric and Aerosol Chemistry. Springer, pp. 55–95.

Whalley, L.K., Blitz, M.A., Desservettaz, M., Seakins, P.W., Heard, D.E., 2013. Reporting the sensitivity of laser-induced fluorescence instruments used for HO_2 detection to an interference from RO_2 radicals and introducing a novel approach that enables HO_2 and certain RO_2 types to be selectively measured. Atmos Meas Tech 6, 3425–3440. https://doi.org/10.5194/amt-6-3425-2013

Whalley, L.K., Edwards, P.M., Furneaux, K.L., Goddard, A., Ingham, T., Evans, M.J., Stone, D., Hopkins, J.R., Jones, C.E., Karunaharan, A., Lee, J.D., Lewis, A.C., Monks, P.S., Moller, S.J., Heard, D.E., 2011. Quantifying the magnitude of a missing hydroxyl radical source in a tropical rainforest. Atmos Chem Phys 11, 7223–7233. https://doi.org/10.5194/acp-11-7223-2011

Whalley, L.K., Stone, D., Dunmore, R., Hamilton, J., Hopkins, J.R., Lee, J.D., Lewis, A.C., Williams, P., Kleffmann, J., Laufs, S., Woodward-Massey, R., Heard, D.E., 2018a. Understanding in situ ozone production in the summertime through radical observations and modelling studies during the Clean air for London project (ClearfLo). Atmospheric Chem. Phys. 18, 2547–2571. https://doi.org/10.5194/acp-18-2547-2018

Wolfe, G.M., Cantrell, C., Kim, S., Mauldin III, R.L., Karl, T., Harley, P., Turnipseed, A., Zheng, W., Flocke, F., Apel, E.C., Hornbrook, R.S., Hall, S.R., Ullmann, K., Henry, S.B., DiGangi, J.P., Boyle, E.S., Kaser, L., Schnitzhofer, R., Hansel, A., Graus, M., Nakashima, Y., Kajii, Y., Guenther, A., Keutsch, F.N., 2014. Missing peroxy radical sources within a summertime ponderosa pine forest. Atmos Chem Phys 14, 4715–4732. https://doi.org/10.5194/acp-14-4715-2014

Wolfe, G.M., Marvin, M.R., Roberts, S.J., Travis, K.R., Liao, J., 2016. The Framework for 0-D Atmospheric Modeling (F0AM) v3.1. Geosci Model Dev 9, 3309–3319. https://doi.org/10.5194/gmd-9-3309-2016

Wolfe, G.M., Thornton, J.A., McKay, M., Goldstein, A.H., 2011. Forest-atmosphere exchange of ozone: sensitivity to very reactive biogenic VOC emissions and implications for in-canopy photochemistry. Atmos Chem Phys 11, 7875–7891. https://doi.org/10.5194/acp-11-7875-2011

Wood, E.C., Charest, J.R., 2014. Chemical Amplification - Cavity Attenuated Phase Shift Spectroscopy Measurements of Atmospheric Peroxy Radicals. Anal. Chem. 86, 10266–10273. https://doi.org/10.1021/ac502451m

Wood, E.C., Deming, B.L., Kundu, S., 2017. Ethane-Based Chemical Amplification Measurement Technique for Atmospheric Peroxy Radicals. Environ. Sci. Technol. Lett. 4, 15–19. https://doi.org/10.1021/acs.estlett.6b00438

Zhang, X., Lambe, A.T., Upshur, M.A., Brooks, W.A., Gray Bé, A., Thomson, R.J., Geiger, F.M., Surratt, J.D., Zhang, Z., Gold, A., 2017. Highly oxygenated multifunctional compounds in α-pinene secondary organic aerosol. Environ. Sci. Technol. 51, 5932–5940.

Zheng, W., Flocke, F.M., Tyndall, G.S., Swanson, A., Orlando, J.J., Roberts, J.M., Huey, L.G., Tanner, D.J., 2011. Characterization of a thermal decomposition chemical ionization mass spectrometer for the measurement of peroxy acyl nitrates (PANs) in the atmosphere. Atmos Chem Phys 11, 6529–6547. https://doi.org/10.5194/acp-11-6529-2011

Zhou, X., Zhang, N., TerAvest, M., Tang, D., Hou, J., Bertman, S., Alaghmand, M., Shepson, P.B., Carroll, M.A., Griffith, S., Dusanter, S., Stevens, P.S., 2011. Nitric acid photolysis on forest canopy surface as a source for tropospheric nitrous acid. Nat. Geosci. 4, 440–443. https://doi.org/10.1038/ngeo1164

CHAPTER 2: DEVELOPMENT AND CHARACTERIZATION OF A CHEMICAL AMPLIFIER FOR PEROXY RADICAL MEASUREMENTS IN THE ATMOSPHERE

Table of contents

Chapter 2: Development and characterization of a chemical amplifier for peroxy radical measurements in the atmosphere

The first chapter stressed that HO_2 and RO_2 are key species in atmospheric chemistry, which together with OH, are involved in the oxidation of VOCs and the formation of secondary pollutants such as ozone. Monitoring these short-lived species during intensive field campaigns and comparing the measured concentrations to box model simulations allow assessing the reliability of chemical mechanisms implemented in atmospheric models and, when differences are observed, it suggests aspects of the radical chemistry that should be further investigated. However, as discussed in chapter 1, ambient measurements of peroxy radicals are still challenging and only a few techniques have been used so far for field measurements, i.e FAGE, CIMS and CA using the PERCA and ECHAMP approaches. The former has been widely used during field campaigns for HO_2 while the two others have been rarely used. It was recently discovered that several field measurements of peroxy radicals have likely suffered from interferences. A strong need for further understanding of peroxy radical measurements in the atmosphere is now more noticeable now than ever to address the limitations with each instrument and their reliability.

While the CA technique was proposed more than 30 years ago, difficulties associated to the discovery of the strong dependence of its response to ambient water, the limitation the poor in the analytical techniques for NO_2, and the development of other techniques such as FAGE and CIMS has slowed down its development. Only a few groups in the world are currently using the CA technique for field measurements (Bremen group from Germany, Leicester group from UK, Wood group from US). However, availability of highly sensitive and selective optical analyzers for NO_2 measurements, the development of alternative amplification chemistry based on the use of ethane instead of CO, and the current need to compare different techniques to ensure the reliability of peroxy radical measurements have provided a renewal of interest in the CA technique.

This chapter presents the construction and the characterization of a CA instrument using both the PERCA (CO/NO) and ECHAMP (Ethane/NO) approaches. Operating conditions of both amplification chemistries were optimized and the performance of each approach was assessed. A particular attention was placed on experimentally comparing experimentally observed and modelled trends of the CL with reagent gases and water-vapor amounts in order to evaluate our

understanding of the two amplification chemistries. In addition, the CA response to different types of RO_2 radicals was investigated. This chapter also reports the first field testing of this instrument.

This chapter is composed of:

- accepted publication by the journal, atmospheric environments, including related supplementary material..
- additional supplements describing certain aspects of the development that were not reported in the publication: (i) experiments conducted to identify the best reactor material and (ii) a description of the chemical mechanism used to simulate the amplification chemistry for both PERCA and ECHAMP.

When this Ph.D work was initiated, a laboratory prototype of the CA (only one measurement channel) had already been built by M. Duncianu, a postdoctoral fellow at IMT Lille Douai. I was in charge, with some help from M. Duncianu, to improve the prototype. It required to (i) adding a second measurement channel (simultaneous measurements from amplified and background modes), (ii) building the field version that can be used outdoors (waterproofing, automatization of the measurement sequence, etc.), (ii) optimizing and characterize the two amplification chemistries, and (iii) performing field testing in Douai. In addition I was solely in charge of modeling the amplification chemistry for comparison with the laboratory characterization. The publication was written by me with inputs and suggestions from M. Duncianu.

Characterization of a chemical amplifier for peroxy radical measurements in the atmosphere

Marius Duncianu[1], Ahmad Lahib[1,2], Alexandre Tomas[1], Philip S. Stevens[2,3], and Sébastien Dusanter[1,*]

[1]IMT Lille Douai, Université de Lille, SAGE – Département Sciences de l'Atmosphère et Génie de l'Environnement, 59000 Lille, France

[2]School of Public and Environmental Affairs, Indiana University, Bloomington, IN 47405, USA

[3]Department of Chemistry, Indiana University, Bloomington, IN, USA

*Corresponding author: email: sebastien.dusanter@imt-lille-douai.fr ; Phone: +33327712623 ; IMT Lille Douai, SAGE department, 941 rue Charles Bourseul, 59508 Douai, France

2.1 Abstract

Peroxy radicals (HO_2 and RO_2) are key species in atmospheric chemistry. They are produced during the oxidation of volatile organic compounds (VOCs) and are involved in the formation of photochemical pollutants such as ozone (O_3) and secondary organic aerosols (SOA). However, ambient measurements of these reactive species are still challenging and only a few techniques can achieve both a good selectivity and a detection limit that is low enough for ambient measurements. In this publication we present the characterization of a Chemical Amplifier (CA) using two different approaches for ambient measurements of peroxy radicals, including the PEroxy Radical Chemical Amplifier (PERCA) and the Ethane based CHemical AMPlification (ECHAMP). At 50% Relative Humidity (RH), the experimental CL for PERCA was found to be higher by approximately a factor of 3.7 compared to ECHAMP. The RH-dependence of the CL was also found to be larger for PERCA by a factor of 1.12. Box modeling of the chemistry taking place in the instrument highlighted that the formation of HNO_3 from the HO_2+NO reaction has a strong impact on the CL for both approaches. In addition, experiments conducted to quantify the RO_2–to-HO_2 conversion efficiency for a large range of organic peroxy radicals confirmed that it mainly depends on the organic nitrate ($RONO_2$) formation yield, while the alkyl nitrite (RONO) yield is not limiting the CL in most cases. Ambient measurements using the PERCA approach are shown to illustrate the performances of this new instrument.

Keywords: Instrument development; peroxy radical chemical amplifier; PERCA; ECHAMP; atmosphere

2.2 Introduction

Due to their high reactivity, and therefore short lifetime, peroxy radicals (HO_2, and RO_2, R = $C_xH_yO_z$) are key species in atmospheric chemistry. These radicals are mainly produced when the OH radical reacts with CO, the abundant greenhouse gas methane and volatile organic compounds (VOCs). They are also formed through the photolysis of carbonyl compounds, reactions of alkenes with ozone, and some nighttime reactions involving the NO_3 radical and VOCs (Finlayson-Pitts and Pitts, 2000).

In the atmosphere, there is a rapid propagation chemistry between peroxy radicals, alkoxy radicals (RO) and the hydroxyl radical (OH), forming a group of species known as "ROx" (ROx ≡ HO_2 + RO_2 + RO + OH). Of particular interest, reactions of peroxy radicals with nitric oxide (NO) play a central role in tropospheric chemistry. Indeed, peroxy radicals propagate to OH, which sustains the oxidizing capacity of the atmosphere, and which converts NO into nitrogen dioxide (NO_2), whose photolysis leads to ozone formation. Organic peroxy radicals also play a key role as intermediates in the formation of secondary organic aerosols (SOA) (Kroll and Seinfeld, 2008b). Both of these secondary pollutants, O_3 and SOA, are known to cause severe health effects. Together with OH, peroxy radicals therefore control the global oxidizing capacity of the Earth's atmosphere, and as a consequence, the concentration and distribution of greenhouse gases and secondary pollutants. Understanding the spatial and temporal variability of these radicals and being able to model this variability is key to evaluate future changes in the chemical composition of the atmosphere, with implications for both air quality and climate change.

Despite their important role in the atmosphere, the chemistry of peroxy radicals has yet to be fully understood under a wide range of atmospheric conditions, including remote locations (marine boundary layer) (Berresheim et al., 2002; Creasey et al., 2003), continental low-NO_x regions influenced by biogenic emissions (Archibald et al., 2011; Griffith et al., 2013a; Wolfe et al., 2011), polluted urban areas (Dusanter et al., 2009b; Volkamer et al., 2010), and polar regions (Mao et al., 2010; Read et al., 2008). Some of these studies have reported significant differences between measured and modeled concentrations of RO_x species likely due to an incomplete characterization of ambient trace gases and the use of incomplete chemical mechanisms in models. For instance, peroxy radical measurements can be significantly lower (Griffith et al., 2013a) or higher (Wolfe et

al., 2014) than model predictions in forested areas and significant missing OH sinks, likely leading to an underestimation of the OH-to-peroxy radical propagation rate, have been reported for forested (Griffith et al., 2013a; Heard and Pilling, 2003; Stone et al., 2012) and urbanized (Dusanter et al., 2009b; Griffith et al., 2016; Volkamer et al., 2010) areas.

Measuring peroxy radicals is particularly difficult due to their reactive nature and their low ambient concentrations, which requires highly sensitive techniques with inlets designed to avoid the loss of the targeted radicals. Various instruments using different principles have been developed during the last few decades to perform these measurements, including Matrix Isolation Electron Spin Resonance spectroscopy (MIESR: HO_2, RO_2) (Mihelcic et al., 2003, 1985), Laser-Induced Fluorescence (LIF-FAGE: OH, HO_2, HO_2*; RO_xLIF: HO_2, HO_2+RO_2) (Stevens et al., 1994a; Hendrik Fuchs et al., 2008; Dusanter et al., 2009b; Faloona et al., 2004), Chemical Ionisation Mass Spectrometry using PERCIMS (HO_2, HO_2+RO_2) (Edwards et al., 2003; Hornbrook et al., 2011; Kukui et al., 2008a) and Br-CIMS (HO_2) (Sanchez et al., 2016), PEroxy Radical Chemical Amplification (PERCA: HO_2+RO_2) (Cantrell et al., 1984; Hernández et al., 2001; Kartal et al., 2010; Liu et al., 2009; Wood and Charest, 2014), and the more recent Ethane based CHemical AMPlification (ECHAMP) technique (Wood et al., 2017).

PERCA is an indirect measurement method pioneered by Cantrell and Stedman (Cantrell et al., 1984), which measures the sum of peroxy radicals continuously with high sensitivity. Ambient air is sampled in a reactor where each peroxy radical will lead to the formation of several NO_2 molecules via chain reactions after the addition of high concentrations of NO and CO. Once all the peroxy radicals have been consumed, NO_2 is measured by a suitable detector based on luminol chemiluminescence (Clemitshaw et al., 1997), LIF (Sadanaga et al., 2004), cavity ring-down spectroscopy (CRDS) (Horstjann et al., 2014; Liu et al., 2009; Liu and Zhang, 2014) or cavity attenuated phase-shift spectroscopy (CAPS) (Wood and Charest, 2014).

The amplification chemistry resulting from the addition of NO and CO is shown below:

$$RO_2 + NO \rightarrow RO + NO_2 \quad \text{R1a}$$

$$RO_2 + NO + M \rightarrow RONO_2 + M \quad \text{R1b}$$

$$RO + O_2 \rightarrow R_{-H}O + HO_2 \quad \text{R2}$$

$$RO + NO + M \rightarrow RONO + M \quad \text{R3}$$

$$HO_2 + NO \rightarrow OH + NO_2 \quad \text{R4a}$$

$$HO_2 + NO + M \rightarrow HNO_3 + M \quad \text{R4b}$$

$$HO_2 + wall \rightarrow loss \quad \text{R5}$$

$$OH + CO\ (+O_2) \rightarrow \cdots \rightarrow CO_2 + HO_2 \quad \text{R6}$$

$$OH + NO + M \rightarrow HONO + M \quad \text{R7}$$

$$OH + wall \rightarrow loss \quad \text{R8}$$

With the addition of a large amount of NO in the sampling reactor, RO_2 radicals are converted into HO_2 through the formation of an alkoxyl radical (RO) (R1a & R2). This HO_2, together with the sampled HO_2, are converted into OH (R4a). During this process, several molecules of NO_2 are produced, depending on the competition between propagation (R1a, R2, R4a) and termination (R1b, R3, R4b, R5) reactions. R4b termination reaction is dependent on water vapor amount. Then, several fast interconversions between OH and HO_2 occurs through the reaction of OH with CO (R6) and the reaction of HO_2 with NO (R4a), leading to the formation of additional molecules of NO_2. The number of NO_2 molecules formed during these interconversion steps is called chain length (CL) and is limited by the competition occurring between propagation (R4a, R6) and termination (R4b, R5, R7, R8) reactions of both OH and HO_2. The CL is typically in the range of 100−200 under dry conditions (Clemitshaw et al., 1997; Sadanaga et al., 2004; Wood and Charest, 2014).

The most problematic issue concerning PERCA instruments is the chain length dependence on Relative Humidity (RH), which translates into a RH-dependent sensitivity (Mihele and Hastie, 1998, 2000 Sadanaga et al., 2004). The chain length decreases monotonically with RH, likely due to increased losses of radicals on wet surfaces (Mihele et al., 1999a; Miyazaki et al., 2010) and an increase in the HNO_3 yield in reaction R4b. The latter may involve H_2O dimers or the formation of a HO_2-H_2O complex (Reichert et al., 2003). The effect of water vapor on the branching ratio of R4b was investigated by Butkovskaya et al. (Butkovskaya et al., 2009) who reported a linear increase of the HNO_3 yield with RH, with an enhancement factor of about 8 at 50% RH. A rate constant for the reaction between HO_2-H_2O and NO producing HNO_3 was estimated from this work and was found to be 40 times faster than the rate constant for HO_2+NO→HNO_3. This water vapor

enhancement of the gas-phase termination rate of HO_2 may play an important role in the reduction of the chain length.

The amplification chemistry used in ECHAMP relies on the addition of ethane (C_2H_6) instead of CO as proposed by Wood et al. (Wood et al., 2017). The advantages reported by the authors are a lower sensitivity of the CL to relative humidity and a safer use of the instrument in confined areas since ethane is less toxic than CO. The chemical reactions describing the radical cycling when ethane and NO are added in the reactor are the same as above (R1-R8), with the exception than R6 is replaced by the set of reactions shown below:

$$OH + C_2H_6\ (+O_2) \rightarrow \cdots \rightarrow H_2O + C_2H_5O_2 \quad \text{R9}$$

$$C_2H_5O_2 + NO \rightarrow C_2H_5O + NO_2 \quad \text{R10a}$$

$$C_2H_5O_2 + NO + M \rightarrow C_2H_5ONO_2 \quad \text{R10b}$$

$$C_2H_5O + O_2 \rightarrow CH_3CHO + HO_2 \quad \text{R11}$$

$$C_2H_5O + NO \rightarrow C_2H_5ONO \quad \text{R12}$$

Ethane reacts with OH to produce an ethylperoxyl radical ($C_2H_5O_2$) (R9), which then (i) propagates to HO_2 (R10a, R11) through the formation of an alkoxyl radical (C_2H_5O) or (ii) terminates through the formation of organic nitrate (R10b) or nitrite (R12) compounds. Since the interconversion steps between OH and HO_2 go through the formation of $C_2H_5O_2$ and C_2H_5O, the additional loss of radicals (R10b, R12) will lead to a lower CL than for the PERCA approach. It has been shown that this amplification chemistry leads to chain lengths ranging from 25-30 (RH of 1-10%) (Wood et al., 2017). However, if heterogeneous losses of peroxy radicals on the reactor wall contribute significantly to the total termination rate of radicals in the reactor, the CL for ECHAMP should be less sensitive to RH compared to PERCA since $C_2H_5O_2$ exhibits a lower loss rate on wet surfaces than HO_2 (Mihele et al., 1999a). For example, (Mihele et al., 1999a) reported a wall loss rate on Teflon (PFA) of $2.8 \pm 0.2\ s^{-1}$ for HO_2 and $0.8 \pm 0.1\ s^{-1}$ for $C_2H_5O_2$ under dry conditions and showed that the HO_2 loss rate increases with RH in contrast to organic peroxy radicals. This observation was also confirmed by Miyazaki et al. (Miyazaki et al., 2010) who reported a 6-fold higher removal efficiency of HO_2 on Teflon (PFA) surfaces compared to organic peroxy radicals.

PERCA and ECHAMP instruments used in the field are based on dual-channel sampling systems (Liu et al., 2009; Horstjann et al., 2014; Wood et al., 2017; Kartal et al., 2010) to simultaneously quantify NO_2 under two measurement modes (background and amplified modes). In the background mode, NO and N_2 are injected at the entrance of the sampling reactor and CO or ethane (same volumetric flow rate as N_2) is injected at the exit of the reactor once all the radicals have been terminated. Since CO or ethane are not added together with NO, there is no amplification chemistry. The NO_2 mixing ratio exiting the reactor is the sum of ambient NO_2, a O_3 reaction with NO, and the amount of NO_2 produced during the first peroxy radical-to-OH conversion step (R1a, R2, R4a). For the amplification mode, CO or ethane is injected at the entrance of the reactor while N_2 is injected at the exit, allowing the amplification chemistry of peroxy radicals to take place. The mixing ratio of NO_2 at the exit of the reactor is the sum of that observed during the background mode and the NO_2 produced during amplification. The amount of NO_2 generated during amplification (ΔNO_2) is inferred from the difference between the amplification and background modes.

It is important to note that these instruments will amplify all radicals that can propagate to HO_2, including RO_2 but also OH and RO. While the measurements of a chemical amplifier represent the sum of RO_x, tropospheric concentrations of OH and RO are ~200-1000 times lower than those of HO_2 and RO_2 and the measurements are thus considered as being the sum of HO_2 and RO_2.

The total mixing ratio of peroxy radicals calculated from the amount of NO_2 produced during the amplification stage (ΔNO_2) and the CL is retrieved as shown in Eq. 1.

$$[HO_2] + \Sigma[RO_2] = \frac{\Delta NO_2}{CL} \quad (1)$$

Quantifying the sum of peroxy radicals from Eq. 1 requires calibrating the CL by generating a known concentration of HO_2 or another peroxy radical. The CL is usually only calibrated for a few radicals by generating a known concentration of methyl peroxy (CH_3O_2) and peroxyacetyl ($CH_3C(O)O_2$), both being simultaneously produced from the photolysis of acetone at 254 nm (Miyazaki et al., 2010; Wood and Charest, 2014). Another method used to calibrate the chain length is based on the generation of CH_3O_2 from the photolysis of methyl iodide (CH_3I) in air at 254 nm (Clemitshaw et al., 1997; Green et al., 2006).

This publication reports the construction of a dual-channel chemical amplifier for ambient measurements of peroxy radicals using both the PERCA (CO/NO) and ECHAMP (ethane/NO) approaches. The main objective was to improve our understanding of these two approaches, which will ultimately provide a better assessment of uncertainties associated with chemical amplifier measurements. In this context, optimal operating conditions were identified for each approach and experimental observations were compared to box-model simulations to gauge our understanding of the radical amplification chemistry. The instrument was calibrated using a large range of peroxy radicals, including HO_2 and organic peroxy radicals formed during the OH-oxidation of alkanes, alkenes, aromatics and oxygenated VOCs. These experiments allowed investigating whether the change in CL observed experimentally is consistent with the formation yield of organic nitrate ($RONO_2$) or nitrite (RONO) species reported in the literature for each tested radical. Finally, ambient measurements are reported to illustrate the performances of this instrument.

2.3 Experimental Section

2.3.1 Description of the chemical amplifier

A schematic diagram and photo of the apparatus built at IMT Lille Douai is shown in Figure 2.1. It consists of two sampling reactors operated in amplification and background modes, two monitors to simultaneously measure NO_2 at the exit of the reactors, and two sets of solenoid valves to switch (i) between background and amplification modes in each reactor (SV1a, SV1b, SV2a, SV2b) and (ii) the sampling of the NO_2 monitors between the two reactors (SV3, SV4) as further described below for the measurement sequence.

Ambient air is sampled into two PerFluoroAlkoxy (PFA) reactors (0.635 cm o.d. × 60 cm length, wall thickness 0.08 cm) with two PFA inlets (0.635 cm o.d. × 1.5 cm length) at a total flow rate of approximately 800 cm^3 min^{-1}. The inlets and the reactors are connected together using home-made 3D printed nylon couplers (Figure S2.9) design to add and mix the reagent gases with the sampled air. The reagent gases are mixed with ambient air through two circular channels (2 mm apart) between the sampling inlet and the reactor, each channel being characterized by 5 radial injection holes. This design was adopted to improve the mixing between ambient air and the reagents. All flow rates are regulated by mass flow controllers.

For the amplification channel, NO (84 SCCM-PERCA, 14 SCCM-ECHAMP, 50 ppm in N_2) and CO (80 SCCM, 100%) or ethane (50 SCCM, 30% in N_2) are added upstream the reactor via the nylon injector, while a flow of nitrogen (equivalent to the CO or ethane flow rate) is added downstream the reactor, approximately 60 cm (0.9 s residence time) after the initial injection of CO (or ethane). For the background mode, N_2 is added upstream while CO (or ethane) is added downstream. Four solenoid valves (SV1a, SV1b, SV2a, SV2b) allow switching the addition of CO (or ethane) and nitrogen between the downstream and upstream injection ports, to change the measurement mode in each reactor. Flow rates of CO (or ethane), NO and N_2 have been optimized to get maximize the CL for both amplification chemistries and are discussed in the results section (Table 2.1). At the exit of the reactors, air free of RO_x radicals is transported through additional 6-m long pieces of PFA tubing (0.635 cm o.d.) to the NO_2 monitors at a flow rate of 800 cm^3 min^{-1}.

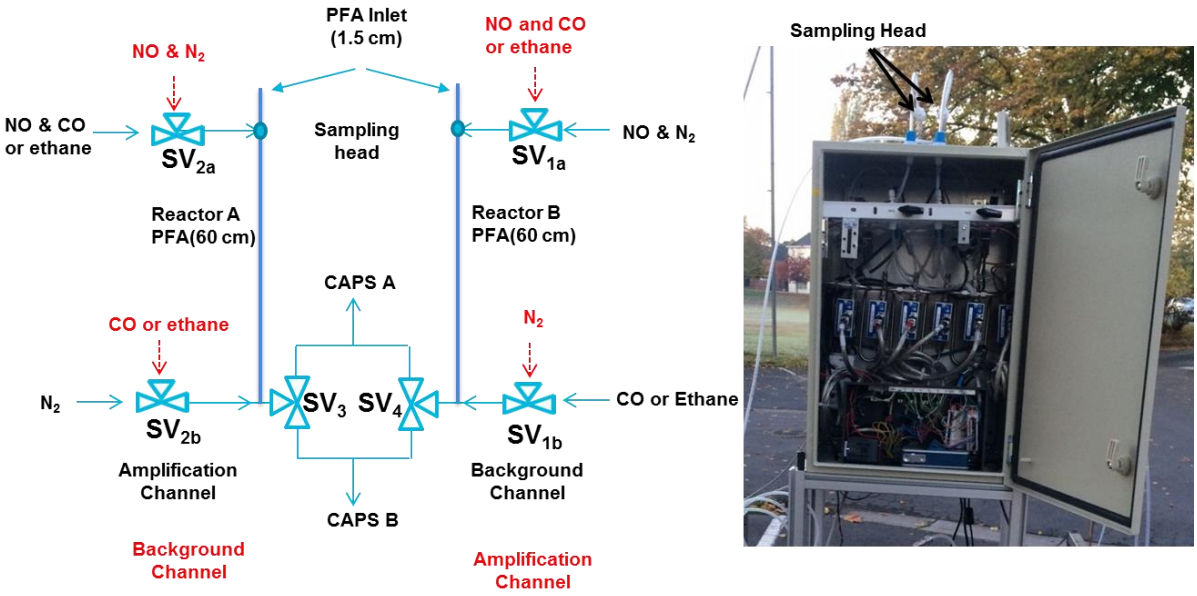

Figure 2.1 Schematic of the IMT Lille Douai PERCA instrument

High sensitivity CAPS (Cavity Attenuated Phase Shift) monitors from AERODYNE Research Inc. were coupled to the reactors to quantify NO_2. For the monitors used in this work, air is sampled through a nafion dryer and enters an 82 cm^3 stainless steel absorption cell held at 27 °C, consisting of two high reflectivity mirrors (R ~ 99.99%). The photons provided to the absorption cell are emitted by a blue light-emitting diode (LED). The light exiting the cell passes through a bandpass

filter centered at 450 nm and is detected by a vacuum photodiode. The NO_2 concentration is derived from the phase-shift observed in the detected signal, which is proportional to the amount of NO_2.

All reagent gases were found to generate spurious signal in the CAPS monitors. The addition of 1-6 ppm of NO (99.995% purity) in the reactors leads to several ppb of NO_2 due to contamination of the NO mixture by NO_2 and a possible conversion of NO into NO_2 in the transfer lines and mass flow controllers. To reduce this spurious signal, the NO reagent gas was purified using an inline chemical filter made of iron(II) sulfate heptahydrate ($FeSO_4.7H_2O$, Fisher scientific). This filter was found to be very efficient with less than 0.2 ppb of NO_2 remaining in the reactor after the addition of 1 ppm of NO. The addition of 10% CO and 2% ethane in the reactors led to a spurious signal equivalent to approximately 1.5 and 3 ppb of NO_2. This signal was found to be proportional to the reagent concentration and is thought to be due to light scattering since these species do not absorb at 450 nm. A lower signal observed for CO seems consistent with lower scattering cross-sections reported in literature for it compared to alkanes (Sneep and Ubachs, 2005; Sutton and Driscoll, 2004).

A sequence of 4 steps of 90-s measurements spanning a 6-min period is required to measure a concentration of peroxy radicals (Figure S2.10): (1) NO_2 is measured from each reactor, with one reactor being operated in background mode and the other reactor in amplification mode; (2) the CAPS sampling inlets are switched between the two reactors; (3) both the measurement mode and the CAPS sampling are switched between the 2 reactors; (4) the CAPS sampling inlets are switched. All NO_2 measurements performed under amplified conditions are averaged together and all measurements performed under background conditions are also averaged together. Only the last 70-s of each NO_2 measurement step are used in the averaging process to calculate ΔNO_2 (see S2.10). This sequence of steps is necessary to cancel out any bias in ΔNO_2 arising from (i) a drift in monitors' zeros and (ii) slightly different behaviors of the 2 reactors (spurious NO_2 signals from reagents, O_3 titration by NO, wall losses of O_3…).

All compressed gas cylinders used in this study were provided commercially: CO (100%, Air Liquide, France**)**, ethane (30±2% in N_2, Linde Co.), NO (50 ppm in N_2, Air Liquide), N_2 (Messer, purity >99.9999%). Volatile organic compounds were purchased from Sigma Aldrich with a purity better than 99%.

2.3.2 Calibration of the Chain Length (CL)

As discussed in the introduction section, the CL can be quantified from Eq. 1 when the instrument samples air containing a known concentration of peroxy radicals. Peroxy radicals were generated in this study through the photolysis of water-vapor at 184.9 nm in a turbulent flow tube, creating an equimolar mixture of OH and HO_2 (Reactions R13-R14). This method is commonly used to calibrate field measurements of OH and HO_2 performed by LIF-FAGE instruments (Dusanter et al., 2008a).

$$H_2O + h\nu\ (\lambda = 184.9nm) \rightarrow OH + H \qquad \text{R13}$$

$$H + O_2 + M \rightarrow HO_2 + M \qquad \text{R14}$$

In this study, OH was quantitatively converted into HO_2 by adding CO in the calibrator as shown in R6 or by adding a volatile organic compound (VOC) to generate a mixture of HO_2 and RO_2 radicals (Lew et al., 2018). For instance, isoprene (C_5H_8) is added inside the calibrator to convert OH into an organic peroxy radical mixture of $C_5H_8(OH)O_2$ isomers. The CO and VOC concentrations were set to convert approximately 99% of OH in less than 2 ms, ensuring a negligible OH loss on the calibrator inner surface. Diluted mixtures of each targeted VOC (Table 2.1) were prepared by injecting the pure compound into 18 liters of zero air (6-L stainless steel canisters at 3 bars). A flow rate of 2.5 SCCM (Standard Cubic Centimeter per Minute) of the diluted CO or VOC mixtures was mixed with 35 SLPM (Standard Liter per Minute) of dry or humid zero air in the calibrator using mass flow controllers. RH was varied in the range 10-90% (T=24±2°C) to produce peroxy radical concentrations within the range 2×10^9-3×10^{10} cm^{-3}.

Series of calibration experiments were performed using CO and all the VOCs reported in Table 2.1. When CO is used, only HO_2 exits the calibrator and the measured CL is characteristic of only one peroxy radical. This CL is defined as $CL_{(HO2)}$ in the following. However, when a VOC is added in the calibrator, an apparent CL is measured for a mixture of HO_2 and RO_2 radicals. Rearranging Eq. 2.1 leads to Eq. 2 for the calculation of this CL, which will depend on the generated RO_2 radical.

$$CL = \frac{\Delta NO_2}{[HO_2]+[RO_2]} \qquad (2)$$

The radical concentrations at the exit of the calibrator are inferred from Eqs 3-4.

$$[HO_2] = (1 + X) \times [H_2O] \times \sigma_{water} \times \Phi_{OH+H} \times (F \times t) \quad (3)$$

$$[RO_2] = (1 + X) \times [H_2O] \times \sigma_{water} \times \Phi_{OH+H} \times (F \times t) \quad (4)$$

Here, HO_2 and RO_2 concentrations are calculated from the water concentration inside the calibrator, $[H_2O]$, its absorption cross-section at 184.9 nm, σ_{water}, the photo dissociation quantum yield, Φ_{OH+H}, the photon flux, F, and the photolysis duration, t. The terms $(1+X)$ and $(1-X)$ account for the non-unity RO_2 yield observed for some VOCs (Table 2.1), X being the HO_2 yield formed along with RO_2 in the reactions of PH with some VOCs, which allows accounting for its direct formation together with the formation of RO_2 radicals from RH+OH reactions. The absorption cross section for H_2O and quantum yield for OH+H reported in several studies are 7.14×10^{-20} cm^2 $molecule^{-1}$ (Cantrell et al., 1997; Creasey et al., 2000) and unity, respectively. The product (F×t) is measured experimentally by ozone actinometry using Eq. 5, where $[O_2]$ is the oxygen concentration, σ_{O2} the oxygen absorption cross section at 184.9 nm (1.21×10^{-20} cm^{-2}) (Dusanter et al., 2008a) that is system dependent, because it depends on the column amont of O_2, and $[O_3]$ the ozone concentration produced in the calibration cell. The latter has to be measured during a calibration experiment.

$$(F \times t) = \frac{[O_3]}{2 \times [O_2] \times \sigma o_2} \quad (5)$$

During a calibration experiment $[O_3]$ was measured as NO_2 by CAPS after titration by NO in one of the reactors operated in background mode, keeping NO at the same mixing ratio as used for PERCA or ECHAMP measurements of peroxy radicals. For this measurement, dry zero air flowed through the calibrator and the mercury lamp was switched ON and OFF several times to determine $[O_3]$ by difference. Ozone concentrations were in the range of 2.5-3.0 ppb. $[H_2O]$ was measured by a LI-COR 840A based on infrared absorption and calibrated versus a dew-point hygrometer (Mitchell S8000). The CAPS instruments were calibrated with an NO_2 standard mixture at 190 ± 3 ppb (2σ) certified by LNE (French National Metrology Institute).

The accuracy of the calibrated CL (Eq. 2) depends on the uncertainty of both the measured ΔNO_2 and the generated peroxy radical concentration. The precision on ΔNO_2 can be neglected since the

use of large radical concentrations during calibration experiments leads to a negligible random error associated to the quantification of the NO_2 signal. If CO is added in the calibrator to only produce HO_2, the accuracy (2σ) on ΔNO_2 (1.5%) is much lower than the accuracy on the generated peroxy radical concentration of 31% (2σ) as reported by Dusanter et al. (2008) for the same calibrator ran under similar operating conditions. A propagation in quadrature leads to a total accuracy of 31% (2σ) for the CL.

The apparent chain length for individual RO_2 radicals, $CL_{(RO2)}$, was computed from Eq. 6. ΔNO_2 is the amount of NO_2 produced when both HO_2 and RO_2 radicals are sampled by the instrument, $CL_{(HO2)}$ is determined during a calibration experiment using CO, and both HO_2 and RO_2 concentrations are calculated from Eqs. 3-5.

$$CL_{(RO_2)} = \frac{\Delta NO_2 - CL_{(HO_2)} \times [HO_2]}{[RO_2]} \quad (6)$$

Direct photolysis of the parent VOCs was investigated during these calibration experiments using dry conditions (RH< 1%). The fraction of ΔNO_2 due to radicals produced by VOC photolysis was quantified for each experiment and was subtracted from ΔNO_2 to calculate $CL_{(RO2)}$ from Eq. 6. Table 2.1 reports the fraction of radicals produced by direct photolysis for each VOC. The amount of NO_2 produced by the radicals generated through the photolysis of VOCs was always lower than 7% of ΔNO_2 (which is due to the sum of those from photolysis of VOCs + water photolysis), with the exception of vinylacetate (14%).

The difference between $CL_{(HO2)}$ and the apparent $CL_{(RO2)}$ should only depends on RO_2-to-HO_2 propagation reactions (R1-R3), which can be factored into a RO_2-to-HO_2 transmission term as shown in Eq. 7, $T_{(RO2)}$ being the fraction of RO_2 radicals propagated to HO_2.

$$CL_{(RO_2)} = CL_{(HO_2)} \times T_{(RO_2)} \quad (7)$$

2.4 Box modeling of the amplification chemistry

The Master Chemical Mechanism (MCM) v3.2 and the F0AM model (Framework for 0-D Modeling) (Wolfe et al., 2016) were used to simulate both the amplification and background modes under different operating conditions of reagents and humidity. A radical wall loss for HO_2 was

added in the chemical mechanism with a first order loss rate parameterized from experimental measurements of radical losses in the PFA reactors (supplementary material S2.11). In addition, since MCM does not include RO+NO reactions, which are not important for atmospheric chemistry but essential for the chemistry occurring in the chemical amplifier, the reaction of C_2H_5O with NO leading to the formation of C_2H_5ONO was added using a rate constant of 4.4×10^{-11} cm^3 $molecule^{-1}$ s^{-1} (Atkinson et al. 1997). MCM does not include the formation of HNO_3 from the HO_2+NO reaction (Butkovskaya et al., 2009, 2007)which is thought to occur through the formation of the $HO_2.H_2O$ complex. A branching ratio for the formation of HNO_3 was included in the MCM to perform sensitivity tests. The branching ratio for this reaction ($k_{HO_2+NO\rightarrow HNO_3}/k_{HO_2+NO\rightarrow OH+NO_2}$) was considered to be 0.5% under dry conditions (Butkovskaya et al., 2007) and dependent on RH with an amplification factor of 8 at 50% RH (Butkovskaya et al., 2009). Sensitivity tests were performed using (1) a water-independent branching ratio of 0.5% (HNO_3/dry in Figures 2.2-2.4), (2) a linear parameterization of the ratio on RH leading to a value of 0.5% under dry conditions and a value 8 time higher at 50% RH (HNO_3/RH_dep in Figures 2.2-2.4), and (3) a parameterization leading to half the water-dependence reported by Butkovskaya et al. (2009) (HNO_3/adj_RH_dep in Figures 2.2-2.4). Uncertainties on the later simulations (dotted lines in Figures 2.2-2.4) were derived as reported in Wood et al. (2007) assuming an error of 25% on the branching ratio under dry conditions and an additional error of 28% associated to the humidity dependence of this ratio.

The model was used to calculate the NO_2 concentration at the exit of each reactor for an initial concentration of HO_2 at the inlet similar to those generated during calibration experiments of the CL. The simulations were run for 5-s of reaction time and the model output of NO_2 at 2-s of reaction time was used to calculate the modeled CL using Eq.2. These simulations have shown that the amount of NO_2 produced from the radical amplification chemistry levels off at approximately 0.5-s of reaction time, e.g. NO_2(0.5-s)/NO_2(5-s)>97.7%.

Table 2.1 Summary table of targeted VOCs.

VOC	*Concentration in calibrator (molecules cm^{-3})*	*OH rate constant* (cm^{3}molecule^{-1}s^{-1})*	*HO_2 yield⁂ VOC+OH reactions* (X) (%)	ΔNO_2(VOC photolysis)/ΔNO_2 (VOC photolysis+water photolysis) (%)
Isoprene	*6.2×10^{12}*	*1.0×10^{-10}*	*6*	*1.7*
Limonene	*3.7×10^{12}*	*1.7×10^{-10} ϕ*	-	*1.9*
m-xylene	*2.5×10^{13}*	*2.3×10^{-11}***	*45*	*0.5*
β-pinene	*7.7×10^{12}*	*7.8×10^{-11}*	-	*3.3*
Methylvinylketone	*3.5×10^{13}*	*2.0×10^{-11}*	-	*3.2*
Acetaldehyde	*3.8×10^{13}*	*1.5×10^{-11}*	-	*0.1*
Pentane	*1.6×10^{14}*	*3.8×10^{-12} ∞*	-	*0.3*
3-methylpentane	*1.2×10^{14}*	*5.2×10^{-12} ∞*	-	-
Cyclohexane	*8.8×10^{13}*	*7.0×10^{-12} ∞*	-	-
Toluene	*1.0×10^{14}*	*5.9×10^{-12}***	*28*	*0.7*
Vinylacetate	*4.8×10^{13}*	*1.3×10^{-11}****	-	*14*
1-pentene	*2.1×10^{13}*	*3.1×10^{-11} "*	-	*5.6*
Cyclopentene	*1.1×10^{13}*	*6.7×10^{-11} "*	-	*6.6*

*(Atkinson et al., 2006); **(Calvert et al., 2011) ; ***(Teruel et al., 2006); "(Atkinson, 1986); ∞(Atkinson, 2003); ϕ (Braure et al., 2014); ⁂ HO_2 yields from MCM V3.2

2.5 Results & Discussion

This section reports a series of characterization and optimization experiments using both PERCA (CO/NO) and ECHAMP (ethane/NO) approaches. The impact of relative humidity on the chain length is investigated for each approach using operating conditions leading to the highest sensitivity. In addition, a comparison of measured CL to values inferred from box modeling is used to test our understanding of each amplification chemistry. The differences observed in CL when calibrating the chemical amplifier with different RO_2 radicals are investigated and contrasted in

terms of differences expected from the formation of organic nitrate (R1b) and nitrite (R3) species. Finally, field measurements are presented to illustrate the performance of this instrument.

2.5.1 Gas Reagents Optimization

A mixture of HO_2 and organic peroxy radicals was generated by adding isoprene to the calibrator as described in the experimental section. The dependence of the measured (symbols) and modeled (lines) chain lengths on reagent gases at 50% RH are shown in Figures 2.2 and 2.3. For PERCA (Figure 2.2), CO and NO were varied in the range 0.6-20% and 0.3-12.5 ppm, respectively. Figures 2.2a shows that both experimental and modeled CL increase with the addition of NO up to 5-6 ppm at a constant CO mixing ratio of 4.5%. When NO is over 6 ppm, the CL starts decreasing due to a faster increase of the OH + NO (R7) reaction rate compared to HO_2 + NO (R4a). Figure 2.2b shows that when CO is varied at a constant NO mixing ratio of 6 ppm, a plateau is reached at CO mixing ratios higher than 10%. Other studies have shown similar results with a plateau reached at approximately 7% (Clemitshaw et al., 1997)(Kartal et al., 2010; Sadanaga et al., 2004), 10% (Sadanaga et al., 2004) and 8.7% CO (Wood et al., 2014) for NO mixing ratios of 3, 3 and 3.3 ppmv, respectively. The difference between these operating conditions that are optimized to get the largest CL may be due to the use of different materials to build the reactors and different reactor designs, which led to different wall losses of radicals.

While the relative NO- and CO-dependencies of the CL are well described by the different models, Figure 2.2b shows that experimental CL values are lower than modelled values by approximately a factor of 2 when the base MCM simulation is considered (see section 2.3, red line), with maximum values around 55 and 120 at 10% CO, respectively. The simulation accounting for the formation of HNO_3 from HO_2+NO with a water-independent branching ratio of 0.5% (HNO_3/dry, grey line) is in better agreement with the measured CL values, with a small overestimation of the model by approximately 15-25%. Implementing the water-enhancement of the HNO_3 yield reported in the literature (see section 2.3) leads to a severe model underestimation by a factor of approximately 2. This issue is further discussed for the 2 amplification chemistries below.

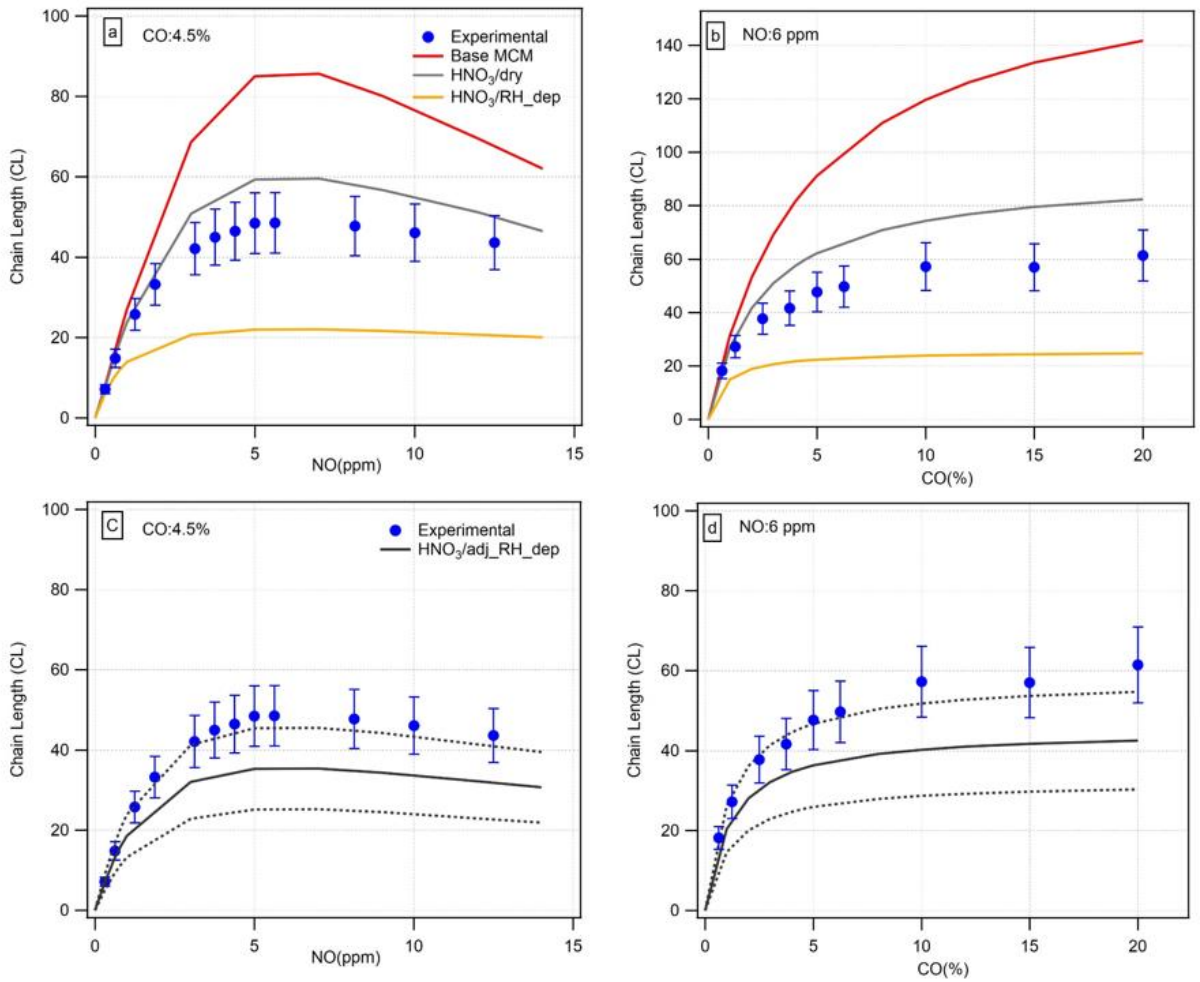

Figure 2.2 Chain length dependences on reagent gases for the PERCA (CO/NO) approach. Experimental and modeled values are shown as markers and lines, respectively. Experiments were performed at ambient temperature (23°C) and 50% RH. Uncertainty on experimental values are 1σ. Panels c,d: dotted lines are uncertainty on modelled values. See section 2.3 for the modeling scenarios.

For the ECHAMP approach, the 2 reagents were varied on a smaller range of concentrations, c.a. 0.4-6.0% for ethane and 0.2-3.1 ppm for NO. Figure 2.3 displays the dependence of both experimental and modeled CL on NO (panel a) and ethane (panel b). The relative dependence on both reagents (curve shape) is similar to that observed for PERCA with optimum CL values for NO and ethane mixing ratios of 0.9 ppm and 2.1%, respectively. These optimum CL values are similar to values reported by Wood et al. (2017) of 1 ppm NO and 2.3% ethane, respectively. The maximum CL is approximately 3 times lower than for the PERCA approach, due to additional losses of radicals through the formation of nitrate (R1b) and nitrite (R3) compounds during the

radical amplification stage. Similarly to the PERCA approach, CL values simulated by the base MCM model are systematically higher than experimental values by a factor of approximately 2. In addition, as clearly seen in Figure 2.3c, the shape of the experimental trace is not well reproduced by the model with a peak in CL at higher NO for the model. Implementing the formation of HNO_3 from HO_2+NO using the water-independent branching ratio has a much lower impact on the modelled CL values than for PERCA with a decrease of the CL by only 5-7%. This lower impact is due to a smaller contribution of this additional loss process to the total loss of radicals in the reactor (larger total loss rate compared to PERCA due to organic nitrite and nitrate formation from R3 and R1b, respectively). Using the water-dependent parameterization of the yield brings the modeled values in much better agreement with the measurements, which contrasts to that observed for the PERCA approach.

Additional simulations were performed for both PERCA and ECHAMP in order to see whether a smaller water-enhancement of the HNO_3 formation yield could reconcile the model/measurement comparison for the two amplification chemistries when uncertainties on modeled and measured CL values are considered. As shown in Figures 2.2 and 2.3 (panels c and d), simulated CL values considering an enhancement factor of 4 at 50% RH (HNO_3/adj_RH_dep) would lead to modeled CL values that are within uncertainties with experimental measurements. Looking at each amplification chemistry separately would lead to the conclusion that the measured CL values and dependences on reagent gases could be relatively well reproduced if the water-dependence reported by only one study in the literature is overestimated by a factor 2. However, a systematic error on the parameterization of the HNO_3 yield in the model should lead to a systematic deviation from the measurements (either positive or negative) for both comparisons (PERCA and ECHAMP). It is clear that while the additional loss of radicals due to HNO_3 formation is important for both PERCA and ECHAMP, the uncertainty related to its parameterization cannot fully account for the model/experiment disagreement observed in this study (model underestimation for PERCA and overestimation for ECHAMP) and additional work is needed to improve our understanding of these amplification chemistries.

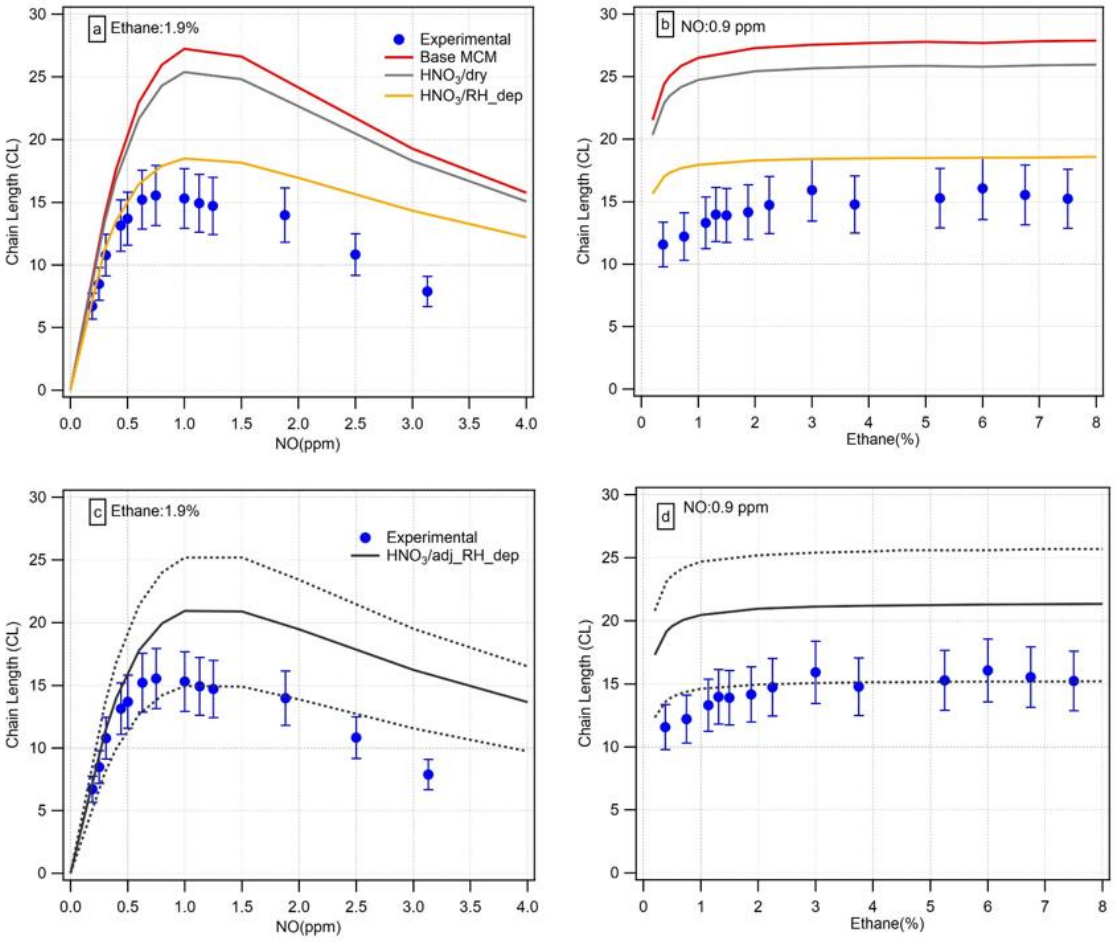

Figure 2.3 Chain length dependences on reagent gases for the ECHAMP (ethane/NO) approach. Experimental and modeled values are shown as markers and lines, respectively. Experiments were performed at ambient temperature (23°C) and 50% RH. Uncertainty on experimental values are 1σ. Panels c,d: dotted lines are uncertainty on modelled values. See section 2.3 for the modeling scenarios.

It is interesting to note that a large impact of radical losses in the inlet of the chemical amplifier on this model/measurement comparison was ruled out. As mentioned in the experimental section, first order wall loss rates of HO_2 and $CH_3CH_2O_2$ were measured experimentally at different RH and were found to be 7.1 s^{-1} and lower than 1 s^{-1}, respectively, at 50% RH. Based on the residence time in the PFA inlet (22 ms) and the first order loss rate observed for HO_2, a conservative upper limit of 11% is estimated for the amount of peroxy radicals lost on the wall. In addition, increasing the total flow rate inside the inlet by a factor of 2 did not significantly impact the measured CL values. It is also interesting to note that setting the wall loss of HO_2 to zero in the base MCM model leads to an increase of the modeled chain length by a factor of 2, indicating that a modification of the

reactor geometry to reduce the surface-to-volume ratio and the use of a more hydrophobic material to build the reactors may help increasing the experimental CL and hence the sensitivity of the instrument.

Table 2-2 Operating conditions for the PERCA and ECHAMP approaches

Parameter	Value
PFA reactor PFA inlet	Length: 60 cm, Outer diameter: 0.635 cm Length:1.5 cm, Outer diameter: 0.635 cm
Sampling flow rate	Approx. 800 SCCM
Reactor residence time Inlet residence time	0.9 s 22 ms
ECHAMP approach (Ethane/NO)	
NO	0.9 ppm
Ethane	2.1%
Experimental CL (50% RH) Modeled CL (50% RH)	15 28
PERCA approach (CO/NO)	
NO	6 ppm
CO	10%
Experimental CL (50% RH) Modeled CL (50% RH)	55 105

2.5.2 Linearity of the chemical amplifier response (ΔNO2) with HO2

The linearity was investigated using the ECHAMP approach by adding CO in the calibrator to only produce HO_2. This experiment was performed using a calibrator equipped with a chemical N_2O filter located between the Hg lamp housing and the turbulent flow tube. The photon flux at 184.9 nm was varied over a factor of 40 by adjusting the concentration of N_2O inside the chemical filter, allowing to vary the HO_2 mixing ratios in the range 2-85 ppt (4.9×10^7-2.1×10^9 cm^{-3}) at a constant RH of 23%. These values encompass ambient concentrations usually observed during field campaigns.

Plotting ΔNO_2 versus HO_2 in Figure 2.4 indicates a good linearity over the tested range of concentrations. A linear regression exhibits a coefficient of determination (R^2) of 0.98 and a

negligible intercept (not statistically significant at 1σ). The CL determined at 23% RH from the slope of this regression line is 24 ± 1 (1σ), which is larger than the CL reported in Figure 2.2d (approx. 15) under similar conditions of reagents at 50% RH, indicating a strong dependence of the CL with RH.

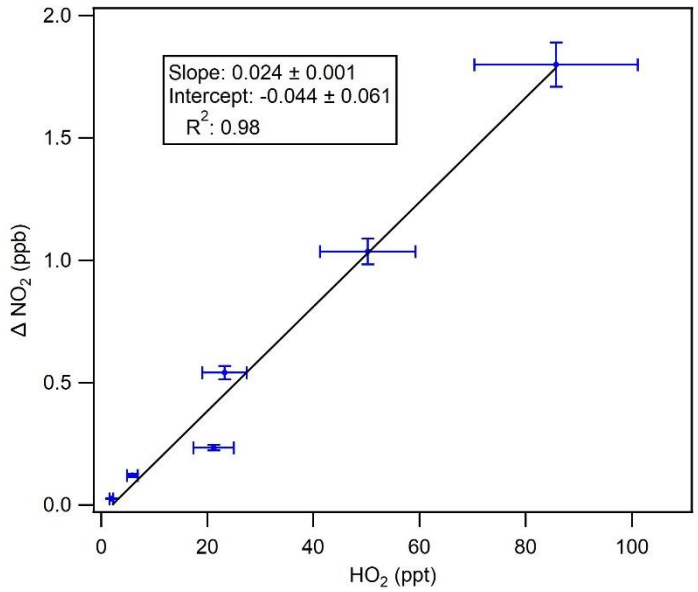

Figure 2.4 Scatter plot of ΔNO_2 with HO_2 for the ECHAMP approach. Experiments performed at a temperature of 23 °C and (23±2) % RH. The solid line represents the linear regression line; Error bars are 1σ uncertainty on NO_2 measurements and HO_2 generation. Errors on slope and intercept are 1σ.

2.5.3 Dependence of the CL on RH

The CL dependence on RH is considered as a major issue for chemical amplification techniques and was investigated for both ECHAMP and PERCA by varying RH in the range 10-85% during calibration experiments (isoprene added in the calibrator). As discussed in the introduction section, the CL decreases when humidity increases due to enhanced radical losses on wet surfaces and the potential impact of water dimers and $HO_2.H_2O$ complex on the gas-phase chemistry. To quantify this effect, the RH-dependence of both the experimental and modeled CL was investigated. Experimental (markers) and modeled (lines) CL for both amplification approaches are shown in Figure 2.5 as a function of RH. Operating conditions used during these experiments are reported in table 2.2 and experiments were performed at a temperature of 23±2°C.

In this figure, the experimental CL decreases with RH for both approaches, with a drop of about a factor of 3-4 between 10 and 70% RH. At 10% RH the CL for PERCA and ECHAMP are different by approximately a factor of 4. However, a larger RH-dependence of the CL is observed for PERCA, leading to a factor 3 of difference between the 2 approaches at 70% RH. These results are consistent with the work of Wood et al. (Wood et al., 2017) who reported a lower impact of RH for the ECHAMP technique.

The RH-dependence of the PERCA CL reported in this study exhibits a similar behavior to what was observed by Sadanaga et al. (Sadanaga et al., 2004) up to 60% RH, but seems steeper for RH values larger than 60%. This dependence is also consistent with a decrease by a factor of 2 at 40% RH compared to dry conditions reported in Wood et al. (2017). The modelled CL values displayed in panels a and b show that the simulations assuming a water-dependence of the HNO_3 formation yield adjusted at half the reported value can describe the RH-dependence of the measured CL within uncertainty, while the other simulations are in disagreement for both the absolute CL value and the RH-dependence.

For the ECHAMP approach, the RH-dependence is similar to observations reported in Wood et al. (2017), where the CL is lower by a factor of 1.5 at 40 % RH compared to dry conditions. The modelled CL displayed in panels c and d lead to similar conclusions than for the PERCA approach, where simulations based on a 2-fold lower-than-reported water-dependence for the HNO_3 formation yield are in agreement with the experimental observations within uncertainty up to 70% RH. These results are consistent with the simulation presented in the supplementary material of Wood et al. (2007).

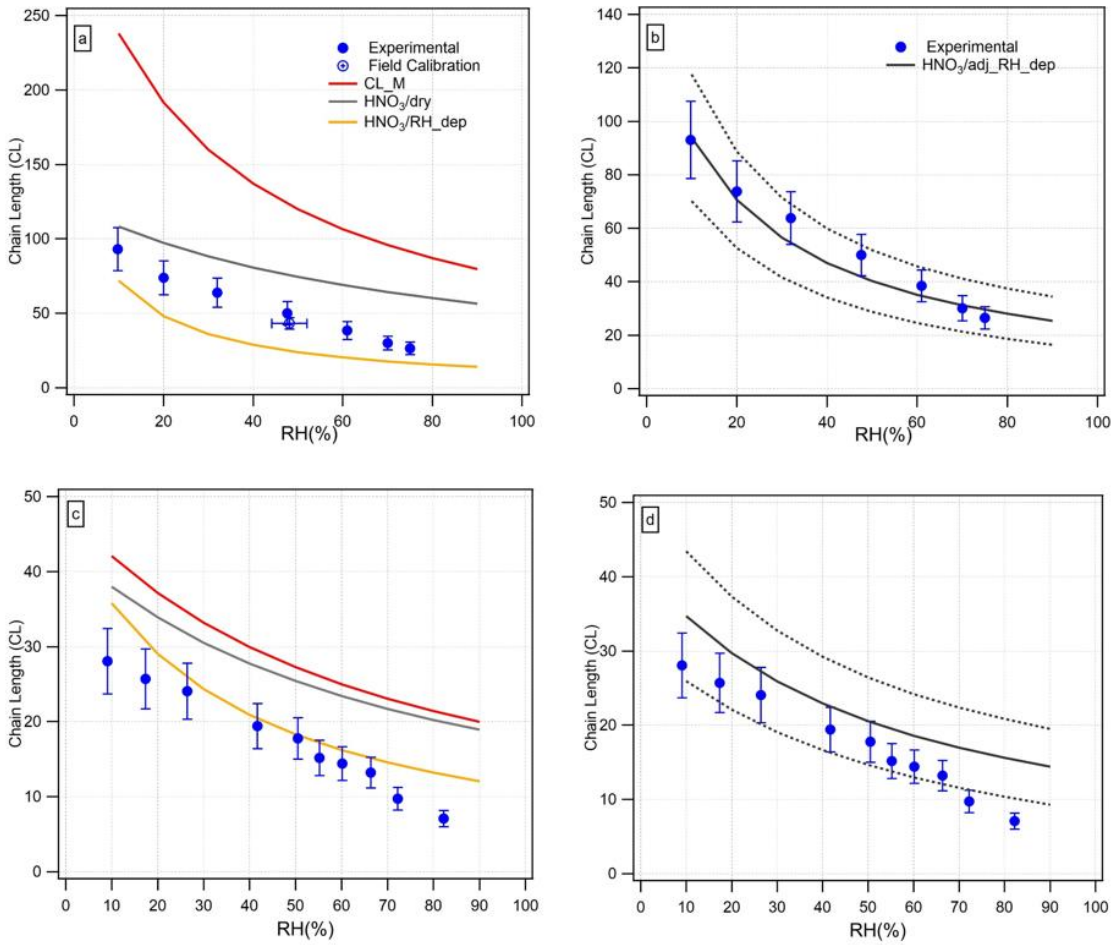

Figure 2.5 Dependences of experimental (markers) and modeled (lines) CL on RH for the PERCA (panels a and b) and ECHAMP (panels c and d) approaches (T = 23±2°C). The empty circle represents calibration experiments performed in the field (see section Field Testing). Uncertainty on experimental values are 1σ. Panels b,d: dotted lines are uncertainty on modelled values. See section 2.3 for the modeling scenarios.

2.5.4 Quantification of $T_{(RO2)}$ for several RO_2 radicals

As mentioned in the introduction section, PERCA and ECHAMP techniques rely on the conversion of RO_2 radicals into HO_2 in order to initiate the amplification chemistry. The propagation reactions involved in this process will only transmit a certain fraction of each RO_2, depending on their organic nitrate (R1b) and nitrite (R2-R3) yields. As a consequence, PERCA and ECHAMP techniques will be blind to the fraction of RO_2 radicals that is not propagated to HO_2. It is important to ensure that PERCA or ECHAMP measurements can be compared to model simulations when

each modeled peroxy radical concentration is weighted by a transmission factor derived from known organic nitrate and nitrite yields.

Experiments were performed to (i) quantify $T_{(RO2)}$ (Eq. 6-7) for a large suite of peroxy radicals and to (ii) contrast measured $T_{(RO2)}$ values to calculations based on organic nitrate and nitrite yields used in atmospheric models for each RO_2. HO_2 and thirteen organic peroxy radicals were produced from the oxidation of CO and VOCs reported in Table 2.1 as described in the experimental section. These experiments were performed at 50% RH and ambient temperature (23±2°C) using the ECHAMP approach and operating conditions set to their optimum values as reported in Table 2.

Due to the large concentration of O_2 in ambient air, nitrite formation is negligible (< 3%) for all RO radicals generated in these experiments, with the exception of methoxyl (CH_3O) which exhibits a 5-fold lower rate constant with O_2. Under normal conditions of temperature and pressure (298 K and 1 atm) and using operating conditions reported in Table 2.2, the nitrite formation yield is estimated to be 8.7% for CH_3O. This higher nitrite yield only concerns the oxidation of acetaldehyde due to the formation of an alkoxyl radical which decomposes to form CH_3O_2.

The measured $T_{(RO2)}$ values are displayed in Table 2.3 and Figure 2.6 as a function of an average yield for nitrate formation. The nitrate yields used in these calculations are from MCM V3.2. This figure clearly indicates that there is a relationship between the two variables, with a decrease of $T_{(RO2)}$ when the yield increases, limonene and β-pinene derived peroxy radicals exhibiting the lowest $T_{(RO2)}$ and highest nitrate yields of approximately 77% and 23%, respectively. These results are consistent with observations reported by Ashbourn et al. (Ashbourn et al., 1998), showing that R1b becomes more significant for large alkyl peroxy radicals, which in turn leads to $T_{(RO2)}$ values lower than unity. While $T_{(RO2)}$ values are scattered within ±10% around the 1:1 line, it is surprising that 9 of the 12 experiments are lower than the 1:1 line. These lower-than-expected values are likely due to the combination of R1b removal reactions and the injection of large concentrations of VOCs in the calibrator to convert OH into peroxy radicals, which, when introduced in the reactor ran under background mode, can lead to a small amplification of the radicals. Tests performed by introducing different concentrations of isoprene in the calibrator showed that the CL is underestimated by less than 10% for this compound under experimental conditions reported in this study. This would bring $T_{(RO2)}$ for isoprene in very good agreement with the known nitrate yield.

A similar impact is expected for the other $T_{(RO2)}$ values measured in this study. In addition, it is interesting to note that lower-than-expected $T_{(RO2)}$ values could also be partly due to NO in homogeneities when ambient air is mixed with the reagents, leading to local concentrations of NO larger than 1 ppm, which in turn can lead to a higher nitrite yield for each RO radical. Indeed, experimental determinations of $T_{(RO2)}$ provide values which are integrated over the reaction time when the reagents are getting mixed with ambient air (NO getting diluted down to 1 ppm). Overall, these results indicate that known nitrate and nitrite yields can be used to scale modelled concentrations of peroxy radicals for comparison with ECHAMP measurements with an uncertainty better than 10%.

It is important to note that these scaling factors will be different for the PERCA approach since a higher NO mixing ratio is used to generate the amplification chemistry. The RO_2-to-HO_2 conversion step will be less efficient due to a higher formation rate of organic nitrites. The nitrite yields are expected to increase from 2-3% to 12-18% for most of the RO radicals used in this study, with a higher increase for CH_3O whose nitrite yield will be close to 36%.

Table 2-3 RO_2 to HO_2 transmission – $T_{(RO2)}$

VOC	*$RONO_2$ yield MCM V3.2 (%)*	$T_{(RO2)}$
Isoprene	10.7	0.84
Limonene	22.8	0.65
m-xylene	7.3	0.91
β-pinene	23.3	0.66
Acetaldehyde	0.1	0.95
Pentane	14.1	0.92
3-methylpentane	12.4	0.74
Cyclohexane	15.0	0.87
Toluene	8.7	0.72
1-pentene	5.9	0.88
Cyclopentene	*4.5*[*]	0.84

* Reference: (Perring et al., 2013)

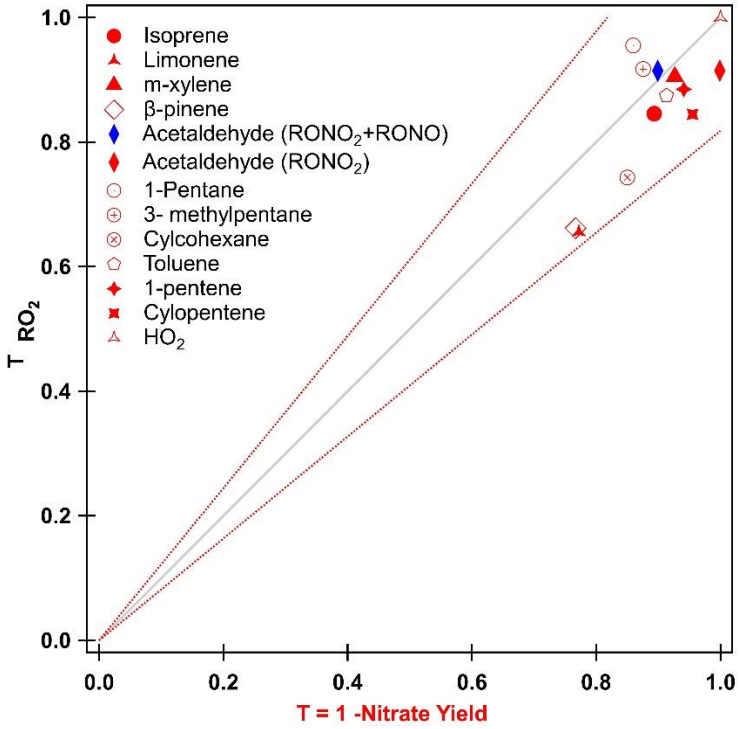

Figure 2.6 Dependence of $T_{(RO2)}$ (ECHAMP approach) on average organic nitrate yields. The blue symbol for acetaldehyde accounts for nitrate & nitrite formation (see text). Plain grey line is 1:1 and dashed red lines are 1.10:1 and 0.90:1.

2.6 Field deployment of the chemical amplifier

The chemical amplifier was first tested in an urban area, close to our laboratory, in the city of Douai, France. These measurements were performed with the PERCA approach, i.e. using CO and NO as reagents (operating conditions from Table 2.2). The measurements were conducted over 3 consecutive days in April 2018 using the sequence shown in Figure S2.10 (supplementary material), which in turn led to a time resolution of 6-min. The overall meteorological conditions allowed to run the instrument under optimal conditions since these 3 days were characterized by clear skies, ambient temperatures between 8 and 25°C, and RH values ranging from 35 to 90%. The only exception was light rain in the early morning of 21 April, during which RH reached 100%. The peroxy radical measurements are shown in Figure 2.7 together with the CL calculated at the measured RH values. The latter varied from approximately 10 up to 75. RO_2+HO_2 mixing ratios ranged from the detection limit up to 20 ppt around 2 pm local time (UTC+2), with sustained

mixing ratios of 5-10 ppt during the late afternoon and nighttime. The magnitude of the measured RO_2+HO_2 mixing ratios and their diurnal variations are similar to trends reported in studies performed at measurements sites under urban influences (Tan et al., 2018a; Whalley et al., 2018a; Wood and Charest, 2014).

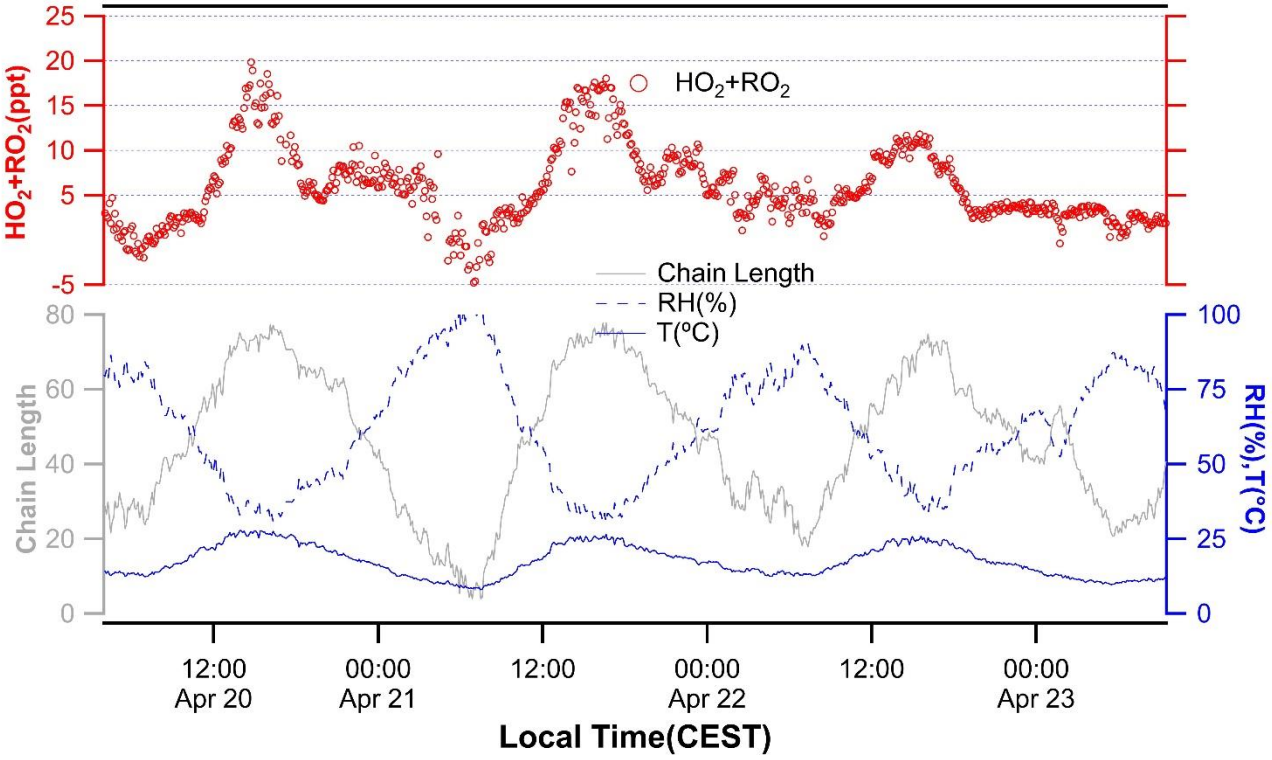

Figure 2.7 **P**eroxy radical measurements performed in Douai (France) by chemical amplification using the PERCA approach

This instrument was then deployed in the Landes forest (France) from 2 to 26 July 2018 as part of the CERVOLAND (Characterization of emissions and reactivity of volatile organic compounds in the Landes forest) field campaign. This forest is mainly composed of pine trees (Pinus Pinaster), which are strong emitters of monoterpenes such as α- and β-pinene. The instrument was coupled to a newly designed 9-m^3 Teflon photo-reactor to investigate in-situ the oxidation of biogenic VOCs (BVOCs). Several experiments were conducted by flushing the photo-reactor with ambient air at different times of the day (nighttime, daytime) to trap air masses characterized by different

chemical compositions. Oxidation experiments were then performed either in the dark or under solar irradiation. Here, we present peroxy radical measurements from one experiment when the photo-reactor was flushed with ambient air during nighttime for 90 minutes. The air mass trapped in the photo-reactor was loaded with large mixing ratios of monoterpenes (14 ppb) and sesquiterpenes (50 ppt). The ambient ozone mixing ratio was low (12-14 ppb) during the flushing period. The air mass was kept in the dark until 12 pm, BVOCs slowly reacting O_3 away (2-4 ppb around 11 am), and was then exposed to solar radiations until 8 pm by uncovering the photo-reactor. Figure 2.8 displays the peroxy radical measurements during these two periods.

Peroxy radicals slowly decreased together with O_3 (O3 42E, Environnement SA) from 1 to 9 am. The mixing ratios dropped from 10 to 2 ppt, and 14 to 2 ppb for peroxy radicals and O_3, respectively. O_3-BVOC reactions were likely the main source of radicals during this time period. Peroxy radicals slowly increased from 9 am to 12 am together with the temperature, indicating that thermo-labile precursors of radicals may have been present in the photo-reactor. Once the photo-reactor was uncovered, peroxy radicals rapidly increased from 6 ppt up to 45 ppt around 3 pm. The latter is similar to previously reported peroxy radicals mixing ratios in forested areas (Stone et al., 2012; Vaughan et al., 2012; Wolfe et al., 2014). During this time period peroxy radical measurements are well correlated with $j(NO_2)$ measured above the photo-reactor (fast CCD spectroradiometer from METCON meteorologieconsult gmbh). Interestingly, O_3 increased at a rate of 3-4 ppb h^{-1} from 12 to 3 pm, reaching a plateau at approximately 20 ppb. These results will be presented in detail in a forthcoming publication.

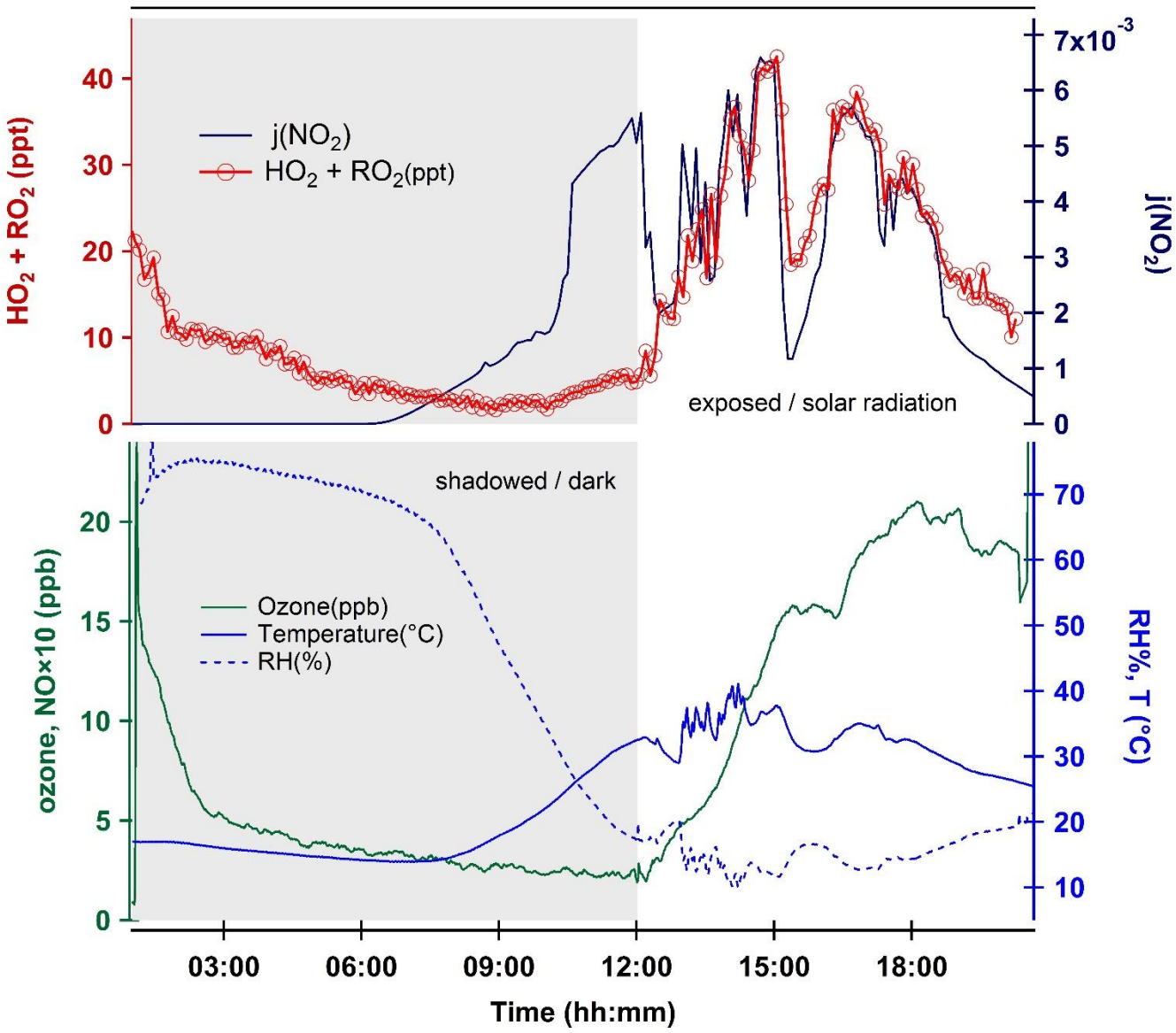

Figure 2.8 Peroxy radical measurements performed in a mobile photo-reactor during the CERVOLAND 2018 field campaign

2.7 Estimation of the detection limit

Lower bounds for the detection limit can be derived from the measurement noise of the 2 CAPS monitors and the RH-dependent CL, assuming that no other sources of noise are present. Measurements of NO_2 by the two CAPS analyzers used in this work exhibit precisions of 10 and

16 ppt (1σ) when zero air is sampled, which translate into detection limits (3σ) of 30 and 48 ppt for 70-seconds of integration (70 occurrences of 1-s NO_2 measurements averaged within each measurement step of 90-s, see supplementary material). This leads to detection limits of 1.3, 2.0, and 3.3 pptv for the ECHAMP approach at RH values of 10, 50, and 80%, respectively, for a total measurement time of 6 min (see measurement sequence in the experimental section). For the PERCA approach, the same procedure leads to detection limits of 0.3, 0.6, and 1.4 ppt at 10, 50, and 80% RH, respectively.

However, detection limits for ambient air measurements are expected to be significantly higher due additional sources of noise such as small fluctuations in reagent flow rates, switches of solenoid valves, and changes in ambient concentrations of NO_2 and O_3, which will degrade the precision on ΔNO_2. In order to better estimate limits of detection, both reactors were run in background mode for long time periods of 3-10 hours during the CERVOLAND field campaign. An experiment of this type is shown in the supplementary material (S4), where ΔNO_2/CL is plotted as a function of time for RH values ranging from 20-30%. A statistical analysis of this series indicate that the mean value of 0.03 ± 0.04 ppt is not statistically significant. The standard deviation of 0.3 ppt translates into a detection limit (3σ) of 0.9 ppt. Assuming that ΔNO_2 is not dependent on RH, since peroxy radicals are not amplified, this would translate into detection limits of 0.7, 1.3, and 3.0 ppt at RH values of 10, 50, and 80 %, respectively. These values are approximately 2 times higher than values calculated from the noise of the CAPS monitors. While these values may still underestimate the detection limit in ambient air, since the O_3 and NO_2 variability is reduced in the photo-reactor, it is clear that detection limits on the order of a few ppt are achievable using the PERCA approach. The ECHAMP approach, which has yet to be tested in the field on this instrument, should exhibit detection limits that are approximately 3 times higher.

2.8 Conclusion

This publication presents the development of a chemical amplifier for ground-based measurements of peroxy radicals in the troposphere. This instrument was used in the laboratory to compare two different approaches regarding the radical amplification chemistry, including the use of CO/NO (PERCA) or ethane/NO (ECHAMP) as reagent gases. Tests performed to identify optimum conditions leading to the highest sensitivity, i.e. the largest chain length, indicate that 10% CO and

6 ppm NO should be used for the PERCA approach, while 2.1% ethane and 0.9 ppm NO are better for ECHAMP. These optimum conditions lead to chain lengths values of approximately 55 and 15 at 50% RH for the PERCA and ECHAMP approaches, respectively. The RH-dependence of the CL was also investigated for both approaches. It was found that the CL decreases with increasing RH, in agreement with previously published studies. The magnitude of the decrease is slightly lower for the ECHAMP technique, with a decrease by a factor 3 and 2.7 for the PERCA and ECHAMP approaches, respectively, when RH is increased from approximately 10 up to 70% at 23±2°C.

The amplification chemistry was modelled using MCM v3.2 for comparison to experimental observations. The model/measurement comparison indicates that modeled CL values overestimate experimental observations by a factor of approximately 2. Additional simulations conducted to assess whether the formation of HNO_3 from HO_2+ NO could impact the CL of chemical amplifiers highlighted that using the yield reported under dry conditions, and a 2-fold lower-than-reported water-dependence for this yield, provides a reasonable description of the CL-dependence on reagent gases and RH for both PERCA and ECHAMP. However, the model overestimation of the ECHAMP CL and underestimation of the PERCA CL seems to indicate that our understanding of the amplification chemistry is still incomplete and deserves addition scrutiny.

The sensitivity of the chemical amplifier to a large range of RO_2 radicals was quantified to determine whether PERCA and ECHAMP measurements can be compared to model simulations when the concentration of each modelled peroxy radical is weighted by a transmission factor derived from known organic nitrate and nitrite yields. This work showed that transmission factors can be calculated from known kinetic parameters and ambient conditions for the pool of organic peroxy radicals tested in this study.

Finally, ambient testing of this chemical amplifier using the PERCA approach showed that this instrument is capable of measuring ambient concentrations of HO_2+RO_2 at levels higher than 1-4 ppt under RH conditions up to 90% once the RH-dependence of the CL has been correctly characterized. Comparisons of the PERCA and ECHAMP techniques to other techniques capable of measuring peroxy radicals would be useful to provide more insight into the accuracy of chemical amplifiers.

Acknowledgments

This work was supported by the French national program LEFE/CHAT INSU. This work was also funded by the French National Research Agency (ANR-11-LABX-0005-01) and the European Funds for Regional Economic Development (FEDER) through the CaPPA (Chemical and Physical Properties of the Atmosphere) project. The CERVOLAND field campaign was supported by the French Environment & Energy Management Agency (Ademe) through the PRIMEQUAL program. This work also benefited from funding from the Région Hauts-de-France, the Ministère de l'Enseignement Supérieur et de la Recherche and the European Fund for Regional Economic Development through the CLIMIBIO project.

The authors want to thank Dr. Sasha Kukui for the loan of a radical calibration source, Prof. Eric Villenave, Dr. Emillie Perraudin and Dr. Pierre-Marie Flaud for the organization of the CERVOLAND field campaign, and Prof. Ezra Wood for useful discussions on the ECHAMP and PERCA techniques.

2.9 Supplementary material

2.9.1 S1 - Inlet/Reactor coupling

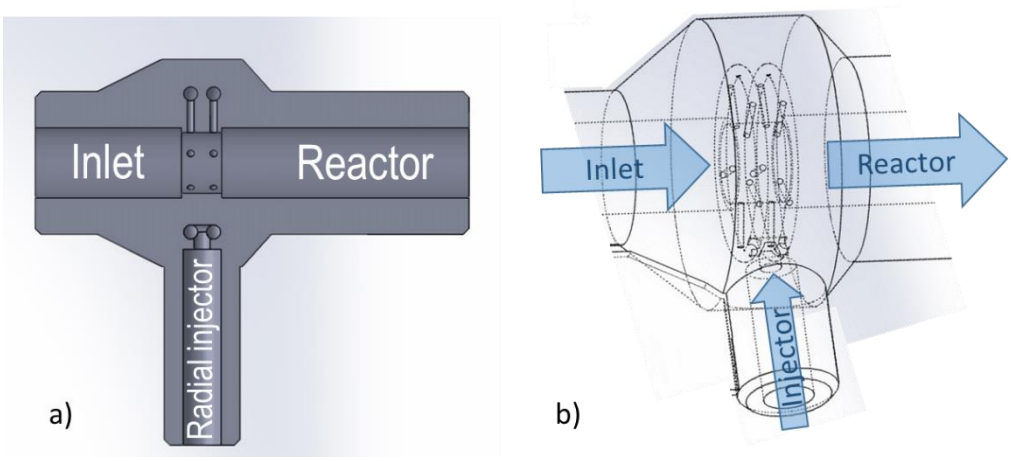

Figure S2.9 a) Schematics of a home-made 3D printed nylon injector in a transversal cut; and b) an enlargement of the double ring, radial injector mixing area, in transparent representation

2.9.2 S2 - Measurement sequence

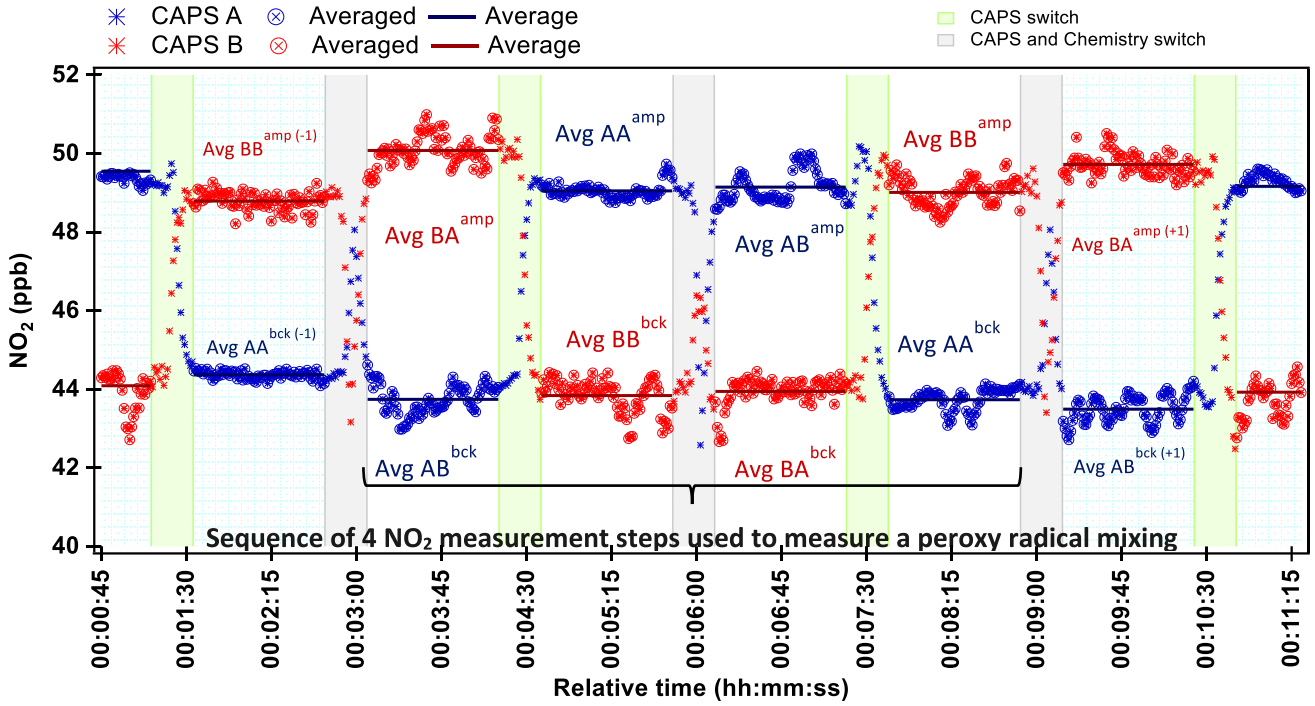

Figure S2.10 Sequence of steps required for the measurement of a peroxy radical mixing ratio. Example of measurements performed during the CERVOLAND field campaign when the chemical amplifier (PERCA approach) was coupled to a photo-reactor (see section 3.5). Peroxy radical mixing ratio of approximately 70 ppt.

Successive switches of the measurement mode in each reactor (amplification / background switch, SV1a,b and SV2a,b) and of the two NO_2 monitors (CAPS switch, SV3 and SV4) are performed to cancel out any potential bias in ΔNO_2 due to (i) a drift in monitors' zeros and (ii) slightly different behaviors of the 2 reactors (spurious NO_2 signals from reagents, O_3 titration by NO, wall losses of O_3…).

All NO_2 measurements performed under amplified conditions are averaged together and all measurements performed under background conditions are also averaged together. Only the last 70-s of each NO_2 measurement step are used in the averaging process to calculate ΔNO_2

ΔNO_2 is calculated as:

$$\Delta NO_2 = [(Avg\ BA^{amp} - Avg\ AB^{bck}) + (Avg\ AA^{amp} - Avg\ BB^{bck}) + (Avg\ AB^{amp} - Avg\ BA^{bck}) + (Avg\ BB^{amp} - Avg\ AA^{bck})]/4$$

Where each *Avg* term stand for the averaged value of an operating mode in amplified (*amp*) or background (*bck*) conditions, first capital letter designating the CAPS detector and the second letter designating the reactor (see Figure 1).

2.9.3 S3 - Wall loss measurements

Wall loss rates for HO_2 and $C_2H_5O_2$ were measured in this study by (i) generating a known concentration of radicals at the entrance of the PFA inlet and by (ii) varying the length of the inlet from 1.5-14 cm keeping all conditions constant. The outer diameter of the inlet and its wall thickness were 0.635 cm and 0.08 cm. $LN(\Delta NO_2)$ was then plotted versus the residence time in the inlet to extract the loss rate (k_w expressed in s^{-1}) from a linear regression fit. This experiment was repeated at different RH values ranging from 10-85%.

Seven determinations of k_w were conducted at different RH values for HO_2 by adding 660 ppm of CO in the calibrator. The results are reported in Figure S3a. Values ranging from 2-12 s^{-1} were observed when RH was varied between 10 and 85%. Plotting k_w as a function of RH indicates that the loss rate increases with humidity and allows proposing the following parameterization based on the linear fit of measurements: $k_{w(HO2)} = 0.13 \times RH + 0.69$ s^{-1}. Mihele et al. (Mihele et al., 1999) reported first order loss rates for HO_2 and PFA reactors (0.635 cm OD) of 2.8±0.2 s^{-1} and 6.3±0.7 s^{-1} under dry conditions and at 50% RH, respectively. While a k_w value of 0.7 s^{-1} derived from the parameterization under dry conditions is lower than the value measured by Mihele et al., the value of 7.2 s^{-1} calculated at 50% is consistent with their work.

Similar experiments were conducted to measure k_w for $C_2H_5O_2$ by adding ethane (380 ppm) instead of CO in the calibrator. When ethane is added in the calibrator, an equimolar mixture of HO_2 and $C_2H_5O_2$ is generated at the exit of the calibrator and the measured k_w values depend on the loss of both HO_2 and $C_2H_5O_2$. Figure S3b displays six experiments performed at RH values ranging from 10-80%. This figure shows that $k_{w(50\%C2H5O2+50\%HO2)}$ ranges from 1-3.5 s^{-1} and does not exhibit a strong dependence on RH. In order to estimate k_w for $C_2H_5O_2$ alone, simulations of the total peroxy radical decay (HO_2+$C_2H_5O_2$) were performed using similar initial concentrations of HO_2 and $C_2H_5O_2$ and values for k_{wHO2} derived from the parameterization discussed above. $k_{wC2H5O2}$ was then adjusted to reach upper and lower bounds of the $k_{w50\%C2H5O2+50\%HO2}$ values observed

experimentally. These results indicate that $k_{w(C2H5O2)}$ is lower than 1 s^{-1} and is not significantly dependent on RH. This is consistent with results published by Mihele et al. (Mihele et al., 1999). A first order loss rate of HO_2 parametrized by $k_{w(HO2)} = 0.13 \times RH + 0.69$ s^{-1} was used for the model simulations presented in the main paper. The loss rate for $C_2H_5O_2$ was neglected in these simulations.

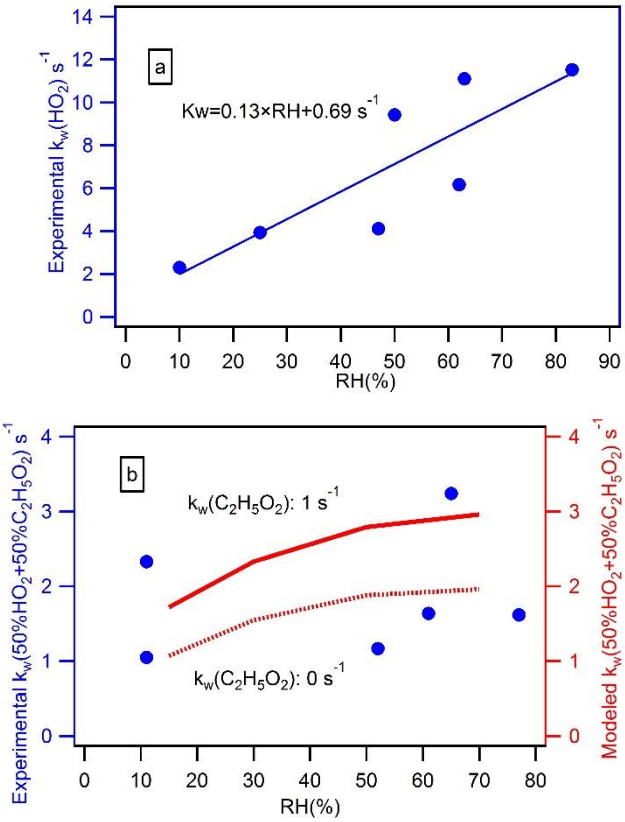

Figure S2.11 (a) $k_{w(HO2)}$ and (b) $k_{w(50\%C2H5O2+50\%HO2)}$ measured at 23±2 °C for the PFA inlet

2.9.4 S4 – Detection limit for the PERCA (CO/NO) approach during CERVOLAND

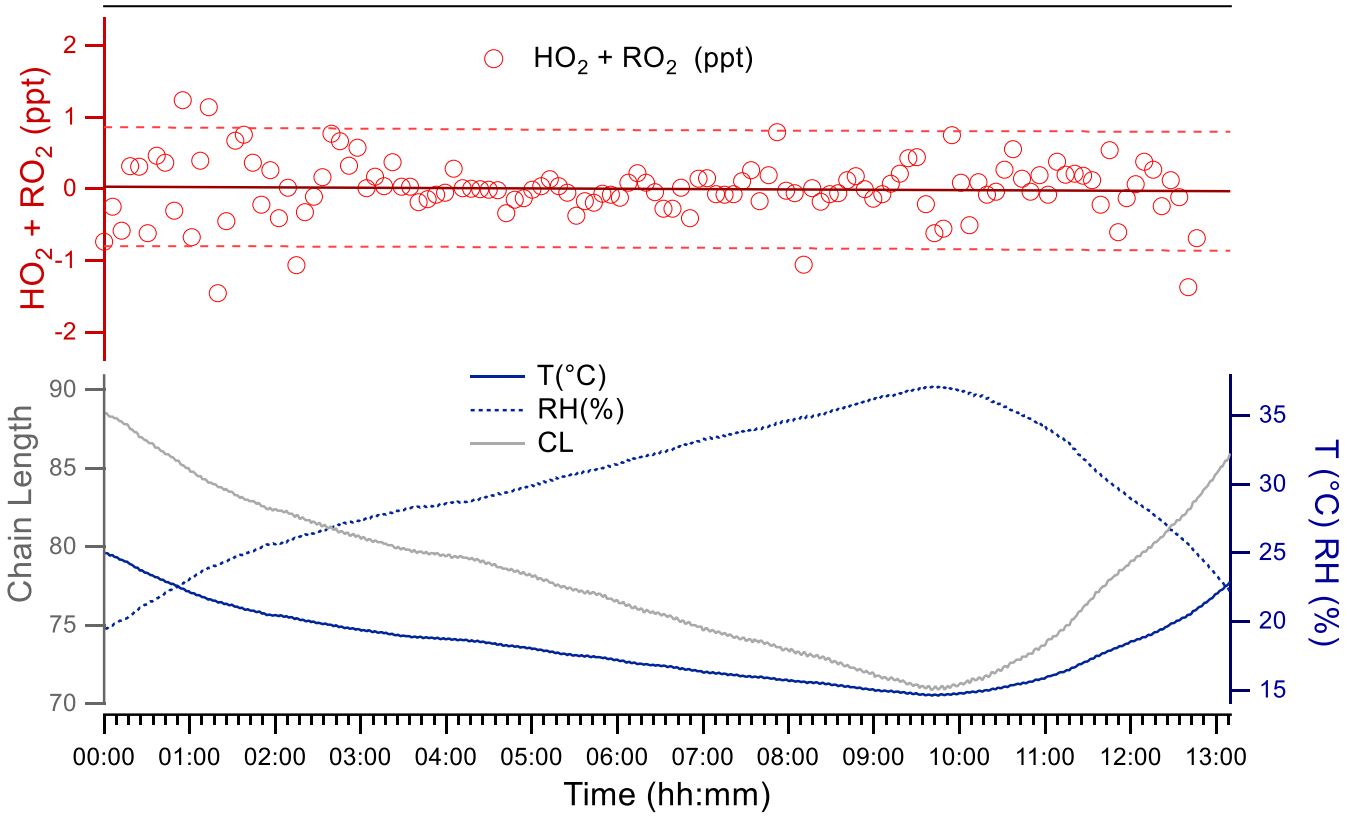

Figure S2.12 Two reactors operated in background mode for a duration of 12 hours to estimate limits of detection. $\sum HO_2 + RO_2 = \Delta NO_2/CL$ shown as a function of time. The dashed red lines represent the 95% confidence interval. Chain length, temperature and relative humidity are also shown on the bottom panel.

2.9.5 S5-Identification of the best material for the CA reactors

The chain length of the PERCA system is strongly impacted by the removal of radicals on the reactor walls (Fig S2.13-14). In order to identify a material exhibiting a low radical wall loss rate, the CL was measured in reactors made of different types of materials (Figures S2.13 & S2.14) using the same operating conditions (reagent gases, sample flow rate, radical generation, T: 25 °C, RH: 50%). For these measurements, both NO and CO were varied to check whether the same trends were observed for each tested materials. These tests were performed using the ECHAMP approach

but it is expected that similar results would be observed with the PERCA approach since wall losses of HO_2 will be similar. The materials tested were PTFE, PFA, pyrex, tygon and silcosteel.

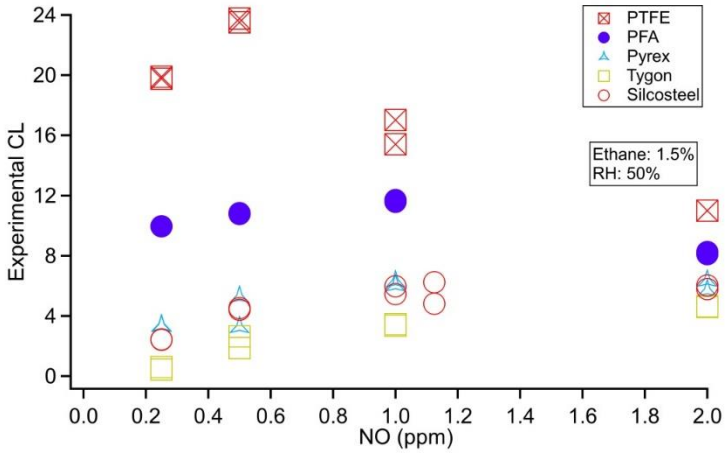

Figure S2.13 Dependence of the CL on NO for reactors made of different types of materials

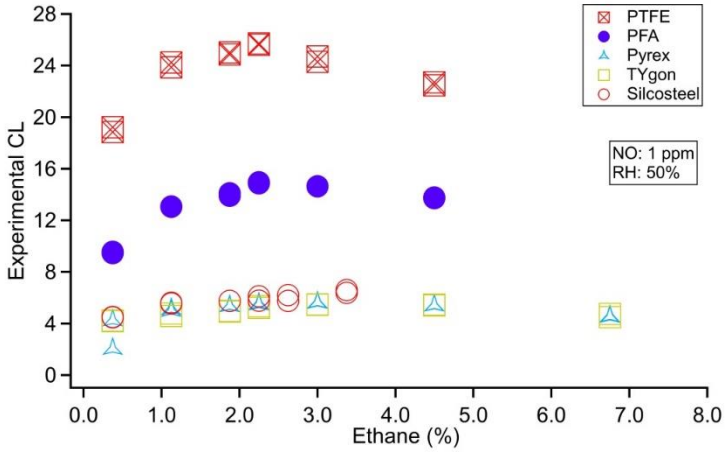

Figure S2.14 Dependence of the CL on ethane for reactors made of different types of materials

As can be seen from Figure S2.14, the CL increases with NO at a constant ethane mixing ratio of 1.5% until it reaches a maximum at approximately 1 ppm of NO for all materials, with the exception of PTFE which exhibits a maximum CL at 0.5 ppm of NO. In addition, the CL observed for PTFE at 0.5 ppm of NO is approximately two times higher than for PFA and more than six times higher than other materials. When ethane is varied (Figure S2.14), keeping NO constant at 1 ppm, a maximum chain length is observed at mixing ratio of 2-3 % for all materials wirh PTFE still exhibiting significantly higher CL than the other materials. From these two figures, it is clear

that PTFE and PFA reactors lead to the highest CL of 24 and 15 at 1.9-2.5 % ethane, respectively. This indicates that these two materials lead to lower radical loss rates on their walls. However, the CL for the PTFE reactor was not stable over time and decreased after a few days of experiments to a value close to that observed for PFA. This behavior is likely due to the aging of the reactor surface. We therefore decided to select the PFA reactors, which provided the highest stable chain length over time under the optimum operating conditions.

2.9.6 S6-Chemical Mechanisms used to model the PERCA and ECHAMP chemistries

Table S2.4 Reaction scheme used to model the CL for PERCA and ECHAMP.

Radical propagation reactions

Ethane/NO Chemistry
$HO_2 + NO \rightarrow OH + NO_2$
$OH + C_2H_6 (+ O_2) \rightarrow H_2O + C_2H_5O_2$
$C_2H_5O_2 + NO \rightarrow C_2H_5O + NO_2$
$C_2H_5O + O_2 \rightarrow CH_3CHO + HO_2$
CO/NO Chemistry
$HO_2 + NO \rightarrow OH + NO_2$
$OH + CO + O_2 \rightarrow CO_2 + HO_2$
Radical Termination reactions
Ethane/NO chemistry
$C_2H_5O + NO + M \rightarrow C_2H_5ONO + M$
$C_2H_5O_2 + NO + M \rightarrow C_2H_5ONO_2 + M$
$HO_2 + NO + M \rightarrow HNO_3 + M$
$HO_2 + wall \rightarrow non\text{-}radical\ product$
$OH + NO + M \rightarrow HONO + M$
$OH + HO_2 \rightarrow H_2O + O_2$
$HO_2 + NO_2 + M \leftrightarrow HO_2NO_2 + M$
$C_2H_5O_2 + NO_2 + M \leftrightarrow C_2H_5O_2NO_2 + M$
$C_2H_5O_2 + wall \rightarrow non\text{-}radical\ product$
CO/NO Chemistry
$OH + NO + M \rightarrow ONO + M$
$HO_2 + NO + M \rightarrow HNO_3 + M$
$HO_2 + wall \rightarrow non\text{-}radical\ product$
$HO_2 + NO_2 + M \leftrightarrow HO_2NO_2 + M$
$OH + HO_2 \rightarrow H_2O + O_2$

2.10 References

Acker, K., Möller, D., Wieprecht, W., Meixner, F.X., Bohn, B., Gilge, S., Plass-Dülmer, C., Berresheim, H., 2006. Strong daytime production of OH from HNO2 at a rural mountain site. Geophys. Res. Lett. 33. https://doi.org/10.1029/2005GL024643

Ahmed, M., Blunt, D., Chen, D., Suits, A.G., 1997. UV photodissociation of oxalyl chloride yields four fragments from one photon absorption. J. Chem. Phys. 106, 7617–7624.

Albrecht, S.R., Novelli, A., Hofzumahaus, A., Kang, S., Baker, Y., Mentel, T., Wahner, A., Fuchs, H., 2019. Measurements of hydroperoxy radicals (HO2) at atmospheric concentrations using bromide chemical ionisation mass spectrometry. Atmos Meas Tech 12, 891–902. https://doi.org/10.5194/amt-12-891-2019

Amedro, D., Miyazaki, K., Parker, A., Schoemaecker, C., Fittschen, C., 2012a. Atmospheric and kinetic studies of OH and HO2 by the FAGE technique. J. Environ. Sci. 24, 78–86. http://dx.doi.org/10.1016/S1001-0742(11)60723-7

Archibald, A.T., Levine, J.G., Abraham, N.L., Cooke, M.C., Edwards, P.M., Heard, D.E., Jenkin, M.E., Karunaharan, A., Pike, R.C., Monks, P.S., Shallcross, D.E., Telford, P.J., Whalley, L.K., Pyle, J.A., 2011. Impacts of HOx regeneration and recycling in the oxidation of isoprene: Consequences for the composition of past, present and future atmospheres. Geophys. Res. Lett. 38, n/a-n/a. https://doi.org/10.1029/2010GL046520

Ashbourn, S.F.M., Jenkin, M.E., Clemitshaw, K.C., 1998. Laboratory Studies of the Response of a Peroxy Radical Chemical Amplifier to HO2 and a Series of Organic Peroxy Radicals. J. Atmospheric Chem. 29, 233–266. https://doi.org/10.1023/a:1005992316512

Assaf, E., Tanaka, S., Kajii, Y., Schoemaecker, C., Fittschen, C., 2017. Rate constants of the reaction of C2–C4 peroxy radicals with OH radicals. Chem. Phys. Lett. 684, 245–249. https://doi.org/10.1016/j.cplett.2017.06.062

Atkinson, R., 2003. Kinetics of the gas-phase reactions of OH radicals with alkanes and cycloalkanes. Atmos Chem Phys 3, 2233–2307. https://doi.org/10.5194/acp-3-2233-2003

Atkinson, R., 2000. Atmospheric chemistry of VOCs and NOx. Atmos. Environ. 34, 2063–2101. http://dx.doi.org/10.1016/S1352-2310(99)00460-4

Atkinson, R., 1986. Kinetics and mechanisms of the gas-phase reactions of the hydroxyl radical with organic compounds under atmospheric conditions. Chem. Rev. 86, 69–201. https://doi.org/10.1021/cr00071a004

Atkinson, R., Arey, J., 2003. Atmospheric Degradation of Volatile Organic Compounds. Chem. Rev. 103, 4605–4638. https://doi.org/10.1021/cr0206420

Atkinson, R., Baulch, D.L., Cox, R.A., Crowley, J.N., Hampson, R.F., Hynes, R.G., Jenkin, M.E., Rossi, M.J., Troe, J., 2007. Evaluated kinetic and photochemical data for atmospheric chemistry: Volume III – gas phase reactions of inorganic halogens. Atmos Chem Phys 7, 981–1191. https://doi.org/10.5194/acp-7-981-2007

Atkinson, R., Baulch, D.L., Cox, R.A., Crowley, J.N., Hampson, R.F., Hynes, R.G., Jenkin, M.E., Rossi, M.J., Troe, J., 2004. Evaluated kinetic and photochemical data for atmospheric chemistry: Volume I - gas phase reactions of O_x, HO_x, NO_x and SO_x species. Atmos Chem Phys 4, 1461–1738. https://doi.org/10.5194/acp-4-1461-2004

Atkinson, R., Baulch, D.L., Cox, R.A., Crowley, J.N., Hampson, R.F., Hynes, R.G., Jenkin, M.E., Rossi, M.J., Troe, J., IUPAC Subcommittee, 2006. Evaluated kinetic and photochemical data for atmospheric chemistry: Volume II – gas phase reactions of organic species. Atmos Chem Phys 6, 3625–4055. https://doi.org/10.5194/acp-6-3625-2006

Atkinson, R., Baulch, D.L., Cox, R.A., Hampson, R.F., Kerr, J.A., Rossi, M.J., Troe, J., 1997a. Evaluated Kinetic, Photochemical and Heterogeneous Data for Atmospheric Chemistry: Supplement V. IUPAC Subcommittee on Gas Kinetic Data Evaluation for Atmospheric Chemistry. J. Phys. Chem. Ref. Data 26, 521–1011. https://doi.org/10.1063/1.556011

Atkinson, Roger., Tuazon, E.C., Aschmann, S.M., 1995. Products of the Gas-Phase Reactions of O3 with Alkenes. Environ. Sci. Technol. 29, 1860–1866. https://doi.org/10.1021/es00007a025

Avzianova, E.V., Ariya, P.A., 2002. Temperature-dependent kinetic study for ozonolysis of selected tropospheric alkenes. Int. J. Chem. Kinet. 34, 678–684. https://doi.org/10.1002/kin.10093

Bailey, A.E., Heard, D.E., Paul, P.H., Pilling, M.J., 1997. Collisional quenching of OH (A 2Σ+, v′ = 0) by N2, O2 and CO2 between 204 and 294 K. Implications for atmospheric measurements of OH by laser-induced fluorescence. J Chem Soc Faraday Trans 93, 2915–2920. https://doi.org/10.1039/A701582H

Baker, J., Aschmann, S.M., Arey, J., Atkinson, R., 2002. Reactions of stabilized criegee intermediates from the gas-phase reactions of O3 with selected alkenes. Int. J. Chem. Kinet. 34, 73–85. https://doi.org/10.1002/kin.10022

Baklanov, A.V., Krasnoperov, L.N., 2001. Oxalyl Chloride A Clean Source of Chlorine Atoms for Kinetic Studies. J. Phys. Chem. A 105, 97–103.

Berresheim, H., Elste, T., Plass-Dülmer, C., Eiseleb, F.L., Tannerb, D.J., 2000. Chemical ionization mass spectrometer for long-term measurements of atmospheric OH and H2SO4. Int. J. Mass Spectrom. 202, 91–109. http://dx.doi.org/10.1016/S1387-3806(00)00233-5

Berresheim, H., Elste, T., Tremmel, H.G., Allen, A.G., Hansson, H.C., Rosman, K., Dal Maso, M., Mäkelä, J.M., Kulmala, M., O'Dowd, C.D., 2002. Gas-aerosol relationships of H2SO4, MSA, and OH: Observations in the coastal marine boundary layer at Mace Head, Ireland. J. Geophys. Res. Atmospheres 107, PAR 5-1-PAR 5-12. https://doi.org/10.1029/2000JD000229

Bossolasco, A., Faragó, E.P., Schoemaecker, C., Fittschen, C., 2014. Rate constant of the reaction between CH3O2 and OH radicals. Chem. Phys. Lett. 593, 7–13. https://doi.org/10.1016/j.cplett.2013.12.052

Boyd, A.A., Flaud, P.-M., Daugey, N., Lesclaux, R., 2003. Rate Constants for RO2 + HO2 Reactions Measured under a Large Excess of HO2. J. Phys. Chem. A 107, 818–821. https://doi.org/10.1021/jp026581r

Braure, T., Bedjanian, Y., Romanias, M.N., Morin, J., Riffault, V., Tomas, A., Coddeville, P., 2014. Experimental Study of the Reactions of Limonene with OH and OD Radicals: Kinetics and Products. J. Phys. Chem. A 118, 9482–9490. https://doi.org/10.1021/jp507180g

Brune, W.H., Baier, B.C., Thomas, J., Ren, X., Cohen, R.C., Pusede, S.E., Browne, E.C., Goldstein, A.H., Gentner, D.R., Keutsch, F.N., Thornton, J.A., Harrold, S., Lopez-Hilfiker, F.D., Wennberg, P.O., 2016. Ozone production chemistry in the presence of urban plumes. Faraday Discuss. 189, 169–189. https://doi.org/10.1039/C5FD00204D

Burkert, J., Behmann, T., Andrés Hernández, M.D., Stöbener, D., Weißenmayer, M., Perner, D., Burrows, J.P., 2001. Measurements of peroxy radicals in a forested area of Portugal. Field Stud. Atmospheric Chem. Volatile Org. Compd. Emit. Eucalyptus For. FIELDVOC94 3, 327–338. https://doi.org/10.1016/S1465-9972(01)00014-9

Butkovskaya, N., Kukui, A., Le Bras, G., 2007. HNO3 Forming Channel of the HO2 + NO Reaction as a Function of Pressure and Temperature in the Ranges of 72−600 Torr and 223−323 K. J. Phys. Chem. A 111, 9047–9053. https://doi.org/10.1021/jp074117m

Butkovskaya, N., Rayez, M.-T., Rayez, J.-C., Kukui, A., Le Bras, G., 2009. Water Vapor Effect on the HNO3 Yield in the HO2 + NO Reaction: Experimental and Theoretical Evidence. J. Phys. Chem. A 113, 11327–11342. https://doi.org/10.1021/jp811428p

Calvert, J., Mellouki, A., Orlando, J., 2011. Mechanisms of atmospheric oxidation of the oxygenates. OUP USA.

Cantrell, C.A., Shetter, R.E., Calvert, J.G., 1996. Dual-Inlet Chemical Amplifier for Atmospheric Peroxy Radical Measurements. Anal. Chem. 68, 4194–4199. https://doi.org/10.1021/ac960639e

Cantrell, C.A., Stedman, D.H., Wendel, G.J., 1984. Measurement of atmospheric peroxy radicals by chemical amplification. Anal. Chem. 56, 1496–1502. https://doi.org/10.1021/ac00272a065

Cantrell, C.A., Zimmer, A., Tyndall, G.S., 1997. Absorption cross sections for water vapor from 183 to 193 nm. Geophys. Res. Lett. 24, 2195–2198. https://doi.org/10.1029/97GL02100

Chan, C.Y., Hard, T.M., Mehrabzadeh, A.A., George, L.A., O'Brien, R.J., 1990. Third-generation FAGE instrument for tropospheric hydroxyl radical measurement. J. Geophys. Res. Atmospheres 95, 18569–18576. https://doi.org/10.1029/JD095iD11p18569

Chen, S., Ren, X., Mao, J., Chen, Z., Brune, W.H., Lefer, B., Rappenglück, B., Flynn, J., Olson, J., Crawford, J.H., 2010. A comparison of chemical mechanisms based on TRAMP-2006 field data. Atmos. Environ. 44, 4116–4125. http://dx.doi.org/10.1016/j.atmosenv.2009.05.027

Chen, X., Millet, D.B., Singh, H.B., Wisthaler, A., Apel, E.C., Atlas, E.L., Blake, D.R., Bourgeois, I., Brown, S.S., Crounse, J.D., de Gouw, J.A., Flocke, F.M., Fried, A., Heikes, B.G., Hornbrook, R.S., Mikoviny, T., Min, K.-E., Müller, M., Neuman, J.A., O'Sullivan, D.W., Peischl, J., Pfister, G.G., Richter, D., Roberts, J.M., Ryerson, T.B., Shertz, S.R., Thompson, C.R., Treadaway, V., Veres, P.R., Walega, J., Warneke, C., Washenfelder, R.A., Weibring, P., Yuan, B., 2019. On the sources and sinks of atmospheric VOCs: an integrated analysis of recent aircraft campaigns over North America. Atmos Chem Phys 19, 9097–9123. https://doi.org/10.5194/acp-19-9097-2019

Clemitshaw, K., 2004. A Review of Instrumentation and Measurement Techniques for Ground-Based and Airborne Field Studies of Gas-Phase Tropospheric Chemistry. Crit. Rev. Environ. Sci. Technol. 34, 1–108. https://doi.org/10.1080/10643380490265117

Clemitshaw, K.C., Carpenter, L.J., Penkett, S.A., Jenkin, M.E., 1997. A calibrated peroxy radical chemical amplifier for ground-based tropospheric measurements. J. Geophys. Res. Atmospheres 102, 25405–25416. https://doi.org/10.1029/97JD01902

Commane, R., Floquet, C.F.A., Ingham, T., Stone, D., Evans, M.J., Heard, D.E., 2010. Observations of OH and HO2 radicals over West Africa. Atmos Chem Phys 10, 8783–8801. https://doi.org/10.5194/acp-10-8783-2010

Creasey, D.J., Evans, G.E., Heard, D.E., Lee, J.D., 2003. Measurements of OH and HO2 concentrations in the Southern Ocean marine boundary layer. J. Geophys. Res. Atmospheres 108, n/a-n/a. https://doi.org/10.1029/2002JD003206

Creasey, D.J., Heard, D.E., Lee, J.D., 2000. Absorption cross-section measurements of water vapour and oxygen at 185 nm. Implications for the calibration of field instruments to measure OH, HO2 and RO2 radicals. Geophys. Res. Lett. 27, 1651–1654. https://doi.org/10.1029/1999GL011014

Dolgorouky, C., Gros, V., Sarda-Esteve, R., Sinha, V., Williams, J., Marchand, N., Sauvage, S., Poulain, L., Sciare, J., Bonsang, B., 2012. Total OH reactivity measurements in Paris during the 2010 MEGAPOLI winter campaign. Atmos Chem Phys 12, 9593–9612. https://doi.org/10.5194/acp-12-9593-2012

Dusanter, S., Stevens, P.S., 2017. Recent Advances in the Chemistry of OH and HO^2 Radicals in the Atmosphere: Field and Laboratory Measurements, in: Advances in Atmospheric Chemistry. pp. 493–579. https://doi.org/10.1142/9789813147355_0007

Dusanter, S., Vimal, D., Stevens, P.S., 2008a. Technical note: Measuring tropospheric OH and HO_2 by laser-induced fluorescence at low pressure. A comparison of calibration techniques. Atmos Chem Phys 8, 321–340. https://doi.org/10.5194/acp-8-321-2008

Dusanter, S., Vimal, D., Stevens, P.S., Volkamer, R., Molina, L.T., 2009a. Measurements of OH and HO_2 concentrations during the MCMA-2006 field campaign – Part 1: Deployment of the Indiana University laser-induced fluorescence instrument. Atmos Chem Phys 9, 1665–1685. https://doi.org/10.5194/acp-9-1665-2009

Dusanter, S., Vimal, D., Stevens, P.S., Volkamer, R., Molina, L.T., Baker, A., Meinardi, S., Blake, D., Sheehy, P., Merten, A., Zhang, R., Zheng, J., Fortner, E.C., Junkermann, W., Dubey, M., Rahn, T., Eichinger, B., Lewandowski, P., Prueger, J., Holder, H., 2009b. Measurements of OH and HO_2 concentrations during the MCMA-2006 field campaign – Part 2: Model comparison and radical budget. Atmos Chem Phys 9, 6655–6675. https://doi.org/10.5194/acp-9-6655-2009

Edwards, G.D., Cantrell, C.A., Stephens, S., Hill, B., Goyea, O., Shetter, R.E., Mauldin, R.L., Kosciuch, E., Tanner, D.J., Eisele, F.L., 2003. Chemical Ionization Mass Spectrometer Instrument for the Measurement of Tropospheric HO2 and RO2. Anal. Chem. 75, 5317–5327. https://doi.org/10.1021/ac034402b

Edwards, P.M., Evans, M.J., Furneaux, K.L., Hopkins, J., Ingham, T., Jones, C., Lee, J.D., Lewis, A.C., Moller, S.J., Stone, D., Whalley, L.K., Heard, D.E., 2013. OH reactivity in a South East Asian tropical rainforest during the Oxidant and Particle Photochemical Processes (OP3) project. Atmos Chem Phys 13, 9497–9514. https://doi.org/10.5194/acp-13-9497-2013

Ehn, M., Thornton, J.A., Kleist, E., Sipilä, M., Junninen, H., Pullinen, I., Springer, M., Rubach, F., Tillmann, R., Lee, B., 2014. A large source of low-volatility secondary organic aerosol. Nature 506, 476.

Elshorbany, Y.F., Kleffmann, J., Kurtenbach, R., Lissi, E., Rubio, M., Villena, G., Gramsch, E., Rickard, A.R., Pilling, M.J., Wiesen, P., 2010. Seasonal dependence of the oxidation capacity of the city of Santiago de Chile. Atmospheric Chem. Mech. Sel. Pap. 2008 Conf. 44, 5383–5394. https://doi.org/10.1016/j.atmosenv.2009.08.036

Faloona, I.C., Tan, D., Lesher, R.L., Hazen, N.L., Frame, C.L., Simpas, J.B., Harder, H., Martinez, M., Di Carlo, P., Ren, X., 2004. A laser-induced fluorescence instrument for detecting tropospheric OH and HO2: Characteristics and calibration. J. Atmospheric Chem. 47, 139–167.

Faragó, E.P., Schoemaecker, C., Viskolcz, B., Fittschen, C., 2015. Experimental determination of the rate constant of the reaction between C2H5O2 and OH radicals. Chem. Phys. Lett. 619, 196–200. https://doi.org/10.1016/j.cplett.2014.11.069

Finlayson-Pitts, B.J., Jr, J.N.P., 2000. {CHAPTER} 5 - Kinetics and Atmospheric Chemistry, in: Finlayson-Pitts, B.J., Pitts, J.N. (Eds.), Chemistry of the Upper and Lower Atmosphere. Academic Press, San Diego, pp. 130–178. https://doi.org/10.1016/B978-012257060-5/50007-1

Finlayson-Pitts, B.J., Pitts, J.N. (Eds.), 2000. Acknowledgments, in: Chemistry of the Upper and Lower Atmosphere. Academic Press, San Diego, pp. xxi–xxii. https://doi.org/10.1016/B978-012257060-5/50002-2

Finlayson-Pitts, B.J., Pitts Jr, J.N., 2000. CHAPTER 6 - Rates and Mechanisms of Gas-Phase Reactions in Irradiated Organic – NOx – Air Mixtures, in: Chemistry of the Upper and Lower Atmosphere. Academic Press, San Diego, pp. 179–263.

Fittschen, C., Al Ajami, M., Batut, S., Ferracci, V., Archer-Nicholls, S., Archibald, A.T., Schoemaecker, C., 2019. ROOOH: a missing piece of the puzzle for OH measurements in low-NO environments? Atmos Chem Phys 19, 349–362. https://doi.org/10.5194/acp-19-349-2019

Fittschen, C., Whalley, L.K., Heard, D.E., 2014. The Reaction of CH3O2 Radicals with OH Radicals: A Neglected Sink for CH3O2 in the Remote Atmosphere. Environ. Sci. Technol. 48, 7700–7701. https://doi.org/10.1021/es502481q

Fleming, Z.L., Monks, P.S., Rickard, A.R., Heard, D.E., Bloss, W.J., Seakins, P.W., Still, T.J., Sommariva, R., Pilling, M.J., Morgan, R., Green, T.J., Brough, N., Mills, G.P., Penkett, S.A., Lewis, A.C., Lee, J.D., Saiz-Lopez, A., Plane, J.M.C., 2006. Peroxy radical chemistry and the control of ozone photochemistry at Mace Head, Ireland during the summer of 2002. Atmos Chem Phys 6, 2193–2214. https://doi.org/10.5194/acp-6-2193-2006

Fuchs, H., Bohn, B., Hofzumahaus, A., Holland, F., Lu, K.D., Nehr, S., Rohrer, F., Wahner, A., 2011. Detection of HO_2 by laser-induced fluorescence: calibration and interferences from RO_2 radicals. Atmos Meas Tech 4, 1209–1225. https://doi.org/10.5194/amt-4-1209-2011

Fuchs, H., Brauers, T., Dorn, H.P., Harder, H., Häseler, R., Hofzumahaus, A., Holland, F., Kanaya, Y., Kajii, Y., Kubistin, D., Lou, S., Martinez, M., Miyamoto, K., Nishida, S., Rudolf, M., Schlosser, E., Wahner, A., Yoshino, A., Schurath, U., 2010. Technical Note: Formal blind intercomparison of HO_2 measurements in the atmosphere simulation chamber SAPHIR during the HOxComp campaign. Atmos Chem Phys 10, 12233–12250. https://doi.org/10.5194/acp-10-12233-2010

Fuchs, H., Holland, F., Hofzumahaus, A., 2008. Measurement of tropospheric RO2 and HO2 radicals by a laser-induced fluorescence instrument. Rev. Sci. Instrum. 79, 084104. https://doi.org/10.1063/1.2968712

Fuchs, H., Tan, Z., Hofzumahaus, A., Broch, S., Dorn, H.P., Holland, F., Künstler, C., Gomm, S., Rohrer, F., Schrade, S., Tillmann, R., Wahner, A., 2016. Investigation of potential interferences in the detection of atmospheric ROx radicals by laser-induced fluorescence under dark conditions. Atmos Meas Tech 9, 1431–1447. https://doi.org/10.5194/amt-9-1431-2016

Geyer, A., Alicke, B., Konrad, S., Schmitz, T., Stutz, J., Platt, U., 2001. Chemistry and oxidation capacity of the nitrate radical in the continental boundary layer near Berlin. J. Geophys. Res. Atmospheres 106, 8013–8025. https://doi.org/10.1029/2000JD900681

Goldstein, A.H., Galbally, I.E., 2007. Known and Unexplored Organic Constituents in the Earth's Atmosphere. Environ. Sci. Technol. 41, 1514–1521. https://doi.org/10.1021/es072476p

Green, T.J., Reeves, C.E., Brough, N., Edwards, G.D., Monks, P.S., Penkett, S.A., 2003. Airborne measurements of peroxy radicals using the PERCA technique. J Env. Monit 5, 75–83.

Green, T.J., Reeves, C.E., Fleming, Z.L., Brough, N., Rickard, A.R., Bandy, B.J., Monks, P.S., Penkett, S.A., 2006. An improved dual channel PERCA instrument for atmospheric measurements of peroxy radicals. J. Environ. Monit. 8, 530–536. https://doi.org/10.1039/B514630E

Griffith, S.M., Hansen, R.F., Dusanter, S., Michoud, V., Gilman, J.B., Kuster, W.C., Veres, P.R., Graus, M., de Gouw, J.A., Roberts, J., Young, C., Washenfelder, R., Brown, S.S., Thalman, R., Waxman, E., Volkamer, R., Tsai, C., Stutz, J., Flynn, J.H., Grossberg, N., Lefer, B., Alvarez, S.L., Rappenglueck, B., Mielke, L.H., Osthoff, H.D., Stevens, P.S., 2016. Measurements of hydroxyl and hydroperoxy radicals during CalNex-LA: Model comparisons and radical budgets. J. Geophys. Res. Atmospheres 121, 4211–4232. https://doi.org/10.1002/2015JD024358

Griffith, S.M., Hansen, R.F., Dusanter, S., Stevens, P.S., Alaghmand, M., Bertman, S.B., Carroll, M.A., Erickson, M., Galloway, M., Grossberg, N., Hottle, J., Hou, J., Jobson, B.T., Kammrath, A., Keutsch, F.N., Lefer, B.L., Mielke, L.H., O'Brien, A., Shepson, P.B., Thurlow, M., Wallace, W., Zhang, N., Zhou,

X.L., 2013a. OH and HO_2 radical chemistry during PROPHET 2008 and CABINEX 2009 – Part 1: Measurements and model comparison. Atmos Chem Phys 13, 5403–5423. https://doi.org/10.5194/acp-13-5403-2013

Groß, C., Dillon, T., Schuster, G., Lelieveld, J., Crowley, J., 2014. Direct kinetic study of OH and O3 formation in the reaction of CH3C (O) O2 with HO2. J. Phys. Chem. A 118, 974–985.

Guenther, A., Hewitt, C.N., Erickson, D., Fall, R., Geron, C., Graedel, T., Harley, P., Klinger, L., Lerdau, M., McKay, W.A., Pierce, T., Scholes, B., Steinbrecher, R., Tallamraju, R., Taylor, J., Zimmerman, P., 1995. A global model of natural volatile organic compound emissions. J. Geophys. Res. Atmospheres 100, 8873–8892. https://doi.org/10.1029/94JD02950

Guenther, A.B., Jiang, X., Heald, C.L., Sakulyanontvittaya, T., Duhl, T., Emmons, L.K., Wang, X., 2012. The Model of Emissions of Gases and Aerosols from Nature version 2.1 (MEGAN2.1): an extended and updated framework for modeling biogenic emissions. Geosci Model Dev 5, 1471–1492. https://doi.org/10.5194/gmd-5-1471-2012

Hanke, M., Uecker, J., Reiner, T., Arnold, F., 2002. Atmospheric peroxy radicals: ROXMAS, a new mass-spectrometric methodology for speciated measurements of HO2 and ∑RO2 and first results. Int. J. Mass Spectrom. 213, 91–99. http://dx.doi.org/10.1016/S1387-3806(01)00548-6

Hard, T.M., O'Brien, R.J., Chan, C.Y., Mehrabzadeh, A.A., 1984. Tropospheric free radical determination by fluorescence assay with gas expansion. Environ. Sci. Technol. 18, 768–777. https://doi.org/10.1021/es00128a009

Hasson, A.S., Tyndall, G.S., Orlando, J.J., 2004. A Product Yield Study of the Reaction of HO2 Radicals with Ethyl Peroxy (C2H5O2), Acetyl Peroxy (CH3C(O)O2), and Acetonyl Peroxy (CH3C(O)CH2O2) Radicals. J. Phys. Chem. A 108, 5979–5989. https://doi.org/10.1021/jp048873t

Hasson, A.S., Tyndall, G.S., Orlando, J.J., Singh, S., Hernandez, S.Q., Campbell, S., Ibarra, Y., 2012. Branching Ratios for the Reaction of Selected Carbonyl-Containing Peroxy Radicals with Hydroperoxy Radicals. J. Phys. Chem. A 116, 6264–6281. https://doi.org/10.1021/jp211799c

He, Y., Zhou, X., Hou, J., Gao, H., Bertman, S.B., 2006. Importance of dew in controlling the air-surface exchange of HONO in rural forested environments. Geophys. Res. Lett. 33. https://doi.org/10.1029/2005GL024348

Heal, M.R., Heard, D.E., Pilling, M.J., Whitaker, B.J., 1995. On the Development and Validation of FAGE for Local Measurement of Tropospheric OH and H02. J. Atmospheric Sci. 52, 3428–3441. https://doi.org/10.1175/1520-0469(1995)052<3428:OTDAVO>2.0.CO;2

Heard, D.E., 2006. ATMOSPHERIC FIELD MEASUREMENTS OF THE HYDROXYL RADICAL USING LASER-INDUCED FLUORESCENCE SPECTROSCOPY. Annu. Rev. Phys. Chem. 57, 191–216. https://doi.org/10.1146/annurev.physchem.57.032905.104516

Heard, D.E., Pilling, M.J., 2003. Measurement of OH and HO2 in the Troposphere. Chem. Rev. 103, 5163–5198. https://doi.org/10.1021/cr020522s

Hemmi, N., Suits, A.G., 1997. Photodissociation of oxalyl chloride at 193 nm probed via synchrotron radiation. J. Phys. Chem. A 101, 6633–6637.

Hendrik Fuchs, Frank Holland, Andreas Hofzumahaus, 2008. Measurement of tropospheric RO2 and HO2 radicals by a laser-induced fluorescence instrument. Rev. Sci. Instrum. 79, 084104. https://doi.org/10.1063/1.2968712

Hernández, M.D.A., Burkert, J., Reichert, L., Stöbener, D., Meyer-Arnek, J., Burrows, J.P., Dickerson, R.R., Doddridge, B.G., 2001. Marine boundary layer peroxy radical chemistry during the AEROSOLS99 campaign: Measurements and analysis. J. Geophys. Res. Atmospheres 106, 20833–20846. https://doi.org/10.1029/2001JD900113

Hewitt, C.N., Lee, J.D., MacKenzie, A.R., Barkley, M.P., Carslaw, N., Carver, G.D., Chappell, N.A., Coe, H., Collier, C., Commane, R., Davies, F., Davison, B., DiCarlo, P., Di Marco, C.F., Dorsey, J.R., Edwards, P.M., Evans, M.J., Fowler, D., Furneaux, K.L., Gallagher, M., Guenther, A., Heard, D.E., Helfter, C., Hopkins, J., Ingham, T., Irwin, M., Jones, C., Karunaharan, A., Langford, B., Lewis, A.C., Lim, S.F., MacDonald, S.M., Mahajan, A.S., Malpass, S., McFiggans, G., Mills, G., Misztal, P., Moller, S., Monks, P.S., Nemitz, E., Nicolas-Perea, V., Oetjen, H., Oram, D.E., Palmer, P.I., Phillips, G.J., Pike, R., Plane, J.M.C., Pugh, T., Pyle, J.A., Reeves, C.E., Robinson, N.H., Stewart, D., Stone, D., Whalley, L.K., Yin, X., 2010. Overview: oxidant and particle photochemical processes above a south-east Asian tropical rainforest (the OP3 project): introduction, rationale, location characteristics and tools. Atmos Chem Phys 10, 169–199. https://doi.org/10.5194/acp-10-169-2010

Hofzumahaus, A., Heard, D. (Eds.), 2015. Assessment of local HOx and ROx Measurement Techniques: Achievements, Challenges, and Fututre Directions.

Holland, F., Hessling, M., Hofzumahaus, A., 1995. In Situ Measurement of Tropospheric OH Radicals by Laser-Induced Fluorescence—A Description of the KFA Instrument. J. Atmospheric Sci. 52, 3393–3401. https://doi.org/10.1175/1520-0469(1995)052<3393:ISMOTO>2.0.CO;2

Honrath, R.E., Lu, Y., Peterson, M.C., Dibb, J.E., Arsenault, M.A., Cullen, N.J., Steffen, K., 2002. Vertical fluxes of NOx, HONO, and HNO3 above the snowpack at Summit, Greenland. Atmos. Environ. 36, 2629–2640. http://dx.doi.org/10.1016/S1352-2310(02)00132-2

Horie, O., Moortgat, G.K., 1991. Decomposition pathways of the excited Criegee intermediates in the ozonolysis of simple alkenes. Int. Conf. Gener. Oxid. Reg. Glob. Scales 25, 1881–1896. https://doi.org/10.1016/0960-1686(91)90271-8

Hornbrook, R.S., Crawford, J.H., Edwards, G.D., Goyea, O., Mauldin Iii, R.L., Olson, J.S., Cantrell, C.A., 2011. Measurements of tropospheric HO_2 and RO_2 by oxygen dilution modulation and chemical ionization mass spectrometry. Atmos Meas Tech 4, 735–756. https://doi.org/10.5194/amt-4-735-2011

Horstjann, M., Andrés Hernández, M.D., Nenakhov, V., Chrobry, A., Burrows, J.P., 2014. Peroxy radical detection for airborne atmospheric measurements using absorption spectroscopy of NO_2. Atmos Meas Tech 7, 1245–1257. https://doi.org/10.5194/amt-7-1245-2014

Hossaini, R., Chipperfield, M.P., Saiz-Lopez, A., Fernandez, R., Monks, S., Feng, W., Brauer, P., von Glasow, R., 2016. A global model of tropospheric chlorine chemistry: Organic versus inorganic sources and impact on methane oxidation. J. Geophys. Res. Atmospheres 121, 14,271-14,297. https://doi.org/10.1002/2016JD025756

Howard, C.J., 1979. Kinetic measurements using flow tubes. J. Phys. Chem. 83, 3–9. https://doi.org/10.1021/j100464a001

Ingham, T., Goddard, A., Whalley, L.K., Furneaux, K.L., Edwards, P.M., Seal, C.P., Self, D.E., Johnson, G.P., Read, K.A., Lee, J.D., Heard, D.E., 2009. A flow-tube based laser-induced fluorescence instrument to measure OH reactivity in the troposphere. Atmos Meas Tech 2, 465–477. https://doi.org/10.5194/amt-2-465-2009

Japar, S., Wu, C., Nikl, H., 1974. Rate constants for the reaction of ozone with olefins in the gas phase. J. Phys. Chem. 78, 2318–2320.

Jenkin, M.E., Clemitshaw, K.C., 2000. Ozone and other secondary photochemical pollutants: chemical processes governing their formation in the planetary boundary layer. Atmos. Environ. 34, 2499–2527. http://dx.doi.org/10.1016/S1352-2310(99)00478-1

Johnson, D., Marston, G., 2008. The gas-phase ozonolysis of unsaturated volatile organic compounds in the troposphere. Chem. Soc. Rev. 37, 699–716. https://doi.org/10.1039/B704260B

Kanaya, Y., Matsumoto, J., Kato, S., Akimoto, H., 2001a. Behavior of OH and HO2 radicals during the Observations at a Remote Island of Okinawa (ORION99) field campaign: 2. Comparison between observations and calculations. J. Geophys. Res. Atmospheres 106, 24209–24223.

Kanaya, Y., Sadanaga, Y., Hirokawa, J., Kajii, Y., Akimoto, H., 2001b. Development of a Ground-Based LIF Instrument for Measuring HOx Radicals: Instrumentation and Calibrations. J. Atmospheric Chem. 38, 73–110. https://doi.org/10.1023/A:1026559321911

Kartal, D., Andrés-Hernández, M.D., Reichert, L., Schlager, H., Burrows, J.P., 2010. Technical Note: Characterisation of a DUALER instrument for the airborne measurement of peroxy radicals during AMMA 2006. Atmos Chem Phys 10, 3047–3062. https://doi.org/10.5194/acp-10-3047-2010

Kerr, R.A., 1991. Hydroxyl, the Cleanser That Thrives on Dirt. Science 253, 1210. https://doi.org/10.1126/science.253.5025.1210

Kim, S., Wolfe, G.M., Mauldin, L., Cantrell, C., Guenther, A., Karl, T., Turnipseed, A., Greenberg, J., Hall, S.R., Ullmann, K., Apel, E., Hornbrook, R., Kajii, Y., Nakashima, Y., Keutsch, F.N., DiGangi, J.P., Henry, S.B., Kaser, L., Schnitzhofer, R., Graus, M., Hansel, A., Zheng, W., Flocke, F.F., 2013. Evaluation of HOx sources and cycling using measurement-constrained model calculations in a 2-methyl-3-butene-2-ol (MBO) and monoterpene (MT) dominated ecosystem. Atmos Chem Phys 13, 2031–2044. https://doi.org/10.5194/acp-13-2031-2013

Kleffmann, J., Kurtenbach, R., Lörzer, J., Wiesen, P., Kalthoff, N., Vogel, B., Vogel, H., 2003. Measured and simulated vertical profiles of nitrous acid—Part I: Field measurements. Atmos. Environ. 37, 2949–2955. https://doi.org/10.1016/S1352-2310(03)00242-5

Koppmann, R., 2007. Volatile organic compounds in the atmosphere. Wiley Online Library.

Kroll, J.H., Clarke, J.S., Donahue, N.M., Anderson, J.G., 2001. Mechanism of HOx Formation in the Gas-Phase Ozone−Alkene Reaction. 1. Direct, Pressure-Dependent Measurements of Prompt OH Yields. J. Phys. Chem. A 105, 1554–1560. https://doi.org/10.1021/jp002121r

Kroll, J.H., Seinfeld, J.H., 2008a. Chemistry of secondary organic aerosol: Formation and evolution of low-volatility organics in the atmosphere. Atmos. Environ. 42, 3593–3624. http://dx.doi.org/10.1016/j.atmosenv.2008.01.003

Kubistin, D., Harder, H., Martinez, M., Rudolf, M., Sander, R., Bozem, H., Eerdekens, G., Fischer, H., Gurk, C., Klüpfel, T., Königstedt, R., Parchatka, U., Schiller, C.L., Stickler, A., Taraborrelli, D., Williams, J., Lelieveld, J., 2010. Hydroxyl radicals in the tropical troposphere over the Suriname rainforest: comparison of measurements with the box model MECCA. Atmos Chem Phys 10, 9705–9728. https://doi.org/10.5194/acp-10-9705-2010

Kukui, A., Ancellet, G., Le Bras, G., 2008a. Chemical ionisation mass spectrometer for measurements of OH and Peroxy radical concentrations in moderately polluted atmospheres. J. Atmospheric Chem. 61, 133–154. https://doi.org/10.1007/s10874-009-9130-9

Kundu, S., Deming, B.L., Lew, M.M., Bottorff, B.P., Rickly, P., Stevens, P.S., Dusanter, S., Sklaveniti, S., Leonardis, T., Locoge, N., Wood, E.C., 2019. Peroxy Radical Measurements by Ethane – Nitric Oxide Chemical Amplification and Laser-Induced Fluorescence/Fluorescence Assay by Gas Expansion during the IRRONIC field campaign in a Forest in Indiana. Atmos Chem Phys Discuss 2019, 1–31. https://doi.org/10.5194/acp-2018-1359

Lee, J.D., McFiggans, G., Allan, J.D., Baker, A.R., Ball, S.M., Benton, A.K., Carpenter, L.J., Commane, R., Finley, B.D., Evans, M., Fuentes, E., Furneaux, K., Goddard, A., Good, N., Hamilton, J.F., Heard, D.E., Herrmann, H., Hollingsworth, A., Hopkins, J.R., Ingham, T., Irwin, M., Jones, C.E., Jones, R.L., Keene, W.C., Lawler, M.J., Lehmann, S., Lewis, A.C., Long, M.S., Mahajan, A., Methven, J., Moller, S.J., Müller, K., Müller, T., Niedermeier, N., O'Doherty, S., Oetjen, H., Plane, J.M.C., Pszenny, A.A.P.,

Read, K.A., Saiz-Lopez, A., Saltzman, E.S., Sander, R., von Glasow, R., Whalley, L., Wiedensohler, A., Young, D., 2010. Reactive Halogens in the Marine Boundary Layer (RHaMBLe): the tropical North Atlantic experiments. Atmos Chem Phys 10, 1031–1055. https://doi.org/10.5194/acp-10-1031-2010

Lee, J.D., Young, J.C., Read, K.A., Hamilton, J.F., Hopkins, J.R., Lewis, A.C., Bandy, B.J., Davey, J., Edwards, P., Ingham, T., Self, D.E., Smith, S.C., Pilling, M.J., Heard, D.E., 2009. Measurement and calculation of OH reactivity at a United Kingdom coastal site. J. Atmospheric Chem. 64, 53–76. https://doi.org/10.1007/s10874-010-9171-0

Lelieveld, J., Butler, T.M., Crowley, J.N., Dillon, T.J., Fischer, H., Ganzeveld, L., Harder, H., Lawrence, M.G., Martinez, M., Taraborrelli, D., Williams, J., 2008. Atmospheric oxidation capacity sustained by a tropical forest. Nature 452, 737.

Lew, M.L., Rickly, P.S., Bottorff, B.P., Sklaveniti, S., Léonardis, T., Locoge, N., Dusanter, S., Kundu, S., Wood, E., Stevens, P.S., 2019. OH and HO2 radical chemistry in a midlatitude forest: Measurements and model comparisons. Atmos Chem Phys Discuss 2019, 1–35. https://doi.org/10.5194/acp-2019-726

Lew, M.M., Dusanter, S., Stevens, P.S., 2018. Measurement of interferences associated with the detection of the hydroperoxy radical in the atmosphere using laser-induced fluorescence. Atmos Meas Tech 11, 95–109. https://doi.org/10.5194/amt-11-95-2018

Lightfoot, P.D., Cox, R.A., Crowley, J.N., Destriau, M., Hayman, G.D., Jenkin, M.E., Moortgat, G.K., Zabel, F., 1992. Organic peroxy radicals: Kinetics, spectroscopy and tropospheric chemistry. Atmospheric Environ. Part Gen. Top. 26, 1805–1961. http://dx.doi.org/10.1016/0960-1686(92)90423-I

Liu, Y., Morales-Cueto, R., Hargrove, J., Medina, D., Zhang, J., 2009. Measurements of Peroxy Radicals Using Chemical Amplification−Cavity Ringdown Spectroscopy. Environ. Sci. Technol. 43, 7791–7796. https://doi.org/10.1021/es901146t

Liu, Y., Zhang, J., 2014. Atmospheric Peroxy Radical Measurements Using Dual-Channel Chemical Amplification Cavity Ringdown Spectroscopy. Anal. Chem. 86, 5391–5398. https://doi.org/10.1021/ac5004689

Madronich, S., Shao, M., Wilson, S.R., Solomon, K.R., Longstreth, J.D., Tang, X.Y., 2015. Changes in air quality and tropospheric composition due to depletion of stratospheric ozone and interactions with changing climate: implications for human and environmental health. Photochem Photobiol Sci 14, 149–169. https://doi.org/10.1039/C4PP90037E

Mao, J., Jacob, D.J., Evans, M.J., Olson, J.R., Ren, X., Brune, W.H., Clair, J.M.S., Crounse, J.D., Spencer, K.M., Beaver, M.R., Wennberg, P.O., Cubison, M.J., Jimenez, J.L., Fried, A., Weibring, P., Walega, J.G., Hall, S.R., Weinheimer, A.J., Cohen, R.C., Chen, G., Crawford, J.H., McNaughton, C., Clarke, A.D., Jaeglé, L., Fisher, J.A., Yantosca, R.M., Le Sager, P., Carouge, C., 2010. Chemistry of hydrogen oxide radicals (HO_x) in the Arctic troposphere in spring. Atmos Chem Phys 10, 5823–5838. https://doi.org/10.5194/acp-10-5823-2010

Martinez, M., Harder, H., Kovacs, T.A., Simpas, J.B., Bassis, J., Lesher, R., Brune, W.H., Frost, G.J., Williams, E.J., Stroud, C.A., Jobson, B.T., Roberts, J.M., Hall, S.R., Shetter, R.E., Wert, B., Fried, A., Alicke, B., Stutz, J., Young, V.L., White, A.B., Zamora, R.J., 2003. OH and HO2 concentrations, sources, and loss rates during the Southern Oxidants Study in Nashville, Tennessee, summer 1999. J. Geophys. Res. Atmospheres 108, n/a-n/a. https://doi.org/10.1029/2003JD003551

Martinez, M., Harder, H., Kubistin, D., Rudolf, M., Bozem, H., Eerdekens, G., Fischer, H., Klüpfel, T., Gurk, C., Königstedt, R., Parchatka, U., Schiller, C.L., Stickler, A., Williams, J., Lelieveld, J., 2010. Hydroxyl radicals in the tropical troposphere over the Suriname rainforest: airborne measurements. Atmos Chem Phys 10, 3759–3773. https://doi.org/10.5194/acp-10-3759-2010

Martinez, M., Harder, H., Ren, X., Lesher, R.L., Brune, W.H., 2004. Measuring atmospheric naphthalene with laser-induced fluorescence. Atmos Chem Phys 4, 563–569. https://doi.org/10.5194/acp-4-563-2004

Matsumi Yutaka, Kono Mitsuhiko, Ichikawa Toshio, Takahashi Kenshi, Kondo Yutaka, 2002. Laser-Induced Fluorescence Instrument for the Detection of Tropospheric OH Radicals. Bull. Chem. Soc. Jpn. 75, 711–717. https://doi.org/doi:10.1246/bcsj.75.711

Mellouki, A., Wallington, T.J., Chen, J., 2015. Atmospheric Chemistry of Oxygenated Volatile Organic Compounds: Impacts on Air Quality and Climate. Chem. Rev. 115, 3984–4014. https://doi.org/10.1021/cr500549n

Mentel, T.F., Springer, M., Ehn, M., Kleist, E., Pullinen, I., Kurtén, T., Rissanen, M., Wahner, A., Wildt, J., 2015. Formation of highly oxidized multifunctional compounds: autoxidation of peroxy radicals formed in the ozonolysis of alkenes – deduced from structure–product relationships. Atmos Chem Phys 15, 6745–6765. https://doi.org/10.5194/acp-15-6745-2015

Mihelcic, D., Holland, F., Hofzumahaus, A., Hoppe, L., Konrad, S., Müsgen, P., Pätz, H.W., Schäfer, H.J., Schmitz, T., Volz-Thomas, A., Bächmann, K., Schlomski, S., Platt, U., Geyer, A., Alicke, B., Moortgat, G.K., 2003. Peroxy radicals during BERLIOZ at Pabstthum: Measurements, radical budgets and ozone production. J. Geophys. Res. Atmospheres 108, n/a-n/a. https://doi.org/10.1029/2001JD001014

Mihelcic, D., Müsgen, P., Ehhalt, D.H., 1985. An improved method of measuring tropospheric NO2 and RO2 by matrix isolation and electron spin resonance. J. Atmospheric Chem. 3, 341–361. https://doi.org/10.1007/bf00122523

Mihelcic, D., Volz-Thomas, A., Pätz, H.W., Kley, D., Mihelcic, M., 1990. Numerical analysis of ESR spectra from atmospheric samples. J. Atmospheric Chem. 11, 271–297. https://doi.org/10.1007/bf00118353

Mihele, C.M., Hastie, D.R., 2003. Radical chemistry at a forested continental site: Results from the PROPHET 1997 campaign. J. Geophys. Res. Atmospheres 108. https://doi.org/10.1029/2002JD002888

Mihele, C.M., Hastie, D.R., 2000. Optimized Operation and Calibration Procedures for Radical Amplifier-Type Detectors. J. Atmospheric Ocean. Technol. 17, 788–794. https://doi.org/10.1175/1520-0426(2000)017<0788:OOACPF>2.0.CO;2

Mihele, C.M., Hastie, D.R., 1998. The sensitivity of the radical amplifier to ambient water vapour. Geophys. Res. Lett. 25, 1911–1913. https://doi.org/10.1029/98GL01432

Mihele, C.M., Mozurkewich, M., Hastie, D.R., 1999a. Radical loss in a chain reaction of CO and NO in the presence of water: Implications for the radical amplifier and atmospheric chemistry. Int. J. Chem. Kinet. 31, 145–152. https://doi.org/10.1002/(SICI)1097-4601(1999)31:2<145::AID-KIN7>3.0.CO;2-M

Miyazaki, K., Parker, A.E., Fittschen, C., Monks, P.S., Kajii, Y., 2010. A new technique for the selective measurement of atmospheric peroxy radical concentrations of HO_2 and RO_2 using a denuding method. Atmos Meas Tech 3, 1547–1554. https://doi.org/10.5194/amt-3-1547-2010

Monks, P.S., 2005. Gas-phase radical chemistry in the troposphere. Chem. Soc. Rev. 34, 376–395. https://doi.org/10.1039/B307982C

Montzka, S.A., Krol, M., Dlugokencky, E., Hall, B., Jöckel, P., Lelieveld, J., 2011. Small Interannual Variability of Global Atmospheric Hydroxyl. Science 331, 67–69. https://doi.org/10.1126/science.1197640

Müller, M., Mikoviny, T., Jud, W., D'Anna, B., Wisthaler, A., 2013. A new software tool for the analysis of high resolution PTR-TOF mass spectra. Chemom. Intell. Lab. Syst. 127, 158–165.

Nguyen, T.B., Tyndall, G.S., Crounse, J.D., Teng, A.P., Bates, K.H., Schwantes, R.H., Coggon, M.M., Zhang, L., Feiner, P., Millller, D.O., Skog, K.M., Rivera-Rios, J.C., Dorris, M., Olson, K.F., Koss, A., Wild, R.J., Brown, S.S., Goldstein, A.H., de Gouw, J.A., Brune, W.H., Keutsch, F.N., Seinfeld, J.H., Wennberg, P.O., 2016. Atmospheric fates of Criegee intermediates in the ozonolysis of isoprene. Phys Chem Chem Phys 18, 10241–10254. https://doi.org/10.1039/C6CP00053C

Nölscher, A.C., Williams, J., Sinha, V., Custer, T., Song, W., Johnson, A.M., Axinte, R., Bozem, H., Fischer, H., Pouvesle, N., Phillips, G., Crowley, J.N., Rantala, P., Rinne, J., Kulmala, M., Gonzales, D., Valverde-Canossa, J., Vogel, A., Hoffmann, T., Ouwersloot, H.G., Vilà-Guerau de Arellano, J., Lelieveld, J., 2012. Summertime total OH reactivity measurements from boreal forest during HUMPPA-COPEC 2010. Atmos Chem Phys 12, 8257–8270. https://doi.org/10.5194/acp-12-8257-2012

Nölscher, A.C., Yañez-Serrano, A.M., Wolff, S., de Araujo, A.C., Lavrič, J.V., Kesselmeier, J., Williams, J., 2016. Unexpected seasonality in quantity and composition of Amazon rainforest air reactivity. Nat. Commun. 7, 10383. https://doi.org/10.1038/ncomms10383

Novelli, A., Hens, K., Tatum Ernest, C., Kubistin, D., Regelin, E., Elste, T., Plass-Dülmer, C., Martinez, M., Lelieveld, J., Harder, H., 2014. Characterisation of an inlet pre-injector laser-induced fluorescence instrument for the measurement of atmospheric hydroxyl radicals. Atmos Meas Tech 7, 3413–3430. https://doi.org/10.5194/amt-7-3413-2014

Orlando, J.J., Tyndall, G.S., 2012. Laboratory studies of organic peroxy radical chemistry: an overview with emphasis on recent issues of atmospheric significance. Chem Soc Rev 41, 6294–6317. https://doi.org/10.1039/C2CS35166H

Orlando, J.J., Tyndall, G.S., Wallington, T.J., 2003. The Atmospheric Chemistry of Alkoxy Radicals. Chem. Rev. 103, 4657–4690. https://doi.org/10.1021/cr020527p

Parker, A.E., Amédro, D., Schoemaecker, C., Fittschen, C., 2011. OH Radical Reactivity Measurements By Fage. Environ. Eng. Manag. J. EEMJ 10.

Paulot, F., Crounse, J.D., Kjaergaard, H.G., Kürten, A., St. Clair, J.M., Seinfeld, J.H., Wennberg, P.O., 2009. Unexpected Epoxide Formation in the Gas-Phase Photooxidation of Isoprene. Science 325, 730–733. https://doi.org/10.1126/science.1172910

Paulson, S.E., Orlando, J.J., 1996. The reactions of ozone with alkenes: An important source of HOx in the boundary layer. Geophys. Res. Lett. 23, 3727–3730. https://doi.org/10.1029/96GL03477

Peeters, J., Müller, J.-F., 2010. HOx radical regeneration in isoprene oxidation via peroxy radical isomerisations. II: experimental evidence and global impact. Phys. Chem. Chem. Phys. 12, 14227–14235.

Peeters, J., Nguyen, T.L., Vereecken, L., 2009. HO x radical regeneration in the oxidation of isoprene. Phys. Chem. Chem. Phys. 11, 5935–5939.

Penkett, S.A., Monks, P.S., Carpenter, L.J., Clemitshaw, K.C., Ayers, G.P., Gillett, R.W., Galbally, I.E., Meyer, C.P., 1997. Relationships between ozone photolysis rates and peroxy radical concentrations in clean marine air over the Southern Ocean. J. Geophys. Res. Atmospheres 102, 12805–12817. https://doi.org/10.1029/97JD00765

Perring, A.E., Pusede, S.E., Cohen, R.C., 2013. An Observational Perspective on the Atmospheric Impacts of Alkyl and Multifunctional Nitrates on Ozone and Secondary Organic Aerosol. Chem. Rev. 113, 5848–5870. https://doi.org/10.1021/cr300520x

Praske, E., Otkj\a er, R.V., Crounse, J.D., Hethcox, J.C., Stoltz, B.M., Kjaergaard, H.G., Wennberg, P.O., 2018. Atmospheric autoxidation is increasingly important in urban and suburban North America. Proc. Natl. Acad. Sci. 115, 64–69. https://doi.org/10.1073/pnas.1715540115

Pugh, T.A.M., MacKenzie, A.R., Hewitt, C.N., Langford, B., Edwards, P.M., Furneaux, K.L., Heard, D.E., Hopkins, J.R., Jones, C.E., Karunaharan, A., Lee, J., Mills, G., Misztal, P., Moller, S., Monks, P.S., Whalley, L.K., 2010. Simulating atmospheric composition over a South-East Asian tropical rainforest: performance of a chemistry box model. Atmos Chem Phys 10, 279–298. https://doi.org/10.5194/acp-10-279-2010

Read, K.A., Lewis, A.C., Bauguitte, S., Rankin, A.M., Salmon, R.A., Wolff, E.W., Saiz-Lopez, A., Bloss, W.J., Heard, D.E., Lee, J.D., Plane, J.M.C., 2008. DMS and MSA measurements in the Antarctic Boundary Layer: impact of BrO on MSA production. Atmos Chem Phys 8, 2985–2997. https://doi.org/10.5194/acp-8-2985-2008

Reichert, L., Andrés Hernández, M.D., Stöbener, D., Burkert, J., Burrows, J.P., 2003. Investigation of the effect of water complexes in the determination of peroxy radical ambient concentrations: Implications for the atmosphere. J. Geophys. Res. Atmospheres 108, ACH 4-1-ACH 4-16. https://doi.org/10.1029/2002JD002152

Ren, X., Edwards, G.D., Cantrell, C.A., Lesher, R.L., Metcalf, A.R., Shirley, T., Brune, W.H., 2003. Intercomparison of peroxy radical measurements at a rural site using laser-induced fluorescence and Peroxy Radical Chemical Ionization Mass Spectrometer (PerCIMS) techniques. J. Geophys. Res. Atmospheres 108. https://doi.org/10.1029/2003JD003644

Ren, X., van Duin, D., Cazorla, M., Chen, S., Mao, J., Zhang, L., Brune, W.H., Flynn, J.H., Grossberg, N., Lefer, B.L., Rappenglück, B., Wong, K.W., Tsai, C., Stutz, J., Dibb, J.E., Thomas Jobson, B., Luke, W.T., Kelley, P., 2013. Atmospheric oxidation chemistry and ozone production: Results from SHARP 2009 in Houston, Texas. J. Geophys. Res. Atmospheres 118, 5770–5780. https://doi.org/10.1002/jgrd.50342

Ren, Y., Grosselin, B., Daële, V., Mellouki, A., 2017. Investigation of the reaction of ozone with isoprene, methacrolein and methyl vinyl ketone using the HELIOS chamber. Faraday Discuss 200, 289–311. https://doi.org/10.1039/C7FD00014F

Rickly, P., Stevens, P.S., 2018. Measurements of a potential interference with laser-induced fluorescence measurements of ambient OH from the ozonolysis of biogenic alkenes. Atmos Meas Tech 11, 1–16. https://doi.org/10.5194/amt-11-1-2018

Sadanaga, Y., Matsumoto, J., Sakurai, K., Isozaki, R., Kato, S., Nomaguchi, T., Bandow, H., Kajii, Y., 2004. Development of a measurement system of peroxy radicals using a chemical amplification/laser-induced fluorescence technique. Rev. Sci. Instrum. 75, 864–872. https://doi.org/doi:http://dx.doi.org/10.1063/1.1666985

Sanchez, J., Tanner, D.J., Chen, D., Huey, L.G., Ng, N.L., 2016. A new technique for the direct detection of HO2 radicals using bromide chemical ionization mass spectrometry (Br-CIMS): initial characterization. Atmos Meas Tech 9, 3851–3861. https://doi.org/10.5194/amt-9-3851-2016

Sander, S., Friedl, R., Golden, D., Kurylo, M., Huie, R., Orkin, V., Moortgat, G., Ravishankara, A., Kolb, C., Molina, M., 2003. NASA/JPL Data Evaluation, JPL Publication 02-25 Evaluation No 14. Jet Propuls. Lab. Pasadena CA.

Sander, S., Golden, D., Kurylo, M., Moortgat, G., Wine, P., Ravishankara, A., Kolb, C., Molina, M., Finlayson-Pitts, B., Huie, R., 2006. Chemical kinetics and photochemical data for use in atmospheric studies evaluation number 15. Pasadena, CA: Jet Propulsion Laboratory, National Aeronautics and Space ….

Schultz, M., Heitlinger, M., Mihelcic, D., Volz-Thomas, A., 1995. Calibration source for peroxy radicals with built-in actinometry using H2O and O2 photolysis at 185 nm. J. Geophys. Res. Atmospheres 100, 18811–18816. https://doi.org/10.1029/95JD01642

Sindelarova, K., Granier, C., Bouarar, I., Guenther, A., Tilmes, S., Stavrakou, T., Müller, J.-F., Kuhn, U., Stefani, P., Knorr, W., 2014. Global data set of biogenic VOC emissions calculated by the MEGAN model over the last 30 years. Atmos Chem Phys 14, 9317–9341. https://doi.org/10.5194/acp-14-9317-2014

Sinha, V., Williams, J., Lelieveld, J., Ruuskanen, T.M., Kajos, M.K., Patokoski, J., Hellen, H., Hakola, H., Mogensen, D., Boy, M., Rinne, J., Kulmala, M., 2010. OH Reactivity Measurements within a Boreal Forest: Evidence for Unknown Reactive Emissions. Environ. Sci. Technol. 44, 6614–6620. https://doi.org/10.1021/es101780b

Sklaveniti, S., Locoge, N., Stevens, P.S., Wood, E., Kundu, S., Dusanter, S., 2018. Development of an instrument for direct ozone production rate measurements: measurement reliability and current limitations. Atmos Meas Tech 11, 741–761. https://doi.org/10.5194/amt-11-741-2018

Sneep, M., Ubachs, W., 2005. Direct measurement of the Rayleigh scattering cross section in various gases. J. Quant. Spectrosc. Radiat. Transf. 92, 293–310. https://doi.org/10.1016/j.jqsrt.2004.07.025

Spataro, F., Ianniello, A., 2014. Sources of atmospheric nitrous acid: State of the science, current research needs, and future prospects. J. Air Waste Manag. Assoc. 64, 1232–1250. https://doi.org/10.1080/10962247.2014.952846

Stavrakou, T., Peeters, J., Müller, J.-F., 2010. Improved global modelling of HO x recycling in isoprene oxidation: evaluation against the GABRIEL and INTEX-A aircraft campaign measurements. Atmospheric Chem. Phys. 10, 9863–9878.

Stevens, P.S., Mather, J.H., Brune, W.H., 1994a. Measurement of tropospheric OH and HO2 by laser-induced fluorescence at low pressure. J. Geophys. Res. Atmospheres 99, 3543–3557. https://doi.org/10.1029/93JD03342

Stone, D., Whalley, L.K., Heard, D.E., 2012. Tropospheric OH and HO2 radicals: field measurements and model comparisons. Chem. Soc. Rev. 41, 6348–6404. https://doi.org/10.1039/C2CS35140D

Sutton, J.A., Driscoll, J.F., 2004. Rayleigh scattering cross sections of combustion species at 266, 355, and 532 nm for thermometry applications. Opt Lett 29, 2620–2622. https://doi.org/10.1364/OL.29.002620

Tan, D., Faloona, I., Simpas, J.B., Brune, W., Shepson, P.B., Couch, T.L., Sumner, A.L., Carroll, M.A., Thornberry, T., Apel, E., Riemer, D., Stockwell, W., 2001. HO x budgets in a deciduous forest: Results from the PROPHET summer 1998 campaign. J. Geophys. Res. Atmospheres 106, 24407–24427. https://doi.org/10.1029/2001JD900016

Tan, Z., Fuchs, H., Lu, K., Hofzumahaus, A., Bohn, B., Broch, S., Dong, H., Gomm, S., Häseler, R., He, L., Holland, F., Li, X., Liu, Y., Lu, S., Rohrer, F., Shao, M., Wang, B., Wang, M., Wu, Y., Zeng, L., Zhang, Y., Wahner, A., Zhang, Y., 2017. Radical chemistry at a rural site (Wangdu) in the North China Plain: observation and model calculations of OH, HO2 and RO2 radicals. Atmos Chem Phys 17, 663–690. https://doi.org/10.5194/acp-17-663-2017

Tan, Z., Lu, K., Hofzumahaus, A., Fuchs, H., Bohn, B., Holland, F., Liu, Y., Rohrer, F., Shao, M., Sun, K., Wu, Y., Zeng, L., Zhang, Y., Zou, Q., Kiendler-Scharr, A., Wahner, A., Zhang, Y., 2019. Experimental budgets of OH, HO2, and RO2 radicals and implications for ozone formation in the Pearl River Delta in China 2014. Atmos Chem Phys 19, 7129–7150. https://doi.org/10.5194/acp-19-7129-2019

Tan, Z., Lu, K., Hofzumahaus, A., Fuchs, H., Bohn, B., Holland, F., Liu, Y., Rohrer, F., Shao, M., Sun, K., Wu, Y., Zeng, L., Zhang, Y., Zou, Q., Kiendler-Scharr, A., Wahner, A., Zhang, Y., 2018a. Experimental budgets of OH, HO$_\mathbf2$ and RO$_\mathbf2$ radicals and implications for ozone formation in the Pearl River Delta in China 2014. Atmospheric Chem. Phys. Discuss. 2018, 1–28. https://doi.org/10.5194/acp-2018-801

Tan, Z., Rohrer, F., Lu, K., Ma, X., Bohn, B., Broch, S., Dong, H., Fuchs, H., Gkatzelis, G.I., Hofzumahaus, A., Holland, F., Li, X., Liu, Y., Liu, Y., Novelli, A., Shao, M., Wang, H., Wu, Y., Zeng, L., Hu, M., Kiendler-Scharr, A., Wahner, A., Zhang, Y., 2018b. Wintertime photochemistry in Beijing: observations of ROx radical concentrations in the North China Plain during the BEST-ONE campaign. Atmos Chem Phys 18, 12391–12411. https://doi.org/10.5194/acp-18-12391-2018

Teruel, M.A., Lane, S.I., Mellouki, A., Solignac, G., Le Bras, G., 2006. OH reaction rate constants and UV absorption cross-sections of unsaturated esters. Atmos. Environ. 40, 3764–3772. https://doi.org/10.1016/j.atmosenv.2006.03.003

Vaughan, S., Ingham, T., Whalley, L.K., Stone, D., Evans, M.J., Read, K.A., Lee, J.D., Moller, S.J., Carpenter, L.J., Lewis, A.C., Fleming, Z.L., Heard, D.E., 2012. Seasonal observations of OH and HO_2 in the remote tropical marine boundary layer. Atmospheric Chem. Phys. 12, 2149–2172. https://doi.org/10.5194/acp-12-2149-2012

Villena, G., Kleffmann, J., Kurtenbach, R., Wiesen, P., Lissi, E., Rubio, M.A., Croxatto, G., Rappenglück, B., 2011. Vertical gradients of HONO, NOx and O3 in Santiago de Chile. Atmos. Environ. 45, 3867–3873. https://doi.org/10.1016/j.atmosenv.2011.01.073

Volkamer, R., Sheehy, P., Molina, L.T., Molina, M.J., 2010. Oxidative capacity of the Mexico City atmosphere – Part 1: A radical source perspective. Atmos Chem Phys 10, 6969–6991. https://doi.org/10.5194/acp-10-6969-2010

Whalley, L., Stone, D., Heard, D., 2012. New insights into the tropospheric oxidation of isoprene: combining field measurements, laboratory studies, chemical modelling and quantum theory, in: Atmospheric and Aerosol Chemistry. Springer, pp. 55–95.

Whalley, L.K., Blitz, M.A., Desservettaz, M., Seakins, P.W., Heard, D.E., 2013. Reporting the sensitivity of laser-induced fluorescence instruments used for HO_2 detection to an interference from RO_2 radicals and introducing a novel approach that enables HO_2 and certain RO_2 types to be selectively measured. Atmos Meas Tech 6, 3425–3440. https://doi.org/10.5194/amt-6-3425-2013

Whalley, L.K., Edwards, P.M., Furneaux, K.L., Goddard, A., Ingham, T., Evans, M.J., Stone, D., Hopkins, J.R., Jones, C.E., Karunaharan, A., Lee, J.D., Lewis, A.C., Monks, P.S., Moller, S.J., Heard, D.E., 2011. Quantifying the magnitude of a missing hydroxyl radical source in a tropical rainforest. Atmos Chem Phys 11, 7223–7233. https://doi.org/10.5194/acp-11-7223-2011

Whalley, L.K., Stone, D., Dunmore, R., Hamilton, J., Hopkins, J.R., Lee, J.D., Lewis, A.C., Williams, P., Kleffmann, J., Laufs, S., Woodward-Massey, R., Heard, D.E., 2018a. Understanding in situ ozone production in the summertime through radical observations and modelling studies during the Clean air for London project (ClearfLo). Atmospheric Chem. Phys. 18, 2547–2571. https://doi.org/10.5194/acp-18-2547-2018

Wolfe, G.M., Cantrell, C., Kim, S., Mauldin III, R.L., Karl, T., Harley, P., Turnipseed, A., Zheng, W., Flocke, F., Apel, E.C., Hornbrook, R.S., Hall, S.R., Ullmann, K., Henry, S.B., DiGangi, J.P., Boyle, E.S., Kaser, L., Schnitzhofer, R., Hansel, A., Graus, M., Nakashima, Y., Kajii, Y., Guenther, A., Keutsch, F.N., 2014. Missing peroxy radical sources within a summertime ponderosa pine forest. Atmos Chem Phys 14, 4715–4732. https://doi.org/10.5194/acp-14-4715-2014

Wolfe, G.M., Marvin, M.R., Roberts, S.J., Travis, K.R., Liao, J., 2016. The Framework for 0-D Atmospheric Modeling (F0AM) v3.1. Geosci Model Dev 9, 3309–3319. https://doi.org/10.5194/gmd-9-3309-2016

Wolfe, G.M., Thornton, J.A., McKay, M., Goldstein, A.H., 2011. Forest-atmosphere exchange of ozone: sensitivity to very reactive biogenic VOC emissions and implications for in-canopy photochemistry. Atmos Chem Phys 11, 7875–7891. https://doi.org/10.5194/acp-11-7875-2011

Wood, E.C., Charest, J.R., 2014. Chemical Amplification - Cavity Attenuated Phase Shift Spectroscopy Measurements of Atmospheric Peroxy Radicals. Anal. Chem. 86, 10266–10273. https://doi.org/10.1021/ac502451m

Wood, E.C., Deming, B.L., Kundu, S., 2017. Ethane-Based Chemical Amplification Measurement Technique for Atmospheric Peroxy Radicals. Environ. Sci. Technol. Lett. 4, 15–19. https://doi.org/10.1021/acs.estlett.6b00438

Zhang, X., Lambe, A.T., Upshur, M.A., Brooks, W.A., Gray Bé, A., Thomson, R.J., Geiger, F.M., Surratt, J.D., Zhang, Z., Gold, A., 2017. Highly oxygenated multifunctional compounds in α-pinene secondary organic aerosol. Environ. Sci. Technol. 51, 5932–5940.

Zheng, W., Flocke, F.M., Tyndall, G.S., Swanson, A., Orlando, J.J., Roberts, J.M., Huey, L.G., Tanner, D.J., 2011. Characterization of a thermal decomposition chemical ionization mass spectrometer for the measurement of peroxy acyl nitrates (PANs) in the atmosphere. Atmos Chem Phys 11, 6529–6547. https://doi.org/10.5194/acp-11-6529-2011

Zhou, X., Zhang, N., TerAvest, M., Tang, D., Hou, J., Bertman, S., Alaghmand, M., Shepson, P.B., Carroll, M.A., Griffith, S., Dusanter, S., Stevens, P.S., 2011. Nitric acid photolysis on forest canopy surface as a source for tropospheric nitrous acid. Nat. Geosci. 4, 440–443. https://doi.org/10.1038/ngeo1164

CHAPTER 3: Implementation of the ROxLIF technique on a Laser-Induced Fluorescence/Fluorescence Assay by Gas Expansion instrument

Table of contents

Chapter 3. Implementation of the RO_xLIF technique on a Laser-Induced Fluorescence/Fluorescent Assay by Gas Expansion instrument

3.1 Introduction

Atmospheric measurements of peroxy radicals are a challenging task owing to their high reactivity and low atmospheric concentrations. As discussed in the first chapter, instruments dedicated to the measurement of peroxy radicals must exhibit a high detection sensitivity and good selectivity. Reliable determinations of the radical concentrations are further complicated by potential losses of these short-lived species on inlet surfaces and thus instruments must be designed to minimize wall effects. In this work, we worked on the RO_xLIF technique, which allows a speciation between HO_2 and the pool of organic peroxy radicals (RO_2) through their selective conversion into OH and their detection by LIF-FAGE.

The FAGE instrument used in this work was developed at Indiana University over the last decade (Dusanter et al., 2009a; Griffith et al., 2013a) and has been used for measuring OH, HO_2 and HO_2^* in several field campaigns (Dusanter et al., 2009b; Griffith et al., 2016, 2013b; Kundu et al., 2019; Lew et al., 2018). The objective of this work was to couple a RO_2 conversion unit on the inlet of the existing FAGE setup to extend the radical measurements to HO_2+RO_2. This chapter reports the design and the construction of the conversion unit, its characterization and an optimization of operating conditions, and the first field testing performed at the Indiana University Research and Teaching Preserve (IURTP). Both experimental and modeling work were performed to provide a detailed characterization of the instrument.

3.2 Description of the Indiana University RO_xLIF instrument

The principle of RO_xLIF has been described in chapter 1 (section 1.3.4) and only a brief summary is given below. The sampled RO_2 radicals (together with OH) are converted into HO_2 by adding NO and CO in a flow-tube which is coupled to the inlet of the FAGE instrument. This HO_2 (together with the sampled ambient HO_2) is then sampled with FAGE, converted into OH by added

NO, and quantified by laser induced fluorescence at low pressure. The following sections present (i) the design of the RO_xLIF conversion flow-tube and its coupling to the FAGE detection cell, (ii) the modeling of the RO_xLIF chemistry inside the flow tube, and (iii) the characterization of different aspects of the RO_xLIF apparatus (wall loss of HO_2, RO_2-to-HO_2 conversion time in the flow-tube, dependence of the conversion chemistry on reagent gas amount, sensitivity to OH, HO_2 and RO_2).

3.2.1 Experimental apparatus

This section describes the Indiana University (IU)-FAGE and IU-RO_xLIF setups that have together the capability of measuring OH, HO_2 (or HO_2^*) and RO_2 radicals. For this study we only used one detection cell, which was coupled to the conversion flow-tube, and the following only focuses on HO_x and RO_x measurements. In this section, we present the design and the characteristics of the conversion flow-tube, the modulation approach used to sequentially measure HO_x and RO_x, and the calibration procedure. In the following we will refer to HO_2 and HO_2+RO_2 measurement modes instead of HO_x and RO_x modes for ambient measurements since the OH mixing ratio is negligible compared to those of HO_2 and RO_2 in the troposphere.

3.2.1.1 RO_2-to-HO_2 conversion flow-tube

As shown in Figure 3.1, ambient air is sampled at a total flow rate of 2.1 standard liter per minute (slpm) into a cylindrical flow tube made of aluminum (Length: 45 cm, inner diameter: 5.1 cm), which is internally coated with a mixture of PFA and FEP (KECO coating, ING). The air flow is expanded through a flat shaped nozzle (nickel, orifice: 0.635 mm) from ambient pressure to of 28 torr that was measured by a MKS Baratron gauge (range: 1000 Torr). The reagent gases CO (10% in N_2, Matheson Inc), NO (500 ppm, Indiana Oxygen) and N_2 (99.99%, Indiana Oxygen) are injected into the flow-tube 2 cm downstream of the sampling nozzle through a Teflon loop (PFA, outer diameter: 0.32 cm) designed with radial holes pointing towards the center of the reactor. The addition of the reagent gases is controlled by 3 mass flow controllers (MFC, MKS) and 3 solenoid valves (Parker, valve type 71215). The MFCs and valves are controlled by LabVIEW software and

a USB-6343 DAQ board from National Instruments that allows automatic switching the reagent gases to alternate between the HO_x and RO_x measurement modes.

When the reactor is operated in RO_x mode, 3.5 standard cubic centimeter per minute (sccm) of NO (500 ppm in N_2) and 80 sccm of CO (10% in N_2) are added to the entrance of the flow-tube to enable optimum conversion of RO_2 into HO_2 (see section 3.4.2). The mixing ratios of NO and CO in the flow-tube are 0.83 ppm and 0.38%, respectively. NO is then replaced by 3.5 sccm of N_2 (99.99% purity) when the flow-tube is operated in HO_x mode. At the end of the tube the air flow is split into two paths. One path leads to the FAGE detection cell where the air is sampled through another inlet nozzle (Conical shaped, aluminum that is coated with PFA & FEP, opening angle: 70°, orifice: 2 mm) at a flow rate of 1.5 slpm. The other path removes the excess flow of 0.6 splm through pumping. The sampling point for the detection cell is about 1.2 cm from the end of the of the flow-tube. Two different designs have been built and tested for this nozzle (conical as described above or flat, see figure 3.1). The conical nozzle was found to provide a better sensitivity and was chosen for the IU-RO_xLIF apparatus for this study.

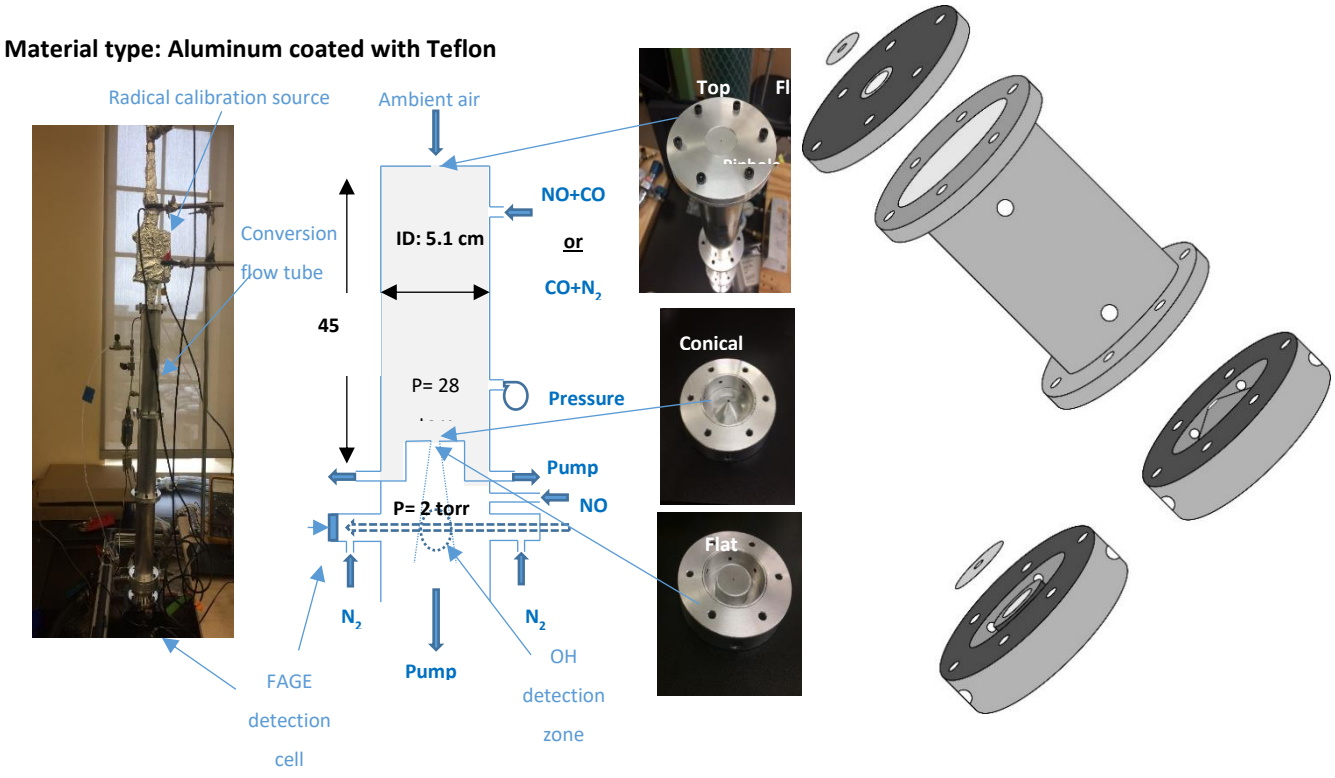

Figure 3.1: Schematic of the IU RO_xLIF instrument. Top flat nozzle for sampling air into reactor and two different designs of transfer inlet (conical and flat).

The conversion flow-tube is made up of 3 sections (internal diameter of 5.1 cm) with one length of 25 cm and two lengths of 20 cm. This setup allows varying the residence time of gases inside the flow-tube to determine the radical loss rate on the wall, which is an important parameter required to model the conversion chemistry. Both the conversion flow-tube and FAGE are connected to individual pumps (Edwards XDS 35i) controlled at pressures of 28 and 2 Torr, respectively.

3.2.1.2 Quantification of HO_2 using IU-FAGE

As mentioned above, the OH detection system used in this work is the Indiana University FAGE instrument used for HO_x measurements in the troposphere and described in detail elsewhere (Dusanter et al., 2009a; Griffith et al., 2013a). This instrument is composed of a high repetition rate laser, a low pressure sampling cell and gated photon counting detection of OH.

The laser system is composed of a Q-switched Spectra-Physics Navigator II YHP40-532Q pump laser that produces 7-8 W of radiation at 532 nm and at a repetition rate of 10 kHz. This Nd:YAG laser pumps a tunable Sirah Credo dye laser to produce radiation at 616 nm. The dye mixture used for this laser consists of 0.24 and 1.02 g/L of Rhodamine 640 and Rhodamine 610, respectively, in ethanol. The 616-nm beam is then focused into a BBO (Beta Barium Borate) doubling crystal, resulting in conversion to 6 – 20 mW of radiation at 308 nm (~20-ns pulse width).

OH radicals are excited using the $A^2\Sigma^+(\upsilon'=0) \leftarrow X^2\Pi(\upsilon''=0)$ transition near 308 nm (Stevens et al., 1994) to reduce the potential formation of OH in the detection cell from ozone photolysis since the ozone absorption cross section at 308 nm is approximately 25 times lower than at 282 nm (Stevens et al., 1994) where the transition occurs. The $Q_1(3)$ transition at 308.1541 nm is one of the strongest in the OH spectrum near 308 nm and the laser is tuned on the top of this transition for all ambient measurements (refered to as on-resonnance in the following discussion). To locate this transition, the fluorescence signal from a reference cell containing a large concentration of OH generated by thermal decomposition of water vapor is used. A wavelength scan is performed at the beginning of each experiment (typically from 308.09 to 308.17 nm) to determine the laser wavelength at which the $Q_1(3)$ transition occurs as shown in Figure 3.2. Since the wavelength scale of the laser drifts over time (due to changes in dye temperature, ambient temperature, etc.) the scan is performed periodically to ensure the correct transition is excited. The reference cell is made of aluminum and the OH fluorescence from this cell is detected using a PMT detector (Hamamatsu R5946U-50), a preamplifier (Stanford Research System SR445) and a gated photon counter (Stanford Research Systems SR 400).

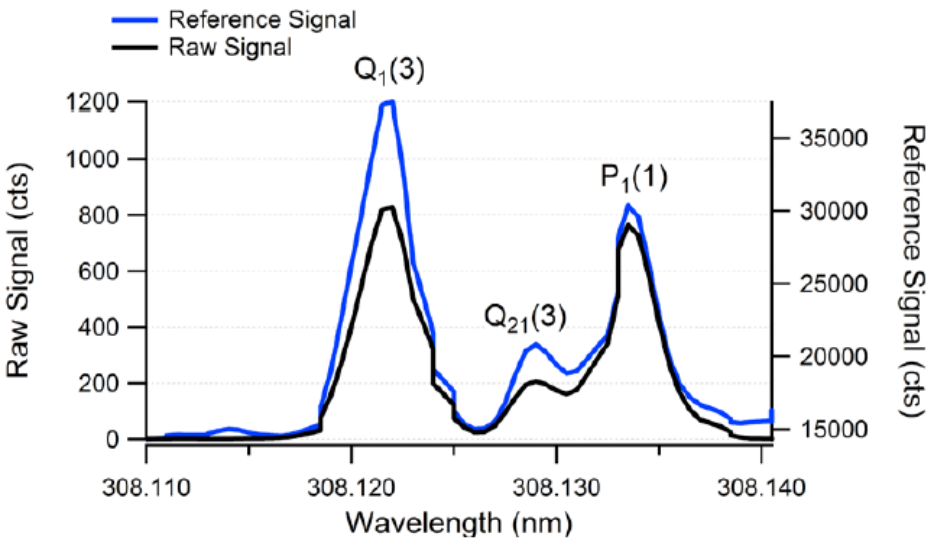

Figure 3.2 Rovibrational peaks observed near 308 nm during laboratory experiments. All OH measurements are performed at the wavelength where the $Q_1(3)$ transition occurs. The blue and black curves represent the fluorescence signals from the reference and FAGE detection cells during a calibration experiment where a large concentration of OH is provided to FAGE.

The FAGE detection cell can be described along three axes: air expansion, laser excitation of OH, detection of OH fluorescence, as shown in Fig 3.3. As mentioned above for the RO_xLIF setup, a flow of 1.5 slpm of air is sampled from the conversion flow-tube through the nozzle (conical inlet) and is expanded at a pressure of 2 torr inside the detection cell. The low pressure allows for a longer OH fluorescence lifetime since quenching rates of excited OH by nitrogen, oxygen and water are reduced, which in turn allows temporal filtering between the laser scattered light and the OH fluorescence. A flow of NO (1% in Nitrogen, flow rate: 0.85 sccm, see section 3.2.1.1) is injected into the detection cell through a Teflon loop located approximately 2.5 cm after the sampling point and 17.5 cm before the detection axis in order to convert HO_2 into OH. The 308 nm laser beam is directed through an optical fiber (ThorLabs, 12 m) and delivered to the detection cell through a fiber launcher (ThorLabs) into a multi-pass optical cell (White design, mirror R>99.9% at 308-nm, 24-passes). The latter allows increases in the fluorescence generated thereby improving the instrumental sensitivity (Dusanter et al., 2009b). The OH fluorescence is collected through two coated lenses (f=75-mm, CVI Laser) and a band-pass filter centered at 308 nm (Barr Associates, transmission: 65%, bandwidth: 5-nm, OD>5 at other wavelengths) and detected by a MCP-PMT (Micro Channel Plate Photomultiplier Tube 325, Photek Ltd, UK) which is activated

slightly after the laser using a gating Module (GM300-3N, Photek Ltd). The MCP pulses are processed by a preamplifier (PA200-10P, Photek Ltd) and counted by a gated SRS 400 (Stanford Research System) photon counter. A concave mirror (100-cm diameter, 40-cm focus lens, Melles Griot) is placed on the opposite side of the detector to approximately double the collected OH fluorescence.

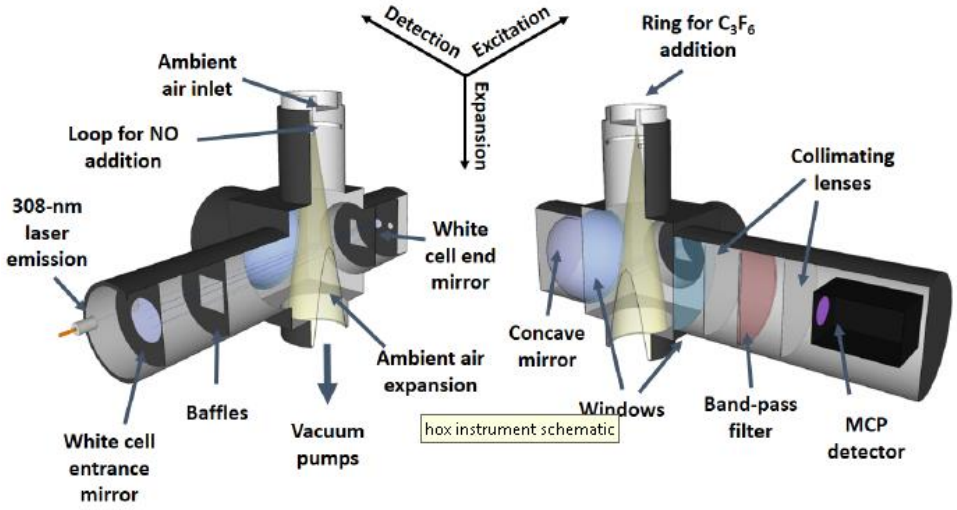

Figure 3.3 OH Schematic of the IU LIF-FAGE instrument. Cross sections showing the sampling/excitation (left) and detection (right) axes (Dusanter et al., 2008).

The gated photon counting system is composed of a BNC 565 delay generator that (i) activates the MCP-PMT detector shortly after the laser pulse for a duration of 770 ns and (ii) triggers the SRS photon counter after each laser pulse to count the pulses generated in a time with window of 450 ns. Properly timing the detection and counting windows ensures that the laser scatter from the excitation is separated from the OH fluorescence. The counting window is timed such that the MCP-PMT pulse detection is significantly delayed from laser emission, but close enough to capture most of the OH fluorescence.

The FAGE instrument is not a zero-background technique and thus a background signal (off-resonance signal) must be measured to derive the net signal produced by the OH fluorescence. Ambient measurements of OH require the ability to quickly tune the laser on- and off-resonance

with the OH transition to derive the net OH fluorescence signal (referred to as S_{XX} in the following, where XX = OH, HO_2, HO_x, RO_x):

$$S_{XX} = S_{XX}(on - resonance) - S_{XX}(off - resonance) \qquad (3.1)$$

The OH fluorescence signal (Sxx) is the number of photons detected by the MPC-PMT within the counting window and is expressed in counts. The acquisition rate for both on & off –resonance signals is 1 second and the net OH fluorescence signal is reported in counts per second (cps) for IU-FAGE.

HO_2 radicals are measured indirectly in the FAGE detection cell through chemical conversion of OH from the addition of NO (chapter 1, section 1.2.4). The conversion efficiency of HO_2 into OH and potential interferences from the conversion of RO_2 radicals have been reported by Lew et al. (2018) for different configurations of IU-FAGE that were used in the field, including CalNex-2010 (Griffith et al., 2016), CABINEX-2009 (Griffith et al., 2013a) and MCMA-2006 (Dusanter et al., 2009b, 2009a). This study showed that the conversion efficiency of HO_2 into OH was higher for instrument configurations utilizing lower sampling flow rates which resulted in longer reaction times between the peroxy radicals and NO before OH detection. Lew et al. (2018) quantified the conversion efficiency of several types of RO_2 into HO_2 (and subsequently into OH) at two different NO concentrations (1.4×10^{13} & 9×10^{11} cm^{-3}) under the same instrument conditions (3 torr). This work showed that for isoprene-derived RO_2 radicals that convert efficiently into HO_2 their conversion into OH was reduced by a factor of 30-50 at the lowest NO concentration while the conversion of HO_2 was only reduced by a factor of 4-5. The low NO concentration is therefore preferred to reduce the contribution of RO_2 radicals during the IU-FAGE HO_2 measurement mode.

3.2.2 Quantification of OH fluorescence signals using FAGE and RO_xLIF

The fluorescence signals detected for OH and HO_x (addition of NO to the FAGE detection cell) when FAGE is uncoupled from the conversion flow tube, and signals detected for HO_x and RO_x when the RO_xLIF apparatus is used are referred to as S_{OH}, S_{HOx}, S_{HOx}^{FT}, and S_{ROx}^{FT}, respectively. A similar nomenclature is used to denote sensitivity factors derived from calibrations performed on FAGE and RO_xLIF. For FAGE, a calibration will lead to the sensitivities for OH (referred to as

C_{OH}) and HO_2 (C_{HO_2}). For RO_xLIF, a calibrations lead to the sensitivity for HO_2 (C_{HO2}^{FT}) and RO_2 (C_{RO2}^{FT}).

3.2.2.1 Quantification of OH fluorescence signals during OH and HO_x modes for FAGE

When FAGE is used to measure OH in ambient air, i.e. NO is not added in the detection cell, the net fluorescence signal S_{OH} is given by equation (3.2):

$$S_{OH} = [OH] \times C_{OH} \times Pw \qquad (3.2)$$

Where, C_{OH} is the instrument sensitivity to OH expressed as the number of photon counts per second produced per cm^3 of OH and normalized to the laser power (cps cm^{-3} mW^{-1}), and Pw the laser power (mW). It is common to normalize the sensitivity to the laser power since the generated signal depends linearly on this parameter.

Similarly for HO_x, the detected fluorescence signal is given by Equation 3.3 when NO is added in the detection cell:

$$S_{HOx} = \left([OH] + [HO_2] \times f_{HO_2}\right) \times C_{OH} \times Pw \qquad (3.3)$$

Where, f_{HO_2} is the fraction of HO_2 converted into OH before detection. The instrument sensitivity to HO_2, C_{HO_2}, can thus be defined as follows Equation 3.4:

$$C_{HO_2} = f_{HO_2} \times C_{OH} \quad (3.4)$$

3.2.2.2 Quantification of fluorescence signals during HO_x and RO_x modes for ROx-LIF

In the RO_xLIF technique, NO is continuously added to FAGE since only HO_2 is exiting the conversion flow-tube. The modulation between HO_x and RO_x modes in the conversion flow-tube leads to measurement of either $OH+HO_2$ or $OH+HO_2+RO_2$. Note that only a fraction of the sampled radicals will survive along the conversion flow-tube and sensitivity factors for RO_xLIF are lower than for FAGE.

As mentioned previously, sequential measurements of HO_x and RO_x are achieved by rapidly switching the reagent gases delivered to the conversion flow-tube, i.e. switching between $CO+N_2$ and CO+NO (see section 1.2.4& 3.2.1.1), respectively. During the HO_x mode, addition of

CO converts OH into HO_2, which is then measured as HO_2 by FAGE. The relation between detected signal, S_{HOx}^{FT}, and the radical amounts is shown in Equation 3.5. Derivation of this equation assumes that all OH are quickly converted into HO_2 without any loss.

$$S_{HOx}^{FT} = C_{HO2}^{FT}([OH] + [HO_2]) \times Pw \qquad (3.5)$$

Here [OH] and [HO_2] denotes the radical concentrations sampled by the instrument. The sensitivity of the RO_xLIF instrument to HO_2, C_{HO2}^{FT}, is derived from calibration experiments (see section 3.2.2.1).

During the RO_x mode, the injection of both NO and CO leads to the conversion of OH and organic peroxy radicals into HO_2 on a timescale of 0.3-0.6 s (see section 1.2.4). The detected signal, $S_{RO_x}^{FT}$, is the sum of $S_{HO_x}^{FT}$ (Eq. 3.5) and the signal generated by the fraction of converted RO_2 radicals that survived along the flow-tube (f_{RO2}^{FT}).

$$S_{ROx}^{FT} = \left[\alpha \times C_{HO2}^{FT}([OH] + [HO_2]) + C_{RO2}^{FT}[RO_2]\right] \times Pw \qquad (3.6)$$

Here [RO_2] denotes the RO_2 concentration sampled by the instrument. The RO_xLIF sensitivity to RO_2, C_{RO2}^{FT}, is determined from calibrations performed on the RO_xLIF apparatus through the generation of specific RO_2 radicals (see section 1.2.5). α is multiplicatory factor accounts the decrease in C_{HO2}^{FT} when NO is added.

For ambient measurements, the measured S_{HOx}^{FT} signal and the calibrated C_{HO2}^{FT} sensitivity can be used to derive the concentration of HO_2 radicals by rearranging Eq. 3.5 since OH is several orders of magnitude lower than HO_2. The RO_2 concentration can then be derived by rearranging Eq. 3.6, subtracting the measured S_{HOx} from S_{ROx} and using a calibration factor, C_{RO2}^{FT}. It is important to note that this approach assumes that C_{RO2}^{FT} is similar for all RO_2 radicals; this hypothesis was verified by Fuchs et al. (2008) and was also tested in the results section (3.4.4).

3.2.3 Calibration of the instrument

3.2.3.1 Description of the calibration source

The radical source used to calibrate FAGE and RO_xLIF is similar to the calibrator described for the PERCA system (chapter 2) and the principle was detailed in chapter 1 (section 1.2.5).

Briefly, the approach is based on the photolysis of water in air at 184.9 nm to produce equal concentrations of both OH and HO_2. The concentrations produced are derived from ozone actinometry as described in chapter 1 (Eq. 1.4-1.6).

The radical source used in this study is shown in Figure 3.4. The calibrator consists of a rectangular flow reactor made of aluminum (1.27×1.27×30-cm) equipped with quartz window on two sides. A low-pressure mercury lamp (UVP Inc.) is secured in an aluminum housing on one side of the reaction and a photodiode (UDT 555-UV) is secured to the opposite side to measure changes in the the lamp emission flux at 184.9 nm. The lamp housing is continuously purged with nitrogen to avoid the accumulation of ozone which would be produced from oxygen photolysis. The lamp emission is filtered by a 185-nm filter (Acton Research) before the irradiation zone in the calibrator and another 185-nm filter is attached to the photodiode. The lamp and photodiode housings can be moved along the reactor to characterize the loss of radicals (see section in 3.2.4.2).

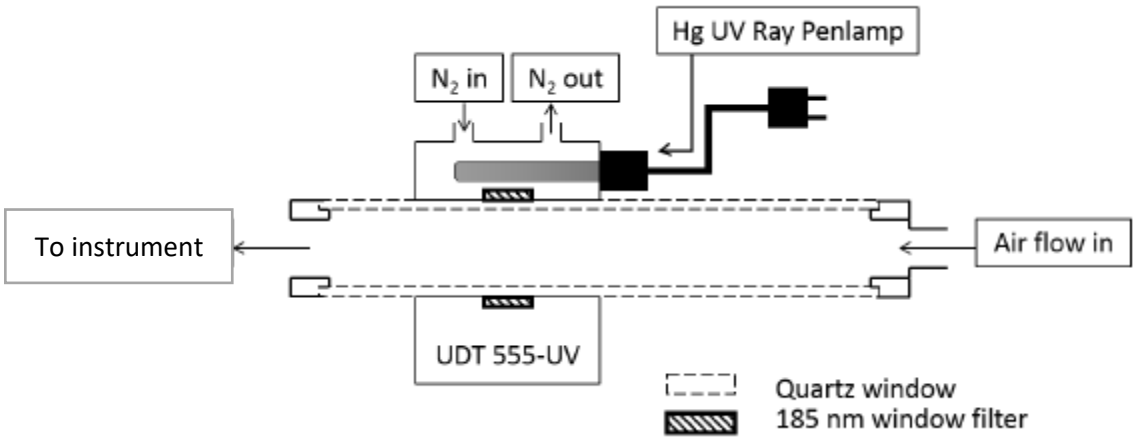

Figure 3.4 Schematic diagram of the RO_xLIF and FAGE calibration source (Lew et al., 2018).

For the generation of HO_2, OH is reacted with CO that is continuously added to the calibrator (chapter 2, section 2.3.2). The HO_2 concentration at the exit of the calibrator is then calculated as the sum of both OH and HO_2 concentrations produced from water photolysis (Eqs. 1.4-1.6, chapter 1). For the generation of a specific RO_2 radical, CO is replaced by a VOC, which leads to a mixture of HO_2 and RO_2. The concentrations of HO_2 and RO_2 can be calculated from Eqs. 3 and 4 (chapter 2) accounting for the potential prompt formation of HO_2 when the VOC

reacts with OH. During calibration, a 50 slpm flow of zero air was delivered to the calibration source with the relative humidity varied between 10-70% at 22±2°C producing both OH and HO_2 at concentrations ranging from 8×10^{8}-2×10^{10} cm^{-3}.

3.2.3.2 Characterization of the calibration source

The actinometry is used to calculate the product of the photon flux and the residence time within the photolysis region in the calibrator (F×t in Eq. 1.4, chapter 1) and requires knowledge of the concentration of ozone produced within the calibrator to derive the concentrations of OH and HO_2 produced in the calibrator. In order to quickly determine [O_3] during a calibration experiment, which is proportional to the 184.9 nm photon flux, the relationship between the ozone produced and the photodiode signal was characterized (Figure 3.5).

Dry zero air flowed through the calibrator at 50 slpm and different ozone concentrations were generated by varying the lamp intensity by varying the mercury lamp voltage with a variac. The ozone generated was measured by an ozone monitor (Teledyne M400E) exhibiting a limit of detection <0.4 ppbv for an integration time of 0.5 minutes. Figure 3.5 shows a calibration curve that relates the amount of ozone produced in the calibrator in ppbv to the photodiode signal expressed in volts. This calibration curve is checked periodically to ensure its validity and is used to convert the measured photodiode signal into an ozone concentration during a calibration experiment.

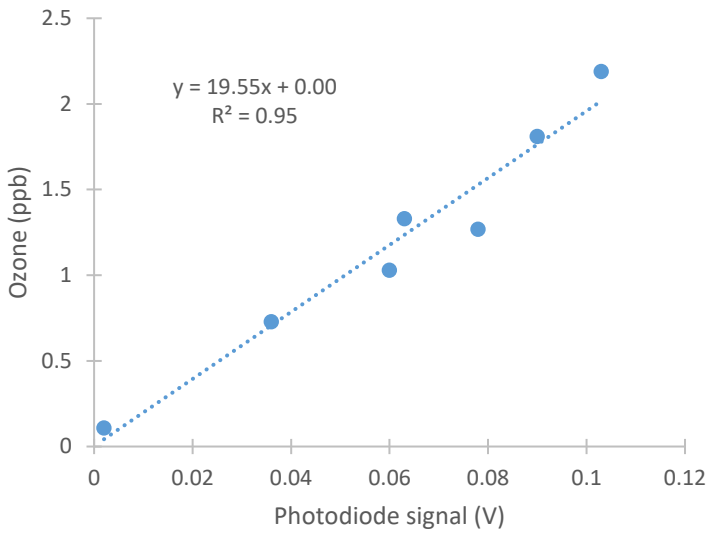

Figure 3.5 Ozone-photodiode signal relationship for the RO_x calibrator

While the actinometry approach allows calculating the radical concentrations generated in the irradiated zone, losses of these radicals on the calibrator wall can be significant and need to be accounted for to derive the radical concentrations exiting the calibrator. The loss rate of HO_2 and OH on the calibrator wall was measured as a function of the distance between the lamp position and the calibrator exit, assuming first order conditions for the loss reactions:

$$[HO_x]_t = [HO_x]_0 \exp(-k_{w(HO_x)} t) \quad (3.7)$$

Where, $[HO_x]_t$ is the OH or HO_2 radical concentration exiting the calibrator after a residence time, t, within the calibrator, $[HO_x]_0$ is the radical concentration generated and calculated from Eqs. 1.4-1.6 (chapter 1), and $k_{W(HOx)}$ is the wall loss rate constant.

The loss of radicals was quantified by varying their residence time inside the calibrator while monitoring the change in S_{OH} and S_{HO2} during FAGE calibrations. Figures 3.6 & 3.7 show data from experiments performed at a total flow rate of 10 slpm in the calibrator at 52% RH and 23°C. The lamp position was varied from 5 to 13.5 cm from the exit of the calibrator, which corresponds to residence times ranging from 50 to 130 ms assuming plug-flow conditions. The net OH signal shown in Fig. 3.6 decreases with increasing time indicating a first order loss rate of 7.6 s^{-1}. This corresponds to a loss of about 30 % of OH for a residence time of 50 ms, which is similar to that observed by Dusanter et al. (2008a) at a total flow rate of 50 slpm for the same calibrator. In

contrast, the HO_2 loss rate inside the calibrator is not significant as shown in Figure 3.7. The net HO_2 signal remains constant as the residence time is varied. A negligible HO_2 wall loss is also consistent with that observed by Dusanter et al. (2008a). The decrease in the Reynolds number from 13240 at 50 slpm (highly turbulent conditions) to 2650 at 10 slpm (transition regime for turbulent-laminar conditions) does not drastically change the radical loss rate.

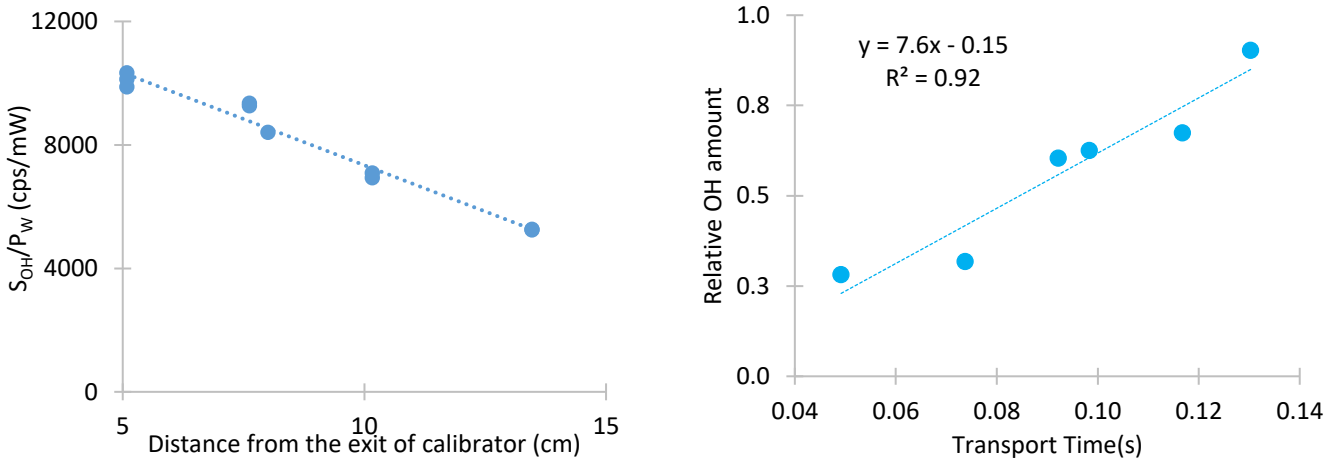

Figure 3.6 Quantification of OH wall losses within the calibrator: (a) net OH signal vs. distance between the exit of the calibrator and the radical production zone, and (b) OH wall loss rate (k_{WOH}).

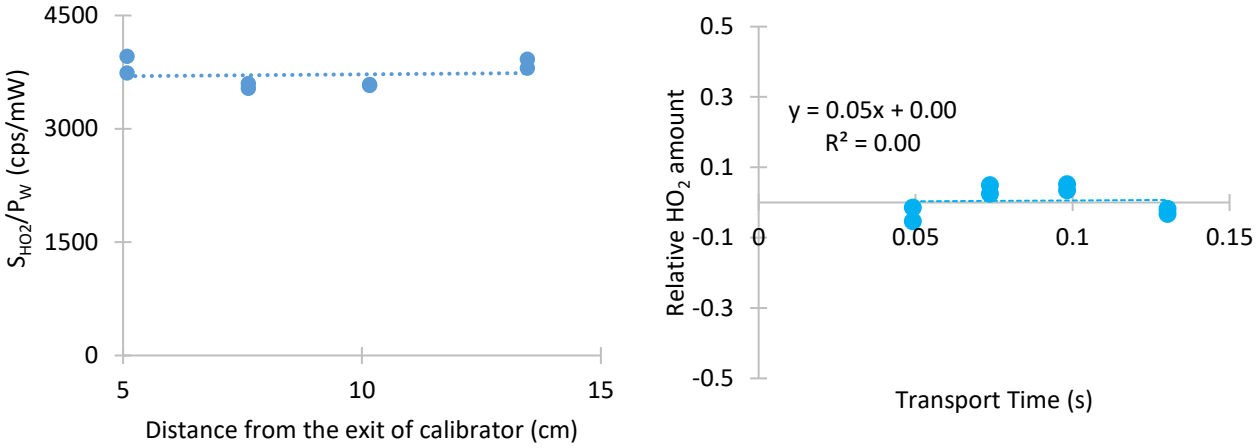

Figure 3.7 Quantification of HO_2 wall losses within the calibrator: (a) HO_2 net signal vs. distance between the exit of the calibrator and the radical production zone; (b) HO_2 wall loss rate (k_{WHO2}).

3.2.3.3 Calibration procedures of OH, HO_2 and RO_2 sensitivities

When FAGE is used to measure OH in ambient air, the sensitivity C_{OH} is derived from calibration experiments where a known concentration of OH is provided to the instrument using the calibration source described above:

$$C_{OH} = \frac{S_{OH}}{[OH]_0 \times L_{OH} \times Pw} \qquad (3.8)$$

Where $[OH]_0$ is the concentration of OH produced inside the calibrator and L_{OH} the fraction of OH exiting the calibrator (lower than 1 due to wall losses, calculated from k_{WOH} determined above and the residence time of OH in the calibrator).

Similarly for HO_2, the sensitivity is derived from calibration experiments using Equation 3.9 when NO is added in the FAGE detection cell:

$$C_{HO_2} = \frac{S_{HOx} - S_{OH}}{[HO_2]_0 \times L_{HO_2} \times Pw} \qquad (3.9)$$

Where $S_{HOx} - S_{OH}$ represents the signal generated by the detection of the converted HO_2 radicals, $[HO_2]_0$ the concentration of HO_2 and L_{HO_2} is the fraction of HO_2 exiting the calibrator, which is the unity for our calibrator, see section 3.2.3.2.

For the RO_xLIF apparatus, the detection sensitivity of HO_2 or RO_2 is also determined by generating known concentrations of these peroxy radicals from the calibration source (see section 3.2.3.1) During the HO_x mode, the HO_2 detection sensitivity (C_{HO2}^{FT}) (Equation 3.10) is determined by injecting CO in the calibrator to quickly convert OH into HO_2 (section 3.2.3.1), the latter being the only radical species exiting the calibrator:

$$C_{HO_2}^{FT} = \frac{S_{HOx}^{FT}}{([OH]_0 + [HO_2]_0) \times Pw} \tag{3.10}$$

Where S_{HOx}^{FT} is the measured net fluorescent signal, and $[OH]_0$ and $[HO_2]_0$ are the radical concentrations. It should be noted that the CO concentration is adjusted to convert 99% of OH in less than 5 ms in order to avoid wall losses of OH. Since HO_2 is not lost in the calibrator, the radical concentration don't need to be corrected for wall losses in Eq 3.10.

During the RO_x mode, a similar procedure is used to determine the sensitivity to RO_2 radicals. As described in section 3.2.4.1, CO is replaced by a VOC in the calibrator to generate a mixture of HO_2 and RO_2. The net signal generated from peroxy radicals, S_{ROx}^{FT} in Equation 3.11, now contains contributions from both the generated HO_2 and RO_2. Since the VOC concentration is adjusted to convert all OH in less than 2 ms, the concentration of RO_2 is equal to the initial OH concentration since RO_2 radical wall losses are lower than for HO_2, determined during the characterization of the PERCA instrument (chapter 2). However, the reaction of some VOCs with OH leads to the prompt formation of both HO_2 and RO_2 with yields of X (X<1) and 1-X, respectively (see chapter 2, section 2.5.4).

$$S_{ROx}^{FT} = (\alpha \times C_{HO2}^{FT}(1 + X)[HO_2]_0 + (C_{RO2}^{FT})(1 - X)[OH]_0) \times Pw \tag{3.11}$$

Rearranging Equation 3.11, the RO_2 detection sensitivity is derived as follows:

$$C_{RO_2}^{FT} = \frac{1}{1 - X}\left(\frac{S_{ROx}^{FT}}{[OH]_0 \times P_W} - \alpha \times C_{HO_2}^{FT}(1 + X)\right) \tag{3.12}$$

3.3 Modeling of the flow-tube conversion chemistry

The simulations were performed to investigate the conversion efficiency of different organic peroxy radicals at different concentrations of reagent gases, flow-tube pressures and residence times

3.3.1 F0AM

The framework for 0-D Modeling, F0AM (Wolfe et al., 2016), was used to simulate the chemistry occurring within the conversion flow-tube under different operating conditions. The model was constrained by initial concentrations of HO_2 and RO_2 radicals exiting the calibrator (8×10^8-2×10^{10} cm^{-3}), concentrations of reagent gases (NO: 0-2.4 ppm and CO: 0-1 %) and other parameters (pressure: 10-50 torr, temperature: 23°C and relative humidity: 40-50 %).

The gas mixture in the reactor is assumed to be homogeneous. The conversion chemistry was modeled over 2 s (time-steps of 0.1 s), which is longer than the estimated residence time of 1 s in the flow-tube when all the sections are used (see section 3.2.1.1). The wall loss rate of HO_2 was implemented in the model as quantified from laboratory experiments (1.11 s^{-1} for a FEP/PFA coating at 28 Torr, see section 3.4.1).

3.3.2 Chemical mechanism

A subset of the MCM (master chemical Mechanism) version 3.3.1 was extracted for the different hydrocarbons used in this study to generate RO_2 species in the calibrator (Table 1). This led to chemical mechanisms containing 71-1974 reactions and 29-610 species, including inorganic reactions.

Table 3.1: Specification of the chemical mechanisms used in this study

Hydrocarbon	Peroxy radicals	Number of reactions	Number of species
Methane	CH_3O_2	71	29
Ethane	$C_2H_5O_2$	168	57
Toluene	HO_2, $C_5H_5CH_2O_2$, TLBIPERO2[a]	862	291
Isoprene	$C_5H_5(OH)O_2$	1974	610

Reaction added to MCM	k (cm^3 s^{-1} or s^{-1})
RO_2 + Wall→ loss	0.35[b]
HO_2 + Wall→ loss	1.11[c]
RO + Wall→ loss	5.4[d]
OH + Wall→ loss	5.4[d]
CH_3O + NO→ CH_3ONO	4.9×10^{-12}[e]
C_2H_5O + NO→C_2H_5ONO[f]	4.2×10^{-11} [e]

a: notation from MCM, b: Estimated using the measured ratio k(RO_2+wall)/k(HO_2+wall)=0.3 from Mihele et al., (1999), c: experimentaly measured; d: Fuchs et al., 2008, e: Sander et al., (2003), f: same rate constant used for other RO(C>2)+NO reactions

The reaction of RO + NO was added in the chemical mechanisms because MCM does not include thys type of reactions, which are not important under atmospheric conditions. Rate constants of 4.9×10^{-12} cm^3 $molecule^{-1}$ s^{-1} and 4.2×10^{-11} cm^3 $molecule^{-1}$ s^{-1} were used for CH_3O +NO and C_2H_5O +NO, respectively.

3.4 Characterization of the instrument

This section reports experimental and modelling results for the characterization of different aspects of the RO_xLIF instrument: (1) wall loss of HO_2 inside the conversion flow-tube, (2) dependences of the RO_2-to-HO_2 conversion chemistry on operating conditions, (3) sensitivity factors, and (4) figures of merit.

3.4.1 HO_2 Wall loss in the conversion flow-tube

The wall loss rate of HO_2 was measured by varying the length of the flow-tube at a constant sampling flow rate of 2.1 slpm and a flow-tube pressure of 28 torr. At the exit of the flow-tube a flow of 1.5 slpm was sampled into FAGE whose detection cell pressure was held at 2 torr using the conical nozzle. Under these conditions, the sampled gas changes from a supersonic to subsonic flow at a downstream distance from the nozzle of x_M (Heal et al., 1995). In this region, called expansion zone, the flow is moving faster than sound speed creating a separation between the added reagents and the sampled gases. However, after the distance x_M, the gases begin mixing. In this work, x_M was determined using Equation 3.13 (Heal et al. 1995) and was found to be 0.22 cm.

$$\frac{x_M}{d} = 0.67\left(\frac{P_0}{P_b}\right)^{\frac{1}{2}} \qquad (3.13)$$

Here, P_b is the background pressure (28 torr), P_0 the ambient pressure, and d the diameter of the pinhole. The supersonic regime zone occurs up to a distance of about 0.22 cm downstream of the pinhole, which is negligible compared to the total length of the flow tube. In the subsonic region, the residence time is determined assuming plug flow conditions. Calculated residence times are 0.6, 1.0 and 1.5 s for total flow-tube lengths of 25, 45 (25+20) and 65 (25+20+20) cm, respectively.

In these experiments, RO_xLIF was run in HO_x mode resulting in only HO_2 being sampled into the flow-tube because of added CO. The radical concentrations generated were 1×10^{10}-2×10^{10} cm^{-3} for a total air flow rate of 50 slpm at 18 and 43% RH (21±2°C), respectively. The HO_2 wall loss rate was determined using the same approach as for the PERCA reactors (section 3.9.3), assuming first order loss (Howard, 1979):

$$[S_{HOx}^{FT}(\mathrm{t})] = [S_{HOx}^{FT}(0\mathrm{s})]\exp\left(-\mathrm{k}_{\mathrm{w_{HO_2}}}\mathrm{t}\right) \qquad (3.14)$$

Where $S_{HOx}^{FT}(0\mathrm{s})$ is the extrapolated initial signal, $\mathrm{k}_{\mathrm{w_{HO_2}}}$ is the HO_2 loss rate constanr in s^{-1}.

Three to five measurements were conducted for each residence time as shown in Figure 3.8. Normalizing the signals to $S_{HOx}^{FT}(0.\mathrm{s})$ and plotting the logarithm of the normalized signals versus the residence time yields an average (black symbols) kw_{HO2} of 1.11±0.08 (1σ) s^{-1} under the conditions mentioned above (28 torr, 43 & 18 % RH at 21 ± 2°C).

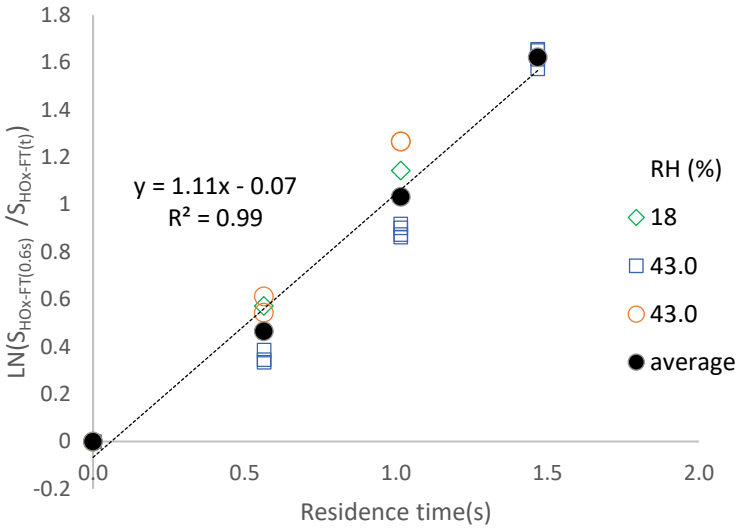

Figure 3.8 HO_2 wall loss in the conversion flow-tube. Slope of the linear fit yields the first order wall loss rate constant, kw_{HO2}.

The value of kw_{HO2} is similar at 18% and 43% RH, which is consistent with observations reported by Fuchs et al. (2008), i.e a wall loss that is independent of RH. However, the loss rate constant found in this work is approximately twice as high as the value published by Fuchs et al. (2008), who reported that k_w at 20 torr for HO_2, OH and RO_2 were 0.5, 5.4 and 0.15 s^{-1}, respectively. It was not possible to measure the OH wall loss rate in this work due to a total consumption of OH within 45 cm of tube length. Assuming that 99% of OH is lost over 45 cm (residence time of 1 s) provides a lower bound of 4.6 s^{-1} for the OH loss rate. While we were not able to accurately determine the OH wall loss rate, this is not an issue to model the RO_2 conversion chemistry in the flow-tube since Fuchs et al. (2008) showed that the contribution of OH losses to the total loss of the radical pool inside the flow-tube was less than 2% due to RO_x partitioning favoring HO_2 (high concentration of CO). It was shown that the loss of HO_2 radicals is the dominant process that limits the transmission of radicals through the flow-tube. No experimental determinations of RO_2 wall loss rates were attempted either in this work or in Fuchs et al. (2008). In both studies, the RO_2 wall loss was estimated using a ratio of $\frac{K_{wRO_2}}{K_{wHO_2}} = 0.3$ reported by Mihele et al. (1999). However, as reported for the PERCA system using PFA tubing (1/4"-OD) (chapter 2, section 2.9.3), the measured loss rate for $CH_3CH_2O_2$ was 7 times lower than for HO_2 at 50 % RH and 23ºC. This large difference between wall losses was also observed by Mihele et al. (1999) who reported a CH_3O_2 wall loss rate that was 6 times lower than for HO_2 in PFA tubes (1/4"-OD) at 50% RH.

The loss rate of HO_2 determined experimentally was used together with a wall loss rate constant of OH (5.4 s^{-1}) (value reported by Fuchs et al.) and a wall loss rate for RO_2 of 0.35 s^{-1} (HO_2 loss rate measured in this work scaled by the ratio reported by Mihele et al.) to model the RO_2 conversion chemistry within the flow-tube.

3.4.2 Dependence of the RO_2-to-HO_2 conversion chemistry on operating conditions

3.4.2.1 Time scale of the RO_2-to-HO_2 conversion chemistry

The reaction time required to achieve optimum conversion of organic peroxy radicals within the flow-tube was first determined by modeling the conversion chemistry using operating conditions reported by Fuchs et al. (2008) for their RO_xLIF instrument. This optimum reaction time is defined as the residence time in the flow tube that will lead to a maximum HO_2 concentration which depends on its formation rate from the conversion of organic peroxy radicals and its loss rate due to homogeneous gas-phase and wall reactions.

Methyl peroxy radicals were chosen for these simulations for comparison with the work of Fuchs et al. (2008). In addition, simulations were also performed for other peroxy radicals (ethyl peroxy, pool of toluene-based peroxy, pool of isoprene-based peroxy) in order to evaluate whether different types of peroxy radicals exhibit different optimum reaction times for their conversion into HO_2.

For CH_3O_2, simulations were performed using different sets of operating conditions as shown in table 3.2. Three sets of conditions were used to (1) compare the model output to that observed by Fuchs et al. (2008) to ensure the reliability of the model results, (2) assess the impact of the higher loss rate of HO_2 quantified for our conversion flow-tube, and (3) determine the time scale expected under our operating conditions of pressure. All simulations were constrained with an initial CH_3O_2 concentration of 1.5×10^9 cm^{-3} at 50% RH and 25°C.

Table 3.2 Time scale of the RO_2 conversion chemistry - comparison of different sets of operating conditions

	Simulation 1	Simulation 2	Simulation 3
Wall loss rate (s^{-1})	Fuchs parameters HO_2: 0.15 RO_2: 0.15 OH: 5.4	This work ***HO_2: 1.11*** RO_2: 0.35 OH: 5.4	This work ***HO_2: 1.11*** RO_2: 0.35 OH: 5.4
Reagent concentrations	Fuchs parameters NO: 0.7 ppmv CO: 0.17%	Fuchs parameters NO: 0.7 ppmv CO: 0.17%	Fuchs parameters NO: 0.7 ppmv CO: 0.17%
Pressure (torr)	Fuchs parameters 20	Fuchs parameters 20	This work ***28***
$[CH_3O_2]$ cm^{-3}	1.5×10^9	1.5×10^9	1.5×10^9

Figure 3.9 reports the results from the 3 simulations. The remaining CH_3O_2 (left axis) and generated HO_2 (right axis) are normalized to the initial CH_3O_2 concentration ($[CH_3O_2]_0$). The first simulation (red) shows the conversion efficiency of CH_3O_2 into HO_2 using operating conditions published in Fuchs et al. (2008). CH_3O_2 is rapidly consumed with only 13% remaining at a reaction time of 0.6 s, which also corresponds to the maximum HO_2 abundance in the flow-tube (62% of initial CH_3O_2). These results are in good agreement with that observed by Fuchs et al., validating the modeling procedure used in this work.

The second simulation (black) shows that the larger wall loss rate of HO_2 observed in this work leads to a similar decay for CH_3O_2 with only 11% remaining at a reaction time of 0.6 s but also leads to a decrease of the maximum HO_2 abundance (50% of initial CH_3O_2) at a shorter reaction time of 0.4 s. The third simulation (dark blue) differs from the previous one by increasing the pressure inside the flow-tube from 20 to 28 torr. As shown in this simulation, increasing the pressure will speed-up the conversion of CH_3O_2 into HO_2 since the absolute concentration of NO is higher, which in turn increases the maximum HO_2 abundance to a value of 60% at 0.3 s. The maximum increase in HO_2 due to RO_2 conversion inside the flow-tube appears to be partly driven by the type of material which it is constructed (affecting wall loss of radicals), with a higher wall

loss rate of HO_2 leading to a lower maximuim concentration. However, increasing the pressure to speed-up the RO_2 conversion allows reducing the amount of HO_2 lost on the wall, which in turn produces a higher HO_2 concentration. Reagent gas concentrations are of course other important operating conditions driving the conversion chemistry which will be discussed in the next 2 sections.

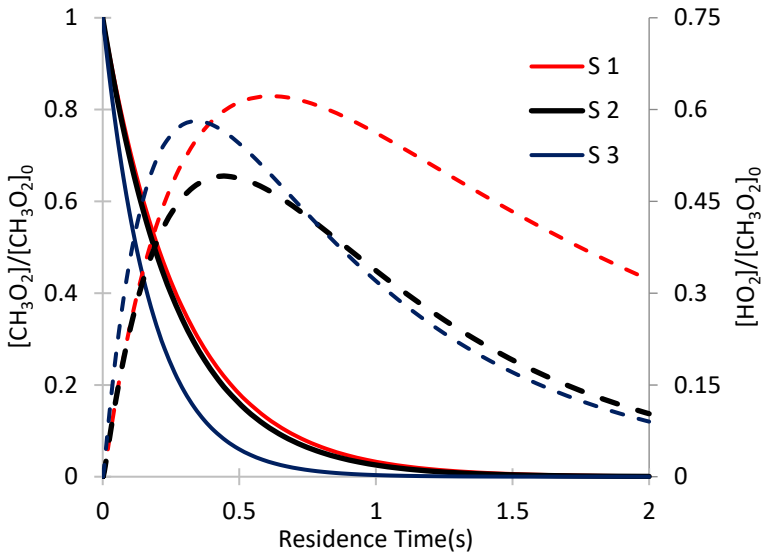

Figure 3.9 Concentrations of CH_3O_2 (left axis, solid lines) and HO_2 (right axis, dashed lines) normalized to the initial CH_3O_2 amount.

Sensitivity tests were performed to assess whether changing the loss rate of OH or CH_3O_2 in these simulations would significantly affect the conversion timing or the generated HO_2 concentration. Table 3 and Figure 3.10 show how the CH_3O_2 and OH loss rates were varied, from 0.35 s^{-1} (CH_3O_2) and 5.4 s^{-1} (OH) in S3 to 0.7 s^{-1} (CH_3O_2) in S4 and 11 s^{-1} (OH) in S5, and how the HO_2 concentration responded to these changes. An increase of the OH and CH_3O_2 wall loss rates by a factor of 2 does not lead to a significant change in the CH_3O_2 and the HO_2 abundances. In addition, the initial concentration of CH_3O_2 was reduced by a factor of 10 (S7) showing that these simulations are not dependent on the initial peroxy radical concentration (negligible impact of self- and cross-radical reactions in the flow-tube).

Table 3.3 Time scale of the RO_2 conversion chemistry – Impact of OH and RO_2 wall loss rates

	Simulation 3	Simulation 4	Simulation 5	Simulation 6
Wall loss rate (s^{-1})	HO_2: 1.11 RO_2: 0.35 OH: 5.4	HO_2:1.11 ***RO_2: 0.7*** OH: 5.4	HO_2:1.11 RO_2: 0.35 ***OH: 11***	HO_2:1.11 RO_2: 0.35 OH: 5.4
Reagent concentrations	NO: 0.7 ppm CO: 0.17%	NO: 0.7 ppm CO: 0.17%	NO: 0.7 ppm CO: 0.17%	NO: 0.7 ppm CO: 0.17%
Pressure (torr)	28	28	28	28
$[CH_3O_2]$ cm^{-3}	1.5×10^9	1.5×10^9	1.5×10^9	***1.5×10^8***

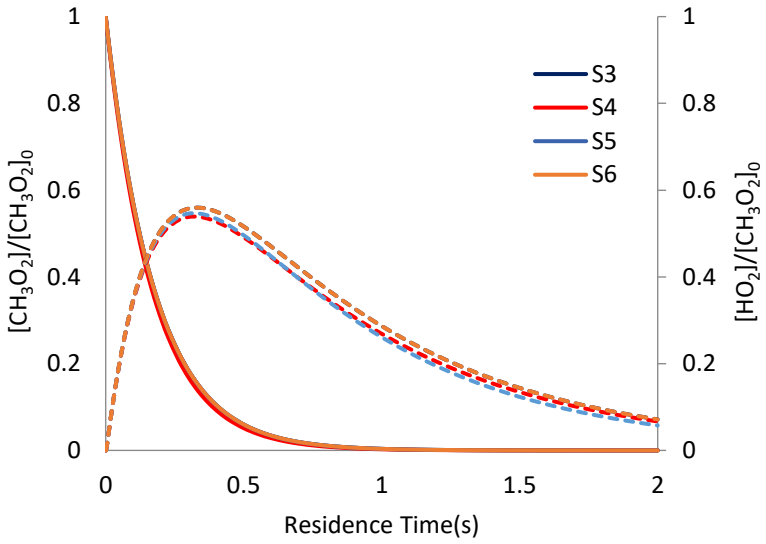

Figure 3.10 Time scale of the CH_3O_2 conversion chemistry. Left axis is for CH_3O_2 (Solid lines) and right axis for HO_2 (dashed lines).

Finally, the conversion chemistry of different RO_2 radicals (ethyl peroxy, pool of toluene-based peroxy, pool of isoprene-based peroxy) was modelled for comparison to S3 (CH_3O_2) in order to assess whether similar concentrations of HO_2 would be produced at the same residence time in the flow tube. These simulations are important to determine whether RO_xLIF exhibits similar

sensitivities to different peroxy radicals. The simulations performed for the different RO_2 species metionned above using operating conditions reported in Table 3.3 for S3 are shown in figure 3.11. It is clear that differences between these simulations are small, with the ethyl peroxy radical exhibiting a faster decay and leading to a higher abundance of HO_2 (60% of initial RO_2). In contrast, the isoprene-based peroxy radicals exhibit both the slowest decay and the lowest abundance of HO_2 (50%). These simulations indicate that the differences in RO_2 decay rates and HO_2 abundances are within 10% and the timings for HO_2 production are similar.

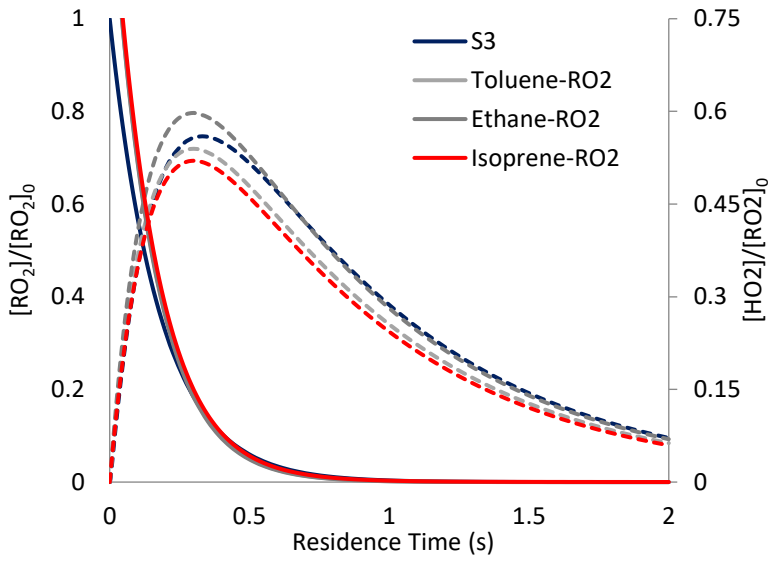

Figure 3.11 Time scale of different RO_2 conversion chemistries. Left axis is for RO_2 (Solid lines) and right axis for HO_2 (dashed lines).

3.4.2.2 Dependence of the RO_2 conversion chemistry on NO

The optimal conversion of RO_2 into HO_2 also depends on the concentrations of both NO and CO reagents. Radical loss rates and pressure used for S3 (Table 3.3) were used to perform additional simulations for the CH_3O_2 conversion chemistry by varying NO while keeping CO constant.

Figure 3.12 shows how the normalized concentrations of CH_3O_2 (left axis) and HO_2 (right axis) evolve over time when NO is varied in the range 0-1.2 ppmv at a CO mixing ratio of 0.17%.

The increase of NO leads to a simultaneous increase in the decay rate of CH_3O_2 and maximum abundance of HO_2, together with a reduction of the reaction time needed to reach the maximum HO_2 abundance. The HO_2 build-up due to RO_2 conversion (dotted lines) increases up to 65% at the highest NO mixing ratio of 1.2 ppmv, with only 5% of CH_3O_2 remaining in the flow-tube. These conditions also lead to the fastest conversion of CH_3O_2 at an optimum residence time of approximately 0.3 s for the detection of HO_2. Since the maximum abundance of HO_2 keeps increasing when NO is increased, these simulations indicate that losses due to radical+NO reactions are less important than the HO_2 wall loss. It is interesting to note that detecting HO_2 at a longer flow-tube residence time than this optimum reaction time, for instance 1 s, would lead to an increase of the fluorescence signal up to 0.5 ppmv NO and a decrease from 0.5 to 1.2 ppmv while a monotonous increase of the signal would be observed over the entire range of NO amounts studied at a shorter residence time of 0.2-0.5 s.

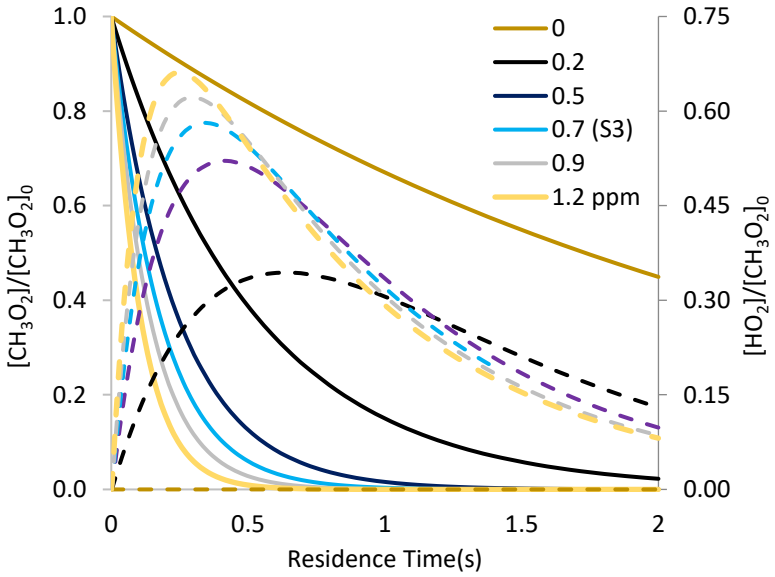

Figure 3.12 Simulations of the CH_3O_2 conversion chemistry – NO dependence. Left axis is for RO_2 (solid lines) and right axis for HO_2 (dashed lines). The NO mixing ratio is indicated in the legend.

Laboratory experiments were conducted to investigate this NO-dependency by generating equimolar concentrations of $C_2H_5O_2$ and HO_2 in the calibrator. This radical source was operated at an air flow rate of 50 slpm and 50% RH (21°C). Ethane (C_2H_6) was added in the calibrator to react 99% of OH in less than 10 ms. This compound was chosen instead of methane due to its higher

reactivity with OH (approx. a factor of 40), which allowed introducing less ethane in the calibrator compared to methane. Both HO_2 and $C_2H_5O_2$ were generated at a concentration of 2×10^{10} cm^{-3}. The reactor length of 45 cm was used, leading to a residence time of 1.0 s. NO (500 ppm in Nitrogen) was varied from 0-2.4 ppm while keeping CO (10% in Nitrogen) at a mixing ratio of 0.47% (see following section for the chosen CO mixing ratio).

As seen in figure 3.13, the net OH fluorescence signal normalized to the laser power starts increasing with NO from 310 cps mW^{-1} up to 510 cps mW^{-1} at approximately 0.8-0.9 ppmv of NO. There is signal detected when no NO is added to the flow-tube due to the HO_2 radicals generated in the calibrator. When NO is increased up to 0.9 ppmv, the propagation rate of RO_2 to HO_2 increases leading to greater fluorescence signal. In contrast, once NO exceeds 0.9 ppmv, the signal begins to decrease as most CH_3O_2 has been converted and only HO_2 losses take place in the flow tube.

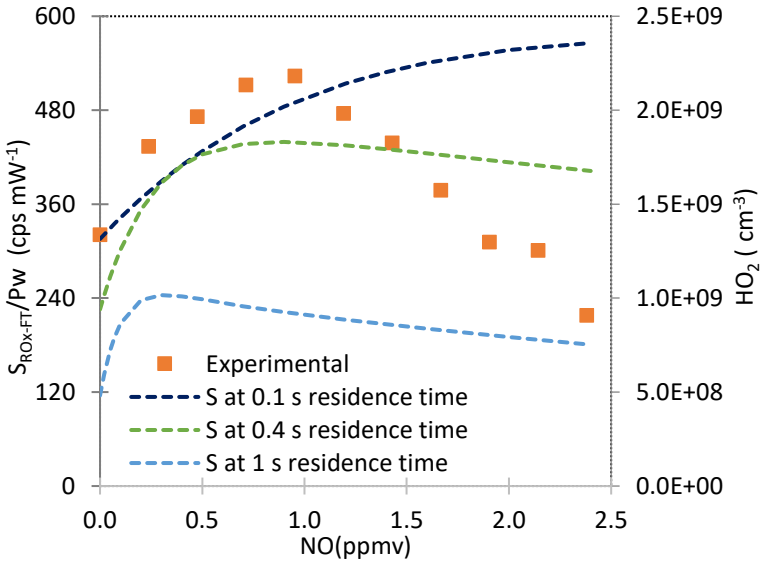

Figure 3.13 Dependence of the $C_2H_5O_2$ conversion chemistry on NO.

These experimental results are compared to modeled trends (dashed lines) as shown in Figure 3.13. The model was constrained by operating conditions used above, i.e. 0-0.8 ppmv NO, 0.47% CO, a pressure of 28 Torr, 47% RH at 21°C, and the generated radical concentrations. The residence times were set at 0.1 s (dark blue), 0.4 s (green) and 1 s (blue) for comparison to the experimental trend. As shown in Figure 3.13, the simulations constrained at residence times of 0.1 or 0.4 s reveals a better agreement with the experimental trend observed for the fluorescence signal

when NO ranges up to 1 ppm. The simulation performed for 1-s of residence time cannot reproduce the relative change observed in the fluorescence signal. In addition , a large discrepancy is observed between the relative change in the fluorescence signal and all the simulated trends in HO_2 when NO keeps increasing above 1 ppm. In the literature, Fuchs et al. (2008) showed a good agreement between their model simulations and experiments for CH_3O_2 at NO mixing ratios lower than 1 ppm, which was the highest mixing ratio used in their study.

3.4.2.3 Dependence of the RO_2 conversion chemistry on CO

Similarly, additional simulations were performed to investigate how the CH_3O_2 conversion chemistry responds to CO when NO is kept constant.

Figure 3.10 shows how the normalized concentrations of CH_3O_2 (left axis) and HO_2 (right axis) evolve over time when CO is varied from 0-1 % at a NO mixing ratio of 0.7 ppmv. As expected, the decay rate of CH_3O_2 is independent of the increase in CO since it only depends on the CH_3O_2 + NO reaction. However, the abundance of HO_2 strongly depends on the presence of CO. The HO_2 abundance due to RO_2 conversion (dotted lines) builds up when CO is increased up to 0.17% and reaches approximately 60% at 0.4 s of reaction time. When CO keeps increasing, the HO_2 abundance stays constant up to 1% CO. At low CO mixing ratios, the loss of OH on the wall decomes important and leads to the low abundance of HO_2. However, when CO increases, the HO_2 abundance also increases due to the fast conversion of OH into HO_2 and the lower wall loss rate of HO_2 compared to OH.

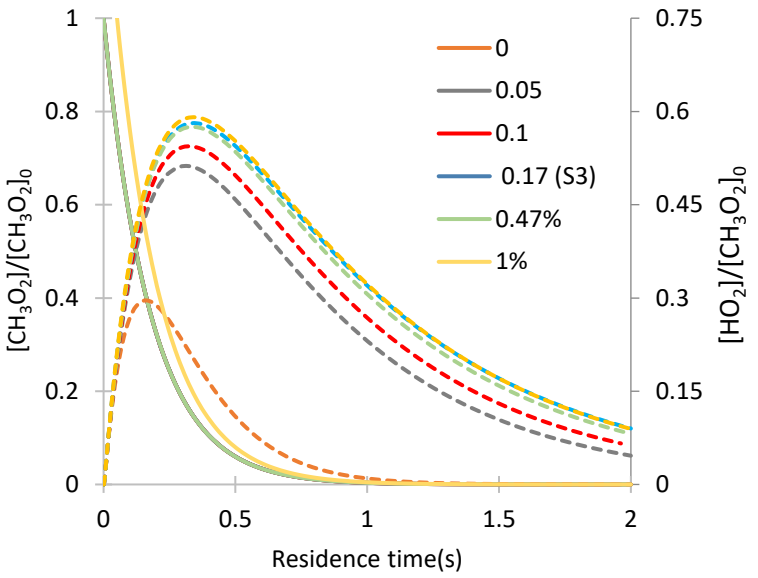

Figure 3.14 Simulations of the CH_3O_2 conversion chemistry – CO dependence. Left axis is for CH_3O_2 (solid lines) and right axis for HO_2 (dashed lines). CO mixing ratios are indicated in the legend.

Laboratory experiments were also performed to investigate the dependence of the fluorescence signal on CO while keeping NO constant. These experiments were performed under the same operating conditions as above for the NO dependence, with CO being varied from 0-1% and NO kept at 0.8 ppmv. Ethane was also added in the calibrator to generate $C_2H_5O_2$ and HO_2. The measured OH fluorescence signal and its dependence on CO are shown in figure 3.15. The net signal normalized to the laser power starts increasing with CO from 250 cps mW^{-1} and reaches a maximum value of 450 cps mW^{-1} at a CO mixing ratio of approximately 0.2%. In contrast to NO, the CO addition is not necessary to convert $C_2H_5O_2$ into HO_2. CO is rather added to reduce radical losses on the wall. When CO is added, a cycle of reactions that interconvert HO_2 and OH between each other is initiated with a partitioning shifted towards HO_2. Since HO_2 exhibits a lower wall loss rate than OH, the abundance of the radicals increases in the flow tube. The change in signal observed between 0.2-0.5% of CO is small, indicating that the conversion chemistry is almost insensitive to the CO mixing ratio above a threshold value of 0.2%. This corresponds to a HO_2-to-OH ratio of approximately 100 at 1 s residence time in the model, which is sufficient to avoid a significant loss of OH on the reactor walls.

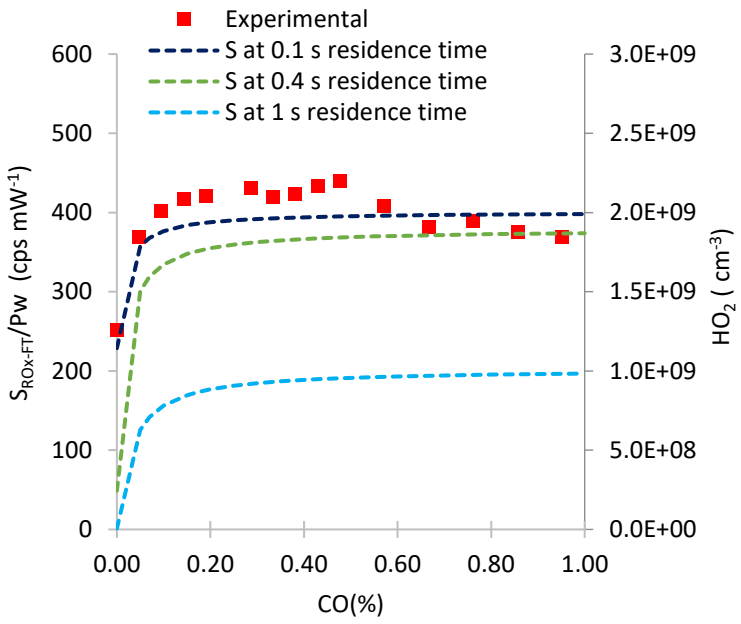

Figure 3.15 Experimental and modeled dependences of the $C_2H_5O_2$ conversion chemistry on CO

For comparison to the experimental observations reported in Figure 3.15, model simulations were also performed at 3 different residence times of 0.1, 0.4 and 1 s with $C_2H_5O_2$ and HO_2 constrained to the generated concentrations. These simulations seems to indicate that a better agreement is observed between the relative changes in the fluorescence signal and simulated HO_2 concentrations when a residence time of 0.1 s is considered, similar to that observed for the NO-dependence. It seems likely that the flow tube residence time is much shorter than calculated from plug-flow conditions and is between 0.1 and 0.4 s.

3.4.2.4 Dependence of the RO_2 conversion chemistry on pressure

Simulations related to the dependence of the CH_3O_2 conversion chemistry on the total pressure are shown in Figure 3.16. The model is constrained by keeping the reagent gases NO and CO at optimum concentrations, i.e. 6.2×10^{11} molecule cm^{-3} of NO (0.8 ppm at 28 Torr) and 1.5×10^{15} molecule cm^{-3} of CO (0.17% at 28 Torr), respectively. The initial concentration of CH_3O_2 was set at 1.5×10^{9} cm^{-3} at 50% RH and 25°C. Wall loss rates of 5.4, 1.11 and 0.35 s^{-1} were used for OH, HO_2 and CH_3O_2, respectively. Figure 3.16 shows how the normalized concentrations of

CH_3O_2 (left axis) and HO_2 (right axis) evolve over time when the flow-tube pressure is adjusted to 10, 28 and 50 Torr. The conversion efficiency of CH_3O_2 into HO_2 is almost independent of pressure.

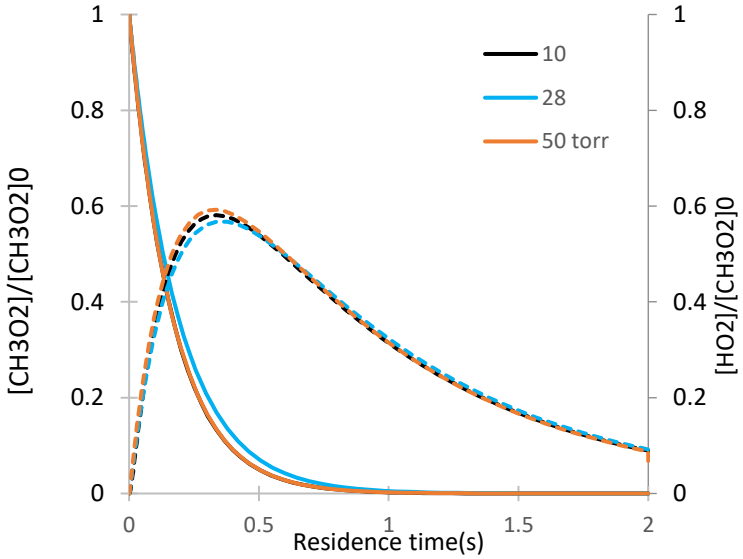

Figure 3.16 Model simulations of the CH_3O_2 conversion chemistry – Pressure dependence. The black, blue and orange curves correspond to pressures of 10, 28 and 50 torr, respectively.

3.4.2.5 Conclusions on operating conditions

Operating conditions used on the RO_xLIF setup built at Indiana University and details about its design are summarized in Table 3.4. Simulations performed for different types of RO_2 radicals (CH_3O_2, $C_2H_5O_2$, toluene-based RO_2, isoprene-based RO_2) indicate that these RO_2 radicals should exhibit the same conversion efficiency within 10% under the conditions reported in Table3.4.

These operating conditions will lead to a detection efficiency of RO_2 of approximately 30% at a residence time of 1 s (calculated from plug flow considerations). However, comparing experimental observations of the fluorescence signal when both NO and CO are varied independently to model simulations seems to indicate that the residence time in the flow-tube is shorter than 1 s by at least a factor of 2. If the residence time is lower than 0.5 s, the detection

efficiency of RO_2 will be in the range 40-60%. In addition to the HO_2 produced from RO_2 conversion, it is calculated that 20% of the sampled HO_2 radicals will also be transferred to FAGE based on the measured wall loss rate of HO_2.

Table 3.4 Characteristics of the IU-ROx-LIF instrument.

	Parameter	value
Conversion flow tube	Inlet nozzle orifice	Flat shaped, 0.635 mm
	Length × diameter	45 × 5.1 cm
	Sample flow rate	2.1 slpm
	Pressure	28 torr
	Flow residence time	1 s (45 cm long flow-tube)
	Reagent mixing ratio	0.8 ppmv NO, 0.4% CO
Fluorescence cell	Transfer nozzle orifice	Conical shaped, 2 mm
	Sample flow rate	1.5 slpm
	Pressure	2 torr
	Reagent mixing ratio	5.7 ppmv NO

3.4.3 Calibration of $\mathbf{C_{OH}}$ and $\mathbf{C_{HO_2}}$ (FAGE)

When the conversion flow-tube was decoupled from FAGE to perform the calibrations, the conical nozzle was not changed for a smaller diameter nozzle and as a consequence, both the sampling flow rate and the detection cell pressure increased. The sampling flow rate increased from 1.5 to 2.7 SLPM and the pressure from 2.0 to 3.6 Torr. The flow rate of NO (Matheson, 1% in Nitrogen) was kept at 0.85 SCCM for these 2 configurations. It is important to note that the impact of the change in pressure on both the NO concentration and the residence time (sampling orifice-to-OH detection axis) was counterbalanced by the change in sampling flow rate. For both configurations, RO_xLIF (P=2 Torr, sampling flow rate=1.5 SLPM) and FAGE (P=3.6 Torr,

sampling flow rate=2.7 SLPM), the NO concentration was 3.6×10^{11} molecule cm^{-3} and the residence times were similar due to the adjustment of the volumetric flow rate on the pressure. We therefore consider that the conversion efficiency of HO_2 into OH is not impacted and potential interferences on HO_2 measurements from the conversion of RO_2 radicals should be similar. In addition, the FAGE sensitivity towards OH and HO_2 is expected to be similar between the 2 configurations since the loss in OH fluorescence due to an increase of the quenching rate when the pressure is higher is counterbalanced by the gain in OH density (see Figures 6 and 7 in Faloona et al., 2004). Faloona et al. showed that between 2.0 Torr (2.7 hPa) and 3.6 Torr (4.8 hPa) the modelled sensitivity of their FAGE instrument (same design than IU-FAGE) are similar and the measured sensitivity factors towards OH and HO_2 were similar (within 10-20%) between the 2 pressures.

The radical source described in section 3.2.3.1 was used to calibrate the FAGE response to both OH and HO_2. For HO_2 calibrations, a flow of CO (36 sccm, 10% in nitrogen) was added in the calibrator to titrate all OH radicals into HO_2. The addition of NO in the FAGE detection cell led to a mixing ratio of 31.5 ppm (3.6×10^{11} molecule cm^{-3} at 2.0 Torr) when calibrating the HO_2 response. The sensitivity factors for OH and HO_2 were determined from the net OH fluorescence signal detected during the calibration experiments using Equations 3.8 and 3.9, respectively. The radical source was operated at an air flow rate of 50 slpm and RH was varied from 10-60% (22±2°C). The concentration of OH and HO_2 radicals inside the calibrator was varied between 2×10^{9} and 2×10^{10} cm^{-3}.

Water vapor is known to be a more efficient quencher of excited OH radicals than N_2 or O_2 (Bailey et al., 1997). As a result, the FAGE sensitivity towards both OH and HO_2 decreases as the concentration of water increases. Figure 3.17 displays the measured sensitivity factors C_{OH} (blue markers) and C_{HO_2} (red markers) and their water dependence. The intercept of the regression line with the y-axis (water mixing ratio of 0%) corresponds to the sensitivity under dry conditions. The measured sensitivity factors for OH and HO_2 were 4.7×10^{-7} and 3.4×10^{-8} cps cm^3 mW^{-1} under dry conditions, respectively. The observed water dependence for both OH and HO_2 (slope of the regression lines normalized to the dry sensitivity) are similar since it is only due to the quenching of the excited OH radicals. This water dependence corresponds to a loss of approximately 27% of the fluorescence signal per percent of water for IU-FAGE.

The OH sensitivity determined in this study is relatively close to what was previously determined in Dusanter et al. (2008) for IU-FAGE, c.a. values of (7.2-9.1) $\times 10^{-7}$ cps cm^3 mW^{-1}. In contrast, the HO_2 sensitivity is lower than values reported in Dusanter et.al (2008), c.a. (6.8-8.6) $\times 10^{-7}$ cps cm^3 mW^{-1}, due to the use of a low NO concentration herein, leading to a lower conversion of HO_2 in the FAGE nozzle before OH detection. The conversion efficiency, f_{HO_2}, was computed from Eq. 3.4 using several calibration experiments including the one shown in Fig. 3.16 and was found to be 13.8%. In Dusanter et al. (2008), a conversion efficiency close to 100% was observed from the use of a larger NO concentration. Measurements of f_{HO_2} at different sampling flow rates, pressures and NO concentrations have been reported for IU-FAGE in Lew et al. (2018). A maximum conversion of 67% was reported at a NO concentration of 2.9×10^{13} cm^{-3}, a sampling flow rate of 3.4 slpm, and 4.2 torr of pressure.

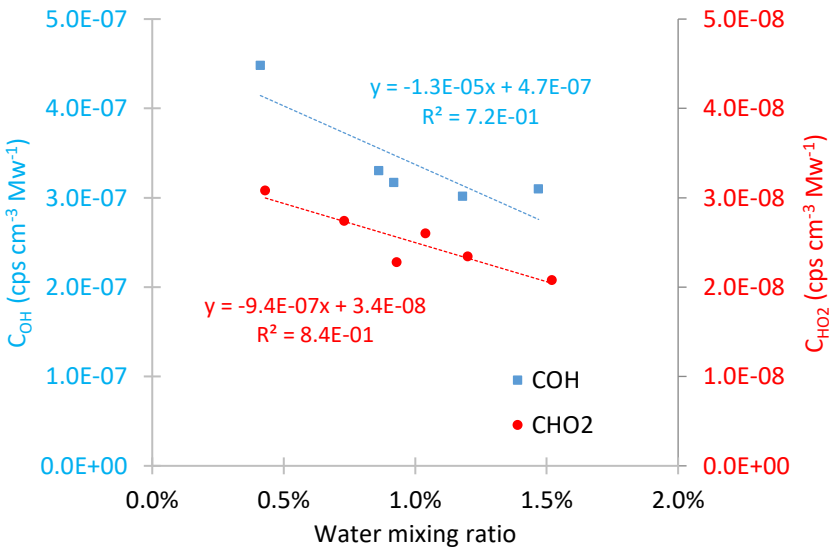

Figure 3.17: FAGE OH (blue markers) & HO_2 (red markers) sensitivity factors as a function of water mixing ratios.

In this study, a low NO concentration is used for HO_2 measurements in order to minimize the interference from RO_2 radicals (chapter 1, section 1.3.1). As mentioned previously, several laboratory studies have shown that HO_2 measurements by FAGE are prone to interferences associated with RO_2 radicals, especially from the rapid decomposition of β-hydroxyalkoxy radicals and the rapid reaction of the resulting β-hydroxyalkyl radicals with O2 (Fuchs et al., 2011; Lew et

al., 2018; Whalley et al., 2013). Fuchs et al. (2011) reported that the RO_2 conversion can be suppressed at low NO, and Whalley et al. (Whalley et al., 2013) highlighted that decreasing NO in the detection cell reduces the OH formation from RO_2 conversion faster than OH formation from HO_2 conversion, thus allowing to discriminate between HO_2 and interfering RO_2 if measurements are sequentially performed at 2 different NO flows (low and high).

For the RO_xLIF technique, while the conversion of RO_2 into HO_2 is not an issue during the RO_x measurement mode, it is important to reduce this interference during the HO_x mode. Indeed, the conversion of RO_2 during this mode would lead to an underestimation of ambient RO_2 when the latter is calculated from the subtraction between the RO_x and HO_x measurements. Recently, Lew et al. (2018) have characterized this type of interferences for IU-FAGE and have reported it under different sets of operating conditions. It was shown that up to 80% of isoprene-based RO_2 radicals and a similar fraction of other β-hydroxyalkoxy radicals can be converted to HO_2, while the conversion efficiency was lower for other types of RO_2 (e.g. 15% for propane-based RO_2 radicals).

In this study, we quantified the conversion efficiency of HO_2 into OH (f_{HO_2}) and of RO_2 into HO_2 ($f_{RO2\rightarrow HO2}$) and OH ($f_{RO2\rightarrow OH}$) using the methodology described in Lew et al. (2018) for CH_3O_2, isoprene-based and β-pinene-based peroxy radicals. The last two types of peroxy radicals are expected to be amongst the species which will exhibit the highest interference on FAGE. For these experiments, methane, isoprene and β-pinene were added to the radical calibrator. The results are reported in Table 3.5. Under the low NO conditions, the conversion of RO_2 into HO_2 is less than 1% for CH_3O_2 and less than 31% for isoprene-based and β-pinene-based peroxy radicals. From the $f_{RO2\rightarrow HO2}$ value of 31% (highest conversion efficiency observed for β-hydroxyalkoxy radicals), the assumption that the pool of ambient peroxy radical is composed of HO_2 (50%), CH_3O_2 (25%) and β-hydroxy alkoxy radicals (25%), it is estimated that ambient RO_2 would be underestimated by approximately 15% with this instrument.

Table 3.5 conversion of organic peroxy radicals into HO_x in the FAGE detection cell.

RO_2	f_{HO2} (%)	$f_{RO2\rightarrow HO2}$ (%)	$f_{RO2\rightarrow OH}$ (%)
	13.8±1.2(1σ)		
Methyl peroxy		< 1	<0.1
β-pinene-based		25.4	3.6
Isoprene-based		31.2	4.4

3.4.4 Calibration of $C_{HO_2}^{FT}$ and $C_{RO_2}^{FT}$ (ROxLIF)

For these calibrations, CO (30% in Nitrogen, Matheson Inc) or methane (25% methane in Argon, Matheson Inc) were added in the calibrator to generate either HO_2 or an equimolar mixture of HO_2 and CH_3O_2, respectively. Methane and CO concentrations were adjusted to ensure the consumption of approximately 99% of OH in less than 10 ms. RH was varied from 15-65% (25±2°C) leading to the production of both HO_2 and CH_3O_2 in the concentration range of 6×10^9 - 2×10^{10} cm^{-3}.

Figure 3.18 displays fluorescence signals recorded during a calibration experiment, methane being added in the calibrator, and switching between HO_x (blue and grey) and RO_x (orange) modes. The on-resonance signal in RO_x mode is approximately twice as high as in the HO_x mode, showing the system's capability of detecting CH_3O_2 radicals. Indeed, an increase of the signal in the RO_x model compared to the HO_x mode arises from the conversion of CH_3O_2 into HO_2.

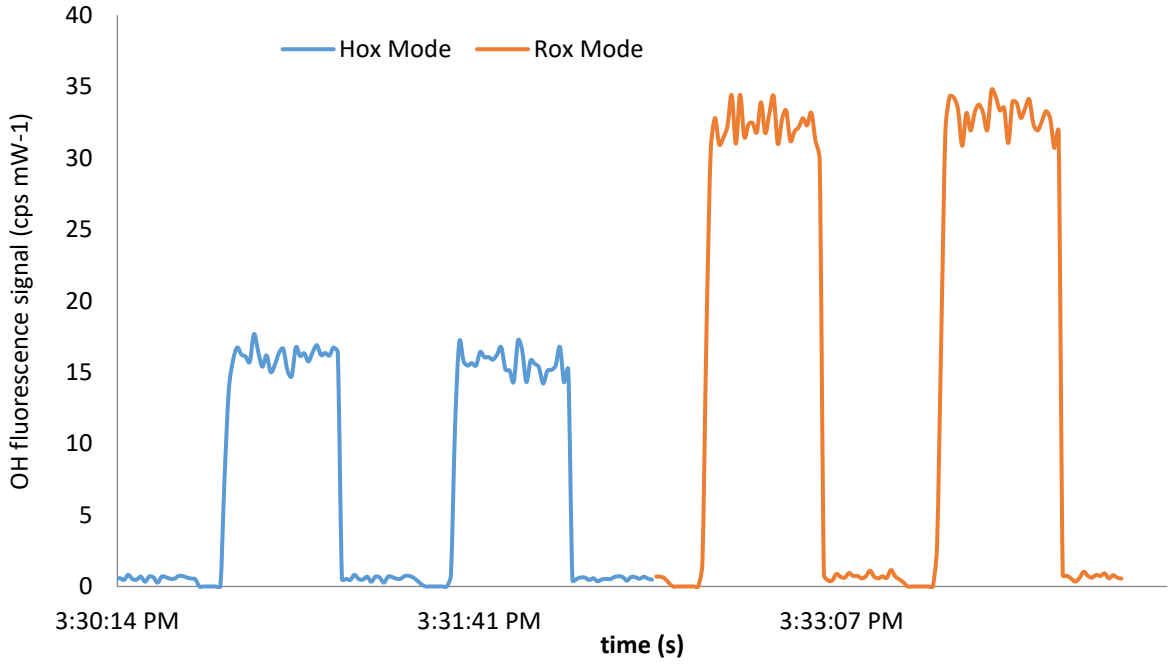

Figure 3.18 Calibration of the RO_xLIF sensitivity towards CH_3O_2 and HO_2 radicals – Switch between HO_x and RO_x modes (raw data). $[HO_2] = [CH_3O_2] = 3\times10^9$ cm^{-3}, RH = 48±2%, T = 22±2°C, 45-cm long flow-tube.

The sensitivity factors for HO_2 and RO_2 were determined at two different residence times by changing the length of the flow-tube, ca. 0.6 s (25 cm long flow-tube) and 1 s (45 cm long flow-tube). The sensitivity towards HO_2 was measured during the HO_x mode by adding CO to the calibrator and a sensitivity coefficient was calculated at the different residence times using Eq.3.10. For CH_3O_2, CO was replaced by methane in the calibrator and the sensitivity was calculated for the RO_x signal using Eq. 3.12.

The calibrated sensitivity factors, $C_{HO_2}^{FT}$ and $C_{CH_3O_2}^{FT}$, are displayed in Fig. 3.19 shows the trends as a function of humidity (water mixing ratio). Similarly to FAGE calibrations, the y-intercepts of the regression lines correspond to the sensitivity factors under dry conditions. The sensitivity for HO_2 and CH_3O_2 under dry conditions are 5.7×10^{-9} cps cm^{-3} mW^{-1} and 7.2×10^{-9} cps cm^{-3} mW^{-1}, respectively. Interestingly, the HO_2 sensitivity is lower by 26 % compared to CH_3O_2. The larger CH_3O_2 sensitivity is consistent with observations reported in Fuchs et al. (2018), with values of 1.44×10^{-7} and 1.2×10^{-7} cps cm^{-3} mW^{-1} for the sensitivity of CH_3O_2 and HO_2, respectively.

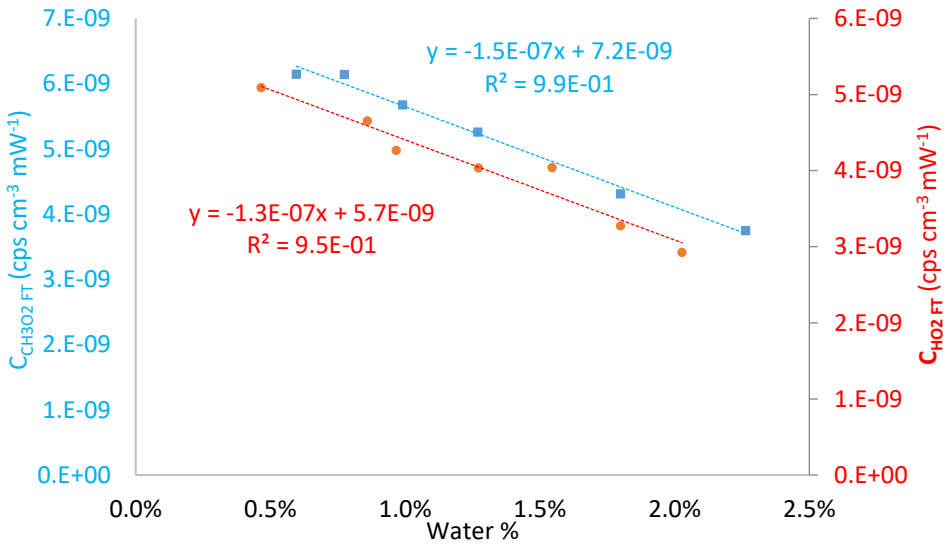

Figure 3.19 RO_xLIF CH_3O_2 (blue markers) & HO_2 (red markers) sensitivity factors as a function of water mixing ratios. Flow-tube length of 45-cm.

The sensitivity factors for the RO_xLIF instrument are dependent on water vapor, similarly to that discussed above for FAGE since the same fluorescence technique is used to detect OH. Figure 3.19 displays the trends observed for $C_{HO_2}^{FT}$ *and* $C_{CH_3O_2}^{FT}$ when the humidity is varied. A close

inspection of this figure shows that the RO_xLIF sensitivity decreases by 23 and 21% per % of water for HO_2 and RO_2, respectively. This water dependence is slightly lower than that observed for the FAGE response to OH and HO_2 (approx. 27%).

Table3.6 reports sensitivity factors measured at different residence times in the flow tube and under dry conditions. It is clear from this table that both $C_{HO_2}^{FT}$ *and* $C_{CH_3O_2}^{FT}$ decrease when the residence time is increased from 0.55 to 1 s. This trend was further investigated below using the F0AM model.

Table 3.6 Experimental sensitivity factors for CH_3O_2 and HO_2 at different residence times.

	Residence Time(s)	HO_2 (HO_x mode)	CH_3O_2 (RO_x mode)
Experimental Sensitivity (cps cm^{-3} mW^{-1})	0	3.70×10^{-8}	0
	0.55	1.45×10^{-8}	2.4×10^{-8}
	1	5.7×10^{-9}	7.2×10^{-9}

Simulations constrained by the initial concentrations of HO_2 in the HO_x mode and RO_2 in the RO_x mode conditions were performed for comparison with the measured sensitivity factors. Here we compare the relative changes in sensitivity (normalizing the sensitivity factors to that observed without the conversion flow-tube for HO_2, i.e. 3.70×10^{-8} cps cm^{-3} mW^{-1}, and to that observed at 0.55 s of residence time for CH_3O_2, i.e. 2.4×10^{-8} cps cm^3 mW^{-1}) to the relative changes in modelled concentrations of HO_2 (normalized by the initial radical concentration for HO_2, and by the modelled HO_2 concentration at 0.5 s of residence time for CH_3O_2). Other operating conditions can be found in Table 3.2. The results are shown in Figures 3.20 and 3.21 for HO_2 and CH_3O_2, respectively, where 3 different HO_2 wall loss rates have been used: 1.1, 1.35 and 1.7 s^{-1}, corresponding to the experimental determination (see section 3.4), an upper bound of the experimental determination (+3σ, error on the determination) and adjusted to fit the relative change observed for $C_{HO_2}^{FT}$ in Figure 3.20.

The comparison shown in Figure 3.20 for HO_2 indicates that the previously measured HO_2 loss rate of 1.1 s^{-1} cannot explain the relative decrease in sensitivity observed in these experiments as

the residence time is increased. Using the upper bound value is also not sufficient and the wall loss rate must be increased to 1.7 s^{-1} to correctly describe the relative change in $C_{HO_2}^{FT}$. This behavior is not well understood and may indicate that the wall loss rate changed since it was measured in section 3.4. This particular aspect needs to be further investigated in future characterization tests of the ROxLIF apparatus.

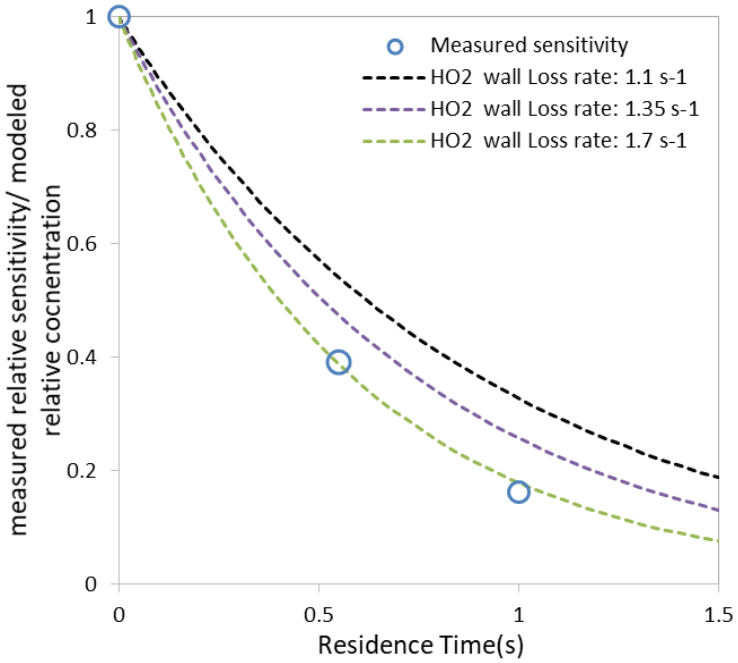

Figure 3.20 Experimental (markers) and modeled (dashed lines) dependences of $C_{HO_2}^{FT}$ on the flow-tube residence time.

Similar to HO_2, the relative change in the measured CH_3O_2 sensitivity for dry conditions is displayed in Figure 3.21 (left axis, blue symbol) and compared to 3 different simulations (right axis, dashed lines) with different HO_2 wall loss rates. The relative change in RO_2 sensitivity between 0.55 and 1.0 s of residence time seems to be better described by the simulation performed with a wall loss rate of 1.7 s^{-1}.

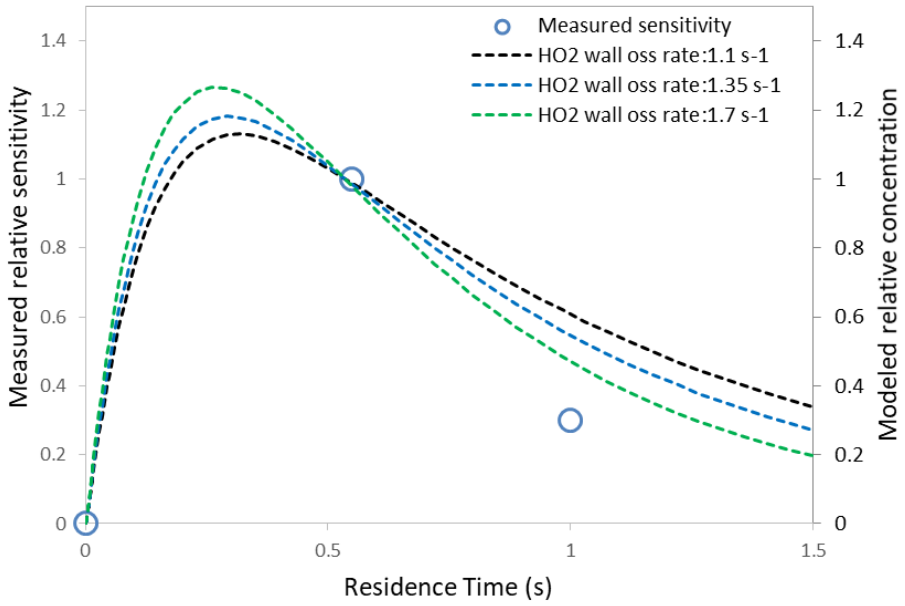

Figure 3.21 Experimental (markers) and modeled (dashed lines) dependences of $C_{CH_3O_2}^{FT}$ on the flow-tube residence time.

Finally, the sensitivity factors for different alkane-peroxy radicals ($C_2H_5O_2$ and $C_3H_7O_2$) have been measured adding ethane and propane in the calibrator and compared to the CH_3O_2 sensitivity at dry condition. The results reported in Table 3.7 indicate that the sensitivity for these different alkane peroxy radical is similar (within 10%). These experimental results are consistent with the model results discussed in section 3.4.2.1 indicating a similar conversion efficiency for different RO_2 radicals. However, the RO_2 radicals tested are all short chain species and additional work is needed to test other types of peroxy radicals such as those generated from the oxidation of alkenes, aromatics and oxygenated VOCs. Fuchs et al. (2008) and Whalley et al. (2013) have shown that their RO_xLIF instruments had the same sensitivity for differenet alkane peroxy radicals (within 10%). More generally, alkoxy radicals of large alkanes C>4 have the tendency to decompose or isomerize in competition to the reaction with O_2. Thus, large alkyl peroxy radicals may generally have a reduced detection sensitivity compared to CH_3O_2 (Atkinson et al., 1997a).

Table 3.7 Measured relative sensitivity of the ROxLIF instrument for different RO_2

Hydrocarbon	Peroxy radicals	Relative sensitivity $C_{RO_2}^{FT}/C_{CH_3O_2}^{FT}$	Absolute sensitivity (cps cm^3 mW^{-1})
Methane	CH_3O_2	1	7.2×10^{-9}
Ethane	$CH_3CH_2O_2$	0.86	6.17×10^{-9}
propane	$C_2H_5CH_2O_2$, $(CH_3)_2CHCH_2O_2$	1.03	7.40×10^{-9}

3.4.5 Conclusions about calibrations

The sensitivity of FAGE towards OH and HO_2 and RO_xLIF towards HO_2 and RO_2 have been determined using the water-photolysis technique as a calibrated source of OH, HO_2 and RO_2 radicals, RO_2 being generated through the addition of selected VOCs in the calibrator. The low NO concentration of 3.6×10^{11} cm^{-3} used in the FAGE detection cell reduced the RO_2-to-OH conversion to approximately 4% (upper limit for β-hydroxyperoxy radicals) and led to a reduction of the HO_2-to-OH conversion to 13.8%. The HO_2 sensitivity for RO_xLIF was found to be approximately 6 times lower than for FAGE due to significant losses of this radical in the conversion flow-tube. A counter-intuitive observation is that the RO_2 sensitivity for RO_xLIF is larger than that for HO_2 by approximately 26%, which is due to a lower loss of HO_2 molecules produced from RO_2 conversion due to their shorter residence time in the flow-tube.

For RO_xLIF, comparing the observed relative change in HO_2 sensitivity (from laboratory calibrations) and the relative change in HO_2 concentrations simulated by the model when the residence time in the flow tube is varied indicates that the wall loss rate of HO_2, which was measured experimentally before the calibration experiments, has to be increased from 1.1 to 1.7 s^{-1}. It is unclear whether the wall loss rate changed between these experiments and further work is needed to investigate this issue. Comparing the relative change in RO_2 sensitivity and in the HO_2 concentration produced from RO_2 conversion indicates reasonable agreement.

The sensitivity for 3 different RO_2 radicals generated from the OH reaction with methane, ethane and propane were similar within 10%. Additional work should be performed to investigate whether the sensitivity could significantly different for larger peroxy radicals exhibiting different chemical behavior.

3.4.6 Figures of merit under laboratory conditions

The RO_xLIF performances are characterized below using (1) detection limits for both HO_2 and the sum of RO_2 radicals and (2) the measurement accuracy. The detection limit is the lowest radial concentration required to generate a fluorescence signal that is larger than the precision observed in the off-resonance signal. LODs are defined for a given signal to noise ratio (SNR=1, 2, or 3):

$$LOD_{HO_2} = \frac{SNR \times \sigma_p}{C^{FT}_{HO_2} \times P_w} \quad (3.15)$$

$$LOD_{RO_2} = \frac{SNR \times \sigma_p}{C^{FT}_{RO_2} \times P_w} \quad (3.16)$$

Here σ_p is the standard deviation of the background signal integrated during t seconds at N samples/second (Dusanter et al., 2009a) (Eq. 3.17). In this equation, $\sigma_{off-resonance}$ is the standard deviation of the off-resonance signal follows Poisson statistics at the native time resolution (here 1 s).

$$\sigma_p = \frac{\sigma_{off-resonance}}{\sqrt{Nt}} \quad (3.17)$$

As seen from Eqs. 3.15-3.16, the LOD will depend on the instrument sensitivity for the targeted radical, the laser power inside the detection cell, and the scattering in the off-resonance signal due to laser power fluctuations, changes in Rayleigh and Mie scattering efficiency, and changes in solar scattered light (Dusanter et al., 2009a). For the FAGE technique based on photon counting, the off-resonance signal statistic follows a Poisson distribution and $\sigma_{off-resonance}$ can be calculated as the square root of the measured off-resonance signal ($\sigma_{off-resonance} = \sqrt{S_{off-resonance}}$) .

A 5-hours period of 1-s off-resonance signals measured in the laboratory is shown in Figure 3.22. Dry zero air was provided to the instrument. NO was continuously added in the detection cell for

HO_2 measurements and the laser power in the cell was 2 mW on average, similar to the laser power used during field measurements. The precision for the off-resonance signal (σ_p) is 0.2 cps for an integration time of 5 min. The measured sensitivity factors for HO_2 and RO_2 under dry conditions (Table 3.6) are 5.7×10^{-9} and 7.2×10^{-9} cps cm^{-3} mW^{-1}, respectively. Assuming a water mixing ratio of 1%, these sensitivity factors drop to 4.4×10^{-9} and 5.7×10^{-9} cps cm^{-3} mW^{-1} for HO_2 and RO_2, respectively. The limits of detection derived for HO_2 (Blue dashed line) and RO_2 (red dashed line) for 5-min measurements are shown in Figure 3.22. Average LOD values for both HO_2 and RO_2 are approximately 2×10^{7} cm^{-3} for a S/N of 1.

The measurement accuracy depends on the error associated with the UV photolysis of water vapor calibration and is estimated to be ±18% (1σ) (Dusanter et al., 2008).

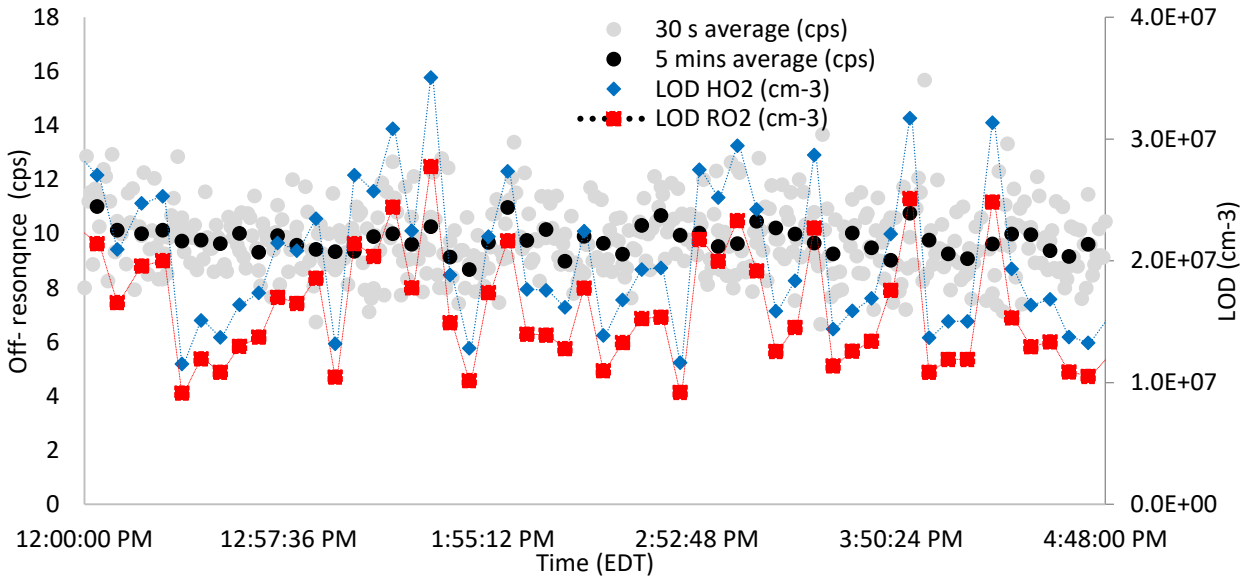

Figure 3.22 Limits of detection for HO_2 (Blue symbols) and RO_2 (red symbols) under laboratory conditions. The gray symbols represent 1 s measurements and black symbols 5 min average.

3.5 Deployment at the Indiana University Research and Teaching Preserve

The first ambient measurements of RO_2 and HO_2 with this instrument were held at the Griffy Woods Field Lab in Bloomington, Indiana (US), during the indoor Radical & Aerosol Chemistry

Experiment (iRACE) in collaboration with Purdue University during the months of July and August 2019. The objective of this field campaign was to investigate how indoor radical chemistry can lead to the formation of secondary organic aerosol (SOA).

For the RO_x-LIF instrument, the iRACE study was a good opportunity to perform field testing at this forested site including both outdoor and indoor measurements. In addition, the deployment of the RO_x-LIF instrument at this site allowed comparison with measurements during previous observations of radical species made at the same site during the 2015 IRRONIC campaign (Indiana Radical Reactivity and Ozone productioN InterComparison) (Kundu et al., 2019; Sklaveniti et al., 2018). This section only presents the ROx-LIF measurements to illustrate the capabilities of this new instrument. A thorough analysis of the field data is outside the scope of this manuscript and will be conducted later when all the measurements performed during iRACE are available.

3.5.1 Ambient (outdoor) campaign

3.5.1.1 Description of the field site and collocated measurements

Figure 3.23 shows the location of the measurement site (39.7908N, 86.502W), which is located 2.5 km east from the Bloomington University campus. This site was previously described by Kundu et al. (2019) and Sklaveniti et al. (2018) for the IRRONIC 2015 field campaign. The measurement infrastructure is part of the Indiana University Research and Teaching Preserve (IURTP) and is located at the interface between a mixed deciduous forest (sugar maple, sycamore, tulip polar, ash and hickory trees) and a moderately sized clearing. Deciduous trees are known to be strong emitters of isoprene (Kundu et al., 2019). The site is located about 1 km northeast of a road with moderate volume of traffic and can therefore be impacted by anthropogenic emissions.

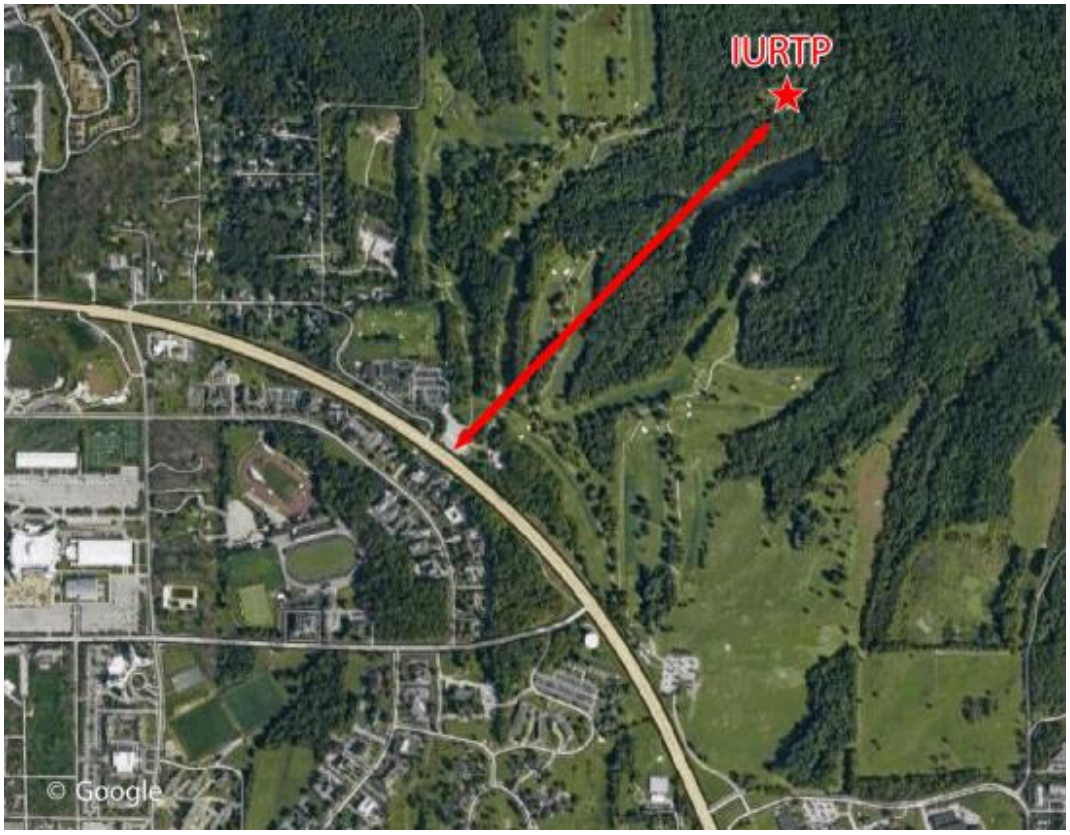

Figure 3.23 Map of the sampling site (Kundu et al., 2019). The star symbol represents the Indiana University Research and Teaching Preserve (IURTP). The arrow represents a distance of 1 km.

The RO_xLIF instrument was setup as described in section 3.2.1.1. Briefly, 2.1 slpm of ambient air was expanded into the conversion flow-tube (45-cm length). The reagent gas CO (80 sccm, 10% Matheson Inc) was added 2 cm downstream from the entrance of the flow tube for HO_2 measurements while CO and NO (3.5 sccm, 500 ppm, Indiana Oxygen) were added together for HO_2 + RO_2 measurements. The switch between the two measurement modes and the recording of the fluorescence signal was automated for this campaing through development with Labview software and the use of National instrument DAQ boards and solenoid valves. At the end of the conversion flow-tube, the air was split between FAGE equipped with the conical shaped nozzle and additional pumps. The measurement sequence was based on 5 minutes in the HO_x mode and 5 minutes in the RO_x mode. During each five minutes segment, several on/off-resonance modultations were performed to acquire the net OH fluorescence signal (on/off cycle of 0.5 minute, with 0.3 minute on-resonance and 0.2 min off-resonance). The laser power inside the FAGE

detection cell was 3 mW on average. Outdoor RO_xLIF measurements were performed from 17 to 24 July and indoor measurements from 2 to 5 August, while the entire campaign was conducted over the 2 month of July and August. The reason for the short of covering of RO_xLIF measurements during this campaign is that the FAGE detection cell had to be shared between OH and HO_2^* measurements (IU-FAGE configuration) and HO_2 and RO_2 measurements (RO_xLIF configuration). The RO_xLIF instrument was calibrated before, during and after the campaign by generating known concentrations of HO_2 and CH_3O_2 radicals (see calibration section for more details). However, calibrations performed before the campaign were invalidated due to technical issues (wrong position of the injector loop for CO and NO in the conversion flow-tube) and only calibrations performed during and after the campaign were used.

In addition to RO_xLIF, other measurements were performed during iRACE. This includes measurements of HONO (LP-LIF-FAGE, IU), total OH reactivity (TOHLM, IU), NO_x (Thermo 490 , IU), ozone (Teledyne 400 E, IU), water (LI-COR 6262, IU) and VOCs using a TD-GC/FID-FID (Markes Unity 2/Agilent 7890B, IU), a Proton Transfer Reaction-Mass Spectrometer (PTR-MS, IONICON 500, Purdue University) and off-line sampling on solid sorbent and DNPH cartridges (IMT Lille Douai). A few instruments were also deployed for particles, including an APS ans a SMPS (Purdue University.). Temperature and relative humidity were measured by the IU Met Station (NOVICK) and $J(NO_2)$ by a spectroradiometer. Information about instrumental limits of detection and time resolutions are given in Table 3.8.

Table 3.9 characteristics of the instruments used during iRACE by various institutions

	Institution	Technique/instrument	LOD, time resolution
NO & NO_2	Indiana University	Thermo 490C	50 ppt, 10 s
Ozone	Indiana University	Teledyne 400E	0.5 ppb, 10 s
HO_2 and RO_2	Indiana University	RO_xLIF	$(2\text{-}4)\times10^7$ cm^{-3} for HO_2 $(1.5\text{-}3)\times10^7$ cm^{-3} for RO_2 5 min, S/N=1
HONO, OH & HO_2	Indiana University	LP LIF-FAGE	Data not available yet
Offline cartridges	IMT Lille Douai	DNPH, solid sorbent	Data not available yet
Water mixing ratio	Indiana University	LI-COR 6262	
T & RH	IU Met station	NOVICK	
PTRMS	IU Purdue	IONICON 500	Data not available yet
APS, SMPS	IU Purdue		Data not available yet
TD-GC/FID-FID	Indiana University	Agilent 7890B	Data not available yet
OH reactivity	Indiana University	IU-TOHLM	Data not available yet
JNO_2		Spectroradiometer	

3.5.1.2 Description of ambient air masses

Emissions at the iRACE site were dominated by biogenic processes, isoprene being the most emitted species (Kundu et al., 2019; Sklaveniti et al., 2018). This area can also be influenced by anthropogenic emissions from traffic and urban emissions from the city located on the East side. However, this pollution rarely reached the site due to wind directions bringing air masses emission from the city located west of the the site (Sklaveniti et al., 2018). Daytime maximum mixing ratios of NO and NO_2 were approximately 300 pptv and 1.5 ppbv, respectively. The 1-h average mixing ratios of NO, NO_2, O_3 and H_2O (%) as well as 1-h average values of JNO_2 are displayed in Figure 3.20. The ozone mixing ratio varied from the limit of detection on 18 July during the night to a maximum value of approximately 40 ppbv during most of the mid-days. The maximum NO mixing ratio ranged from 0.15-0.3 ppbv during the morning peak (between 7 and 9 AM).

During the IRRONIC-2015 (Kundu et al., 2019) campaign held at the same measurement site and same period (July-August), the highest measured VOCs were low molecular weight alkanes (C_2-C_5) (5.7±3.9 ppbv on a daytime average) followed by isoprene 3.6 ppbv. NO mixing ratios were between 0.2 and 0.8 ppbv during early morning (09:00-11:00 local time h), and NO_2 mixing ratios

ranged from 0.3-3 ppbv. The 24-average O_3 concentration was 40 ppbv mid-day, with maximum values at 71 ppbv during daytime.

Due to technical issues, the GC did not measure during the whole campaign. Continuous measurements started on 23 of July. The preliminary isoprene mixing ratios (time series data not available yet) ranged from 10-15 ppbv at the daytime peak before 23rd July and decreased to less than 8 ppbv after. This decrease is consistent with reduced isoprene emissions due to lower daytime temperatures (mid-day temperatures of 32°C before 23rd July and 25°C after).

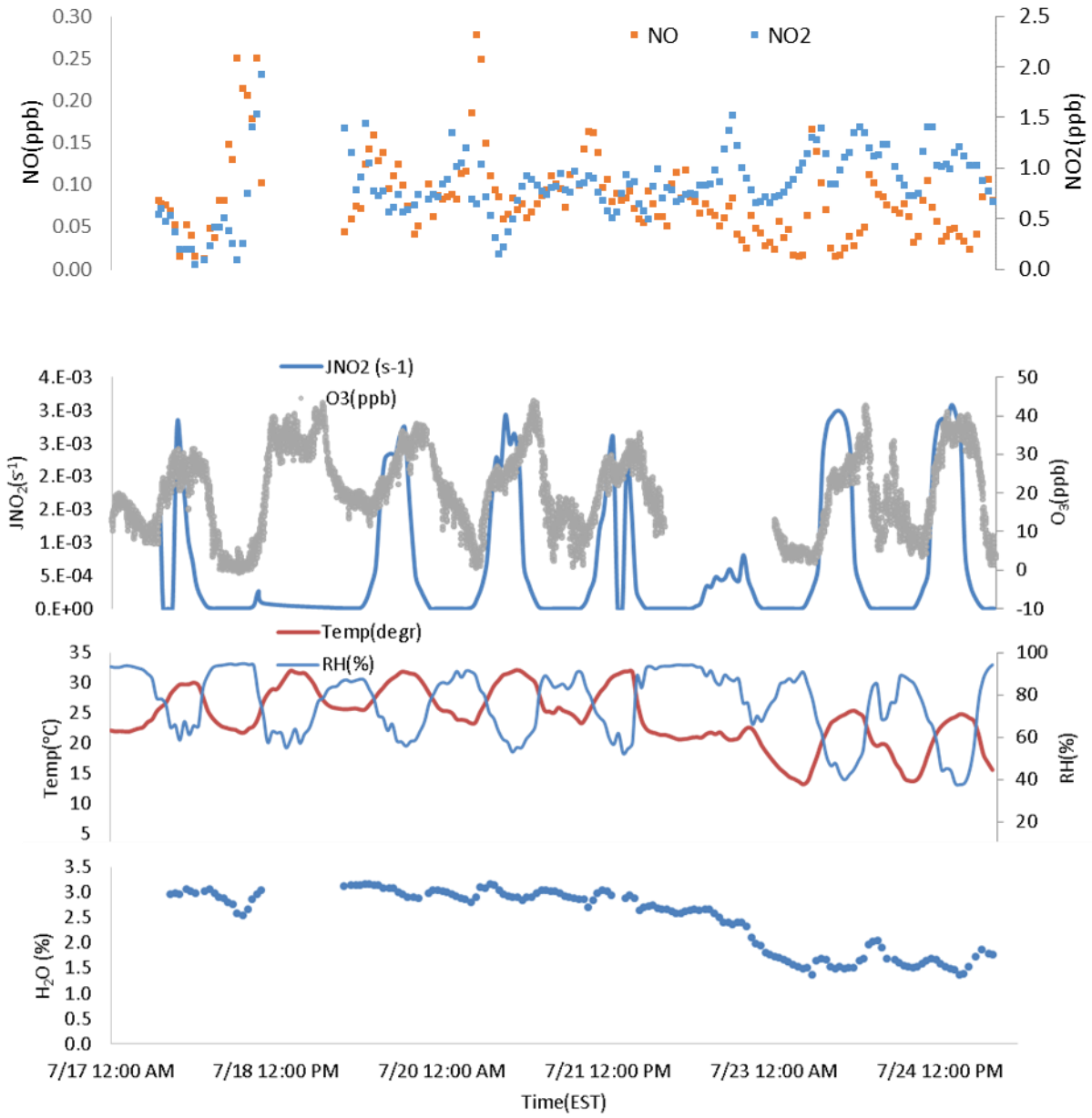

Figure 3.24 Time series of NO, NO_2, J(NO_2), O_3, T, RH, and H_2O from July 17 to July 24, 2019 during the iRACE field campaign.

3.5.1.3 *Description of the RO_xLIF measurements*

During the time period allocated to the use of RO_xLIF (July 17 to July 25), ambient measurements of RO_2 and HO_2 were only performed on 6 days due to bad weather conditions (1day), and the need to calibrate the instrument (2 days). Nighttime measurements were only

successful on the first and last two nights of the campaign due to inlet clogging (insects getting stuck in the nozzle orifice). The limits of detection for HO_2 and RO_2 were (2-4)×10^7 cm^{-3} and (1.5-3)×10^7 cm^{-3}, respectively, for 5-minute average measurements and a S/N of 1. These limits of detection are close to the values observed in the laboratory before the field measurements (2×10^7 cm^{-3}).

Time series of 5-min and 20 min average ambient measurements of RO_2 and HO_2 are shown in Figure 3.25. RO_2 and HO_2 measurements ranged from the LOD up to 2.5×10^9 cm^{-3}, exhibiting a strong diurnal cycle characteristic of the photolytic nature of these radicals. A good correlation is observed between HO_2 and RO_2 as well as each of these measurements and J(NO_2). The measured concentrations are similar to measurements performed at the same site during IRRONIC-2015, where Kundu et al. (2019) reported a maximum measured concentration of 2×10^9 cm^{-3} for HO_2+RO_2 with their ECHAMP chemical amplifier. The measurements of HO_2^* performed by IU-FAGE, being the sum of HO_2, isoprene-based peroxy radicals and other alkene-based peroxy radicals due to the use of an elevated NO concentration in the FAGE detection axis peaked at 2×10^9 cm^{-3} cm^{-3}. Peroxy radical measurements performed during PROPHET 1997 & 2008 campaigns in a northern Michigan forest, HO_2^* (Griffith et al., 2013a) or RO_2+HO_2 (Mihele and Hastie, 2003), and in the tropical rain forest in Malaysia, RO_2+HO_2 (Hewitt et al., 2010), also ranged from 2×10^8-2×10^9 cm^{-3}.

The [HO_2]/([HO_2]+[RO_2]) ratio during iRACE is shown in Figure 3.26 for the period between 7:00AM and 7:00PM since nighttime concentrations were often close or below the limit of detection for both HO_2 and RO_2. The average ratio was pretty was fairly constant at a value of 0.5 during the campaign, with the exception of the last day where the ratio increased to 0.8. HO_2 accounted for at least 50% of the pool of peroxy radicals at this site. This last day was characterized by lower isoprene concentrations based on the preliminary GC measurements. RO_2 concentrations were observed with a mid-day average value of 4×10^8 cm^{-3} compared to 1×10^9 cm^{-3} on the previous days with higher isoprene concentrations.

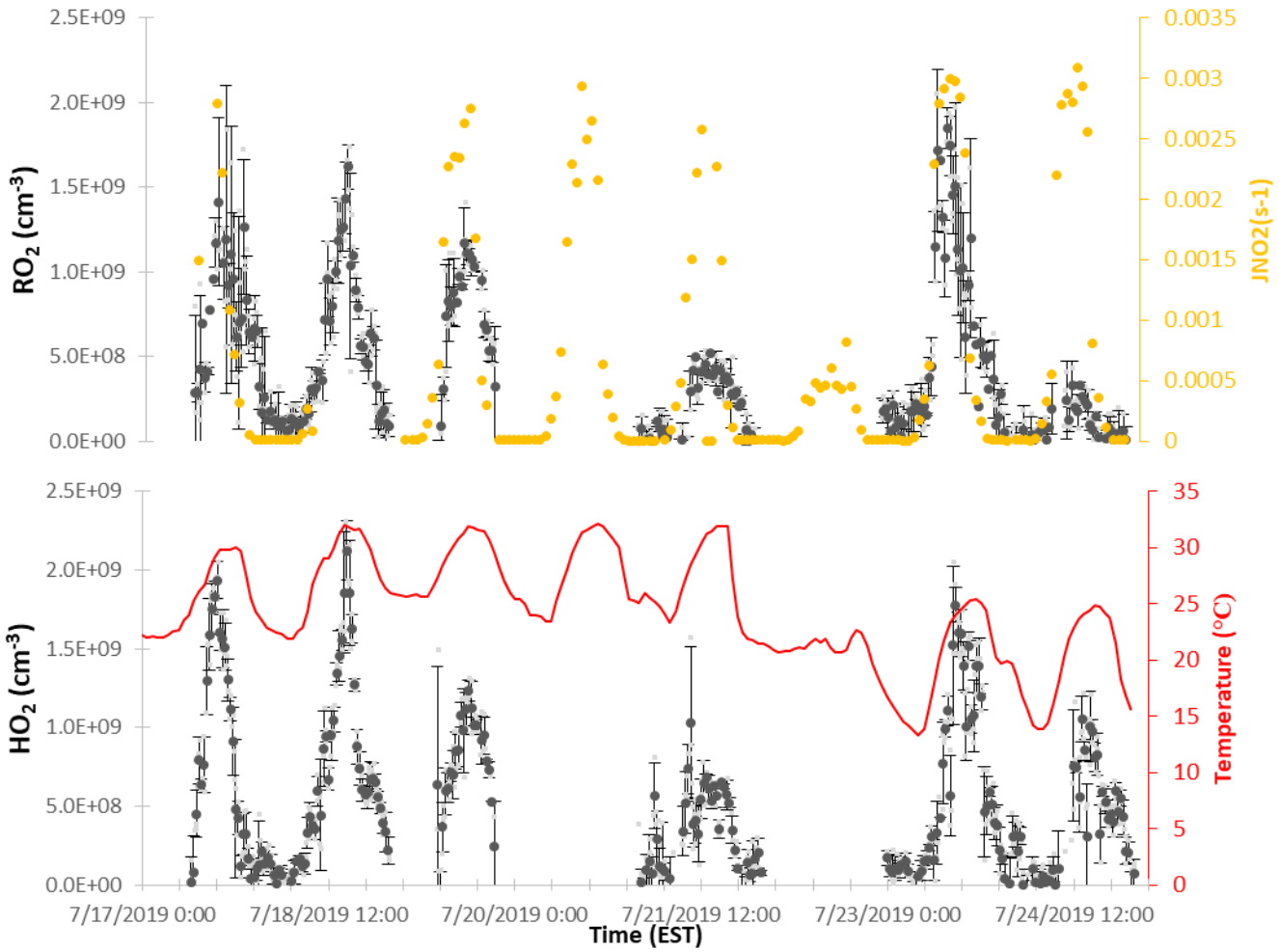

Figure 3.25 Time series of RO_2 and HO_2 from July 17 to July 24, 2019 during the iRACE field campaign. The light and dark markers are 5-min and 20 mins average measurements, respectively. J(NO_2) and T are also shown.

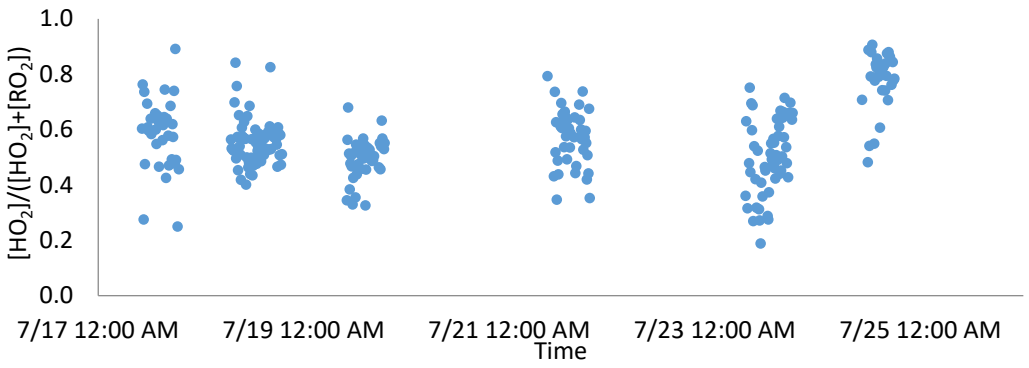

Figure 3.26 10 mins average ratios of $[HO_2]$ over $[HO_2]+[RO_2]$ measured between 7:00 AM and 7:00 PM during the iRACE campaign.

This first deployment of the RO_xLIF instrument for ambient measurements of peroxy radicals showed its capability for measuring both HO_2 and RO_2 with detection limits close to that observed during laboratory testing. The similarities observed between the above measurements and those performed previously at the same site and other forested sites indicate that this instrument is behaving correctly. Additional work is now needed to thoroughly analyse the measured concentrations using box modeling.

3.5.2 Indoor campaign

After outdoor measurements, the RO_xLIF was moved inside the RTP Building to measure indoor peroxy radicals during the iRACE campaign. The indoor RO_2 and HO_2 radicals were measured inside a 20 m^2 room between the 2nd and 5th of August, 2019. The room had 1 window facing east which allowed direct sunlight to enter in the morning. In this section, we only report measurements made on the 2nd of August (Figure 3.27) when various indoor residential activities took place, including cleaning and peeling off clementines.

During this day the ventilation system of the room was active while cleaning activities were performed using a terpene-containing cleaner (pine-Sol). Figure 3.27 displays the measurements of HO_2 (black symbols) and RO_2 (red symbols) with an integration time of 0.5 min (0.3 min of on-resonance and 0.2 min of off-resonance measurements) and mixing ratios of indoor ozone (blue line) during a 12-h period. Background concentrations of both HO_2 and RO_2 were on the order of

4-5×10^8 cm^{-3} during periods of no activity. These concentrations clearly increased in the 10^9 cm^{-3} range with a concomitant decrease in ozone during each mopping episode in the presence or absence of sunlight (indicated by higher $J(NO_2)$ values). This suggests that the mopping episodes initiated radical oxidation chemistry through the ozonolysis of terpenes that led to the production of RO_2 and HO_2. The monoterpenes present in pine oil (a primary component of terpene-based cleaners such as Pine-Sol), such as α- and β-pinene as well as limonene, can be oxidized either by O_3 entering the house through air exchange with outdoor (ventilation), leading to the production of RO_2 and HO_2 species as wall as OH. On the same day, 3 clementines were peeled at 2 PM inside the room. During the peeling episode, the concentration of RO_2 and HO_2 increased from < 5×10^8 cm^{-3} to approximately 1.5×10^9 cm^{-3} together with a decrease of ozone. The concentrations of peroxy radicals produced during this episode were lower than the concentrations produced by mopping.

An interesting feature of each of these episodes is the faster decrease of RO_2 radicals compared to HO_2. The fate of peroxy radicals indoor will mainly depend on their cross- and self-reactions but also on their reaction with NO. Comparing the rate constant of HO_2+NO (8.7×10^{-12} cm^3 $molecule^{-1}$ s^{-1}) to the rate constant of CH_3O_2+NO (7.9×10^{-12} cm^3 $molecule^{-1}$ s^{-1}), $C_2H_5O_2$+NO (9.3×10^{-12} cm^3 $molecule^{-1}$ s^{-1}) and limonene-based peroxy radicals+NO (9.2×10^{-12} cm^3 $molecule^{-1}$ s^{-1}) shows that the loss rate of HO_2 and RO_2 should be similar, with a slightly faster loss of RO_2 compared to HO_2 if reactions of peroxy radicals with NO were their main sink in this environment. In contrast, comparing the rate constant of HO_2+HO_2 (3.3×10^{-12} cm^3 $molecule^{-1}$ s^{-1} at a mixing ratio of 1% water) to the rate constants of CH_3O_2+HO_2 (5.4×10^{-12} cm^3 $molecule^{-1}$ s^{-1}), $C_2H_5O_2$+HO_2 (8.4×10^{-12} cm^3 $molecule^{-1}$ s^{-1}) and limonene-based peroxy radicals+HO_2 (2.2×10^{-11} cm^3 $molecule^{-1}$ s^{-1}) shows that the loss rate of RO_2 should be much faster than for HO_2, especially for monoterpene-based RO_2. A close inspection of Figure 3.27 shows a fast decrease of both RO_2 and HO_2 when RO_2 is larger than 5×10^8 cm^{-3} and a slower decrease of HO_2 once most RO_2 have been reacted away, which is consistent with HO_2+HO_2 and RO_2+HO_2 being the main sinks of peroxy radicals during these experiments.

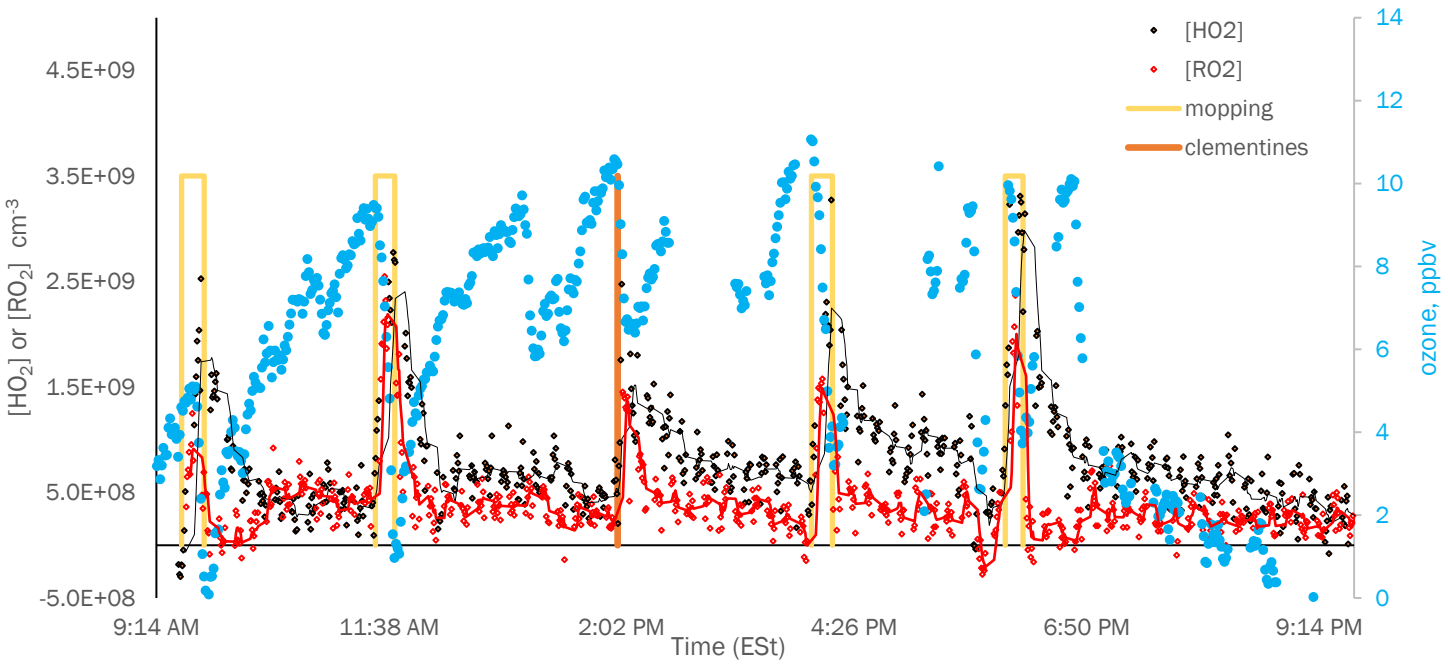

Figure 3.27 Indoor measurements of RO_2 and HO_2 during mopping activities on August 2nd. The yellow rectangles indicate mopping events and the orange vertical line marks the clementine peeling.

3.5.3 Figures of merit under field conditions

Measurements of the background signal of the RO_xLIF instrument were performed on the 25th of July for more than 2 hours (9:30 AM-12 PM) under ambient conditions (outdoor). The extracted off-resonance signals from the two measurement modes (HO_x and RO_x) are displayed in Figure 3.28. The precision on the off-resonance signal was 0.3 cps at 1σ and 5 min integration time for both modes. No difference was observed between HO_x and RO_x off-resonance signals with and without the presence of NO in the conversion flow-tube, respectively. The calibrated sensitivity for HO_2 and RO_2 under dry conditions ranged between $(4.8\text{-}5.3)\times10^{-9}$ and $(6.3\text{-}7.8)\times10^{-9}$ cps cm^{-3} mW^{-1}, respectively. These sensitivity factors are approximately two times higher than the values reported in Table 3.6 from post-calibrations performed in the laboratory. However, a similar water-dependence was observed for the field calibrations and the post-calibrations. We believe that the difference in sensitivity observed between these two sets of calibrations is due to the approach used to normalize the sensitivity factors to the laser power. In this approach, the laser power is measured at the detection cell before the entrance mirror (white cell configuration). Different alignments in

the coupling between the fiber launcher and the detection cell can lead to different transmissions of the laser light inside the cell. Indeed, if half the photons are blocked by the entrance mirror, the sensitivity normalized to the laser power measured at the exit of the fiber will appear half as high. It is therefore important to calibrate the instrument under the same configuration (fiber-detection cell coupling) as used in the field to ensure a reliable retrieval of ambient radical concentrations.

The limit of detection observed for HO_2 (blue dashed line) and RO_2 (red dashed line) are shown in Figure 3.28. The light-grey dots represent the background signal at an integration time of 0.2 min while black dots are 5-min averages. The average LOD for HO_2 was $(2\text{-}4)\times10^7$ cm^{-3} and that for RO_2 was slightly better at $(1.5\text{-}3)\times10^7$ cm^{-3} for S/N= 1.

As already mentioned, the error associated with the UV-water photolysis calibration technique of ±18% (1σ; Dusanter et al., 2008) represents the accuracy of these peroxy radical measurements.

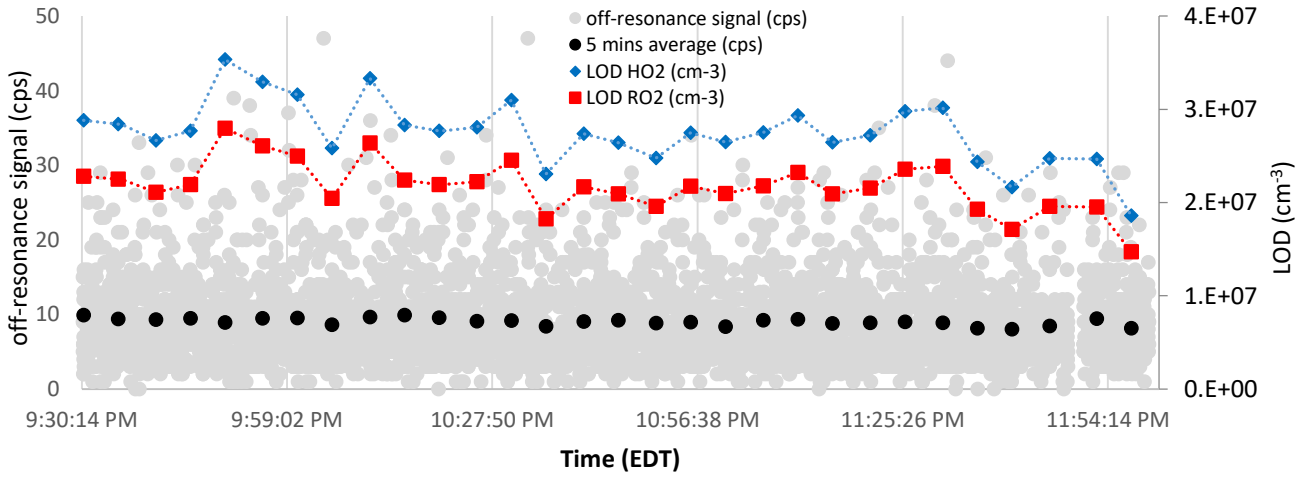

Figure 3.28 Limits of detection for HO_2 (blue markers) and RO_2 (red markers) measurements for a duration of 2.5 hours.

3.6 Conclusions

The objective of this work was to assemble and couple a RO_2 conversion flow-tube on the inlet of an existing LIF-FAGE instrument to extend the measurement capability of this instrument to HO_2+RO_2. A second objective consisted of deploying the new apparatus in the field to test it for real ambient measurements and to assess its performances. The construction of the conversion flow-tube, its characterization in the laboratory and the field deployment were achieved at Indiana University (USA) over a period of 18 months.

This work involved the design and construction of the flow-tube and attaching it to the existing IU-FAGE instrument. The different parts of the flow-tube were built by the IU Mechanical Instrument Services. It also required was the coding a Labview software program to automate the measurement sequence. The operating conditions for the conversion flow-tube were optimized to maximize the instrument sensitivity to HO_2 and RO_2 through both laboratory experiments and model simulations. Optimum conditions were identified by varying several parameters such as the concentration of the reagent gases (CO, NO), the pressure and the residence time in the flow-tube. The conditions selected for this RO_xLIF instrument are 0.8 ppmv NO, 0.4% CO, 28 torr reactor pressure and 1 second residence time.

The sensitivity of the instrument toward HO_2 and RO_2 radicals was calibrated using the UV-water photolysis method and was compared to model simulations in order to see how well sensitivity changes with flow-tube residence time are understood. The sensitivity factors for HO_2 and CH_3O_2 were found to be of the same order of magnitude, with the sensitivity towards CH_3O_2 being 26% higher than for HO_2. In addition, the sensitivity towards other peroxy radicals (methane, propane and ethane-RO_2) was also calibrated. The results indicate that these RO_2 radicals generate a similar response on the RO_xLIF instrument (within 10%), which was found to be consistent with model simulations. The calibrated sensitivity is water dependent, as observed for FAGE, and is of the same order of magnitude, ca. 20-27 % reduction in sensitivity per % of water, which can be explained by the quenching of the OH fluorescence. The error associated with the UV-water photolysis calibration technique is estimated to be ±18% at 1σ, which represents the accuracy of the HO_2 and RO_2 measurements.

The first field application of the new RO_xLIF apparatus was performed at the Indiana University Research and Teaching Preserve (IURTP) as part of the IRACE field campaign during summer 2019. Ambient measurements of RO_2 and HO_2 were found to range between 4×10^8 and 2.5×10^9 cm^{-3} in this forested environment, consistent with previous measurements of peroxy radicals performed at the same site. In addition, indoor measurements performed during the same campaign highlighted the dynamic of peroxy radical concentrations during cleaning activities. Limits of detection determined from the precision of the off-resonance signals were about 2×10^7 cm^{-3} for HO_2 and RO_2 , using 5-minute integration times and a signal-to-noise ratio of 1. This field testing demonstrated that this instrument is capable of measuring concentrations of peroxy radicals in various environments.

However, several aspects need to be further evaluated to ensure the reliability of the measurements. Additional tests need to be done using different coating materials for the inner surface of the flow-tube in order to reduce the loss of radicals to gain understanding of why the radical loss may have changed during the characterizations tests described above. It is also important to experimentally investigate the effect of pressure on the RO_xLIF response when CO/NO are kept at the same concentration. The sensitivity for different RO_2 radicals also need to be tested to ensure that all RO_2 exhibit similar sensitivities, especially NO_3-adduct RO_2 radicals which are expected to exhibit a lower response (Whalley et al., 2018b). Lastly, potential interefences should also be investigated, including the thermal decomposition of peroxy nitric acid (HO_2NO_2) and methyl peroxy nitric acid ($CH_3O_2NO_2$) in the conversion flow-tube (Whalley et al., 2018b).

Future improvements for this instrument may concern: (i) a longer and wider flow-tube to reduce the surface to volume ratio, which in turn should lead to a decrease of HO_2 wall losses, (ii) the use of different coating materials to further reduce HO_2 wall losses as discussed above, (iii) a shorter residence time in the flow-tube (0.5-0.6 s) to increase the signal detected from the conversion of RO_2 (60-65 % of sampled RO_2 detected instead of 40%).

Fianly, the indoor and outdoor measurements performed in July-August 2019 during the iRACE campaign will be interpreted together with the concomitant measurements of trace gases and aerosols.

3.7 References

Acker, K., Möller, D., Wieprecht, W., Meixner, F.X., Bohn, B., Gilge, S., Plass-Dülmer, C., Berresheim, H., 2006. Strong daytime production of OH from HNO2 at a rural mountain site. Geophys. Res. Lett. 33. https://doi.org/10.1029/2005GL024643

Ahmed, M., Blunt, D., Chen, D., Suits, A.G., 1997. UV photodissociation of oxalyl chloride yields four fragments from one photon absorption. J. Chem. Phys. 106, 7617–7624.

Albrecht, S.R., Novelli, A., Hofzumahaus, A., Kang, S., Baker, Y., Mentel, T., Wahner, A., Fuchs, H., 2019. Measurements of hydroperoxy radicals (HO2) at atmospheric concentrations using bromide chemical ionisation mass spectrometry. Atmos Meas Tech 12, 891–902. https://doi.org/10.5194/amt-12-891-2019

Amedro, D., Miyazaki, K., Parker, A., Schoemaecker, C., Fittschen, C., 2012a. Atmospheric and kinetic studies of OH and HO2 by the FAGE technique. J. Environ. Sci. 24, 78–86. http://dx.doi.org/10.1016/S1001-0742(11)60723-7

Archibald, A.T., Levine, J.G., Abraham, N.L., Cooke, M.C., Edwards, P.M., Heard, D.E., Jenkin, M.E., Karunaharan, A., Pike, R.C., Monks, P.S., Shallcross, D.E., Telford, P.J., Whalley, L.K., Pyle, J.A., 2011. Impacts of HOx regeneration and recycling in the oxidation of isoprene: Consequences for the composition of past, present and future atmospheres. Geophys. Res. Lett. 38, n/a-n/a. https://doi.org/10.1029/2010GL046520

Ashbourn, S.F.M., Jenkin, M.E., Clemitshaw, K.C., 1998. Laboratory Studies of the Response of a Peroxy Radical Chemical Amplifier to HO2 and a Series of Organic Peroxy Radicals. J. Atmospheric Chem. 29, 233–266. https://doi.org/10.1023/a:1005992316512

Assaf, E., Tanaka, S., Kajii, Y., Schoemaecker, C., Fittschen, C., 2017. Rate constants of the reaction of C2–C4 peroxy radicals with OH radicals. Chem. Phys. Lett. 684, 245–249. https://doi.org/10.1016/j.cplett.2017.06.062

Atkinson, R., 2003. Kinetics of the gas-phase reactions of OH radicals with alkanes and cycloalkanes. Atmos Chem Phys 3, 2233–2307. https://doi.org/10.5194/acp-3-2233-2003

Atkinson, R., 2000. Atmospheric chemistry of VOCs and NOx. Atmos. Environ. 34, 2063–2101. http://dx.doi.org/10.1016/S1352-2310(99)00460-4

Atkinson, R., 1986. Kinetics and mechanisms of the gas-phase reactions of the hydroxyl radical with organic compounds under atmospheric conditions. Chem. Rev. 86, 69–201. https://doi.org/10.1021/cr00071a004

Atkinson, R., Arey, J., 2003. Atmospheric Degradation of Volatile Organic Compounds. Chem. Rev. 103, 4605–4638. https://doi.org/10.1021/cr0206420

Atkinson, R., Baulch, D.L., Cox, R.A., Crowley, J.N., Hampson, R.F., Hynes, R.G., Jenkin, M.E., Rossi, M.J., Troe, J., 2007. Evaluated kinetic and photochemical data for atmospheric chemistry: Volume III – gas phase reactions of inorganic halogens. Atmos Chem Phys 7, 981–1191. https://doi.org/10.5194/acp-7-981-2007

Atkinson, R., Baulch, D.L., Cox, R.A., Crowley, J.N., Hampson, R.F., Hynes, R.G., Jenkin, M.E., Rossi, M.J., Troe, J., 2004. Evaluated kinetic and photochemical data for atmospheric chemistry: Volume I - gas phase reactions of O_x, HO_x, NO_x and SO_x species. Atmos Chem Phys 4, 1461–1738. https://doi.org/10.5194/acp-4-1461-2004

Atkinson, R., Baulch, D.L., Cox, R.A., Crowley, J.N., Hampson, R.F., Hynes, R.G., Jenkin, M.E., Rossi, M.J., Troe, J., IUPAC Subcommittee, 2006. Evaluated kinetic and photochemical data for atmospheric chemistry: Volume II – gas phase reactions of organic species. Atmos Chem Phys 6, 3625–4055. https://doi.org/10.5194/acp-6-3625-2006

Atkinson, R., Baulch, D.L., Cox, R.A., Hampson, R.F., Kerr, J.A., Rossi, M.J., Troe, J., 1997a. Evaluated Kinetic, Photochemical and Heterogeneous Data for Atmospheric Chemistry: Supplement V. IUPAC Subcommittee on Gas Kinetic Data Evaluation for Atmospheric Chemistry. J. Phys. Chem. Ref. Data 26, 521–1011. https://doi.org/10.1063/1.556011

Atkinson, Roger., Tuazon, E.C., Aschmann, S.M., 1995. Products of the Gas-Phase Reactions of O3 with Alkenes. Environ. Sci. Technol. 29, 1860–1866. https://doi.org/10.1021/es00007a025

Avzianova, E.V., Ariya, P.A., 2002. Temperature-dependent kinetic study for ozonolysis of selected tropospheric alkenes. Int. J. Chem. Kinet. 34, 678–684. https://doi.org/10.1002/kin.10093

Bailey, A.E., Heard, D.E., Paul, P.H., Pilling, M.J., 1997. Collisional quenching of OH (A 2Σ+, v′ = 0) by N2, O2 and CO2 between 204 and 294 K. Implications for atmospheric measurements of OH by laser-induced fluorescence. J Chem Soc Faraday Trans 93, 2915–2920. https://doi.org/10.1039/A701582H

Baker, J., Aschmann, S.M., Arey, J., Atkinson, R., 2002. Reactions of stabilized criegee intermediates from the gas-phase reactions of O3 with selected alkenes. Int. J. Chem. Kinet. 34, 73–85. https://doi.org/10.1002/kin.10022

Baklanov, A.V., Krasnoperov, L.N., 2001. Oxalyl Chloride A Clean Source of Chlorine Atoms for Kinetic Studies. J. Phys. Chem. A 105, 97–103.

Berresheim, H., Elste, T., Plass-Dülmer, C., Eiseleb, F.L., Tannerb, D.J., 2000. Chemical ionization mass spectrometer for long-term measurements of atmospheric OH and H2SO4. Int. J. Mass Spectrom. 202, 91–109. http://dx.doi.org/10.1016/S1387-3806(00)00233-5

Berresheim, H., Elste, T., Tremmel, H.G., Allen, A.G., Hansson, H.C., Rosman, K., Dal Maso, M., Mäkelä, J.M., Kulmala, M., O'Dowd, C.D., 2002. Gas-aerosol relationships of H2SO4, MSA, and OH: Observations in the coastal marine boundary layer at Mace Head, Ireland. J. Geophys. Res. Atmospheres 107, PAR 5-1-PAR 5-12. https://doi.org/10.1029/2000JD000229

Bossolasco, A., Faragó, E.P., Schoemaecker, C., Fittschen, C., 2014. Rate constant of the reaction between CH3O2 and OH radicals. Chem. Phys. Lett. 593, 7–13. https://doi.org/10.1016/j.cplett.2013.12.052

Boyd, A.A., Flaud, P.-M., Daugey, N., Lesclaux, R., 2003. Rate Constants for RO2 + HO2 Reactions Measured under a Large Excess of HO2. J. Phys. Chem. A 107, 818–821. https://doi.org/10.1021/jp026581r

Braure, T., Bedjanian, Y., Romanias, M.N., Morin, J., Riffault, V., Tomas, A., Coddeville, P., 2014. Experimental Study of the Reactions of Limonene with OH and OD Radicals: Kinetics and Products. J. Phys. Chem. A 118, 9482–9490. https://doi.org/10.1021/jp507180g

Brune, W.H., Baier, B.C., Thomas, J., Ren, X., Cohen, R.C., Pusede, S.E., Browne, E.C., Goldstein, A.H., Gentner, D.R., Keutsch, F.N., Thornton, J.A., Harrold, S., Lopez-Hilfiker, F.D., Wennberg, P.O., 2016. Ozone production chemistry in the presence of urban plumes. Faraday Discuss. 189, 169–189. https://doi.org/10.1039/C5FD00204D

Burkert, J., Behmann, T., Andrés Hernández, M.D., Stöbener, D., Weißenmayer, M., Perner, D., Burrows, J.P., 2001. Measurements of peroxy radicals in a forested area of Portugal. Field Stud. Atmospheric Chem. Volatile Org. Compd. Emit. Eucalyptus For. FIELDVOC94 3, 327–338. https://doi.org/10.1016/S1465-9972(01)00014-9

Butkovskaya, N., Kukui, A., Le Bras, G., 2007. HNO3 Forming Channel of the HO2 + NO Reaction as a Function of Pressure and Temperature in the Ranges of 72−600 Torr and 223−323 K. J. Phys. Chem. A 111, 9047–9053. https://doi.org/10.1021/jp074117m

Butkovskaya, N., Rayez, M.-T., Rayez, J.-C., Kukui, A., Le Bras, G., 2009. Water Vapor Effect on the HNO3 Yield in the HO2 + NO Reaction: Experimental and Theoretical Evidence. J. Phys. Chem. A 113, 11327–11342. https://doi.org/10.1021/jp811428p

Calvert, J., Mellouki, A., Orlando, J., 2011. Mechanisms of atmospheric oxidation of the oxygenates. OUP USA.

Cantrell, C.A., Shetter, R.E., Calvert, J.G., 1996. Dual-Inlet Chemical Amplifier for Atmospheric Peroxy Radical Measurements. Anal. Chem. 68, 4194–4199. https://doi.org/10.1021/ac960639e

Cantrell, C.A., Stedman, D.H., Wendel, G.J., 1984. Measurement of atmospheric peroxy radicals by chemical amplification. Anal. Chem. 56, 1496–1502. https://doi.org/10.1021/ac00272a065

Cantrell, C.A., Zimmer, A., Tyndall, G.S., 1997. Absorption cross sections for water vapor from 183 to 193 nm. Geophys. Res. Lett. 24, 2195–2198. https://doi.org/10.1029/97GL02100

Chan, C.Y., Hard, T.M., Mehrabzadeh, A.A., George, L.A., O'Brien, R.J., 1990. Third-generation FAGE instrument for tropospheric hydroxyl radical measurement. J. Geophys. Res. Atmospheres 95, 18569–18576. https://doi.org/10.1029/JD095iD11p18569

Chen, S., Ren, X., Mao, J., Chen, Z., Brune, W.H., Lefer, B., Rappenglück, B., Flynn, J., Olson, J., Crawford, J.H., 2010. A comparison of chemical mechanisms based on TRAMP-2006 field data. Atmos. Environ. 44, 4116–4125. http://dx.doi.org/10.1016/j.atmosenv.2009.05.027

Chen, X., Millet, D.B., Singh, H.B., Wisthaler, A., Apel, E.C., Atlas, E.L., Blake, D.R., Bourgeois, I., Brown, S.S., Crounse, J.D., de Gouw, J.A., Flocke, F.M., Fried, A., Heikes, B.G., Hornbrook, R.S., Mikoviny, T., Min, K.-E., Müller, M., Neuman, J.A., O'Sullivan, D.W., Peischl, J., Pfister, G.G., Richter, D., Roberts, J.M., Ryerson, T.B., Shertz, S.R., Thompson, C.R., Treadaway, V., Veres, P.R., Walega, J., Warneke, C., Washenfelder, R.A., Weibring, P., Yuan, B., 2019. On the sources and sinks of atmospheric VOCs: an integrated analysis of recent aircraft campaigns over North America. Atmos Chem Phys 19, 9097–9123. https://doi.org/10.5194/acp-19-9097-2019

Clemitshaw, K., 2004. A Review of Instrumentation and Measurement Techniques for Ground-Based and Airborne Field Studies of Gas-Phase Tropospheric Chemistry. Crit. Rev. Environ. Sci. Technol. 34, 1–108. https://doi.org/10.1080/10643380490265117

Clemitshaw, K.C., Carpenter, L.J., Penkett, S.A., Jenkin, M.E., 1997. A calibrated peroxy radical chemical amplifier for ground-based tropospheric measurements. J. Geophys. Res. Atmospheres 102, 25405–25416. https://doi.org/10.1029/97JD01902

Commane, R., Floquet, C.F.A., Ingham, T., Stone, D., Evans, M.J., Heard, D.E., 2010. Observations of OH and HO2 radicals over West Africa. Atmos Chem Phys 10, 8783–8801. https://doi.org/10.5194/acp-10-8783-2010

Creasey, D.J., Evans, G.E., Heard, D.E., Lee, J.D., 2003. Measurements of OH and HO2 concentrations in the Southern Ocean marine boundary layer. J. Geophys. Res. Atmospheres 108, n/a-n/a. https://doi.org/10.1029/2002JD003206

Creasey, D.J., Heard, D.E., Lee, J.D., 2000. Absorption cross-section measurements of water vapour and oxygen at 185 nm. Implications for the calibration of field instruments to measure OH, HO2 and RO2 radicals. Geophys. Res. Lett. 27, 1651–1654. https://doi.org/10.1029/1999GL011014

Dolgorouky, C., Gros, V., Sarda-Esteve, R., Sinha, V., Williams, J., Marchand, N., Sauvage, S., Poulain, L., Sciare, J., Bonsang, B., 2012. Total OH reactivity measurements in Paris during the 2010 MEGAPOLI winter campaign. Atmos Chem Phys 12, 9593–9612. https://doi.org/10.5194/acp-12-9593-2012

Dusanter, S., Stevens, P.S., 2017. Recent Advances in the Chemistry of OH and HO^2 Radicals in the Atmosphere: Field and Laboratory Measurements, in: Advances in Atmospheric Chemistry. pp. 493–579. https://doi.org/10.1142/9789813147355_0007

Dusanter, S., Vimal, D., Stevens, P.S., 2008a. Technical note: Measuring tropospheric OH and HO_2 by laser-induced fluorescence at low pressure. A comparison of calibration techniques. Atmos Chem Phys 8, 321–340. https://doi.org/10.5194/acp-8-321-2008

Dusanter, S., Vimal, D., Stevens, P.S., Volkamer, R., Molina, L.T., 2009a. Measurements of OH and HO_2 concentrations during the MCMA-2006 field campaign – Part 1: Deployment of the Indiana University laser-induced fluorescence instrument. Atmos Chem Phys 9, 1665–1685. https://doi.org/10.5194/acp-9-1665-2009

Dusanter, S., Vimal, D., Stevens, P.S., Volkamer, R., Molina, L.T., Baker, A., Meinardi, S., Blake, D., Sheehy, P., Merten, A., Zhang, R., Zheng, J., Fortner, E.C., Junkermann, W., Dubey, M., Rahn, T., Eichinger, B., Lewandowski, P., Prueger, J., Holder, H., 2009b. Measurements of OH and HO_2 concentrations during the MCMA-2006 field campaign – Part 2: Model comparison and radical budget. Atmos Chem Phys 9, 6655–6675. https://doi.org/10.5194/acp-9-6655-2009

Edwards, G.D., Cantrell, C.A., Stephens, S., Hill, B., Goyea, O., Shetter, R.E., Mauldin, R.L., Kosciuch, E., Tanner, D.J., Eisele, F.L., 2003. Chemical Ionization Mass Spectrometer Instrument for the Measurement of Tropospheric HO2 and RO2. Anal. Chem. 75, 5317–5327. https://doi.org/10.1021/ac034402b

Edwards, P.M., Evans, M.J., Furneaux, K.L., Hopkins, J., Ingham, T., Jones, C., Lee, J.D., Lewis, A.C., Moller, S.J., Stone, D., Whalley, L.K., Heard, D.E., 2013. OH reactivity in a South East Asian tropical rainforest during the Oxidant and Particle Photochemical Processes (OP3) project. Atmos Chem Phys 13, 9497–9514. https://doi.org/10.5194/acp-13-9497-2013

Ehn, M., Thornton, J.A., Kleist, E., Sipilä, M., Junninen, H., Pullinen, I., Springer, M., Rubach, F., Tillmann, R., Lee, B., 2014. A large source of low-volatility secondary organic aerosol. Nature 506, 476.

Elshorbany, Y.F., Kleffmann, J., Kurtenbach, R., Lissi, E., Rubio, M., Villena, G., Gramsch, E., Rickard, A.R., Pilling, M.J., Wiesen, P., 2010. Seasonal dependence of the oxidation capacity of the city of Santiago de Chile. Atmospheric Chem. Mech. Sel. Pap. 2008 Conf. 44, 5383–5394. https://doi.org/10.1016/j.atmosenv.2009.08.036

Faloona, I.C., Tan, D., Lesher, R.L., Hazen, N.L., Frame, C.L., Simpas, J.B., Harder, H., Martinez, M., Di Carlo, P., Ren, X., 2004. A laser-induced fluorescence instrument for detecting tropospheric OH and HO2: Characteristics and calibration. J. Atmospheric Chem. 47, 139–167.

Faragó, E.P., Schoemaecker, C., Viskolcz, B., Fittschen, C., 2015. Experimental determination of the rate constant of the reaction between C2H5O2 and OH radicals. Chem. Phys. Lett. 619, 196–200. https://doi.org/10.1016/j.cplett.2014.11.069

Finlayson-Pitts, B.J., Jr, J.N.P., 2000. {CHAPTER} 5 - Kinetics and Atmospheric Chemistry, in: Finlayson-Pitts, B.J., Pitts, J.N. (Eds.), Chemistry of the Upper and Lower Atmosphere. Academic Press, San Diego, pp. 130–178. https://doi.org/10.1016/B978-012257060-5/50007-1

Finlayson-Pitts, B.J., Pitts, J.N. (Eds.), 2000. Acknowledgments, in: Chemistry of the Upper and Lower Atmosphere. Academic Press, San Diego, pp. xxi–xxii. https://doi.org/10.1016/B978-012257060-5/50002-2

Finlayson-Pitts, B.J., Pitts Jr, J.N., 2000. CHAPTER 6 - Rates and Mechanisms of Gas-Phase Reactions in Irradiated Organic – NOx – Air Mixtures, in: Chemistry of the Upper and Lower Atmosphere. Academic Press, San Diego, pp. 179–263.

Fittschen, C., Al Ajami, M., Batut, S., Ferracci, V., Archer-Nicholls, S., Archibald, A.T., Schoemaecker, C., 2019. ROOOH: a missing piece of the puzzle for OH measurements in low-NO environments? Atmos Chem Phys 19, 349–362. https://doi.org/10.5194/acp-19-349-2019

Fittschen, C., Whalley, L.K., Heard, D.E., 2014. The Reaction of CH3O2 Radicals with OH Radicals: A Neglected Sink for CH3O2 in the Remote Atmosphere. Environ. Sci. Technol. 48, 7700–7701. https://doi.org/10.1021/es502481q

Fleming, Z.L., Monks, P.S., Rickard, A.R., Heard, D.E., Bloss, W.J., Seakins, P.W., Still, T.J., Sommariva, R., Pilling, M.J., Morgan, R., Green, T.J., Brough, N., Mills, G.P., Penkett, S.A., Lewis, A.C., Lee, J.D., Saiz-Lopez, A., Plane, J.M.C., 2006. Peroxy radical chemistry and the control of ozone photochemistry at Mace Head, Ireland during the summer of 2002. Atmos Chem Phys 6, 2193–2214. https://doi.org/10.5194/acp-6-2193-2006

Fuchs, H., Bohn, B., Hofzumahaus, A., Holland, F., Lu, K.D., Nehr, S., Rohrer, F., Wahner, A., 2011. Detection of HO_2 by laser-induced fluorescence: calibration and interferences from RO_2 radicals. Atmos Meas Tech 4, 1209–1225. https://doi.org/10.5194/amt-4-1209-2011

Fuchs, H., Brauers, T., Dorn, H.P., Harder, H., Häseler, R., Hofzumahaus, A., Holland, F., Kanaya, Y., Kajii, Y., Kubistin, D., Lou, S., Martinez, M., Miyamoto, K., Nishida, S., Rudolf, M., Schlosser, E., Wahner, A., Yoshino, A., Schurath, U., 2010. Technical Note: Formal blind intercomparison of HO_2 measurements in the atmosphere simulation chamber SAPHIR during the HOxComp campaign. Atmos Chem Phys 10, 12233–12250. https://doi.org/10.5194/acp-10-12233-2010

Fuchs, H., Holland, F., Hofzumahaus, A., 2008. Measurement of tropospheric RO2 and HO2 radicals by a laser-induced fluorescence instrument. Rev. Sci. Instrum. 79, 084104. https://doi.org/10.1063/1.2968712

Fuchs, H., Tan, Z., Hofzumahaus, A., Broch, S., Dorn, H.P., Holland, F., Künstler, C., Gomm, S., Rohrer, F., Schrade, S., Tillmann, R., Wahner, A., 2016. Investigation of potential interferences in the detection of atmospheric ROx radicals by laser-induced fluorescence under dark conditions. Atmos Meas Tech 9, 1431–1447. https://doi.org/10.5194/amt-9-1431-2016

Geyer, A., Alicke, B., Konrad, S., Schmitz, T., Stutz, J., Platt, U., 2001. Chemistry and oxidation capacity of the nitrate radical in the continental boundary layer near Berlin. J. Geophys. Res. Atmospheres 106, 8013–8025. https://doi.org/10.1029/2000JD900681

Goldstein, A.H., Galbally, I.E., 2007. Known and Unexplored Organic Constituents in the Earth's Atmosphere. Environ. Sci. Technol. 41, 1514–1521. https://doi.org/10.1021/es072476p

Green, T.J., Reeves, C.E., Brough, N., Edwards, G.D., Monks, P.S., Penkett, S.A., 2003. Airborne measurements of peroxy radicals using the PERCA technique. J Env. Monit 5, 75–83.

Green, T.J., Reeves, C.E., Fleming, Z.L., Brough, N., Rickard, A.R., Bandy, B.J., Monks, P.S., Penkett, S.A., 2006. An improved dual channel PERCA instrument for atmospheric measurements of peroxy radicals. J. Environ. Monit. 8, 530–536. https://doi.org/10.1039/B514630E

Griffith, S.M., Hansen, R.F., Dusanter, S., Michoud, V., Gilman, J.B., Kuster, W.C., Veres, P.R., Graus, M., de Gouw, J.A., Roberts, J., Young, C., Washenfelder, R., Brown, S.S., Thalman, R., Waxman, E., Volkamer, R., Tsai, C., Stutz, J., Flynn, J.H., Grossberg, N., Lefer, B., Alvarez, S.L., Rappenglueck, B., Mielke, L.H., Osthoff, H.D., Stevens, P.S., 2016. Measurements of hydroxyl and hydroperoxy radicals during CalNex-LA: Model comparisons and radical budgets. J. Geophys. Res. Atmospheres 121, 4211–4232. https://doi.org/10.1002/2015JD024358

Griffith, S.M., Hansen, R.F., Dusanter, S., Stevens, P.S., Alaghmand, M., Bertman, S.B., Carroll, M.A., Erickson, M., Galloway, M., Grossberg, N., Hottle, J., Hou, J., Jobson, B.T., Kammrath, A., Keutsch, F.N., Lefer, B.L., Mielke, L.H., O'Brien, A., Shepson, P.B., Thurlow, M., Wallace, W., Zhang, N., Zhou,

X.L., 2013a. OH and HO_2 radical chemistry during PROPHET 2008 and CABINEX 2009 – Part 1: Measurements and model comparison. Atmos Chem Phys 13, 5403–5423. https://doi.org/10.5194/acp-13-5403-2013

Groß, C., Dillon, T., Schuster, G., Lelieveld, J., Crowley, J., 2014. Direct kinetic study of OH and O3 formation in the reaction of CH3C (O) O2 with HO2. J. Phys. Chem. A 118, 974–985.

Guenther, A., Hewitt, C.N., Erickson, D., Fall, R., Geron, C., Graedel, T., Harley, P., Klinger, L., Lerdau, M., McKay, W.A., Pierce, T., Scholes, B., Steinbrecher, R., Tallamraju, R., Taylor, J., Zimmerman, P., 1995. A global model of natural volatile organic compound emissions. J. Geophys. Res. Atmospheres 100, 8873–8892. https://doi.org/10.1029/94JD02950

Guenther, A.B., Jiang, X., Heald, C.L., Sakulyanontvittaya, T., Duhl, T., Emmons, L.K., Wang, X., 2012. The Model of Emissions of Gases and Aerosols from Nature version 2.1 (MEGAN2.1): an extended and updated framework for modeling biogenic emissions. Geosci Model Dev 5, 1471–1492. https://doi.org/10.5194/gmd-5-1471-2012

Hanke, M., Uecker, J., Reiner, T., Arnold, F., 2002. Atmospheric peroxy radicals: ROXMAS, a new mass-spectrometric methodology for speciated measurements of HO2 and ∑RO2 and first results. Int. J. Mass Spectrom. 213, 91–99. http://dx.doi.org/10.1016/S1387-3806(01)00548-6

Hard, T.M., O'Brien, R.J., Chan, C.Y., Mehrabzadeh, A.A., 1984. Tropospheric free radical determination by fluorescence assay with gas expansion. Environ. Sci. Technol. 18, 768–777. https://doi.org/10.1021/es00128a009

Hasson, A.S., Tyndall, G.S., Orlando, J.J., 2004. A Product Yield Study of the Reaction of HO2 Radicals with Ethyl Peroxy (C2H5O2), Acetyl Peroxy (CH3C(O)O2), and Acetonyl Peroxy (CH3C(O)CH2O2) Radicals. J. Phys. Chem. A 108, 5979–5989. https://doi.org/10.1021/jp048873t

Hasson, A.S., Tyndall, G.S., Orlando, J.J., Singh, S., Hernandez, S.Q., Campbell, S., Ibarra, Y., 2012. Branching Ratios for the Reaction of Selected Carbonyl-Containing Peroxy Radicals with Hydroperoxy Radicals. J. Phys. Chem. A 116, 6264–6281. https://doi.org/10.1021/jp211799c

He, Y., Zhou, X., Hou, J., Gao, H., Bertman, S.B., 2006. Importance of dew in controlling the air-surface exchange of HONO in rural forested environments. Geophys. Res. Lett. 33. https://doi.org/10.1029/2005GL024348

Heal, M.R., Heard, D.E., Pilling, M.J., Whitaker, B.J., 1995. On the Development and Validation of FAGE for Local Measurement of Tropospheric OH and H02. J. Atmospheric Sci. 52, 3428–3441. https://doi.org/10.1175/1520-0469(1995)052<3428:OTDAVO>2.0.CO;2

Heard, D.E., 2006. ATMOSPHERIC FIELD MEASUREMENTS OF THE HYDROXYL RADICAL USING LASER-INDUCED FLUORESCENCE SPECTROSCOPY. Annu. Rev. Phys. Chem. 57, 191–216. https://doi.org/10.1146/annurev.physchem.57.032905.104516

Heard, D.E., Pilling, M.J., 2003. Measurement of OH and HO2 in the Troposphere. Chem. Rev. 103, 5163–5198. https://doi.org/10.1021/cr020522s

Hemmi, N., Suits, A.G., 1997. Photodissociation of oxalyl chloride at 193 nm probed via synchrotron radiation. J. Phys. Chem. A 101, 6633–6637.

Hendrik Fuchs, Frank Holland, Andreas Hofzumahaus, 2008. Measurement of tropospheric RO2 and HO2 radicals by a laser-induced fluorescence instrument. Rev. Sci. Instrum. 79, 084104. https://doi.org/10.1063/1.2968712

Hernández, M.D.A., Burkert, J., Reichert, L., Stöbener, D., Meyer-Arnek, J., Burrows, J.P., Dickerson, R.R., Doddridge, B.G., 2001. Marine boundary layer peroxy radical chemistry during the AEROSOLS99 campaign: Measurements and analysis. J. Geophys. Res. Atmospheres 106, 20833–20846. https://doi.org/10.1029/2001JD900113

Hewitt, C.N., Lee, J.D., MacKenzie, A.R., Barkley, M.P., Carslaw, N., Carver, G.D., Chappell, N.A., Coe, H., Collier, C., Commane, R., Davies, F., Davison, B., DiCarlo, P., Di Marco, C.F., Dorsey, J.R., Edwards, P.M., Evans, M.J., Fowler, D., Furneaux, K.L., Gallagher, M., Guenther, A., Heard, D.E., Helfter, C., Hopkins, J., Ingham, T., Irwin, M., Jones, C., Karunaharan, A., Langford, B., Lewis, A.C., Lim, S.F., MacDonald, S.M., Mahajan, A.S., Malpass, S., McFiggans, G., Mills, G., Misztal, P., Moller, S., Monks, P.S., Nemitz, E., Nicolas-Perea, V., Oetjen, H., Oram, D.E., Palmer, P.I., Phillips, G.J., Pike, R., Plane, J.M.C., Pugh, T., Pyle, J.A., Reeves, C.E., Robinson, N.H., Stewart, D., Stone, D., Whalley, L.K., Yin, X., 2010. Overview: oxidant and particle photochemical processes above a south-east Asian tropical rainforest (the OP3 project): introduction, rationale, location characteristics and tools. Atmos Chem Phys 10, 169–199. https://doi.org/10.5194/acp-10-169-2010

Hofzumahaus, A., Heard, D. (Eds.), 2015. Assessment of local HOx and ROx Measurement Techniques: Achievements, Challenges, and Fututre Directions.

Holland, F., Hessling, M., Hofzumahaus, A., 1995. In Situ Measurement of Tropospheric OH Radicals by Laser-Induced Fluorescence—A Description of the KFA Instrument. J. Atmospheric Sci. 52, 3393–3401. https://doi.org/10.1175/1520-0469(1995)052<3393:ISMOTO>2.0.CO;2

Honrath, R.E., Lu, Y., Peterson, M.C., Dibb, J.E., Arsenault, M.A., Cullen, N.J., Steffen, K., 2002. Vertical fluxes of NOx, HONO, and HNO3 above the snowpack at Summit, Greenland. Atmos. Environ. 36, 2629–2640. http://dx.doi.org/10.1016/S1352-2310(02)00132-2

Horie, O., Moortgat, G.K., 1991. Decomposition pathways of the excited Criegee intermediates in the ozonolysis of simple alkenes. Int. Conf. Gener. Oxid. Reg. Glob. Scales 25, 1881–1896. https://doi.org/10.1016/0960-1686(91)90271-8

Hornbrook, R.S., Crawford, J.H., Edwards, G.D., Goyea, O., Mauldin Iii, R.L., Olson, J.S., Cantrell, C.A., 2011. Measurements of tropospheric HO_2 and RO_2 by oxygen dilution modulation and chemical ionization mass spectrometry. Atmos Meas Tech 4, 735–756. https://doi.org/10.5194/amt-4-735-2011

Horstjann, M., Andrés Hernández, M.D., Nenakhov, V., Chrobry, A., Burrows, J.P., 2014. Peroxy radical detection for airborne atmospheric measurements using absorption spectroscopy of NO_2. Atmos Meas Tech 7, 1245–1257. https://doi.org/10.5194/amt-7-1245-2014

Hossaini, R., Chipperfield, M.P., Saiz-Lopez, A., Fernandez, R., Monks, S., Feng, W., Brauer, P., von Glasow, R., 2016. A global model of tropospheric chlorine chemistry: Organic versus inorganic sources and impact on methane oxidation. J. Geophys. Res. Atmospheres 121, 14,271-14,297. https://doi.org/10.1002/2016JD025756

Howard, C.J., 1979. Kinetic measurements using flow tubes. J. Phys. Chem. 83, 3–9. https://doi.org/10.1021/j100464a001

Ingham, T., Goddard, A., Whalley, L.K., Furneaux, K.L., Edwards, P.M., Seal, C.P., Self, D.E., Johnson, G.P., Read, K.A., Lee, J.D., Heard, D.E., 2009. A flow-tube based laser-induced fluorescence instrument to measure OH reactivity in the troposphere. Atmos Meas Tech 2, 465–477. https://doi.org/10.5194/amt-2-465-2009

Japar, S., Wu, C., Nikl, H., 1974. Rate constants for the reaction of ozone with olefins in the gas phase. J. Phys. Chem. 78, 2318–2320.

Jenkin, M.E., Clemitshaw, K.C., 2000. Ozone and other secondary photochemical pollutants: chemical processes governing their formation in the planetary boundary layer. Atmos. Environ. 34, 2499–2527. http://dx.doi.org/10.1016/S1352-2310(99)00478-1

Johnson, D., Marston, G., 2008. The gas-phase ozonolysis of unsaturated volatile organic compounds in the troposphere. Chem. Soc. Rev. 37, 699–716. https://doi.org/10.1039/B704260B

Kanaya, Y., Matsumoto, J., Kato, S., Akimoto, H., 2001a. Behavior of OH and HO2 radicals during the Observations at a Remote Island of Okinawa (ORION99) field campaign: 2. Comparison between observations and calculations. J. Geophys. Res. Atmospheres 106, 24209–24223.

Kanaya, Y., Sadanaga, Y., Hirokawa, J., Kajii, Y., Akimoto, H., 2001b. Development of a Ground-Based LIF Instrument for Measuring HOx Radicals: Instrumentation and Calibrations. J. Atmospheric Chem. 38, 73–110. https://doi.org/10.1023/A:1026559321911

Kartal, D., Andrés-Hernández, M.D., Reichert, L., Schlager, H., Burrows, J.P., 2010. Technical Note: Characterisation of a DUALER instrument for the airborne measurement of peroxy radicals during AMMA 2006. Atmos Chem Phys 10, 3047–3062. https://doi.org/10.5194/acp-10-3047-2010

Kerr, R.A., 1991. Hydroxyl, the Cleanser That Thrives on Dirt. Science 253, 1210. https://doi.org/10.1126/science.253.5025.1210

Kim, S., Wolfe, G.M., Mauldin, L., Cantrell, C., Guenther, A., Karl, T., Turnipseed, A., Greenberg, J., Hall, S.R., Ullmann, K., Apel, E., Hornbrook, R., Kajii, Y., Nakashima, Y., Keutsch, F.N., DiGangi, J.P., Henry, S.B., Kaser, L., Schnitzhofer, R., Graus, M., Hansel, A., Zheng, W., Flocke, F.F., 2013. Evaluation of HOx sources and cycling using measurement-constrained model calculations in a 2-methyl-3-butene-2-ol (MBO) and monoterpene (MT) dominated ecosystem. Atmos Chem Phys 13, 2031–2044. https://doi.org/10.5194/acp-13-2031-2013

Kleffmann, J., Kurtenbach, R., Lörzer, J., Wiesen, P., Kalthoff, N., Vogel, B., Vogel, H., 2003. Measured and simulated vertical profiles of nitrous acid—Part I: Field measurements. Atmos. Environ. 37, 2949–2955. https://doi.org/10.1016/S1352-2310(03)00242-5

Koppmann, R., 2007. Volatile organic compounds in the atmosphere. Wiley Online Library.

Kroll, J.H., Clarke, J.S., Donahue, N.M., Anderson, J.G., 2001. Mechanism of HOx Formation in the Gas-Phase Ozone−Alkene Reaction. 1. Direct, Pressure-Dependent Measurements of Prompt OH Yields. J. Phys. Chem. A 105, 1554–1560. https://doi.org/10.1021/jp002121r

Kroll, J.H., Seinfeld, J.H., 2008a. Chemistry of secondary organic aerosol: Formation and evolution of low-volatility organics in the atmosphere. Atmos. Environ. 42, 3593–3624. http://dx.doi.org/10.1016/j.atmosenv.2008.01.003

Kubistin, D., Harder, H., Martinez, M., Rudolf, M., Sander, R., Bozem, H., Eerdekens, G., Fischer, H., Gurk, C., Klüpfel, T., Königstedt, R., Parchatka, U., Schiller, C.L., Stickler, A., Taraborrelli, D., Williams, J., Lelieveld, J., 2010. Hydroxyl radicals in the tropical troposphere over the Suriname rainforest: comparison of measurements with the box model MECCA. Atmos Chem Phys 10, 9705–9728. https://doi.org/10.5194/acp-10-9705-2010

Kukui, A., Ancellet, G., Le Bras, G., 2008a. Chemical ionisation mass spectrometer for measurements of OH and Peroxy radical concentrations in moderately polluted atmospheres. J. Atmospheric Chem. 61, 133–154. https://doi.org/10.1007/s10874-009-9130-9

Kundu, S., Deming, B.L., Lew, M.M., Bottorff, B.P., Rickly, P., Stevens, P.S., Dusanter, S., Sklaveniti, S., Leonardis, T., Locoge, N., Wood, E.C., 2019. Peroxy Radical Measurements by Ethane – Nitric Oxide Chemical Amplification and Laser-Induced Fluorescence/Fluorescence Assay by Gas Expansion during the IRRONIC field campaign in a Forest in Indiana. Atmos Chem Phys Discuss 2019, 1–31. https://doi.org/10.5194/acp-2018-1359

Lee, J.D., McFiggans, G., Allan, J.D., Baker, A.R., Ball, S.M., Benton, A.K., Carpenter, L.J., Commane, R., Finley, B.D., Evans, M., Fuentes, E., Furneaux, K., Goddard, A., Good, N., Hamilton, J.F., Heard, D.E., Herrmann, H., Hollingsworth, A., Hopkins, J.R., Ingham, T., Irwin, M., Jones, C.E., Jones, R.L., Keene, W.C., Lawler, M.J., Lehmann, S., Lewis, A.C., Long, M.S., Mahajan, A., Methven, J., Moller, S.J., Müller, K., Müller, T., Niedermeier, N., O'Doherty, S., Oetjen, H., Plane, J.M.C., Pszenny, A.A.P.,

Read, K.A., Saiz-Lopez, A., Saltzman, E.S., Sander, R., von Glasow, R., Whalley, L., Wiedensohler, A., Young, D., 2010. Reactive Halogens in the Marine Boundary Layer (RHaMBLe): the tropical North Atlantic experiments. Atmos Chem Phys 10, 1031–1055. https://doi.org/10.5194/acp-10-1031-2010

Lee, J.D., Young, J.C., Read, K.A., Hamilton, J.F., Hopkins, J.R., Lewis, A.C., Bandy, B.J., Davey, J., Edwards, P., Ingham, T., Self, D.E., Smith, S.C., Pilling, M.J., Heard, D.E., 2009. Measurement and calculation of OH reactivity at a United Kingdom coastal site. J. Atmospheric Chem. 64, 53–76. https://doi.org/10.1007/s10874-010-9171-0

Lelieveld, J., Butler, T.M., Crowley, J.N., Dillon, T.J., Fischer, H., Ganzeveld, L., Harder, H., Lawrence, M.G., Martinez, M., Taraborrelli, D., Williams, J., 2008. Atmospheric oxidation capacity sustained by a tropical forest. Nature 452, 737.

Lew, M.L., Rickly, P.S., Bottorff, B.P., Sklaveniti, S., Léonardis, T., Locoge, N., Dusanter, S., Kundu, S., Wood, E., Stevens, P.S., 2019. OH and HO2 radical chemistry in a midlatitude forest: Measurements and model comparisons. Atmos Chem Phys Discuss 2019, 1–35. https://doi.org/10.5194/acp-2019-726

Lew, M.M., Dusanter, S., Stevens, P.S., 2018. Measurement of interferences associated with the detection of the hydroperoxy radical in the atmosphere using laser-induced fluorescence. Atmos Meas Tech 11, 95–109. https://doi.org/10.5194/amt-11-95-2018

Lightfoot, P.D., Cox, R.A., Crowley, J.N., Destriau, M., Hayman, G.D., Jenkin, M.E., Moortgat, G.K., Zabel, F., 1992. Organic peroxy radicals: Kinetics, spectroscopy and tropospheric chemistry. Atmospheric Environ. Part Gen. Top. 26, 1805–1961. http://dx.doi.org/10.1016/0960-1686(92)90423-I

Liu, Y., Morales-Cueto, R., Hargrove, J., Medina, D., Zhang, J., 2009. Measurements of Peroxy Radicals Using Chemical Amplification−Cavity Ringdown Spectroscopy. Environ. Sci. Technol. 43, 7791–7796. https://doi.org/10.1021/es901146t

Liu, Y., Zhang, J., 2014. Atmospheric Peroxy Radical Measurements Using Dual-Channel Chemical Amplification Cavity Ringdown Spectroscopy. Anal. Chem. 86, 5391–5398. https://doi.org/10.1021/ac5004689

Madronich, S., Shao, M., Wilson, S.R., Solomon, K.R., Longstreth, J.D., Tang, X.Y., 2015. Changes in air quality and tropospheric composition due to depletion of stratospheric ozone and interactions with changing climate: implications for human and environmental health. Photochem Photobiol Sci 14, 149–169. https://doi.org/10.1039/C4PP90037E

Mao, J., Jacob, D.J., Evans, M.J., Olson, J.R., Ren, X., Brune, W.H., Clair, J.M.S., Crounse, J.D., Spencer, K.M., Beaver, M.R., Wennberg, P.O., Cubison, M.J., Jimenez, J.L., Fried, A., Weibring, P., Walega, J.G., Hall, S.R., Weinheimer, A.J., Cohen, R.C., Chen, G., Crawford, J.H., McNaughton, C., Clarke, A.D., Jaeglé, L., Fisher, J.A., Yantosca, R.M., Le Sager, P., Carouge, C., 2010. Chemistry of hydrogen oxide radicals (HO_x) in the Arctic troposphere in spring. Atmos Chem Phys 10, 5823–5838. https://doi.org/10.5194/acp-10-5823-2010

Martinez, M., Harder, H., Kovacs, T.A., Simpas, J.B., Bassis, J., Lesher, R., Brune, W.H., Frost, G.J., Williams, E.J., Stroud, C.A., Jobson, B.T., Roberts, J.M., Hall, S.R., Shetter, R.E., Wert, B., Fried, A., Alicke, B., Stutz, J., Young, V.L., White, A.B., Zamora, R.J., 2003. OH and HO2 concentrations, sources, and loss rates during the Southern Oxidants Study in Nashville, Tennessee, summer 1999. J. Geophys. Res. Atmospheres 108, n/a-n/a. https://doi.org/10.1029/2003JD003551

Martinez, M., Harder, H., Kubistin, D., Rudolf, M., Bozem, H., Eerdekens, G., Fischer, H., Klüpfel, T., Gurk, C., Königstedt, R., Parchatka, U., Schiller, C.L., Stickler, A., Williams, J., Lelieveld, J., 2010. Hydroxyl radicals in the tropical troposphere over the Suriname rainforest: airborne measurements. Atmos Chem Phys 10, 3759–3773. https://doi.org/10.5194/acp-10-3759-2010

Martinez, M., Harder, H., Ren, X., Lesher, R.L., Brune, W.H., 2004. Measuring atmospheric naphthalene with laser-induced fluorescence. Atmos Chem Phys 4, 563–569. https://doi.org/10.5194/acp-4-563-2004

Matsumi Yutaka, Kono Mitsuhiko, Ichikawa Toshio, Takahashi Kenshi, Kondo Yutaka, 2002. Laser-Induced Fluorescence Instrument for the Detection of Tropospheric OH Radicals. Bull. Chem. Soc. Jpn. 75, 711–717. https://doi.org/doi:10.1246/bcsj.75.711

Mellouki, A., Wallington, T.J., Chen, J., 2015. Atmospheric Chemistry of Oxygenated Volatile Organic Compounds: Impacts on Air Quality and Climate. Chem. Rev. 115, 3984–4014. https://doi.org/10.1021/cr500549n

Mentel, T.F., Springer, M., Ehn, M., Kleist, E., Pullinen, I., Kurtén, T., Rissanen, M., Wahner, A., Wildt, J., 2015. Formation of highly oxidized multifunctional compounds: autoxidation of peroxy radicals formed in the ozonolysis of alkenes – deduced from structure–product relationships. Atmos Chem Phys 15, 6745–6765. https://doi.org/10.5194/acp-15-6745-2015

Mihelcic, D., Holland, F., Hofzumahaus, A., Hoppe, L., Konrad, S., Müsgen, P., Pätz, H.W., Schäfer, H.J., Schmitz, T., Volz-Thomas, A., Bächmann, K., Schlomski, S., Platt, U., Geyer, A., Alicke, B., Moortgat, G.K., 2003. Peroxy radicals during BERLIOZ at Pabstthum: Measurements, radical budgets and ozone production. J. Geophys. Res. Atmospheres 108, n/a-n/a. https://doi.org/10.1029/2001JD001014

Mihelcic, D., Müsgen, P., Ehhalt, D.H., 1985. An improved method of measuring tropospheric NO2 and RO2 by matrix isolation and electron spin resonance. J. Atmospheric Chem. 3, 341–361. https://doi.org/10.1007/bf00122523

Mihelcic, D., Volz-Thomas, A., Pätz, H.W., Kley, D., Mihelcic, M., 1990. Numerical analysis of ESR spectra from atmospheric samples. J. Atmospheric Chem. 11, 271–297. https://doi.org/10.1007/bf00118353

Mihele, C.M., Hastie, D.R., 2003. Radical chemistry at a forested continental site: Results from the PROPHET 1997 campaign. J. Geophys. Res. Atmospheres 108. https://doi.org/10.1029/2002JD002888

Mihele, C.M., Hastie, D.R., 2000. Optimized Operation and Calibration Procedures for Radical Amplifier-Type Detectors. J. Atmospheric Ocean. Technol. 17, 788–794. https://doi.org/10.1175/1520-0426(2000)017<0788:OOACPF>2.0.CO;2

Mihele, C.M., Hastie, D.R., 1998. The sensitivity of the radical amplifier to ambient water vapour. Geophys. Res. Lett. 25, 1911–1913. https://doi.org/10.1029/98GL01432

Mihele, C.M., Mozurkewich, M., Hastie, D.R., 1999a. Radical loss in a chain reaction of CO and NO in the presence of water: Implications for the radical amplifier and atmospheric chemistry. Int. J. Chem. Kinet. 31, 145–152. https://doi.org/10.1002/(SICI)1097-4601(1999)31:2<145::AID-KIN7>3.0.CO;2-M

Mihele, C.M., Mozurkewich, M., Hastie, D.R., 1999b. Radical loss in a chain reaction of CO and NO in the presence of water: Implications for the radical amplifier and atmospheric chemistry. Int. J. Chem. Kinet. 31, 145–152. https://doi.org/10.1002/(SICI)1097-4601(1999)31:2<145::AID-KIN7>3.0.CO;2-M

Miyazaki, K., Parker, A.E., Fittschen, C., Monks, P.S., Kajii, Y., 2010. A new technique for the selective measurement of atmospheric peroxy radical concentrations of HO_2 and RO_2 using a denuding method. Atmos Meas Tech 3, 1547–1554. https://doi.org/10.5194/amt-3-1547-2010

Monks, P.S., 2005. Gas-phase radical chemistry in the troposphere. Chem. Soc. Rev. 34, 376–395. https://doi.org/10.1039/B307982C

Montzka, S.A., Krol, M., Dlugokencky, E., Hall, B., Jöckel, P., Lelieveld, J., 2011. Small Interannual Variability of Global Atmospheric Hydroxyl. Science 331, 67–69. https://doi.org/10.1126/science.1197640

Müller, M., Mikoviny, T., Jud, W., D'Anna, B., Wisthaler, A., 2013. A new software tool for the analysis of high resolution PTR-TOF mass spectra. Chemom. Intell. Lab. Syst. 127, 158–165.

Nguyen, T.B., Tyndall, G.S., Crounse, J.D., Teng, A.P., Bates, K.H., Schwantes, R.H., Coggon, M.M., Zhang, L., Feiner, P., Millller, D.O., Skog, K.M., Rivera-Rios, J.C., Dorris, M., Olson, K.F., Koss, A., Wild, R.J., Brown, S.S., Goldstein, A.H., de Gouw, J.A., Brune, W.H., Keutsch, F.N., Seinfeld, J.H., Wennberg, P.O., 2016. Atmospheric fates of Criegee intermediates in the ozonolysis of isoprene. Phys Chem Chem Phys 18, 10241–10254. https://doi.org/10.1039/C6CP00053C

Nölscher, A.C., Williams, J., Sinha, V., Custer, T., Song, W., Johnson, A.M., Axinte, R., Bozem, H., Fischer, H., Pouvesle, N., Phillips, G., Crowley, J.N., Rantala, P., Rinne, J., Kulmala, M., Gonzales, D., Valverde-Canossa, J., Vogel, A., Hoffmann, T., Ouwersloot, H.G., Vilà-Guerau de Arellano, J., Lelieveld, J., 2012. Summertime total OH reactivity measurements from boreal forest during HUMPPA-COPEC 2010. Atmos Chem Phys 12, 8257–8270. https://doi.org/10.5194/acp-12-8257-2012

Nölscher, A.C., Yañez-Serrano, A.M., Wolff, S., de Araujo, A.C., Lavrič, J.V., Kesselmeier, J., Williams, J., 2016. Unexpected seasonality in quantity and composition of Amazon rainforest air reactivity. Nat. Commun. 7, 10383. https://doi.org/10.1038/ncomms10383

Novelli, A., Hens, K., Tatum Ernest, C., Kubistin, D., Regelin, E., Elste, T., Plass-Dülmer, C., Martinez, M., Lelieveld, J., Harder, H., 2014. Characterisation of an inlet pre-injector laser-induced fluorescence instrument for the measurement of atmospheric hydroxyl radicals. Atmos Meas Tech 7, 3413–3430. https://doi.org/10.5194/amt-7-3413-2014

Orlando, J.J., Tyndall, G.S., 2012. Laboratory studies of organic peroxy radical chemistry: an overview with emphasis on recent issues of atmospheric significance. Chem Soc Rev 41, 6294–6317. https://doi.org/10.1039/C2CS35166H

Orlando, J.J., Tyndall, G.S., Wallington, T.J., 2003. The Atmospheric Chemistry of Alkoxy Radicals. Chem. Rev. 103, 4657–4690. https://doi.org/10.1021/cr020527p

Parker, A.E., Amédro, D., Schoemaecker, C., Fittschen, C., 2011. OH RADICAL REACTIVITY MEASUREMENTS BY FAGE. Environ. Eng. Manag. J. EEMJ 10.

Paulot, F., Crounse, J.D., Kjaergaard, H.G., Kürten, A., St. Clair, J.M., Seinfeld, J.H., Wennberg, P.O., 2009. Unexpected Epoxide Formation in the Gas-Phase Photooxidation of Isoprene. Science 325, 730–733. https://doi.org/10.1126/science.1172910

Paulson, S.E., Orlando, J.J., 1996. The reactions of ozone with alkenes: An important source of HOx in the boundary layer. Geophys. Res. Lett. 23, 3727–3730. https://doi.org/10.1029/96GL03477

Peeters, J., Müller, J.-F., 2010. HOx radical regeneration in isoprene oxidation via peroxy radical isomerisations. II: experimental evidence and global impact. Phys. Chem. Chem. Phys. 12, 14227–14235.

Peeters, J., Nguyen, T.L., Vereecken, L., 2009. HO x radical regeneration in the oxidation of isoprene. Phys. Chem. Chem. Phys. 11, 5935–5939.

Penkett, S.A., Monks, P.S., Carpenter, L.J., Clemitshaw, K.C., Ayers, G.P., Gillett, R.W., Galbally, I.E., Meyer, C.P., 1997. Relationships between ozone photolysis rates and peroxy radical concentrations in clean marine air over the Southern Ocean. J. Geophys. Res. Atmospheres 102, 12805–12817. https://doi.org/10.1029/97JD00765

Perring, A.E., Pusede, S.E., Cohen, R.C., 2013. An Observational Perspective on the Atmospheric Impacts of Alkyl and Multifunctional Nitrates on Ozone and Secondary Organic Aerosol. Chem. Rev. 113, 5848–5870. https://doi.org/10.1021/cr300520x

Praske, E., Otkj\a er, R.V., Crounse, J.D., Hethcox, J.C., Stoltz, B.M., Kjaergaard, H.G., Wennberg, P.O., 2018. Atmospheric autoxidation is increasingly important in urban and suburban North America. Proc. Natl. Acad. Sci. 115, 64–69. https://doi.org/10.1073/pnas.1715540115

Pugh, T.A.M., MacKenzie, A.R., Hewitt, C.N., Langford, B., Edwards, P.M., Furneaux, K.L., Heard, D.E., Hopkins, J.R., Jones, C.E., Karunaharan, A., Lee, J., Mills, G., Misztal, P., Moller, S., Monks, P.S., Whalley, L.K., 2010. Simulating atmospheric composition over a South-East Asian tropical rainforest: performance of a chemistry box model. Atmos Chem Phys 10, 279–298. https://doi.org/10.5194/acp-10-279-2010

Read, K.A., Lewis, A.C., Bauguitte, S., Rankin, A.M., Salmon, R.A., Wolff, E.W., Saiz-Lopez, A., Bloss, W.J., Heard, D.E., Lee, J.D., Plane, J.M.C., 2008. DMS and MSA measurements in the Antarctic Boundary Layer: impact of BrO on MSA production. Atmos Chem Phys 8, 2985–2997. https://doi.org/10.5194/acp-8-2985-2008

Reichert, L., Andrés Hernández, M.D., Stöbener, D., Burkert, J., Burrows, J.P., 2003. Investigation of the effect of water complexes in the determination of peroxy radical ambient concentrations: Implications for the atmosphere. J. Geophys. Res. Atmospheres 108, ACH 4-1-ACH 4-16. https://doi.org/10.1029/2002JD002152

Ren, X., Edwards, G.D., Cantrell, C.A., Lesher, R.L., Metcalf, A.R., Shirley, T., Brune, W.H., 2003. Intercomparison of peroxy radical measurements at a rural site using laser-induced fluorescence and Peroxy Radical Chemical Ionization Mass Spectrometer (PerCIMS) techniques. J. Geophys. Res. Atmospheres 108. https://doi.org/10.1029/2003JD003644

Ren, X., van Duin, D., Cazorla, M., Chen, S., Mao, J., Zhang, L., Brune, W.H., Flynn, J.H., Grossberg, N., Lefer, B.L., Rappenglück, B., Wong, K.W., Tsai, C., Stutz, J., Dibb, J.E., Thomas Jobson, B., Luke, W.T., Kelley, P., 2013. Atmospheric oxidation chemistry and ozone production: Results from SHARP 2009 in Houston, Texas. J. Geophys. Res. Atmospheres 118, 5770–5780. https://doi.org/10.1002/jgrd.50342

Ren, Y., Grosselin, B., Daële, V., Mellouki, A., 2017. Investigation of the reaction of ozone with isoprene, methacrolein and methyl vinyl ketone using the HELIOS chamber. Faraday Discuss 200, 289–311. https://doi.org/10.1039/C7FD00014F

Rickly, P., Stevens, P.S., 2018. Measurements of a potential interference with laser-induced fluorescence measurements of ambient OH from the ozonolysis of biogenic alkenes. Atmos Meas Tech 11, 1–16. https://doi.org/10.5194/amt-11-1-2018

Sadanaga, Y., Matsumoto, J., Sakurai, K., Isozaki, R., Kato, S., Nomaguchi, T., Bandow, H., Kajii, Y., 2004. Development of a measurement system of peroxy radicals using a chemical amplification/laser-induced fluorescence technique. Rev. Sci. Instrum. 75, 864–872. https://doi.org/doi:http://dx.doi.org/10.1063/1.1666985

Sanchez, J., Tanner, D.J., Chen, D., Huey, L.G., Ng, N.L., 2016. A new technique for the direct detection of HO2 radicals using bromide chemical ionization mass spectrometry (Br-CIMS): initial characterization. Atmos Meas Tech 9, 3851–3861. https://doi.org/10.5194/amt-9-3851-2016

Sander, S., Friedl, R., Golden, D., Kurylo, M., Huie, R., Orkin, V., Moortgat, G., Ravishankara, A., Kolb, C., Molina, M., 2003. NASA/JPL Data Evaluation, JPL Publication 02-25 Evaluation No 14. Jet Propuls. Lab. Pasadena CA.

Sander, S., Golden, D., Kurylo, M., Moortgat, G., Wine, P., Ravishankara, A., Kolb, C., Molina, M., Finlayson-Pitts, B., Huie, R., 2006. Chemical kinetics and photochemical data for use in atmospheric studies evaluation number 15. Pasadena, CA: Jet Propulsion Laboratory, National Aeronautics and Space ….

Schultz, M., Heitlinger, M., Mihelcic, D., Volz-Thomas, A., 1995. Calibration source for peroxy radicals with built-in actinometry using H2O and O2 photolysis at 185 nm. J. Geophys. Res. Atmospheres 100, 18811–18816. https://doi.org/10.1029/95JD01642

Sindelarova, K., Granier, C., Bouarar, I., Guenther, A., Tilmes, S., Stavrakou, T., Müller, J.-F., Kuhn, U., Stefani, P., Knorr, W., 2014. Global data set of biogenic VOC emissions calculated by the MEGAN model over the last 30 years. Atmos Chem Phys 14, 9317–9341. https://doi.org/10.5194/acp-14-9317-2014

Sinha, V., Williams, J., Lelieveld, J., Ruuskanen, T.M., Kajos, M.K., Patokoski, J., Hellen, H., Hakola, H., Mogensen, D., Boy, M., Rinne, J., Kulmala, M., 2010. OH Reactivity Measurements within a Boreal Forest: Evidence for Unknown Reactive Emissions. Environ. Sci. Technol. 44, 6614–6620. https://doi.org/10.1021/es101780b

Sklaveniti, S., Locoge, N., Stevens, P.S., Wood, E., Kundu, S., Dusanter, S., 2018. Development of an instrument for direct ozone production rate measurements: measurement reliability and current limitations. Atmos Meas Tech 11, 741–761. https://doi.org/10.5194/amt-11-741-2018

Sneep, M., Ubachs, W., 2005. Direct measurement of the Rayleigh scattering cross section in various gases. J. Quant. Spectrosc. Radiat. Transf. 92, 293–310. https://doi.org/10.1016/j.jqsrt.2004.07.025

Spataro, F., Ianniello, A., 2014. Sources of atmospheric nitrous acid: State of the science, current research needs, and future prospects. J. Air Waste Manag. Assoc. 64, 1232–1250. https://doi.org/10.1080/10962247.2014.952846

Stavrakou, T., Peeters, J., Müller, J.-F., 2010. Improved global modelling of HO x recycling in isoprene oxidation: evaluation against the GABRIEL and INTEX-A aircraft campaign measurements. Atmospheric Chem. Phys. 10, 9863–9878.

Stevens, P.S., Mather, J.H., Brune, W.H., 1994a. Measurement of tropospheric OH and HO2 by laser-induced fluorescence at low pressure. J. Geophys. Res. Atmospheres 99, 3543–3557. https://doi.org/10.1029/93JD03342

Stone, D., Whalley, L.K., Heard, D.E., 2012. Tropospheric OH and HO2 radicals: field measurements and model comparisons. Chem. Soc. Rev. 41, 6348–6404. https://doi.org/10.1039/C2CS35140D

Sutton, J.A., Driscoll, J.F., 2004. Rayleigh scattering cross sections of combustion species at 266, 355, and 532 nm for thermometry applications. Opt Lett 29, 2620–2622. https://doi.org/10.1364/OL.29.002620

Tan, D., Faloona, I., Simpas, J.B., Brune, W., Shepson, P.B., Couch, T.L., Sumner, A.L., Carroll, M.A., Thornberry, T., Apel, E., Riemer, D., Stockwell, W., 2001. HO x budgets in a deciduous forest: Results from the PROPHET summer 1998 campaign. J. Geophys. Res. Atmospheres 106, 24407–24427. https://doi.org/10.1029/2001JD900016

Tan, Z., Fuchs, H., Lu, K., Hofzumahaus, A., Bohn, B., Broch, S., Dong, H., Gomm, S., Häseler, R., He, L., Holland, F., Li, X., Liu, Y., Lu, S., Rohrer, F., Shao, M., Wang, B., Wang, M., Wu, Y., Zeng, L., Zhang, Y., Wahner, A., Zhang, Y., 2017. Radical chemistry at a rural site (Wangdu) in the North China Plain: observation and model calculations of OH, HO2 and RO2 radicals. Atmos Chem Phys 17, 663–690. https://doi.org/10.5194/acp-17-663-2017

Tan, Z., Lu, K., Hofzumahaus, A., Fuchs, H., Bohn, B., Holland, F., Liu, Y., Rohrer, F., Shao, M., Sun, K., Wu, Y., Zeng, L., Zhang, Y., Zou, Q., Kiendler-Scharr, A., Wahner, A., Zhang, Y., 2019. Experimental budgets of OH, HO2, and RO2 radicals and implications for ozone formation in the Pearl River Delta in China 2014. Atmos Chem Phys 19, 7129–7150. https://doi.org/10.5194/acp-19-7129-2019

Tan, Z., Lu, K., Hofzumahaus, A., Fuchs, H., Bohn, B., Holland, F., Liu, Y., Rohrer, F., Shao, M., Sun, K., Wu, Y., Zeng, L., Zhang, Y., Zou, Q., Kiendler-Scharr, A., Wahner, A., Zhang, Y., 2018a. Experimental

budgets of OH, HO$_\mathbf2$ and RO$_\mathbf2$ radicals and implications for ozone formation in the Pearl River Delta in China 2014. Atmospheric Chem. Phys. Discuss. 2018, 1–28. https://doi.org/10.5194/acp-2018-801

Tan, Z., Rohrer, F., Lu, K., Ma, X., Bohn, B., Broch, S., Dong, H., Fuchs, H., Gkatzelis, G.I., Hofzumahaus, A., Holland, F., Li, X., Liu, Y., Liu, Y., Novelli, A., Shao, M., Wang, H., Wu, Y., Zeng, L., Hu, M., Kiendler-Scharr, A., Wahner, A., Zhang, Y., 2018b. Wintertime photochemistry in Beijing: observations of ROx radical concentrations in the North China Plain during the BEST-ONE campaign. Atmos Chem Phys 18, 12391–12411. https://doi.org/10.5194/acp-18-12391-2018

Teruel, M.A., Lane, S.I., Mellouki, A., Solignac, G., Le Bras, G., 2006. OH reaction rate constants and UV absorption cross-sections of unsaturated esters. Atmos. Environ. 40, 3764–3772. https://doi.org/10.1016/j.atmosenv.2006.03.003

Vaughan, S., Ingham, T., Whalley, L.K., Stone, D., Evans, M.J., Read, K.A., Lee, J.D., Moller, S.J., Carpenter, L.J., Lewis, A.C., Fleming, Z.L., Heard, D.E., 2012. Seasonal observations of OH and HO_2 in the remote tropical marine boundary layer. Atmospheric Chem. Phys. 12, 2149–2172. https://doi.org/10.5194/acp-12-2149-2012

Villena, G., Kleffmann, J., Kurtenbach, R., Wiesen, P., Lissi, E., Rubio, M.A., Croxatto, G., Rappenglück, B., 2011. Vertical gradients of HONO, NOx and O3 in Santiago de Chile. Atmos. Environ. 45, 3867–3873. https://doi.org/10.1016/j.atmosenv.2011.01.073

Volkamer, R., Sheehy, P., Molina, L.T., Molina, M.J., 2010. Oxidative capacity of the Mexico City atmosphere – Part 1: A radical source perspective. Atmos Chem Phys 10, 6969–6991. https://doi.org/10.5194/acp-10-6969-2010

Whalley, L., Stone, D., Heard, D., 2012. New insights into the tropospheric oxidation of isoprene: combining field measurements, laboratory studies, chemical modelling and quantum theory, in: Atmospheric and Aerosol Chemistry. Springer, pp. 55–95.

Whalley, L.K., Blitz, M.A., Desservettaz, M., Seakins, P.W., Heard, D.E., 2013. Reporting the sensitivity of laser-induced fluorescence instruments used for HO_2 detection to an interference from RO_2 radicals and introducing a novel approach that enables HO_2 and certain RO_2 types to be selectively measured. Atmos Meas Tech 6, 3425–3440. https://doi.org/10.5194/amt-6-3425-2013

Whalley, L.K., Edwards, P.M., Furneaux, K.L., Goddard, A., Ingham, T., Evans, M.J., Stone, D., Hopkins, J.R., Jones, C.E., Karunaharan, A., Lee, J.D., Lewis, A.C., Monks, P.S., Moller, S.J., Heard, D.E., 2011. Quantifying the magnitude of a missing hydroxyl radical source in a tropical rainforest. Atmos Chem Phys 11, 7223–7233. https://doi.org/10.5194/acp-11-7223-2011

Whalley, L.K., Stone, D., Dunmore, R., Hamilton, J., Hopkins, J.R., Lee, J.D., Lewis, A.C., Williams, P., Kleffmann, J., Laufs, S., Woodward-Massey, R., Heard, D.E., 2018a. Understanding in situ ozone production in the summertime through radical observations and modelling studies during the Clean air for London project (ClearfLo). Atmospheric Chem. Phys. 18, 2547–2571. https://doi.org/10.5194/acp-18-2547-2018

Whalley, L.K., Stone, D., Dunmore, R., Hamilton, J., Hopkins, J.R., Lee, J.D., Lewis, A.C., Williams, P., Kleffmann, J., Laufs, S., Woodward-Massey, R., Heard, D.E., 2018b. Understanding in situ ozone production in the summertime through radical observations and modelling studies during the Clean air for London project (ClearfLo). Atmos Chem Phys 18, 2547–2571. https://doi.org/10.5194/acp-18-2547-2018

Wolfe, G.M., Cantrell, C., Kim, S., Mauldin III, R.L., Karl, T., Harley, P., Turnipseed, A., Zheng, W., Flocke, F., Apel, E.C., Hornbrook, R.S., Hall, S.R., Ullmann, K., Henry, S.B., DiGangi, J.P., Boyle, E.S., Kaser, L., Schnitzhofer, R., Hansel, A., Graus, M., Nakashima, Y., Kajii, Y., Guenther, A., Keutsch, F.N., 2014.

Missing peroxy radical sources within a summertime ponderosa pine forest. Atmos Chem Phys 14, 4715–4732. https://doi.org/10.5194/acp-14-4715-2014

Wolfe, G.M., Marvin, M.R., Roberts, S.J., Travis, K.R., Liao, J., 2016. The Framework for 0-D Atmospheric Modeling (F0AM) v3.1. Geosci Model Dev 9, 3309–3319. https://doi.org/10.5194/gmd-9-3309-2016

Wolfe, G.M., Thornton, J.A., McKay, M., Goldstein, A.H., 2011. Forest-atmosphere exchange of ozone: sensitivity to very reactive biogenic VOC emissions and implications for in-canopy photochemistry. Atmos Chem Phys 11, 7875–7891. https://doi.org/10.5194/acp-11-7875-2011

Wood, E.C., Charest, J.R., 2014. Chemical Amplification - Cavity Attenuated Phase Shift Spectroscopy Measurements of Atmospheric Peroxy Radicals. Anal. Chem. 86, 10266–10273. https://doi.org/10.1021/ac502451m

Wood, E.C., Deming, B.L., Kundu, S., 2017. Ethane-Based Chemical Amplification Measurement Technique for Atmospheric Peroxy Radicals. Environ. Sci. Technol. Lett. 4, 15–19. https://doi.org/10.1021/acs.estlett.6b00438

Zhang, X., Lambe, A.T., Upshur, M.A., Brooks, W.A., Gray Bé, A., Thomson, R.J., Geiger, F.M., Surratt, J.D., Zhang, Z., Gold, A., 2017. Highly oxygenated multifunctional compounds in α-pinene secondary organic aerosol. Environ. Sci. Technol. 51, 5932–5940.

Zheng, W., Flocke, F.M., Tyndall, G.S., Swanson, A., Orlando, J.J., Roberts, J.M., Huey, L.G., Tanner, D.J., 2011. Characterization of a thermal decomposition chemical ionization mass spectrometer for the measurement of peroxy acyl nitrates (PANs) in the atmosphere. Atmos Chem Phys 11, 6529–6547. https://doi.org/10.5194/acp-11-6529-2011

Zhou, X., Zhang, N., TerAvest, M., Tang, D., Hou, J., Bertman, S., Alaghmand, M., Shepson, P.B., Carroll, M.A., Griffith, S., Dusanter, S., Stevens, P.S., 2011. Nitric acid photolysis on forest canopy surface as a source for tropospheric nitrous acid. Nat. Geosci. 4, 440–443. https://doi.org/10.1038/ngeo1164

CHAPTER 4 PRELIMINARY ANALYSIS OF THE ROx INTERCOMPARISON CAMPAIGN

Table of contents

Chapter 4. Preliminary analysis of the RO_x intercomparison campaign

This chapter reports a preliminary analysis of an intercomparison campaign held at the ICARE (Institut de Combustion Aérothermique Réactivité Environnement) institution in Orléans (France). The chemical amplifier described in chapter 2, a FAGE instrument developed at the PC2A laboratory (University of Lille) and a RO_x-CIMS instrument from the LPC2E laboratory (University of Orléans) were coupled to the HELIOS Atmospheric Simulation Chamber (ASC). The 3 instruments measured peroxy radical concentrations simultaneously during several oxidation experiments.

In this chapter, we first describe HELIOS and the various instruments that were coupled to this ASC for the peroxy radical intercomparison. The radical measurements are then compared to and contrasted with box model simulations to get insights into both the reliability of these measurements and the kinetic experiments performed in HELIOS.

4.1 Introduction

Intercomparison exercises are an important stage in the development and validation of analytical instruments and measurement techniques. Such experiments can be performed under controlled conditions in ASC or under more realistic conditions in ambient air during intensive field campaigns. The use of an ASC overcomes the problem of sampling inhomogeneities which cannot be excluded in ambient air (Fuchs et al., 2010; Schlosser et al., 2009). Potential calibration errors during these exercises also represents an important aspect that can be investigated through exchanges of calibration sources.

Few ambient and chamber intercomparison exercises have been conducted for HO_2 and RO_2 measurement techniques during the last decades. Fuchs et al. (2010) performed a formal blind intercomparison for HO_2 measurements involving three FAGE instruments during the HOxComp campaign in ambient air and in the SAHIR chamber at the Forschungszentrum Julich in Germany. All instruments were based on the same calibration scheme, i.e. the water photolysis approach (chapter 1, section 1.2.5). The measurements included three days of sampling of ambient air and six experiments in SAPHIR (Oxidation of various hydrocarbons and ozonolysis of alkenes). For both ambient and SAPHIR observations, the measurements were highly correlated between each

instrument, quantitative agreement was variable. The ambient results revealed significant discrepancies between instruments with regression slopes ranging between 0.59 and 1.46. The measurements performed inside the chamber were in better agreement with regression slopes in the range of 0.69 to 1.26. While these results indicate differences that lies within measurement uncertainties, the linear regressions between measurements performed in SAPHIR were statistically improved when the data was grouped into subsets of similar water-vapor concentrations, suggesting an unknown artifact that is related to water-vapor. An older intercomparison of ambient HO_2 measurements was performed between the Penn State LIF-FAGE instrument and the NCAR/University of Colorado PerCIMS instrument at a rural site in the US, indicating an excellent agreement with a regression slope close to unity (Ren et al. 2003).

Similarly, only a few ambient and chamber intercomparisons have been reported for total peroxy radicals ($[HO_2] + [RO_2]$), and these have produced mixed results. There was only one attempt to intercompare instruments measuring total peroxy radicals inside an ASC, that has been reported involved the Julich RO_xLIF and MIESR instruments (Fuchs et al., 2009). The authors report a comparison during two experiments that led to the formation of HO_2, CH_3O_2, and $C_4H_7O_2$ in the chamber from the OH-oxidation of methane and 1-butene. The results indicated an excellent agreement, with a regression slope of 0.96 and a r^2 factor of 0.85. The most recent ambient intercomparison field study for total peroxy radicals involved a chemical amplifier (ECHAMP) and a FAGE instrument during the IRRONIC field campaign at a forested site in Indiana. While the two instruments were not measuring exactly the same pool of peroxy radicals, measurements of calibration sources based on acetone photolysis and water photolysis were in agreement within 12%. In addition, the comparison of ambient data provided encouraging results that the two instruments were consistent with each other. Another chemical amplifier (PERCA) and the MIESR technique were compared in a rural, semi-polluted site, during the BERLIOZ campaign for two days as reported in Platt et al. (2002). The results indicated a good agreement with a slope of 1.07 and a R^2 factor of 0.91. However, a previous intercomparison campaign conducted in a forest between two chemical amplifiers (PERCA) showed differences up to a factor of 3 (Burkert et al., 2001).

These intercomparison experiments have sometimes highlighted good agreement between instruments, but have also shown some disagreements. In addition, intercomparison experiments involving all types of instruments have yet to be performed.

4.2 Description of HELIOS chamber and the experiments conducted

4.2.1 Characteristics of the HELIOS chamber

HELIOS (Figure 4.1) is one of the largest outdoor chambesr in the world, which has been assembled on the roof of the ICARE building in Orleans (France). A detailed description of the chamber can be found in Ren et al. (2017). This ASC consists of a Teflon FEP film of hemispherical shape (volume of 90 m^3, thickness of 250 µm) that is supported by an epoxy frame. The epoxy frame inside the chamber is covered by Teflon tubes to minimize surface interactions with the air mixture. A movable protective housing system allows the chamber to be quickly opened and closed to control exposure of the mixture to sunlight. The irradiation conditions can be changed from full sunlight to completely dark within 30 s, allowing the study of both daytime and nighttime chemistry. The FEP material is known to be transparent to solar radiation allowing transmission of 88 to 95% of sunlight, depending on the wavelength. The base of the chamber has four access ports to enter the chamber from the laboratory located below. The floor of the chamber is also covered by FEP material (500 µm thickness), so that the whole inner surface of the chamber has the same physico-chemical properties.

Dry zero air is supplied by a generator from AADCO Instruments (737 series) and two fans are installed opposite to each other inside the chamber to mix the reactants within 90 s. Compounds are introduced into the chamber wither by vaporizing a known amount of the liquid chemical in a flow of zero air using a syringe, or by injecting a know volume of a gas mixture. The chamber is flushed with zero air at 800 L min^{-1} each night between experiments to clean the chamber. When ozone is introduced into the chamber, it is generated through photo-dissociation of oxygen using a Pen-RAY mercury lamp in a small flow of zero air.

SF_6 was injected in the chamber as a dilution tracer during the experiments and was measured using the FTIR (see section 4.2.2.1). For all experiments, the dilution rate was calculated to be $k_{SF6} = 1.7\times10^{-5}$ s^{-1}.

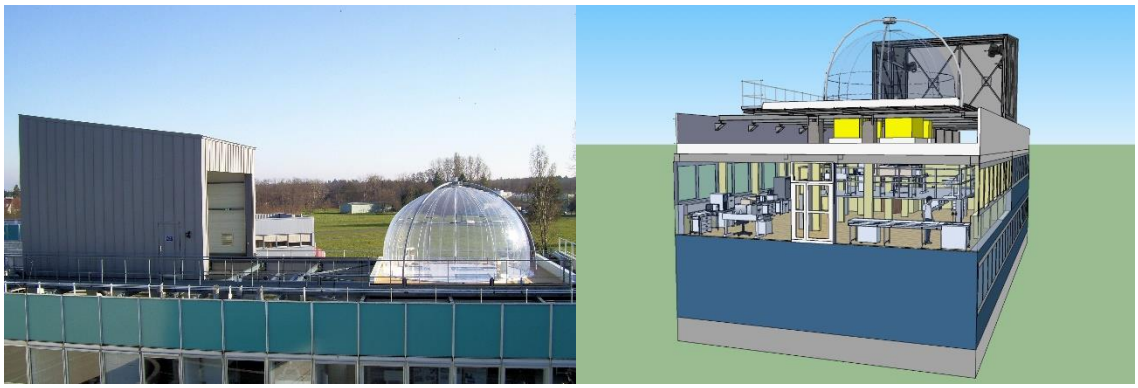

Figure 4.1 Photograph of the HELIOS chamber (Left) and 3D view (Right). (www.helios-cnrs.org)

4.2.2 Instruments coupled to HELIOS

4.2.2.1 Measurements of trace gases and meteorological parameters

Several instruments sampled from HELIOS for the intercomparison experiments (Table 4.1), including a Proton Transfer Reaction-Time of Flight Mass Spectrometer (PTR-ToFMS), monitors for CO, formaldehyde and NO_x, a spectroradiometer and several RH and temperature probes.

The PTR-ToFMS method is based on soft ionization of VOCs using H_3O^+ as reagent ions to produce ionized VOCs that are then detected by a ToFMS detector. H_3O^+ is produced by flowing water-vapor in a high voltage discharge (hollow cathode) and then injected into a reaction chamber (drift tube) to react with the sampled VOCs. VOCs are separated in the ToFMS based on their mass-to-charge ratio (m/z). In this work, the PTR-ToFMS mass spectra were analyzed with the PTR-ToF Data Analyzer Software (Müller et al., 2013) with detection limits as reported elsewhere (Ren et al., 2017) and ranged from 0.1-0.2 ppbv.

The Formaldehyde (HCHO) measurements made use of an Aerolaser AL4021 analyzer which exhibits a detection limit and a precision of ≈100 pptv and 2%, respectively. This analyzer is based on the Hantzsch reaction in liquid phase, involving the reaction of HCHO with acetyl-acetone and ammonia to form 3,5-diacetyl-1,4-dihydrolutidine (DDL).

The NO_x concentrations were measured using a chemiluminescence analyzer from ThermoFisher (Model 42i Trace Level). The analyzer has a detection limit of approximately 50 pptv. A CAPS (Cavity Attenuated Phase Shift) instrument from AERODYNE was also used for selective NO_2

measurements. The supporting measurements of carbon monoxide were performed by in situ FTIR spectroscopy (Bruker Vertex70 spectrometer) coupled to a White-type multipass cell (302.6 m optical path length). Ozone concentrations were measured using a UV-absorption analyzer (HORIBA, APOA 370) with limit of detection of 1 ppbv

Photolysis frequencies of H_2O_2 and NO_2 were measured by a spectroradiometer (Meteorologie Consult GmbH 6007). Six thermocouples (PT-100) and RH probes were distributed through out the chamber to measure temperature and humidity. Temperature differences between measuremnets were within ±1K for the temperature.

Table 4.1 Specifications of instruments used during the peroxy radical intercomparison

	Technique	LOD
CO	FTIR	
VOCs	PTR-ToFMS (IONICON 8000)	0.1-0.2 ppbv
HCHO	Aerolaser AL 4021	≈100 pptv
Ozone	UV-absorption analyzer (HORIBA, APOA 370)	1 ppbv
NO_x	Chemiluminescence analyzer (ThermoFisher, Model 42i Trace Level).	≈50 pptv
$J(H_2O_2)$ and $J(NO_2)$	Spectroradiometer (Meteorologie Consult GmbH 6007)	
Pressure, temperature, relative humidity	Thermocouples (PT-100), Pressure and RH probes.	

4.2.2.2 UL-FAGE: HO_2 and HO_2^*

The UL-FAGE instrument has a design similar to that described in chapter 3. This instrument is made up of two fluorescence cells that are connected in series to measure OH and HO_2 radicals. The technique and its principle have been detailed in chapter 1 and in previous reports (Amedro et al., 2012; Parker et al., 2011). The HO_2 cell is downstream of the OH cell and the pressure in each is about 1.9 torr. Ambient air is pumped at 9.2 L min^{-1} through a 1 mm pinhole using an Edwards GX6/100L pump. OH excitation (308.244 nm/ $Q_1(3)$) is performed by a 5 kHz laser using a frequency doubled dye laser (Sirah Laser PrecisionScan PRSC-24-HPR) pumped by the frequency doubled output of a Nd:YVO4 laser (Spectra Physics Navigator II YHP40-532QW). The detection limits for OH and HO_2 are 3×10^5 and 4×10^6 molecule cm^{-3}, respectively.

In this campaign, the HO_2 detection cell was used to sequentially measure HO_2 (low NO concentration of 3.7×10^{12} molecule cm^{-3} added) and HO_2^* (high NO concentration of 7.3×10^{13} molecule cm^{-3}). The measurement mode was switched every 3-5 minutes for the experiments performed in HELIOS.

4.2.2.3 IMT LILLE DOUAI CA: HO_2+ RO_2

The dual channel Chemical Amplifier (CA) used during the intercomparison campaign was described in Chapter 2. The only difference between the configuration reported in chapter 2 and this campaign was the length of the two reactors, and the length of the Teflon tube bringing the sample to the CAPS detectors, which were extended to 5 and 4 m, respectively. The amplification chemistry used during this campaign was based on the PERCA approach (CO/NO reagents) and the CA is referred to as PERCA in the following.

Briefly, the instrument was operated in two modes (amplified and background modes). In the amplified mode, NO and CO reagent gases are added to the reactor (right after sampling) to convert sampled peroxy radicals (through an amplification chemistry), ambient NO and O_3 into NO_2. In background mode, CO is replaced by N_2, ambient NO and O_3 are converted into NO_2 and the peroxy radicals are not amplified. The difference in NO_2 between the two modes is used to derive the ambient HO_2+RO_2 concentration provided that the Chain Length (CL) of the amplification

chemistry has been adequately characterized. The CL calibrations with the longer reactor are described in the calibration section (4.2.4).

4.2.2.4 Orleans-CIMS: HO_2+ RO_2

The CIMS instrument was used to measure OH and total peroxy radicals (HO_2 + RO_2). The principle of this technique was described in chapter 1 and details on the instrument used during the intercomparison exercise can be found in Kukui et al. (2008). Briefly, the instrument consists of a chemical conversion reactor (CCR), an ion molecule reactor (IMR) and a mass spectrometer. This CIMS has two measurement modes to differentiate between OH and total peroxy radicals. In OH mode, only SO_2 is added to the reactor to convert the sampled OH into H_2SO_4 in the presence of water vapour and oxygen. For total peroxy radical measurements, SO_2 and NO are added to the CCR where RO_2 and HO_2 are converted into OH via reactions with NO. OH is then converted into H_2SO_4, which is ionized into HSO_4^- (NO_3^- reagent ion) in the IMR. Air is sampled at a flow rate of 10 lpm, creating a turbulent flow in the CCR which provides a fast conversion of OH into H_2SO_4.

4.2.3 Description of HELIOS experiments

Several experiments were conducted in HELIOS from 8-16 October 2018 to generate different pools of peroxy radicals as shown in Table 4.2. These experiments are discussed in the following sub-sections.

Table 4.2 Experiments conducted during the peroxy radical intercomparison

Date (2018)	Chemical system	Irradiation conditions	Ranges of RH and T	Peroxy radicals generated
8 Oct.	**Production of HO_2** Oxalyl chloride $(ClCO)_2$ + dihydrogen (H_2)	sunlight	5-45 % 15-35 °C	HO_2
10 Oct.	**Ozonolysis of pentene** Pentene (C_5H_8) + ozone (O_3)	dark	30-50% 15-30°C	Pentene-RO_2 HO_2
12 Oct.	**Production of HO_2 & CH_3O_2** Oxalyl chloride $(ClCO)_2$ + dihydrogen (H_2) + methane (CH_4)	sunlight	65-30% 20-30°C	HO_2 CH_3O_2
15 Oct.	**Ozonolysis of α-pinene** α-pinene ($C_{10}H_{16}$) + ozone (O_3)	dark	50-35% 20-25°C	α-pinene-RO_2 HO_2

4.2.3.1 *Photolysis of oxalyl Chloride in presence of dihydrogen and methane*

The goal of these experiments was to investigate the response of the three instruments to two of the most abundant peroxy radicals in the atmosphere, i.e. HO_2 and CH_3O_2. These radicals were produced from the oxidation of dihydrogen and methane.

Oxalyl chloride, $(ClCO)_2$ has been used a source of chlorine atoms for kinetic experiments. Several studies investigating the $(ClCO)_2$ photodissociation at 193, 248, and 351 nm suggest a two-step mechanism involving the formation of an excited ClCO* radical (R1) (Ahmed et al., 1997), which can then dissociate into Cl and CO (R3) depending on the photolysis wavelength (Baklanov and Krasnoperov, 2001; Hemmi and Suits, 1997) :

$$(ClCO)_2 + h\nu \rightarrow ClCO^* + CO + Cl \qquad \text{R1}$$

$$(ClCO)_2 + h\nu \rightarrow Cl_2 + 2CO \qquad \text{R2}$$

$$ClCO^* \rightarrow Cl + CO \qquad \text{R3}$$

The chlorine atom can react with hydrogen (H_2) or methane (CH_4) to generate hydrogen chloride and HO_2 or CH_3O_2. The reactivity of Cl atoms towards most VOCs is similar to that of OH radical (though often faster), proceeding via H-abstraction. The reaction mechanisms are simplified as follows:

$$Cl + H_2 \xrightarrow{O_2} HCl + HO_2 \qquad \text{R4}$$

$$Cl + CH_4 \xrightarrow{O_2} HCl + CH_3O_2 \qquad \text{R5}$$

The yield of Cl atoms was found to be dependent on the wavelength of the photolysis radiation. The Cl yield was determined by the ICARE group inside the HELIOS under sunlight exposed conditions (unpublished work). The relative yields of CO and Cl were derived by comparing the $(ClCO)_2$ loss rate with the production rates of CO and Cl atoms. The Cl production rate was derived from the measured steady state of HO_2 or CH_3O_2 radical concentrations generated by scavenging Cl by H_2 or CH_4, respectively. Relative Cl yields of unity and 0.45 have been observed at 3% and 30% relative humidity, respectively.

The peroxy radicals generated in the chamber will then react by self- and cross-radical radical reactions:

$$HO_2 + HO_2 + M \rightarrow H_2O_2 + O_2 + M \qquad \text{R6}$$

$$CH_3O_2 + CH_3O_2 \rightarrow CH_3OH + CH_2O + O_2 \qquad \text{R7a}$$

$$CH_3O_2 + CH_3O_2 \rightarrow CH_3O + CH_3O + O_2 \qquad \text{R7b}$$

$$CH_3O_2 + HO_2 \rightarrow CH_3OOH + O_2 \qquad \text{R8}$$

H_2 and CH_4 oxidation experiments were carried out separately in HELIOS on 8 and 12 October 2018, respectively.

4.2.3.2 *Ozonolysis of pentene and α-pinene under dark conditions*

A second group of experiments was designed to investigate the response of the three radical instruments to more peroxy radicals more complex than HO_2 and CH_3O_2. It was chosen to perform ozonolysis experiments of alkenes under dark conditions to generate simple (pentene-based RO_2) and more complex (α-pinene-based RO_2) pools of peroxy radicals. Dark conditions were chosen to exclude photochemical reactions and to simplify the chemistry in the chamber. These two compounds exhibit quite different rate constants with O_3, with α-pinene being much more reactive than pentene. The reaction rate constant for 1-pentene and O_3 has been determined in several studies to be 1.1×10^{-17} cm^3 $molecule^{-1}$ s^{-1} (Avzianova and Ariya, 2002) while the rate constant for α-pinene is approximately 10 times faster with a value of 1.3×10^{-16} cm^3 $molecule^{-1}$ s^{-1} (Duncianu et al., 2012) . Pentene and α-pinene ozonolysis experiments were carried out in HELIOS on 10 and 15 of October 2018, respectively.

Ozonolysis reactions of alkenes form a primary ozonide as described in chapter 1 (section 1.1.1.1), which then rapidly decomposes to produce carbonyls and Criegee biradical products. The excited Criegee biradical can either promptly decompose into radicals and stable products or become collisionally stabilized to form a stabilized Criegee intermediate (Atkinson et al., 1995; Horie and Moortgat, 1991; Nguyen et al., 2016; Ren et al., 2017), which will then slowly decompose into OH or react with water-vapor.

4.2.4 Description of the PERCA calibrations

PERCA was calibrated as setup on HELIOS, i.e. with a longer reaction tube due to practical limitations to couple the inlet of the instrument to the chamber (see section 4.2.2.1). Calibrations were performed using the water-photolysis radical source described in Chapters 1-3. Briefly, a known concentration of water-vapor is photolyzed at 184.9 nm by the emission of a mercury lamp to generate known concentrations of both OH and HO_2. Isoprene was added to the calibrator to convert OH radicals into isoprene-RO_2 radicals as described in chapter 2.

The CIMS calibration source from the LPC2E laboratory was also sampled with the chemical amplifier to check whether the concentrations generated by this calibrator were consistent with those measured by PERCA. This cross-check of calibration sources is essential to determine

whether differences in chamber measurements could be due to calibration issues. The LPC2E calibrator is described in details in Kukui et al. (2008). While this calibration source is also based on the water-photolysis technique, a different actinometry approach was used to assess the generated radical concentrations (N_2O actinometry). The radicals are generated by the photolysis of humid air in a circular flow-tube (D:1.8 cm & L:70 cm). The air flow rate used with this system ranges between 24 and 40 L min^{-1}, leading to turbulent conditions. The UV light emitted by the mercury lamp is directed through a 10×5 mm quartz window and its intensity could be varied using a N_2O chemical filter placed between the lamp housing and the flow tube. The light passes through a 184.9 nm bandpass filter before detection by a phototube after the photolysis zone. Water-vapor is generated by a set of a liquid mass flow controllers and an evaporator (Bronkhorst) and is measured by a humidity sensor placed at the entrance to the calibrator. The water system allows generating relative humidity ranging from 1 to 70 %.

The impact of water on the PERCA chain length is one of the most important effects that has to be taken into account when calibrating this instrument. The CL dependence on water has been discussed based on modelled and experimental considerations as described in Chapters 1 & 2. It was shown that the CL decreases with increasing relative humidity due to additional losses of radicals on the reactor wall and from an increase in the formation yield of HNO_3 of the HO_2+NO reaction. The CL dependence on relative humidity needs to be characterized accurately for each particular setup. As mentioned above, the two reactors of the chemical amplifier were replaced by new Teflon tubes having a length of 5 m (longer than used previously) to be able to place the sampling inlet within the HELIOS chamber.

Full calibrations of the CL as a function of relative humidity were performed three times before (5 October), during (11 October) and after (18 October) the chamber measurements to track the CL over the whole campaign. The results shown in Figure 4.2 reveal that the measured CL (black opem symbols), displayed vs. RH, was not stable over time and a decreasing trend was observed during the campaign. This behavior has been observed experimentally when PTFE reactors were tested on the laboratory prototype (Chapter 2, supplementary section). It was shown that the CL decreased from day to day until it reached a stable value close to that observed for PFA material, which was attributed to the aging of the surface inside the reactor. Interestingly, the calibration performed on 18 October is close to that observed for the regular configuration of the chemical amplifier (Chapter 2, figure 5) once the reactors have been passivated for a long period of time.

For this study we assumed that the CL was decreasing linearly with time and we generated interpolated calibration curves for the other days of the campaign as shown in Figure 4.3 as filled symbols. Only experimental calibrations performed on 5 and 18 October were used to interpolate the CL along the campaign and the calibration performed on 11 October was used as an indicator to check the reliability of these interpolations. As shown in Figure 4.2, the procedure used to interpolate the CL was able to resonably reproduce the values from calibrations on 11 October. The calibration curves shown in Figure 4.2 were used to determine the concentrations of radicals within HELIOS for each of these days.

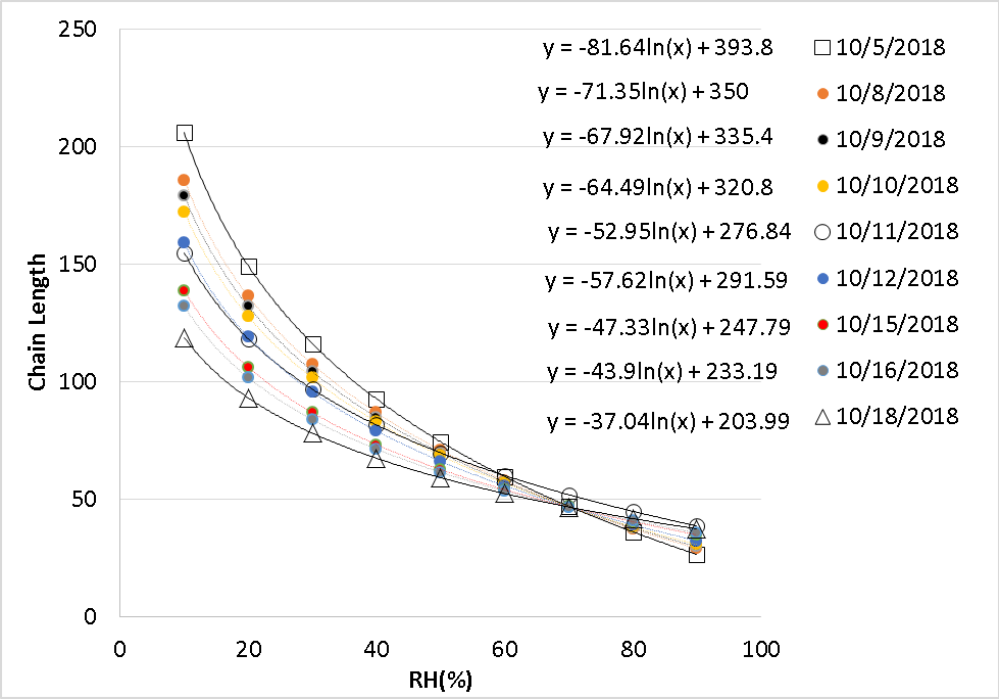

Figure 4.2 Average calibration curves of the chemical amplifier CL during the peroxy radical intercomparison. The curves come from non-linear fits to a logarithmic function. Empty and filled markers are measured and interpolated CL values, respectively.

The CIMS calibration source was tested on PERCA on 11 October. Several concentrations of HO_2+CH_3O_2 ranging from 5×10^9 to 1.6×10^{10} cm^{-3} were generated at RH values ranging from 9 to 29.8% at 28°C. The PERCA instrument was able to retrieve the generated concentrations within 23%.

4.3 Comparison between measured peroxy radicals (CA, SAMU, FAGE)

This section describes the measurements performed during the four experiments reported in Table 4.2. The comparisons between instruments is discussed for each experiment and general conclusions summarizing all the results is presented to provide an overall picture of the comparison exercise.

Here we remind the reader that the chemical amplifier and SAMU measures $HO_2+\sum(1-Y)\times RO_2$, where Y is a parameter accounting for the organic nitrate yield from RO_2+NO and the organic nitrite yield from RO+NO in the conversion chemistry of the two instruments. FAGE measured HO_2 (low NO added in the detection cell) and HO_2* (high NO), the latter being the sum of HO_2 and alkene- and aromatic-based peroxy radicals (see chapter 1, section 1.2.4).

4.3.1 Oxalyl chloride photolysis experiments

4.3.1.1 Dihydrogen / Oxalyl chloride: H_2 + Cl → HO_2

Oxalyl chloride was photolyzed in the presence of H_2 to generate large concentrations of HO_2 inside HELIOS (R4, section 4.2.3.1). This chemical system was used first to test the response of the different instruments to the simplest peroxy radical and to check calibrations through the observation of the HO_2 decay rate when the chamber is rapidly brought into dark condition as performed in other recent studies (Onel et al., 2017a, 2017b) .

The injection sequence of reactants into the chamber is reported in Table 4.3. The experiment started by opening the chamber at 11.13 (zero air, background trace gases, RH<5%) before the injection of other gases to observe the background reactivity in the chamber. Hydrogen was injected at 14:35 (50 ppm in the chamber) and oxalyl chloride two times to increase its mixing ratio to 27 ppbv (14:52) and 92 ppbv (15:55).

Table 4.3 Experimental conditions on 8 October 2018 - H_2 / $(ClCO)_2$

Injection	1st	2nd	3rd
Injection Time	14:35	14:52	15:55
N_2, O_2	Pure air	Pure air	Pure air
Injection of H_2 and $(ClCO)_2$			
H_2 (ppm)	50		-
$(ClCO)_2$ (ppb)		0/27*	13/92*
HCHO, T and RH			
HCHO (ppb)	4		6
RH(%), T(ºC)	30/37		30/37

*before/after injection. All mixing ratios are measured values (with the exception of H_2)

Chemical species released by the chamber (wall desorption or reactivity) or produced from the oxidation of species released by the wall were observed in the chamber, including O_3, NO_2 and HCHO. The ozone concentration started to increase from below the detection limit to a maximum of 5 ppbv at mid-day. NO_2 increased over the experiment to a maximum mixing ratio of 7 ppbv while NO increased from the limit of detection to 0.4 ppbv and rapidly decreased below detection limit after the first injection of oxalyl chloride. Formaldehyde steadily increased over the experiment from the detection limit to a maximum mixing ratio of approximately 7 ppbv. The auxiliary mechanism for the background reactivity of this chamber has recently been reported on the EUROCHAMP-2020 website and confirms the release of these species and additional compounds such as HONO.

The peroxy radicals mixing ratios (HO_2+potential RO_2 generated from the oxidation of VOCs released by the wall) varied from approximately 1 pptv before irradiation (chamber in the dark, dry conditions) to approximately 200 pptv. The PERCA and SAMU measurements are in good agreement most of the time once oxalyl chloride was injected (after 14:52) with differences lower than 20%. A scatter plot of PERCA vs. SAMU is shown in figure 4.4 and indicates a slope of 1.06 and an intercept of 7.3 ppt. However, a close inspection of the comparison before 14:52 indicates that PERCA measured higher mixing ratios than SAMU and a scatter plot of this period (insert in figure 4.4) indicates a slope of approximately 1.6 with an insignificant intercept. Excluding the

period 12:15-14:15 from the analysis (red markers) leads to a slope of 1.09 and an intercept of 1.7 pptv. Indeed, the excluded period corresponds to the chamber humidification when RH was rapidly increased from approximately 3 to 30%. During this period, both FAGE and SAMU measurements did not vary significantly, only PERCA exhibited an increase in the measured mixing ratios. This rapid change in humidity likely disturbed the PERCA measurements, or the calculation of the CL used to derive the peroxy radical mixing ratios, due to either the formation of water-particles in the chamber when water was introduced (observed on SMPS measurements, not shown), a non-negligible time required to equilibrate the amount of water adsorbed on the PERCA reactors inner surface when RH changes rapidly, or the use of RH values measured in the chamber to calculate the CL in the reactors where RH may be lower.

Both the HO_2 and HO_2^* measurements from FAGE are significantly lower than the PERCA and SAMU measurements (approx. 58% of the SAMU measurements, Figure 4.5), which seems to indicate that organic peroxy radicals were present in the chamber perhaps due to the release of VOCs from the wall or some heterogeneous chemistry. Comparing HO_2 and HO_2^* suggest that alkene- and aromatic-based RO_2 were not present.

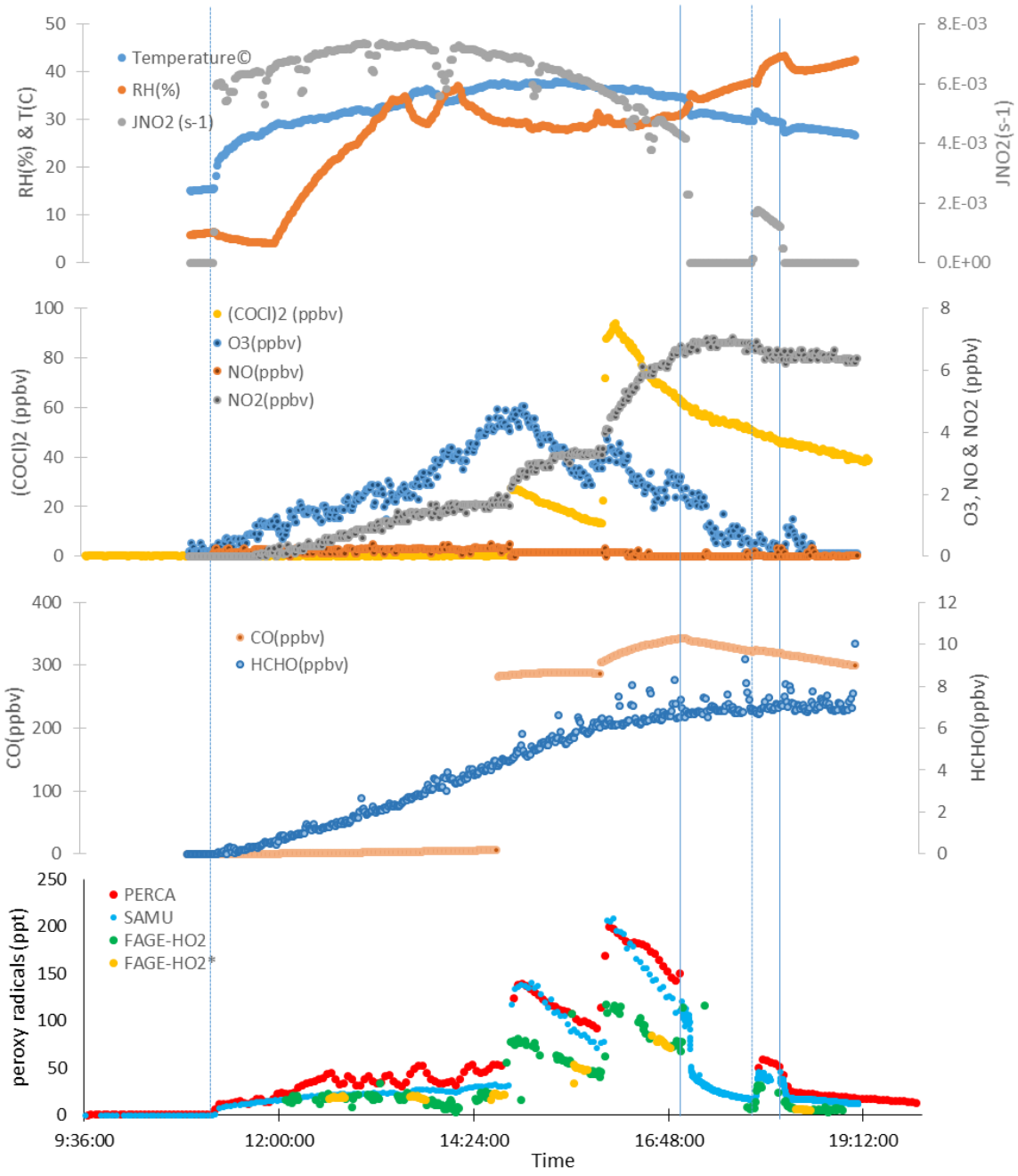

Figure 4.3 Peroxy radical and ancillary measurements for 8 October 2018. Peroxy radicals measured by PERCA (red markers), SAMU (Blue markers) and FAGE (HO_2-green markers & HO2*-yellow markers). Dashed and solid vertical lines refer to the opening and closing of the chamber, respectively.

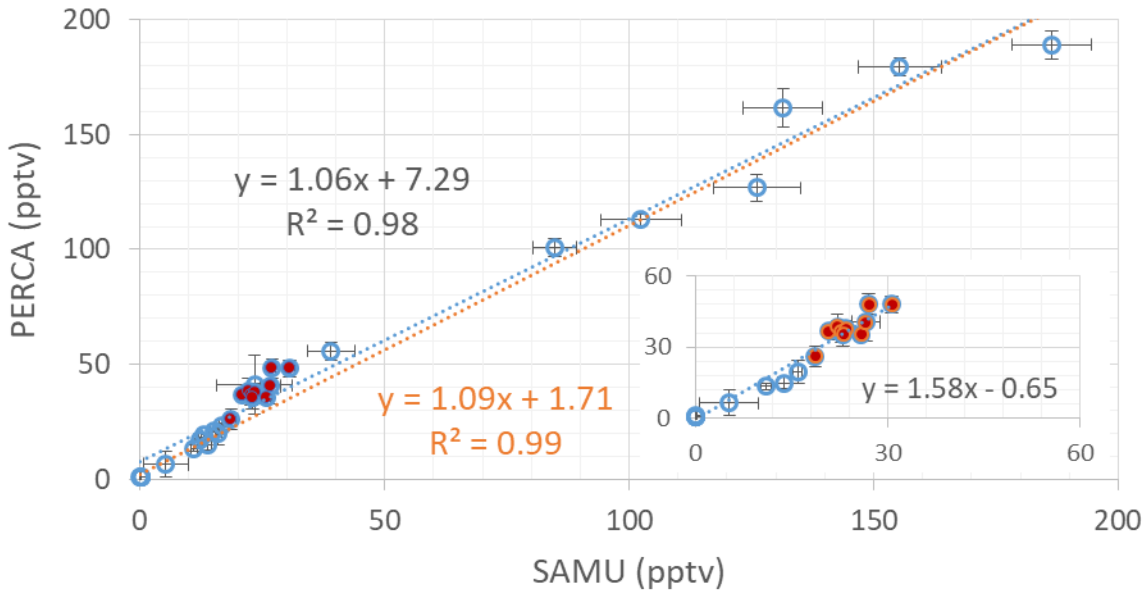

Figure 4.415 Scatter plot between PERCA and SAMU measurements for 8 October 2018 (15-min average). The red markers correspond to measurements performed between 12:15 and 15:15. Error bars are 1σ standard deviations.

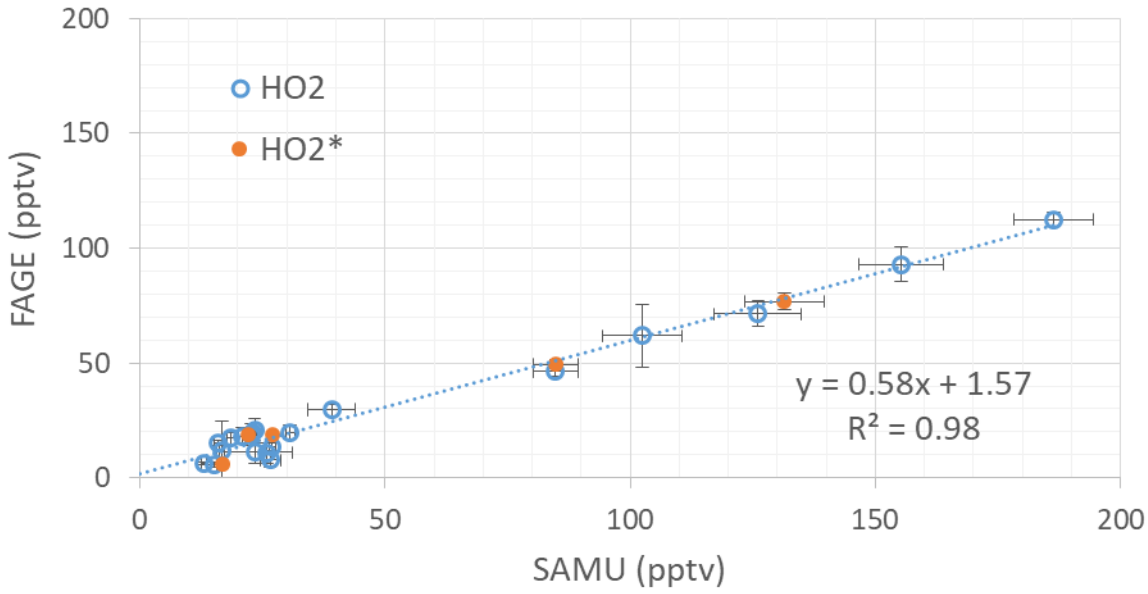

Figure 4.5 Scatter plot between FAGE and SAMU measurements for 8 October 2018 (15-min average). Error bars are 1σ standard deviations.

The chamber was closed at 17:03 and a rapid decay of peroxy radicals was observed by the three radical instruments. Assuming that only HO_2 was present in the chamber, the decay due to its self-reaction should be consistent with the following equation:

$$\frac{1}{[HO_2]} = \frac{1}{[HO_2]_0} + 2kt \qquad (4.1)$$

Here k reflects the HO_2+HO_2 rate constant of 4.5×10^{-12} cm^3 $molecule^{-1}$ s^{-1} at 33% RH.

In order to probe the decay at a high time resolution with PERCA, the switch between amplification and background modes in each reactor and the switch between the CAPS monitors (chapter 2, section 2.3.1) were turned off. This allowed acquiring data at a time resolution of 1 s. The analysis of the data shown in Figure 4.6 indicates that three different decay rates are observed (Figure 4.7). These decays (left to right in Figure 4.7) correspond to the closing period of the chamber (red markers), when the chamber was completely closed (yellow markers) and once a large fraction of the peroxy radicals had disappeared (>80%) (blue markers). The first decay was rejected since it corresponds to a period where the chamber was still partially irradiated by the solar light and radical production was still occuring. The second and third decays indicate that HO_2 was not the only peroxy radical present in the chamber and RO_2 radicals were also likely present as suggested by the difference between FAGE and SAMU or PERCA measurements. The second (faster) decay is mainly attributed to the HO_2+HO_2 reaction while the third (slowest) decay is likely due to RO_2+RO_2 reactions. The second decay rate would lead to a rate constant k of 3.4×10^{-12} cm^3 $molecule^{-1}$ s^{-1} using the PERCA data, which is lower than the self-reaction rate constant of 4.5×10^{-12} cm^3 $molecule^{-1}$ s^{-1} calculated for HO_2+HO_2 at an RH of 33% and a temperature of 30°C using the MCM parameterization (http://mcm.leeds.ac.uk/MCMv3.3.1/home.htt.). The analysis of the observed decay leads to an underestimation of the rate constant due to the assumption that the measured peroxy radicals are only HO_2. Interestingly, the third decay would lead to a rate constant for RO_2+RO_2 on the order of 5×10^{-13} cm^3 $molecule^{-1}$ s^{-1}, which is close to values reported for this type of reactions (Atkinson et al., 2001).

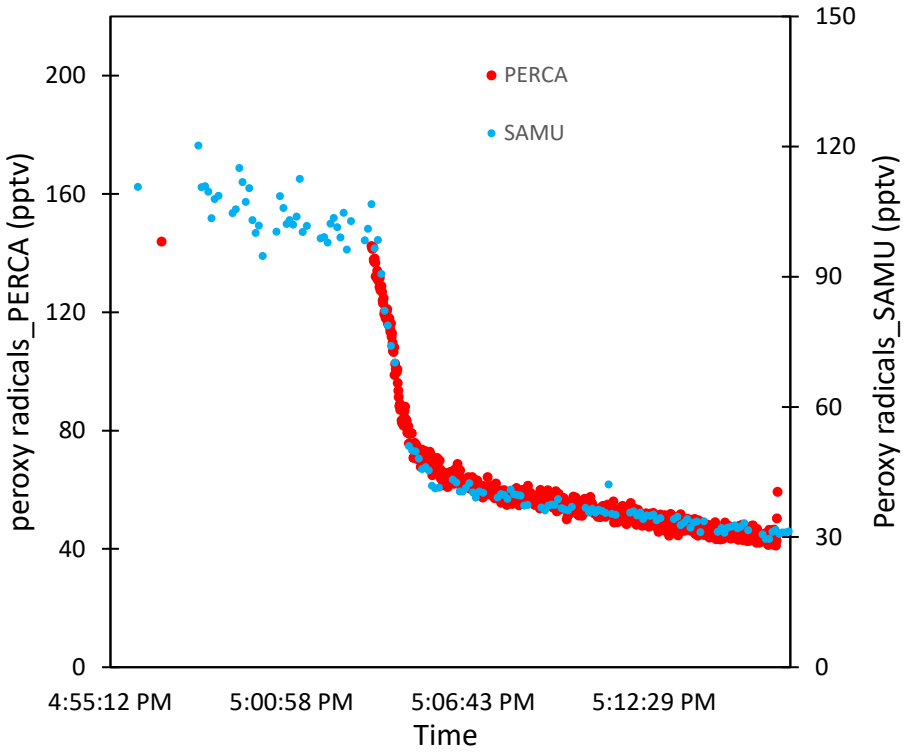

Figure 4.6 Peroxy radical (HO_2+RO_2) measured when the chamber is changed to dark conditions - PERCA (red markers) and SAMU(blue markers).

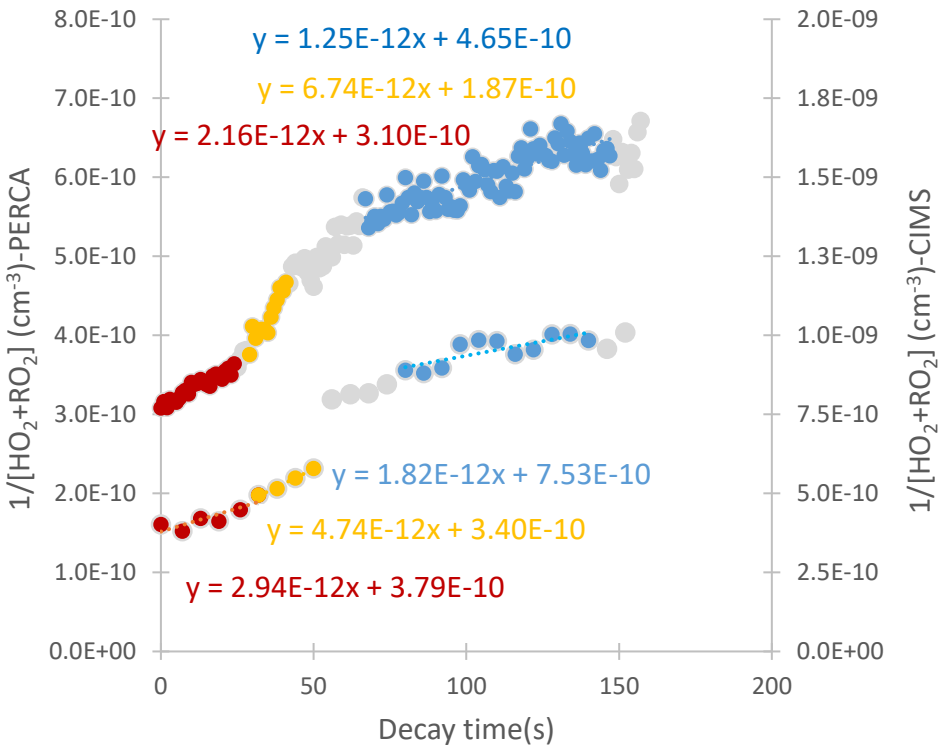

Figure 4.7 Peroxy radical (HO_2+RO_2) decay rates observed by PERCA (upper trace) and SAMU (lower trace) during the closing period of the chamber (red markers), when the chamber was completely closed (yellow markers) and once a large fraction of the peroxy radicals had disappeared (see text, blue markers).

The same analysis performed on the SAMU data (Figure 4.7) leads to similar conclusions. Unfortunately, the HO_2 data acquired during this period by FAGE needs to be revised and could not be used here to check whether the decay was consistent with the self-reaction of HO_2. It was therefore not possible to use this experiment to check the calibration of each instrument.

4.3.1.2 Hydrogen & methane / Oxalyl chloride: H_2, CH_4 + Cl → HO_2, CH_3O_2

A second experiment using **o**xalyl chloride was performed on 12 October. This experiment was conducted to reproduce the formation of HO_2 from H_2 oxidation (8 October) and to switch from HO_2 production to the production of both HO_2 and CH_3O_2 by adding methane to the chamber. The injection sequence is shown in table 4.4. Similar to the experiment performed on 8 October, the experiment started by opening the chamber (zero air, background trace gases, RH approx. 60%). Only one injection of approximately 45 ppbv of oxalyl chloride was performed at 11:20 AM after

the injection of 50 ppm H_2 (10:45). Methane was introduced at a mixing ratio of 20 ppmv at 12:38 PM.

Peroxy radical measurements from PERCA, SAMU and FAGE are shown in Figure 4.8 together with the measured J(NO_2), O_3, NO, NO_2, HCHO, CO and meteorological parameters. As seen during the 8 October experiment, species released by the wall of the chamber or produced from the oxidation of compounds released by the wall were observed in this experiment. Ozone, NO_2, NO and HCHO reached similar maximum mixing ratios of 3, 3, 0.4 and 7 ppbv, respectively, as during the 8 October experiment.

Peroxy radicals increased from less than 1 ppt for the 3 instruments to 20-25 ppt during the first 3 hours after opening the chamber (background reactivity). The peroxy radical concentrations produced from the chamber's background reactivity are similar to that observed on 8 October. Interestingly, the chamber was humidified to 60% RH before irradiation, and the PERCA measurements do not exhibit the same behavior as on 8 October, and are in better agreement with the FAGE HO_2 measurements. This observation seems to corroborate that rapid addition of water in the chamber has an impact on the PERCA measurements.

Table 4.5 Experimental conditions on 12 October 2018 (H_2/CH_4/$(ClCO)_2$)

Injection	1st	2nd	3rd
Injection Time	10:45	11:20	12:38
N_2, O_2	Pure air	Pure air	Pure air
	Injected H_2, $(ClCO)_2$ and CH_4		
H_2 (ppm)	50	-	
$(ClCO)_2$ (ppb)	-	0/45*	
CH_4 (ppm)	-	-	20
	HCHO, RH and T		
HCHO (ppb)	0.4	1.2	3.5
RH(%), T(ºC)	40,29	28/34	30/31

*before/after injection. All mixing ratios are measured values (with the exception of H_2 and CH_4)

Figure 4.8 shows that from 9:36 to 12:38 (before methane injection) the agreement between PERCA and SAMU is worse than on 8 October, with the SAMU measurements being approximately 30% higher. A fit to the scatter plot of PERCA versus SAMU has a slope of 0.72 and an intercept of 4.1 pptv. Similar to the 8 October experiment, the FAGE measurements are significantly lower suggesting the presence of organic peroxy radicals in the chamber. The similar concentrations measured for HO_2 and HO_2^* indicate that these RO_2 radicals, if present, are likely produced from the oxidation of saturated VOCs. A fit to the scatter plot of FAGE HO_2 versus SAMU (Figure 4.10) has a slope of 0.47 while on 8 October a slope of 0.58 was observed (Figure 4.5), i.e. ≈20% lower. The increase of SAMU measurements compared to both PERCA (+30%) and FAGE HO_2 (+20%) under similar experimental conditions than on 8 October may indicate an issue with the calibration of SAMU on this day.

Following the methane injection at 12:38, SAMU exhibits a quick response with an increase of 120 pptv of HO_2+RO_2. The PERCA instrument also measures a signal increase, but of only 82 pptv (approximately 70% of the increase observed for SAMU), which indicates a similar agreement between PERCA and SAMU for the H_2 and H_2/CH_4 mixtures. This can also be seen in Figure 4.9. This increase in HO_2+RO_2 is likely due to a decrease in the total loss rate of peroxy radicals since a certain fraction of HO_2 is replaced by CH_3O_2 whose self and cross- reactions with HO_2 are slower than the self-reaction of HO_2. Indeed, the FAGE instrument indicates a small decrease of HO_2 to approximately 47 pptv, which is consistent with the competition between Cl+H_2 (R4) and Cl+CH_4 (R5). As expected, HO_2^* does not increase due to the small conversion efficiency of CH_3O_2 radicals in the FAGE detection cell (chapter 3, section 3.2.1.2).

An attempt to close the chamber at 11:55 AM was performed to reproduce the radical decay observed on 8 October but technical problems led to reopen the chamber.

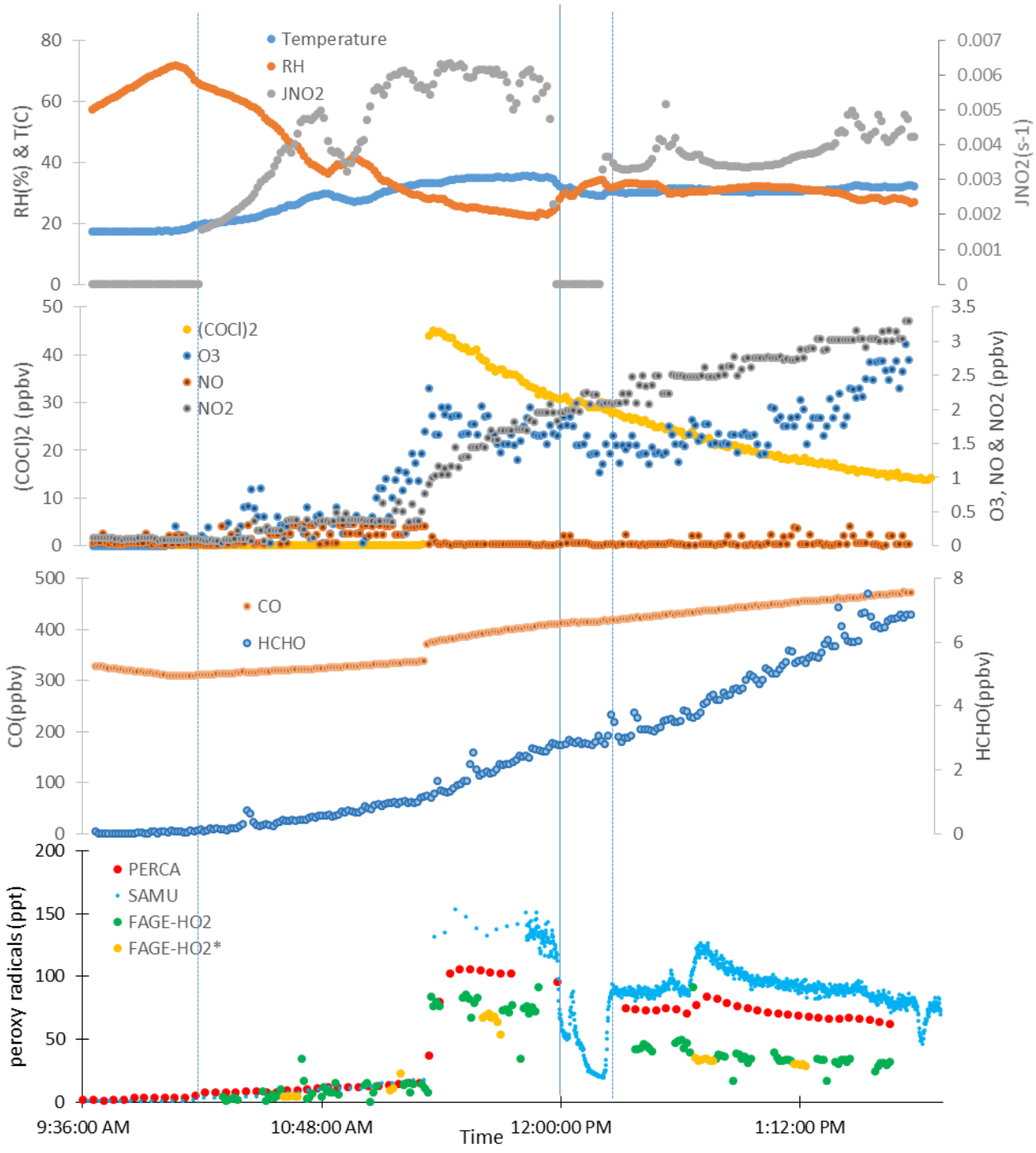

Figure 4.8 Peroxy radical and ancillary measurements for 12 October 2018. Peroxy radicals measured by PERCA (red markers), SAMU (blue markers) and FAGE (HO_2-green markers and HO2*-yellow markers). Dashed and solid vertical lines refer to the opening and closing of the chamber, respectively.

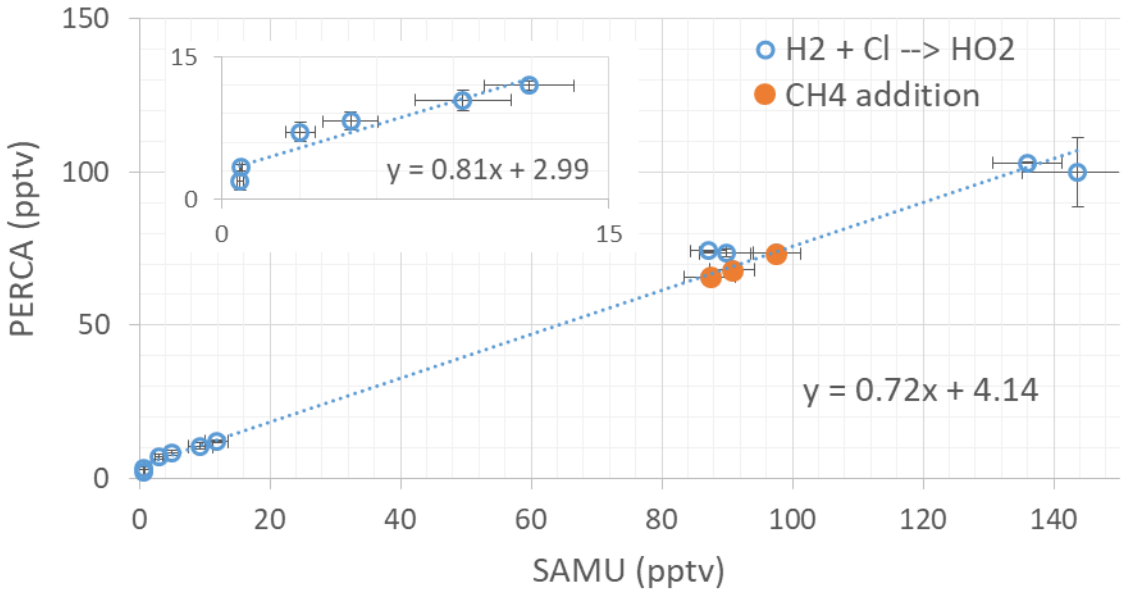

Figure 4.9 Scatter plot between PERCA and SAMU measurements for 12 October 2018 (15-min average). Error bars are 1σ standard deviations.

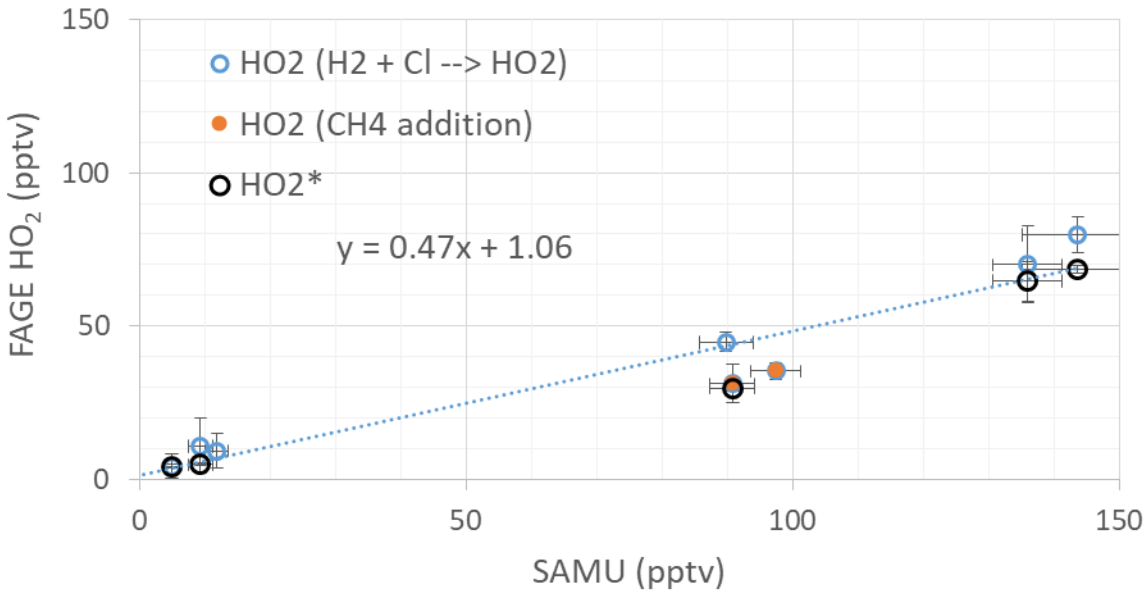

Figure 4.1016 Scatter plot between FAGE and SAMU measurements for 12 October 2018 (15-min average). Error bars are 1σ standard deviations.

4.3.2 Ozonolysis experiments under dark conditions

4.3.2.1 Pentene ozonolysis

The 1-pentene ozonolysis experiment was performed under dark conditions on 10 October 2018. This experiment was designed to generate a complex pool of RO_2 radicals at different concentrations, whose concentrations were adjusted by a stepwise increase of alkene and O_3 concentrations during the experiment.

The amount of O_3 and 1-pentene as well as the time sequence for the incremental additions are summarized in Table 4.5. The experiment started at 9:32 prior the injection of O_3 to probe the background reactivity inside the chamber (zero air, background trace gases, approximately 50% RH) under dark conditions only. The injection procedure started with 31 ppbv of ozone (10:24), followed by 2.48 ppbv of pentene (11:01) (Acros Organic, 97%) to initiate the ozonolysis reaction. Pentene and ozone were then injected 3 times (2.3 ppbv at 13:28, 6 ppbv at 14:53 and 13.1 ppbv at 17:11) and 2 times (36 ppbv at 11:58 and 57.4 ppbv at 16:10), respectively.

Time series of radical mixing ratios measured by PERCA, SAMU and FAGE together with the concomitant measurements are shown in Figure 4.11. HCHO reached a maximum value of 3.7 ppbv, which is slightly lower than observed in the photolysis experiments when the chamber was exposed to the sunlight (8 and 12 October). While in the previous experiments HCHO could not be produced from the $H_2/(ClCO)_2$ chemical system in the chamber, some of the observed formaldehyde in this experiment may be produced during the ozonolysis of 1-pentene. The CO mixing ratio increased during the experiment to reach a value of 163 ppbv at 18:52. NO_2 was observed to increase to approximately 1.4 ppbv in the middle of the experiment while NO mixing ratios were below the detection limit of 50 pptv of the analyzer.

The peroxy radical mixing ratios measured during the 1st hour (background reactivity under dark conditions) were less than 2 pptv for the 3 instruments. After the first injection of O_3 (10:24), prior to injections of pentene, the PERCA measurements increased to approximately 15 pptv while no change was observed for the 2 other instruments. In addition, each time that ozone was re-injected in the chamber in the presence of 1-pentene (11:58 and 16:10), a larger increase in radical concentrations was observed by PERCA compared to SAMU. This behavior seems to indicate that

the configuration of the chemical amplifier used during this intercomparison experiment was sensitive to ozone artifacts.

Table 4.6 Experimental conditions on 10 October 2018 (1-pentene/O_3)

Injection	1st	2nd	3rd	4th	5th	6th	7th
Injection Time	10:24	11:01	11:58	13:28	14:53	16:10	17:11
N_2, O_2	Pure air	Pure air	Pure air	Pure air	Pure air	Pure air	Pure air
	Injected pentene and ozone						
Pentene	0	0/2.48*	2	1.9/4.2*	3.7/9.7*	8.5	7.3/20.4
O_3 (ppb)	2/31*	28	25/61*	55	49	42.6/100	92
	HCHO, RH and T						
HCHO (ppb)	0.1	0.13	0.45	0.7	1	1.6	2.4
RH(%), T(ºC)	55, 16	48, 17	44, 19	35, 23	30, 25	28, 26	30, 26

*before/after injection. All mixing ratios are measured values

After each injection of pentene or O_3, all the radical instruments quickly responded to the change in radical production in the chamber, however, PERCA always measured peroxy radical concentrations that were significantly larger than SAMU. A linear fit to the scatter plot of PERCA versus SAMU is shown in Figure 4.12 has a slope of 1.74 and an intercept of 2.9 pptv. This difference between the two instruments is further discussed in the next section for the α-pinene/O_3 experiment.

The HO_2 measurements from FAGE slowly increased over time (as O_3 and pentene are added to the chamber) from below LOD to 9 pptv (Figure 4.11). A scatter plot of FAGE HO_2 vs. SAMU shown in Figure 4.13 indicates a good correlation with HO_2 accounting for 28% of HO_2+RO_2 from the linear fit. The FAGE HO_2* measurements become significantly higher than HO_2 as the ozonolysis rate of pentene is increased indicating that a small fraction of the RO_2 radicals generated in the chamber (≈ 11%) can be detected by FAGE using a large NO mixing ratio

inside the nozzle. The correlation plot between FAGE HO_2* and SAMU indicate a slope of 36% and an intercept of -0.2 pptv (Figure 4.13).

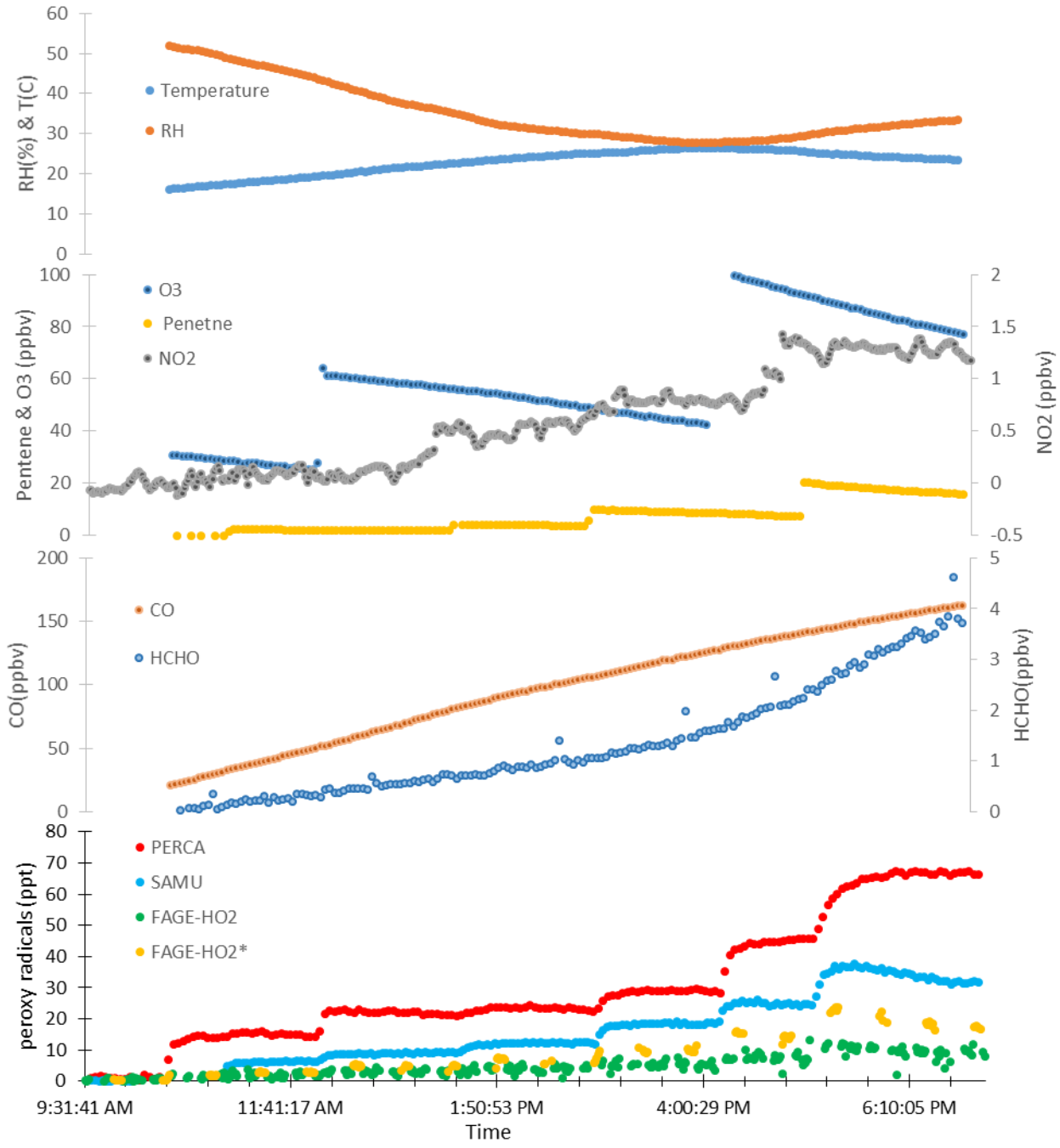

Figure 4.11 Peroxy radical and ancillary measurements during the 1-pentene ozonolysis experiment at HELIOS on the 10 October 2018.

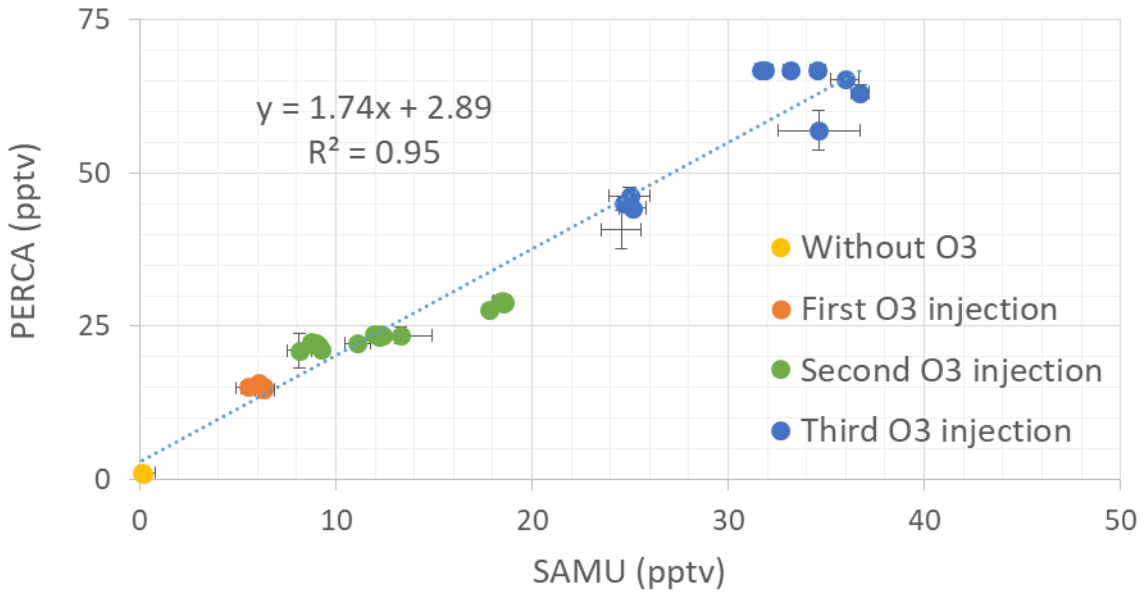

Figure 4.12 Scatter plot between PERCA and SAMU measurements data on the 10 October 2018 (15-min average measurements). Error bars are 1σ standard deviations.

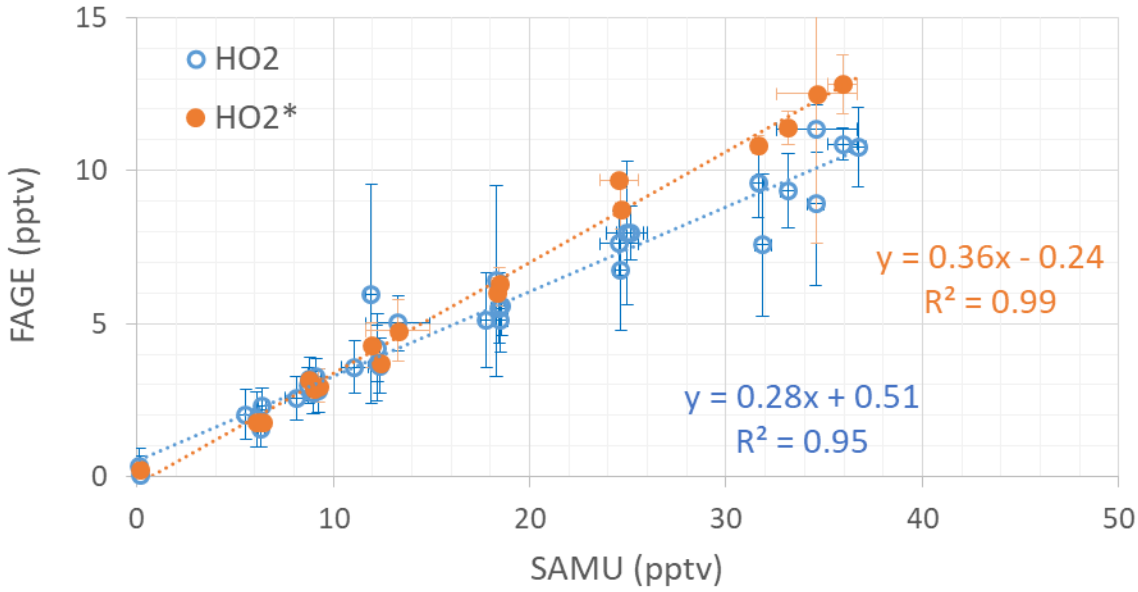

Figure 4.13 Scatter plot between FAGE and SAMU measurements data on the 10 October 2018 (15-min average measurements). Error bars are 1σ standard deviations.

4.3.2.2 α-pinene ozonolysis

The ozonolysis of α-pinene was conducted under dark conditions in Helios on 15 October. This experiment was performed to test the response of the different instruments to a more complex pool of peroxy radicals than in the three previous experiments.

A similar injection pattern than during the pentene/O_3 experiment was used here. The amounts of α-pinene (ACROS Organic, 97%) and ozone introduced in the chamber at each injection step are reported in Table 4.6. The experiment started at 9:10 prior to the injection of α-pinene to probe the background reactivity inside the chamber (zero air, background trace gases, RH of approximately 50%). The injection sequence initially started with 44 ppbv of ozone at 10:10 followed by 2.2 ppbv of α-pinene at 11:24. Further injections of ozone or α-pinene were performed approximately every 90 min throughout the experiment.

Time series of peroxy radicals and ancillary measurements are shown in Figure 4.14. HCHO and CO increased over the experiment to similar levels as observed 1-pentene, with maximum mixing ratios of 4 and 190 ppbv, respectively. NO_2 was present at a lower level of approximately 0.3 ppbv (up to 1.4 ppbv on 10 October) while NO was below the detection limit of the analyzer.

Similar to the pentene/O_3 experiment, peroxy radicals measured before any injections were lower than 2 pptv. The radicals mixing ratios measured by PERCA and SAMU increased up to 22 and 7 pptv, respectively, after the first injection of 44 ppb of ozone at 10:10. This behavior is different from that observed on 10 October where only PERCA measured a higher concentration of peroxy radicals when ozone was first introduced in the chamber. The higher concentration measured by SAMU likely indicates that unsaturated species present in the chamber (background air or adsorbed on the wall) were likely ozonized. However, the increase in mixing ratios observed for PERCA was significantly higher than observed for SAMU, which confirms the additional PERCA response to O_3 observed on 10 October (15 pptv increase in HO_2+RO_2 for 31 ppbv of O_3). The maximum mixing ratios measured by PERCA, SAMU and FAGE after injection of both O_3 and α-pinene were 84, 52 and 20 pptv, respectively.

Similar to the pentene/O_3 experiment, the PERCA measurements were always significantly higher than observed for SAMU. The fit of the scatter plot shown in the upper panel of Figure 4.15 (PERCA vs. SAMU) indicates a slope of 1.2 and an intercept of 12.7 pptv. Forcing the linear

regression to zero leads to a similar slope as for the pentene/O_3 experiment. The lower panel of Figure 4.15 shows the same scatter plot where the measurements have been grouped by O_3 injections. This figure shows that each time that O_3 was injected in the chamber, the intercept of the linear regression increases, likely due to an O_3 artefact on PERCA as pointed out for the pentene/O_3 experiment when only O_3 was injected in the chamber at the beginning of the experiment. Interestingy, the slope of each regression lines (periods when only α-pinene is injected in the chamber) range from 0.7 to 1, similar to the correlations observed during the H_2/$(ClCO)_2$ and H_2/CH_4/$(ClCO)_2$ experiments.

During this experiment, the HO_2 and HO_2* measurements from FAGE were similar, which indicates that RO_2 produced from the ozonolysis of α-pinene are not efficiently converted into HO_2 in FAGE at high NO levels. Figure 4.16 shows the good correlation between FAGE and SAMU measurements with a slope of 0.29 and a negligible intercept of 0.2 pptv.

Table 4.7 Experimental conditions on 15 October 2018 (α-pinene/O_3)

Injection	1st	2nd	3rd	4th	5th	6th	7th
Injection Time	10:10	11:24	12:31	14:02	15:15	16:40	18:20
N_2, O_2	Pure air	Pure air	Pure air	Pure air	Pure air	Pure air	Pure air
	Injected α-pinene and ozone						
α-pinene (ppb)	0	0/2.2*	1.3/4.2*	2.2	1/5.35*	2.5/12.2*	4.5
O_3 (ppb)	0/44*	36		/70*	60	50	41/96*
	HCHO, RH and T						
HCHO (ppb)	0.1	0.33	0.5	1	1.5	2.2	3.4
RH(%), T(ºC)	50, 20	46, 21	42, 22	36, 25	33, 26	30, 28	32, 26

*before/after injection. All mixing ratios are measured values

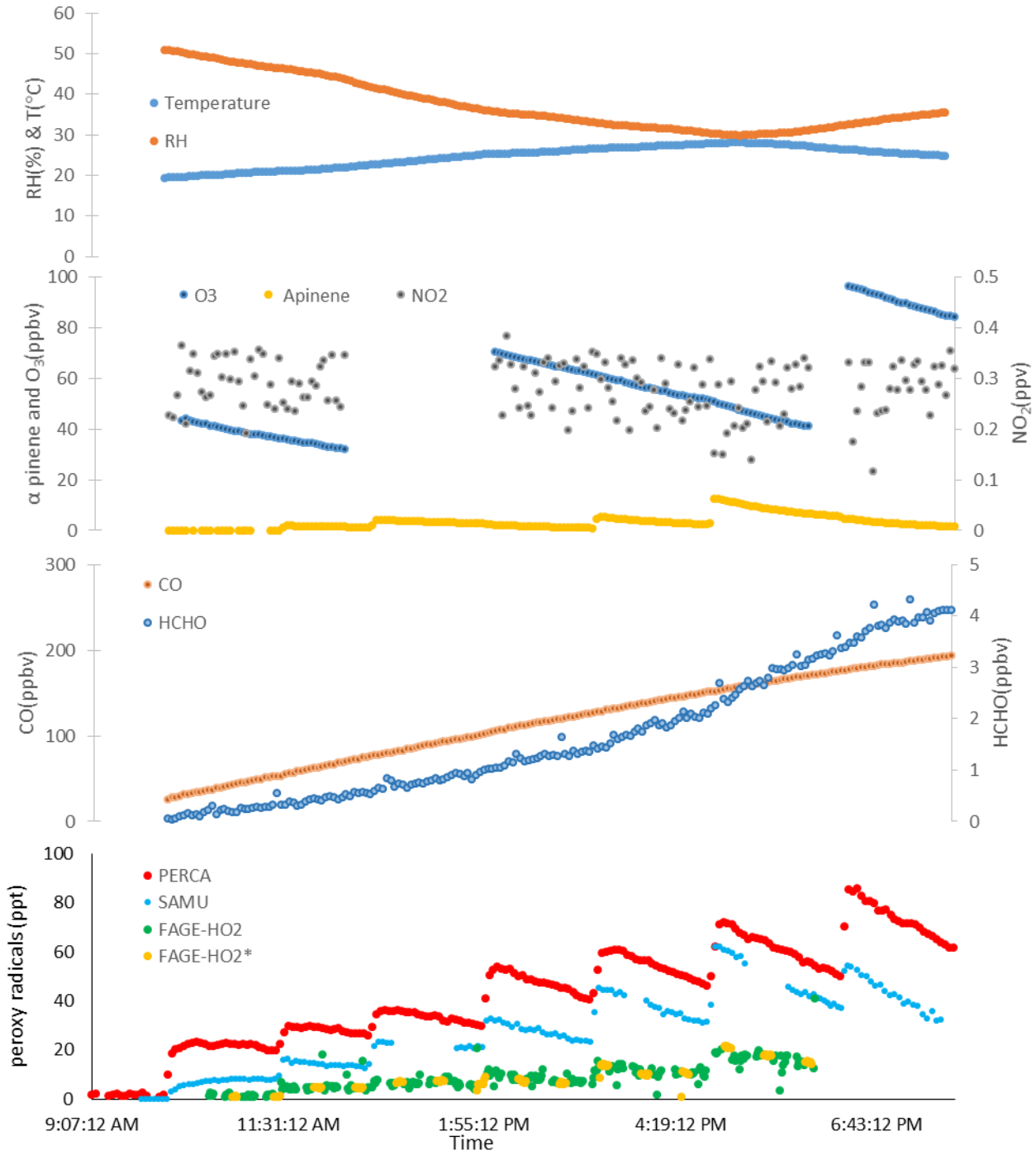

Figure 4.14 Peroxy radicals and ancillary measurements during the α-pinene ozonolysis experiment at HELIOS on the 15 October 2018.

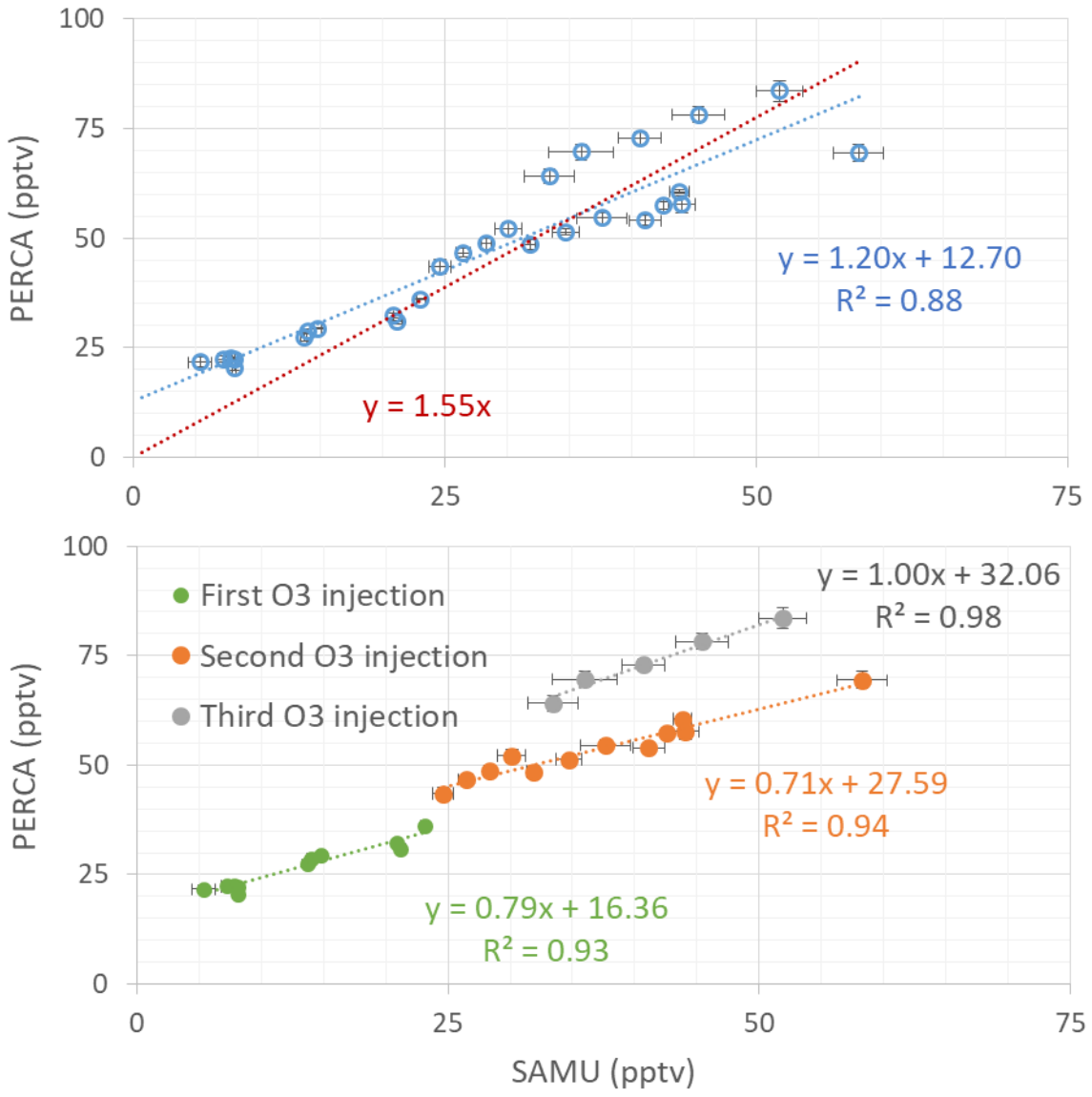

Figure 4.15 Scatter plots between PERCA and SAMU measurements on the 15 October 2018 (15-min average): Upper panel: comparison for the whole dataset, lower panel: measurements have been grouped into datasets depending on the number of O_3 injections. Error bars are 1σ standard deviations.

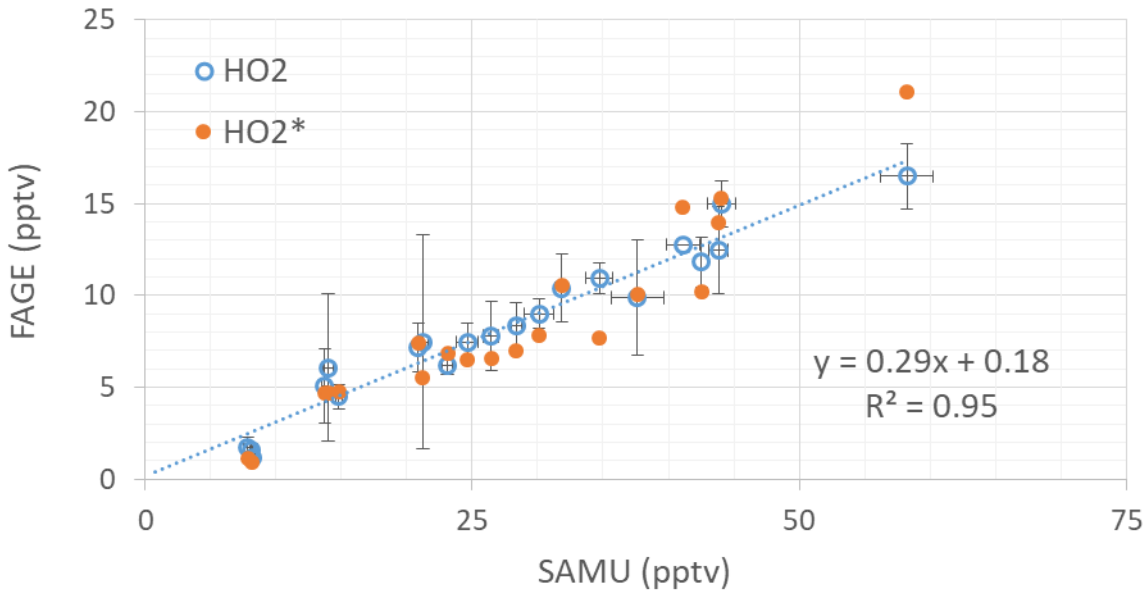

Figure 4.16 Scatter plot between FAGE and SAMU measurements on 15 October 2018 (15-min average). Error bars are 1σ standard deviations.

4.3.3 Conclusions

Several kinetic experiments were conducted in HELIOS to investigate the response of PERCA, SAMU and FAGE to different types of peroxy radicals starting from the simplest chemical system to generate (1) only HO_2 and increasing the complexity of the pool step by step by (2) adding CH_3O_2 and then peroxy radicals produced by the ozonolysis of (3) pentene and (4) α-pinene. PERCA and SAMU measurements were compared directly since both techniques measure the sum of HO_2+RO_2. FAGE measures HO_2 and HO_2^* (but not all RO_2) and as a consequence, the comparison with the other instruments was limited. However, the HO_2 measurements were of particular interest to gain insight into the contribution of HO_2 to the sum HO_2+RO_2.

The experiments conducted to investigate the response of all the instruments to HO_2 and then HO_2+CH_3O_2 showed that the PERCA and SAMU measurements were in agreement within 30%, which is within the measurement uncertainty of the 2 techniques. However, a systematic difference observed between the 2 experiments (PERCA vs. SAMU scatter plots with fits exhibit slopes of 1.09 for the H_2/$(ClCO)_2$ experiment and 0.72 for the H_2/CH_4/$(ClCO)_2$ experiment) pointing to a possible change in the calibration of one or both instruments. During these experiments, it was shown that RO_2 radicals were also produced when the H_2/$(ClCO)_2$ chemical system was used, likely due to the presence of contaminents in the chamber.

The ozonolysis experiments of 1-pentene and α-pinene highlighted that PERCA was very likely prone to an artifact due to the presence of O_3 in the chamber. Grouping all the experiments together and plotting the difference observed between SAMU and PERCA as a function of the measured O_3 mixing ratio in the chamber indicates a good correlation between the 2 quantities as shown in Figure 4.17 and supports the indication of an artifact in PERCA.

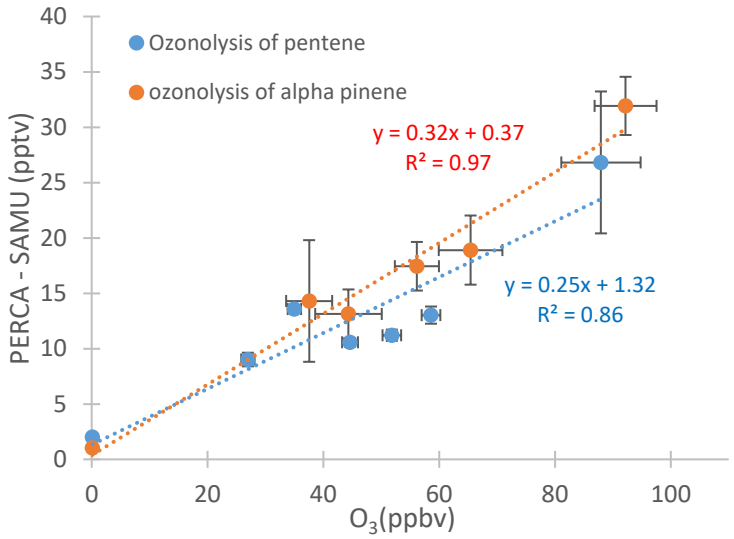

Figure 4.17 Scatter plot of the difference observed between PERCA and SAMU during ozonolysis experiments vs. O_3 mixing ratios. Error bars are 1σ standard deviations.

Several hypothesis can be proposed to explain the PERCA response to O_3:

(1) the formation and subsequent amplification of radicals from O_3-alkene reaction in the amplified channel of PERCA,

(2) the detection of NO_3 radicals and/or Crieege intermediates by PERCA,

The F0AM model was used with the MCMv331 mechanism to investigate whether O_3/pentene or O_3/α-pinene reactions in the amplification and background channels could lead to a significant formation of radicals that would lead to the observed artefact (Figure 4.17). The chemistry was simulated by constraining the model with (i) 82 ppbv of ozone, 17 ppbv of pentene and 5ppm of NO and (ii) 95 ppbv of ozone, 4.5 ppbv of α-pinene and 5ppm of NO, both at 50% RH and 25 °C, for the background mode and an additional 10% of CO for the amplification mode. The model was run for 10 seconds (reaction time in the reactors). The results of these two simulations are shown in figure 4.18. The NO_2 mixing ratios generated during the amplification and background modes are slightly different due to the production of peroxy radicals from O3-

alkene reactions in the reactors as shown in the inserts. The NO_2 mixing ratio in the amplification channel is only 50 and 80 pptv higher than in the background channel for 1-pentene and α-pinene, respectively, which corresponds to 0.7 and 1.1 pptv of peroxy radicals. This effect is too small to explain the discrepancy observed between PERCA and SAMU.

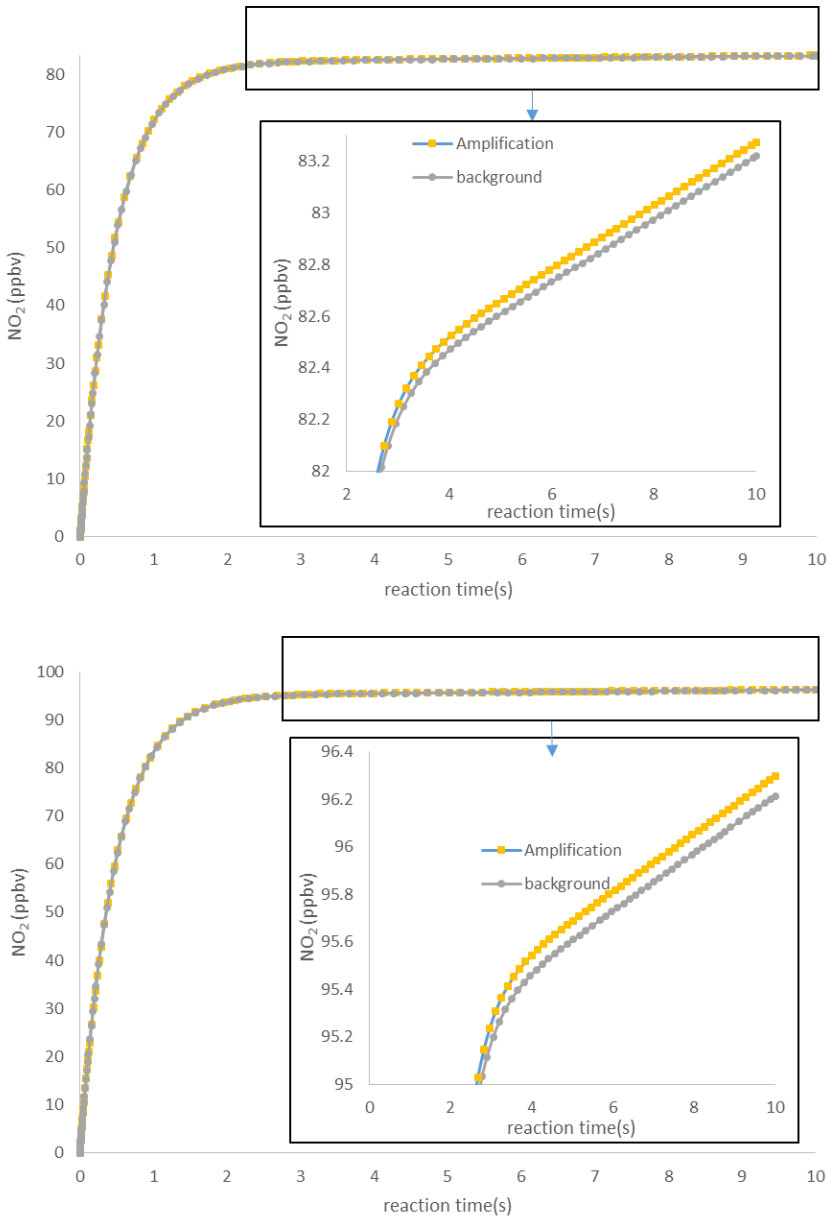

Figure 4.18 Impact of O_3-pentene (upper panel) and O_3-α pinene (lower panel) reactions on NO_2 production in the PERCA reactors run under amplification and background modes. Simulations performed using the highest O_3 mixing ratios observed during the ozonolysis experiments, ca. 82 and 95 ppb for O3+pentene and O3+ α-pinene, respectively.

The amount of NO_3 produced in the chamber for the O_3-pentene experiment was found to range between 2-20 pptv from model simulations described in the next section to model the chamber experiments). While this range of mixing ratios is close to the discrepancy observed between PERCA and SAMU, the range of mixing ratios simulated for the α-pinene/O_3 experiment is much lower (<0.1 pptv) due to the low mixing ratio of NO_2 observed in this experiment. In addition, the reaction rate constant for NO_3+CO is very slow ($<4\times10^{-19}$ cm^3 $molecule^{-1}$ s^{-1}) while the reaction of NO_3 with NO ($\rightarrow 2\ NO_2$) is fast (2.6×10^{-11} cm^3 $molecule^{-1}$ s^{-1}), making the detection of NO_3 by PERCA unlikely. The amount of Criegee intermediates generated in the chamber was also checked in the simulations performed in the next section. It was found that these species were present at mixing ratios lower than 1×10^{-5} pptv for both O_3/pentene and O_3/α-pinene experiments.

The PERCA response to O_3 observed in these experiments is not well understood. However, this artifact is likely due to the use of longer reaction tubes as described in section 4.2.2.3. Indeed, the chemical amplifier was used in the laboratory on flow tube experiments in which large concentrations of ozone were generated. The instrument was used with short reaction tubes as described in chapter 2. During these experiments, no artifact was observed for the measurement of peroxy radicals. The origin of the artifact when long reaction tubes are used needs to be further investigated in the laboratory.

4.4 Modeling comparison

4.4.1 Oxalyl chloride photolysis experiments

4.4.1.1 Hydrogen/Oxalyl chloride mixture: H_2 + Cl → HO_2

Peroxy radical mixing ratios were simulated using the MCM model as described in section 4.3. The model, implementing a subset of MCM V3.3.1 for the H_2 and CH_4 chemistry, was constrained by the measured time series of CO, HCHO, and O_3 as well as photolysis frequencies and meteorological data (pressure, temperature, relative humidity and solar zenith angle) as shown in Table 4.7. For oxalyl chloride and hydrogen, the concentrations of these species were constrained in the model each time they were injected and let free to change after injection.

In this work, sensitivity tests were performed using two different yields of Cl (0.45 and 1) from $(ClCO)_2$ photolysis since these values were respectively observed in HELIOS by the ICARE group (unpublished experiments) at 30 and 5% RH (see section 4.2.3.1). The J-values for $(ClCO)_2$ were calculated using the ratio $J(NO_2)/J((ClCO)_2)=40$ as determined by the ICARE group. This estimation was derived from spectroradiometer measurements of solar iradiance in HELIOS, absorption cross sections measured by Ghosh et al. (Ghosh et al., 2012) and a quantum yield of 1 for the oxalyl chloride photolysis.

Figure 4.19 shows the comparison between peroxy radical measurements of HO_2+RO_2 (PERCA and SAMU) and simulated values for the base MCM model incorporating a Cl yield of 0.45 (base MCM-0.45Cl) or a Cl yield of 1 (base MCM-1.0Cl). Two additional simulations using MCM-1.0Cl and implementing an additional source of peroxy radicals, either HO_2 (MCM-1.0Cl-S>HO_2) or CH_3O_2 (MCM-1.0Cl-S>CH_3O_2), were performed to reproduce the chamber reactivity observed when the chamber was irradiated before any injections. For all these simulations, the decay rate of $(ClCO)_2$ was well reproduced by the model (Figure 4.20), indicating that the photolysis rate of the radical precursor was well constrained in the model.

Table 4.8 Specifications of the model used to simulate radical concentrations in the $H_2/(ClCO)_2$ and $H_2/CH_4/(ClCO)_2$ experiments.

Model MCMv331	Inorganic chemistry Photolytic reactions Chemistry of H_2, methane
Added reactions	$(ClCO)_2 \rightarrow Y_{Cl}\,Cl + 2CO$ / $J(NO_2)/40$ (Y_{Cl}=0.45 or 1) $Cl+H_2 \rightarrow HCl + H$ (CH_4+Cl already in the mechanism) $S \rightarrow HO_2$ / scaled with j(HCHO) $S \rightarrow CH_3O_2$ / scaled with j(HCHO)
Constraints	Dilution at the measured rate of k_{SF6}: 1.7×10^{-5} s^{-1} H_2 , $(ClCO)_2$: only constrained when injected (free to change over time) NO, NO_2, O_3, CO, HCHO : constrained by measured time series Sun zenith angle, corrections for J-values based in measured $J(NO_2)$, Temperature, Pressure, Relative humidity: constrained by measured time series

The peroxy radical mixing ratios simulated using the MCM-0.45Cl model (black dotted line) underestimate the measurements of HO_2+RO_2 by 20-35% after the first injection of $(ClCO)_2$. While the Cl yield of unity was measured under almost dry conditions, the simulation incorporating this yield (base MCM-1.0Cl, light gray dotted line) shows better agreement with the measured mixing ratios (within 15%). Both simulations underestimate the measurements performed during the first 3 hours of irradiation (starting at 11:15) when only H_2 had been introduced into the chamber. This behavior indicates that there was another source of peroxy radicals wihin the chamber.

This additional source of radicals is not well understood. An unknown source (S), either for HO_2 (dark grey dotted line) or CH_3O_2 (yellow dotted line) production, was added in the mechanism for the base MCM-1.0Cl model. The production rate of this additional source was scaled to j(HCHO) (constant scaling factor througout experiment) to achieve good agreement between the simulated and measured peroxy radical mixing ratios when the background chamber reactivity was probed. As shown in Figure 4.19, both simulations are able to reproduce the measured peroxy radicals until the first injection of $(ClCO)_2$. However, the simulation implementing the additional formation of HO_2 (dark grey) overestimates the measurements after this injection while the simulation implementing the additional formation of CH_3O_2 (yellow) is in better agreement with the measurements. The composition of the modelled peroxy radical pool presented in the lower panel

of Figure 4.19 (MCM-1.0Cl-S>CH_3O_2) indicates a major contribution of HO_2 compared to CH_3O_2 (<10 pptv).

Comparing the measured (FAGE) and modelled HO_2 in Figure 4.19 indicates that the model overestimates HO_2 by 60-100%. In contrast, RO_2 radicals are underestimated since the difference between the measured HO_2+RO_2 (PERCA, SAMU) and the measured HO_2 (FAGE) is of the order of 40-80 pptv. The presence of a large amount of organic peroxy radicals was consistent with the peroxy radical decays recored by PERCA and SAMU when the chamber was changed to dark conditions (section 4.3.1.1). It is likely that other VOCs were present and reacted with the Cl atoms to produce RO_2 radicals. The release of VOCs from the wall of the chamber is unlikely the cause since only a small amount of these VOCs is expected from a desorption process, which couldn't compete with Cl+H_2 for the amount of H_2 added to the chamber. Potential possibilities may involve (1) heterogenous reactions of Cl atoms with organics adsorbed on the wall, followed by a subsequent release of the peroxy radicals in the chamber and (2) the injection of contaminants in the chamber through the zero air generator or the reactant injection systems.

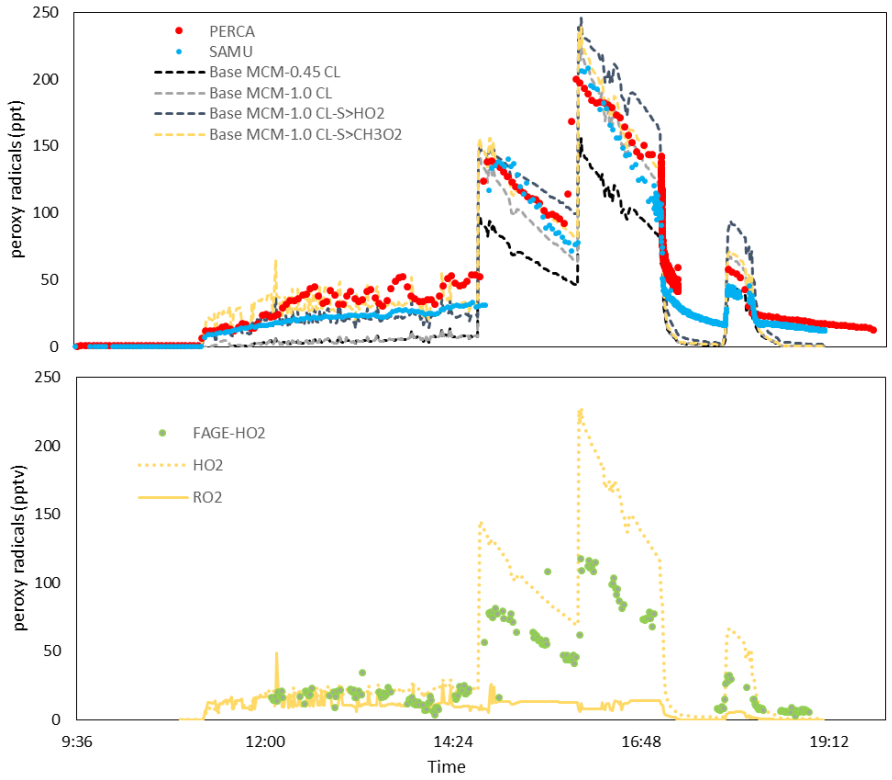

Figure 4.19 Model-measurement comparison of peroxy radicals for the 8 October experiment – $H_2/(ClCO)_2$. Upper panel: Comparison of peroxy radicals measured by PERCA (red markers) and SAMU (blue markers) to model simulations (dashed lines, see text). Lower panel: Comparison of HO_2 radicals measured by FAGE (green markers) to model simulations (MCM-1.0Cl-S>CH_3O_2, dashed yellow line). The modelled CH_3O_2 (solid line) is also shown.

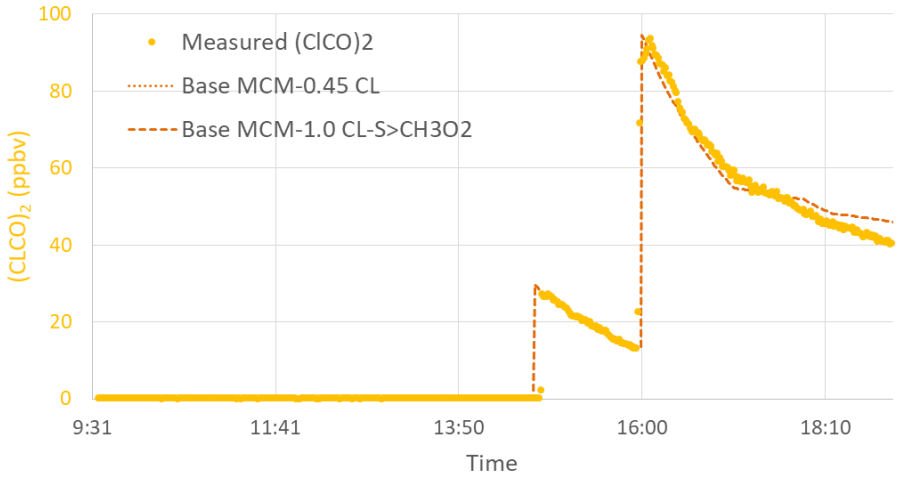

Figure 4.20 Comparison of measured and modelled $(ClCO)_2$ mixing ratios for the 8 October experiment. Only two simulations are shown for clarity. The same results were observed for the 2 other simulations.

4.4.1.2 Hydrogen & Methane/Oxalyl chloride mixture: H_2, CH_4 + Cl → HO_2, CH_3O_2

Model simulations of the photolysis of oxalyl chloride in the presence of H_2 and then methane were performed using the same model procedure than for $H_2/(ClCO)_2$ and the constraints are shown in Table 4.7. Similar to the previous experiment, the model was constrained by the measured concentration of $(ClCO)_2$, H_2, and CH_4 right after their injection into the chamber and these species were then allowed to change over time. In contrast, time series of measured meteorological parameters (RH, Temperature and pressure), HCHO, O_3, CO, NO and NO_2 as well as photolyis frequencies were used to constrain the model. Similar to the $H_2/(ClCO)_2$ simulations, two different yields of Cl from the photolysis of $(ClCO)_2$ were considered as described in Table 4.7. In addition unknown sources of HO_2 or CH_3O_2 radicals were also considered to reproduce the background reactivity of the chamber. These additional sources of radicals were constrained using the same methodology as described in the previous section and as reported in Table 4.7. As shown for the $H_2/(ClCO)_2$ simulations, the simulations also reproduce the decay of $(ClCO)_2$ very well (Figure 4.22), indicating once again that the photolysis rate of the radical precursor was well constrained in the model.

The comparison between HO_2+RO_2 measurements and simulated mixing ratios are shown in Figure 4.21. In contrast to that observed for the $H_2/(ClCO)_2$ experiment, the MCM simulation implementing a Cl yield of 0.45 (base MCM-0.45 Cl, black dashed line) is in agreement with both PERCA and SAMU measurements after the injections of oxalyl chloride, with differences less than 30%. The simulation accounting for a Cl yield of unity (base MCM-1.0 Cl, gray dotted line) overestimates both the PERCA and SAMU measurements by 25-100%. This indicates that while the operating conditions in the chamber were similar between 8-October and 12-October (RH of 22-43%, T of 26-37°C, 50 ppmv H_2, 13-92 ppbv $(ClCO)_2$, J(NO_2) of 1.2×10^{-3}-6.9×10^{-3} s^{-1}), the MCM simulation implementing a Cl yields of 0.45 is better able to reproduce these experimental data while a Cl yield of 1.0 was necessary for the experiment performed on 8-October. This source of the disagreement between the two experiments is unclear and requires additional experiments in HELIOS. Similar to the 8-October experiment, both simulations (base MCM-0.45 Cl and base MCM-1.0 Cl) were not able to reproduce the first 2 hours of background reactivity measurements when the chamber was first exposed to the sunlight. Simulations implementing additional sources of HO_2 (base MCM-0.45 Cl-S>HO_2, dark grey line) and CH_3O_2 (base MCM-0.45 Cl-S>CH_3O_2, yellow line) radicals whose strengths were tweaked to reproduce the background reactivity

measurements indicates a very small impact on the simulated concentrations of peroxy radicals once $(ClCO)_2$ was injected. The bottom panel of Figure 4.21 displays the contribution of both HO_2 and CH_3O_2 radicals for the base MCM simulation implementing a Cl yield of 0.45 and the simulation accounting for an additional source of CH_3O_2 (yellow). This figure shows that before methane injection, the pool of simulated peroxy radicals is mainly HO_2 and is a mixture of about 1/3 HO_2 and 2/3 CH_3O_2 after the injection. Comparing these simulations to the measured HO_2 (FAGE) indicates that both simulations overestimate the measured HO_2 by 30-40%.

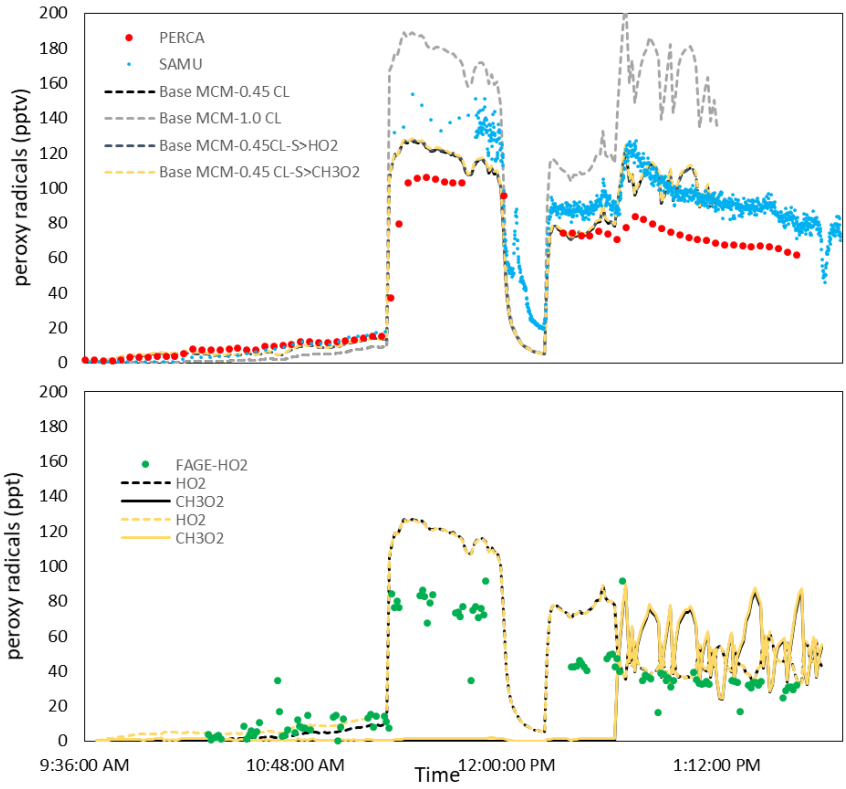

Figure 4.21 Model-measurement comparison of peroxy radicals for the 12 October experiment – H_2/ CH_4/$(ClCO)_2$. Upper panel: Comparison of peroxy radicals measured by PERCA (red markers) and SAMU (blue markers) to model simulations (dashed lines, see text). Lower panel: Comparison of HO_2 radicals measured by FAGE (green markers) to model simulations (MCM-0.45Cl, dashed black line; MCM-0.45Cl-S>CH_3O_2, dashed yellow line). The modelled CH_3O_2 (solid lines) is also shown.

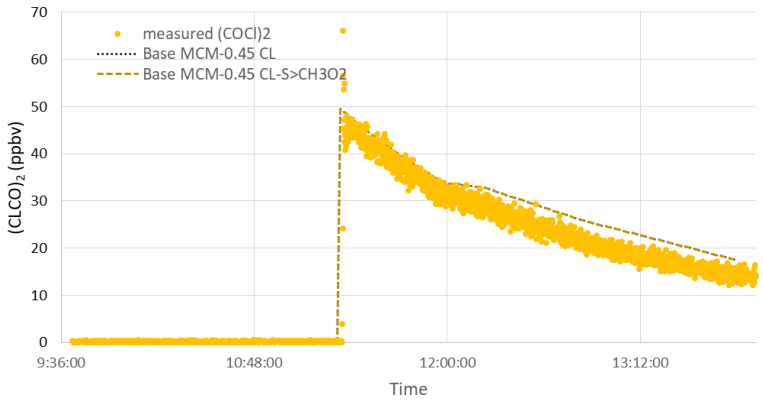

Figure 4.22: Comparison of measured and modelled $(ClCO)_2$ mixing ratios for the 12 October experiment. Only two simulations are shown for clarity. The same results were observed for the 2 other simulations.

4.4.1.3 Conclusions

The simulations performed for the two photolytic experiments led to the following conclusions.

In order to reproduce the HO_2+RO_2 mixing ratios measured by PERCA and SAMU during the H_2/$(ClCO)_2$ experiment conducted at approximately 30% RH and 30°C, a Cl yield of unity for the photolysis of oxalyl chloride needs to be implemented in the model. In contrast, the H_2/CH_4/$(ClCO)_2$ experiment conducted under similar conditions of RH and temperature requires to implement a Cl yield of 0.45. This inconsistency between the two experiments is puzzling and requires further investigations to understand the reason.

The simulated mixing ratios of HO_2 overestimate the measurements performed by FAGE by at least 30% for both experiments. This overestimation was nearly 100% at some reaction times in the H_2/$(ClCO)_2$ experiment. This issue is likely due to the presence of VOCs in the chamber (either in the gas-phase or adsorbed on the Teflon wall) which are not constrained in the model.

The implementation of an additional photolytic source of organic peroxy radicals in the model to reproduce the chamber reactivity when the reactants have not been injected yet has only a small impact on the simulated peroxy radical concentrations once the reactants have been introduced in the chamber.

4.4.2 Ozonolysis experiments under dark conditions

4.4.2.1 Pentene ozonolysis

In order to model this ozonolysis experiment, a subset of MCM v331 containing the pentene chemistry was implemented in the model. The model was constrained by measured mixing ratios of pentene and O_3 measured right after their injection into the chamber, as well as the time series of measured trace gases (CO, HCHO, O_3 and NO_2) and meteorological data (pressure, temperature, relative humidity) as shown in Table 4.8. In addition to the base model, simulations were performed to test the model sensitivity to an additional loss of peroxy radicals, including wall loss and a missing chemical process.

Table 4.9 Specifications of the model used to simulate radical concentrations in the pentene/O_3 and α-pinene/O_3 experiments.

Model MCMv331	Inorganic chemistry 1-pentene or α-pinene MCM subset
Added reaction	$HO_2 \rightarrow$ Loss 7×10^{-3} s^{-1} (for sensitivity tests only) $RO_2 \rightarrow$ Loss 7×10^{-3} s^{-1} (for sensitivity tests only)
Constraints	Dilution at the measured rate of k_{SF6}: 1.7×10^{-5} s^{-1} Pentene, α-pinene, O_3: only constrained when injected (free to change over time) NO_2, CO, HCHO, temperature, pressure and relative humidity: constrained by measured time series NO: Constrained to 50 or 100 pptv for sensitivity tests only (surrogate for a missing chemical process leading to an additional loss of peroxy radicals)

Figure 4.23 shows the PERCA and SAMU measurements of HO_2+RO_2 together with the simulations. The upper panel displays the comparison with the base model (black dotted line) which overestimates the SAMU measurements by approximately a factor of 2. The simulated HO_2 (black dotted line in the lower panel) significanty underestimates the FAGE measurements. Assuming that the difference observed between the modelled and measured mixing ratios of HO_2+RO_2 is due to their loss on the wall of the chamber, it was found necessary to add a wall loss rate constant of 7×10^{3} s^{-1} for all peroxy radicals in the model to bring the simulated mixing ratios of HO_2+RO_2 in better agreement with the SAMU measurements (green dotted line). However, as

shown in the lower panel, the modelled HO_2 (green dotted line) still underestimates the measurements. To the best of our knowledge, a wall loss of peroxy radicals in large atmospheric simulation chambers has never been reported. The loss rate necessary to bring the modelled mixing ratios of HO_2+RO_2 in agreement with the measurements is much larger than any wall loss rates reported for trace gases, including O_3, that usually of the order of 10^{-6} s^{-1}. In addition, if a wall loss of peroxy radicals was operative in the chamber, the same issue should have been observed for the 2 photolytic experiments discussed above. While the wall loss of peroxy radicals is unlikely, this sensitivity test indicates that a larger loss rate of peroxy radicals is necessary to bring the experimental and modeling data into agreement. For instance, constraining the model with a constant NO mixing ratio of 50 pptv would be sufficient to provide this additional loss. Interestingly, the addition of 50 pptv of NO in the model also leads to a better agreement between the modelled and measured HO_2 mixing ratios as shown in the bottom panel of Figure 4.23, indicating that this missing (or model miscalculated) loss process requires the conversion of RO_2 into HO_2.

It is interesting to note that the oxidation rate of 1-pentene is well described by the model since both the 1-pentene and O_3 mixing ratios are well reproduced by the base simulation (Figure 4.24). Constraining the model to 50 pptv NO leads to a larger loss rate for both 1-pentene and O_3, and as a consequence, to a model overestimation of the consumption rate of these 2 species. The increase of the 1-pentene loss rate is likely due to the formation of OH from HO_2+NO. While a conversion of RO_2 into HO_2 seems necessary to improve the agreement between the measured and modelled mixing ratios of peroxy radicals, this process should not ultimately lead to the formation of OH.

Figure 4.25 shows the modelled OH and the speciation of peroxy radicals for both the base MCM simulation and the simulation where NO was constrained to 50 pptv. For the base modeling, OH is simulated at concentrations less than 5×10^5 cm^{-3} and the most abundant RO_2 radicals are PE1ENEAO2, NC3H7O2 and C51NO32O2 (MCM labeling). When NO is constrained in the model, OH increases by a factor of 2-3 and HO_2 is favored compared to RO_2, with a similar partitioning in the pool of organic peroxy radicals as in the base simulation. Unfortunately, the OH measurements performed by FAGE and SAMU are not available yet for comparison, but will be of interest to in further analysis.

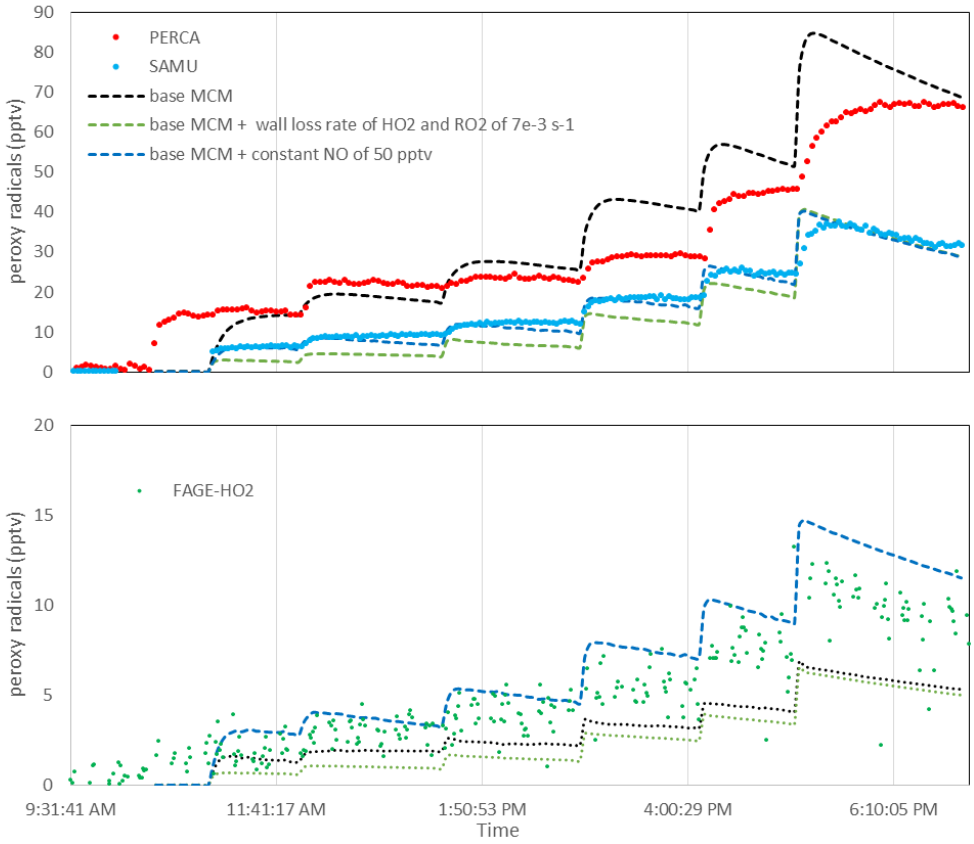

Figure 4.23 Model-measurement comparison of peroxy radicals for the 10 October experiment – 1-pentene/O_3 – Upper panel: Comparison of peroxy radicals measured by PERCA (red markers) and SAMU (blue markers) to model simulations (dashed lines, see text). Lower panel: Comparison of HO_2 radicals measured by FAGE (green markers) to model simulations (dashed lines, see text)

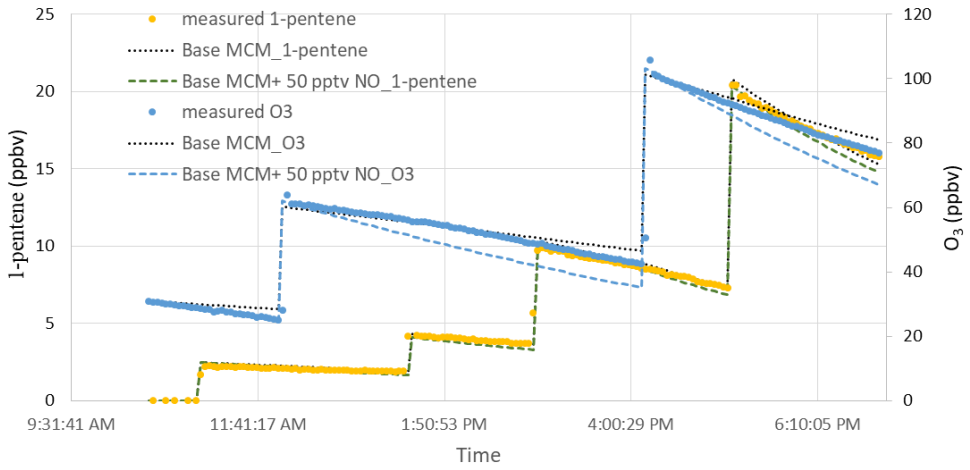

Figure 4.24 Comparison of measured and modeled mixing ratios of 1-pentene and ozone.

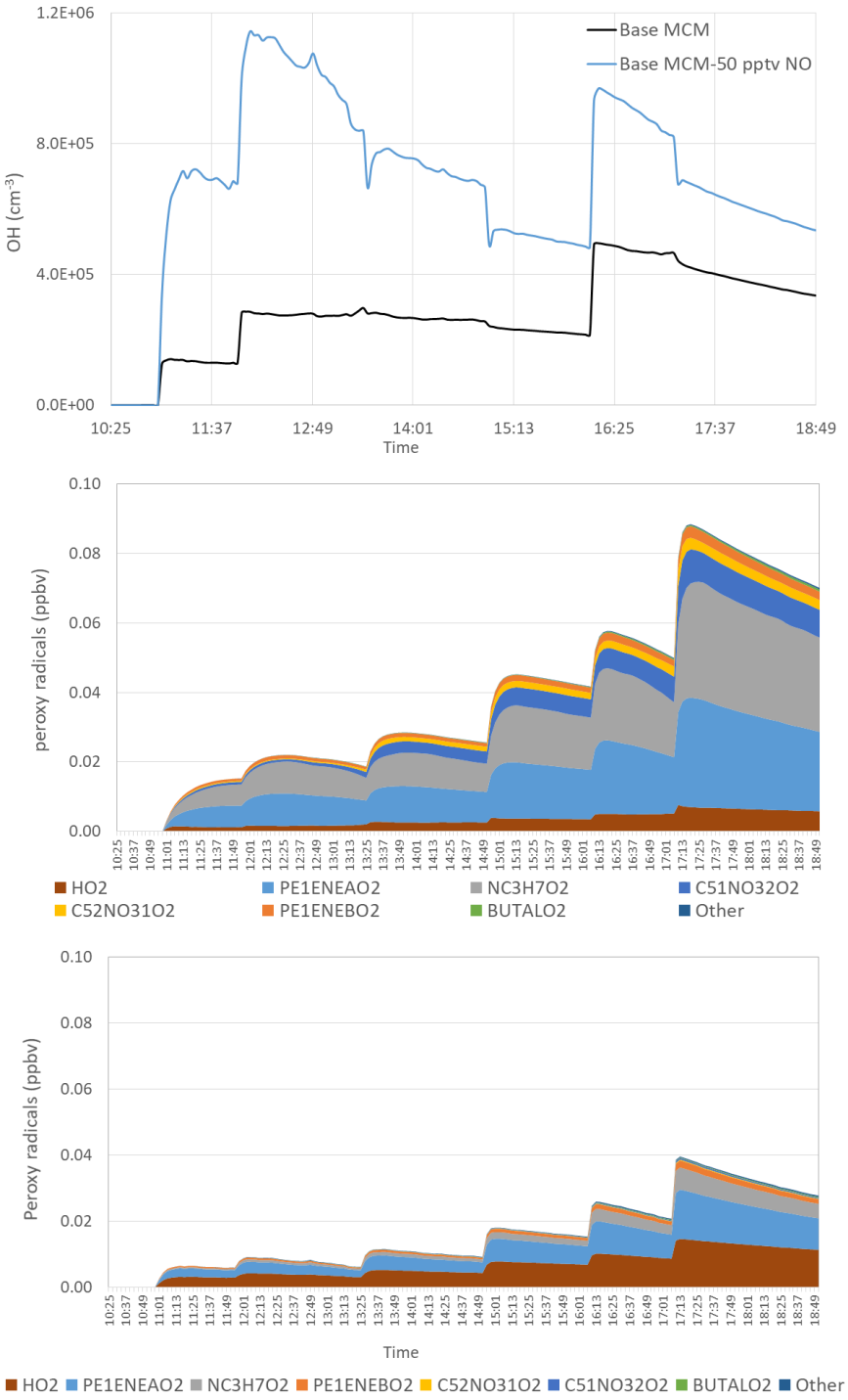

Figure 4.25 Modelled OH and speciation of peroxy radicals for the pentene/O_3 experiment. Upper panel: OH mixing ratios, middle panel: base MCM simulation, lower panel: NO constrained to 50 pptv in the model.

4.4.2.2 α-pinene ozonolysis

Similar to the ozonolysis experiment for 1-pentene, the modeling for this experiment was carried out by constraining the model as shown in Table 4.8, using a subset of the α-pinene chemistry. The model was constrained to the mixing ratios of α-pinene and O_3 measured after injection, time series of measured CO, HCHO, O_3 and NO_2, as well as meteorological data (pressure, temperature, relative humidity).

Figure 4.26 shows the comparison between HO_2+RO_2 measurements (PERCA and SAMU) and simulated mixing ratios from the base model (black dashed line) as well as a model run constrained by an additional loss of peroxy radicals set at the value leading to a good model-measurement agreement for the pentene experiment (i.e. 7×10^{-3} s^{-1}, green dashed line), and model runs constrained to 50 pptv (blue dashed line) and 100 pptv (yellow dashed line) of NO. In the upper panel of this figure, the base simulation of total peroxy radicals indicates unreasonable high mixing ratios, highlighting that an important loss process of peroxy radicals is missing under the low NO_x conditions of this simulation. Adding an additional loss of peroxy radicals as determined for the pentene experiment (either a wall loss or the reaction of peroxy radicals with NO set at 50 pptv) leads to more reasonable mixing ratios of HO_2+RO_2 (<250 pptv). However, these simulations still overestimate the measurements. An additional simulation performed by constraining NO at 100 pptv indicates that the peroxy radical loss required for this chemical system is more than two times higher than observed in the previous experiment (not the rate constants for the reactions of peroxy radicals with NO for pentene-based and α-pinene-based RO_2 are similar). Similar to the pentene experiment, the bottom panel of Figure 4.26 indicates that better agreement is observed between the modeled and measured HO_2 mixing ratios when NO is constrained in the model, highlighting the necessity to convert RO_2 into HO_2.

Figure 4.27 shows that OH in this chemical system is about 2-5 times higher than observed during the ozonolysis of 1-pentene. The middle panel of this figure indicates that the pool of RO_2 is dominated by 2 species when NO is not constrained (C108O2 and C97O2, see Figure 4.28 for structure of these radicals), whose concentrations are drastically reduced relative to the other RO_2 when NO is constrained. It has been recently shown that unimolecular reactions of large peroxy radicals generated by the oxidation of hydrocarbons such as α-pinene could lead to the autoxidation of peroxy radicals (Xu et al., 2019). This loss pathway is not included in MCM and may be the

cause of the missing loss of peroxy radicals observed in these simulations. Additional work is needed to investigate this point.

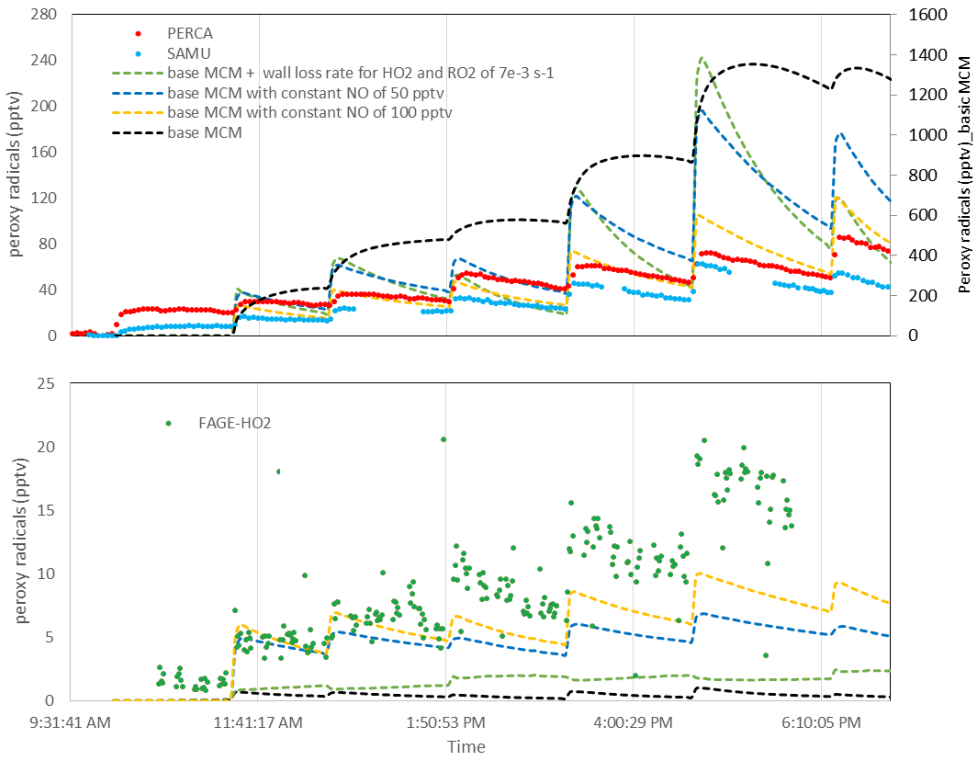

Figure 4.26 Model-measurement comparison of peroxy radicals for the 15 October experiment – α-pinene/O_3. Upper panel: Comparison of peroxy radical measured by PERCA (red markers) and SAMU (blue markers) to different model simulations (dashed lines). Lower panel: Comparison of HO_2 measured by FAGE (green markers) to model simulations (dashed lines).

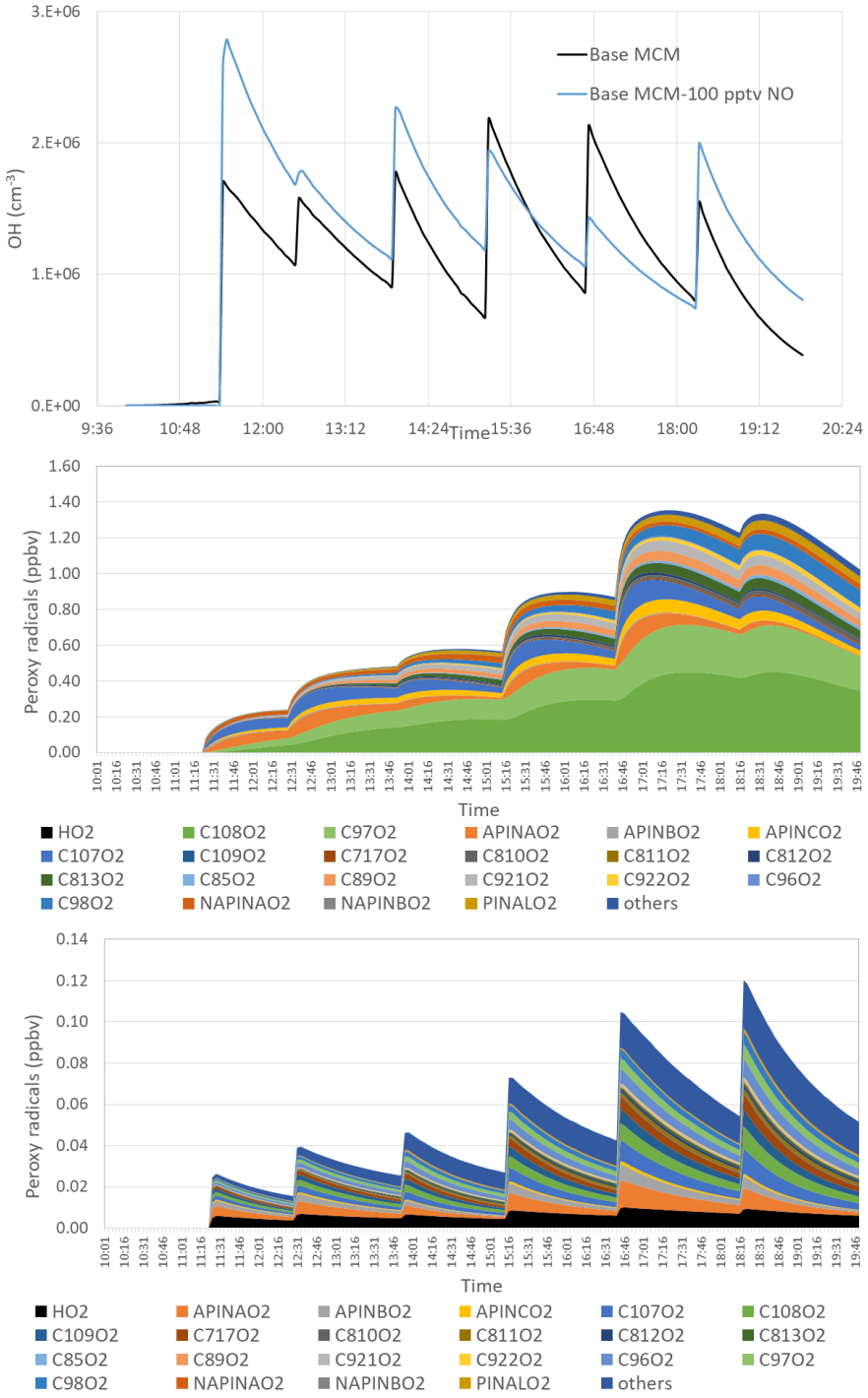

Figure 4.27 Modelled OH and speciation of peroxy radicals for the α-pinene/O_3 experiment. Upper panel: OH mixing ratios, middle panel: base MCM simulation, lower panel: NO constrained to 100 pptv in the model.

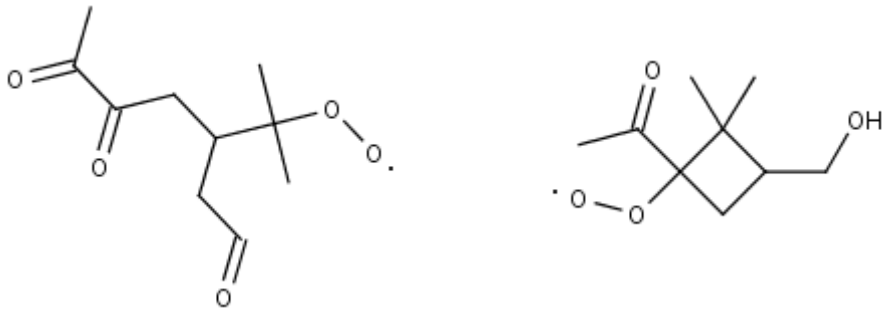

Figure 4.28 Most abundant RO_2 species simulated for the α-pinene/O_3 experiment.

4.4.2.3 Conclusions

The simulations performed for the two O_3-alkene experiments highlighted that the base model was not able to reproduce the measured mixing ratios of peroxy radicals, leading to an overestimation of HO_2+RO_2 and an underestimation of HO_2. In order to reproduce the measured HO_2+RO_2 mixing ratios, the model requires an increase in the propagation rate of organic peroxy radicals to HO_2 without additional propagation to OH. The strength of the process leading to the additional consumption of organic peroxy radicals was found to be higher for radicals generated during the ozonolysis of α-pinene compared to 1-pentene. This behavior may be due to the low amount of NO observed during these experiments (titrated by O_3, below the LOD of 50 pptv of the NO_x analyzer), which may lead to a significant impact of unimolecular reactions of peroxy radicals on the chemistry occurring in the chamber.

4.5 General conclusions

A series of intercomparison experiments was performed at the HELIOS chamber to intercompare the IMT Lille Douai Chemical Amplifier, the University of Lille FAGE instrument and the CIMS instrument from the University of Orléans. Two types of experiments were conducted, under sunlight and dark conditions, to generate different pools of peroxy radicals within the chamber, which helped in investigating the reliability of the different measurement techniques and tested our understanding of oxidation chemistry.

While experiments involving the photolysis of oxalyl chloride to generate HO_2 and HO_2+CH_3O_2 showed that PERCA and SAMU measurements were in agreement within 30%, experiments involving the addition of large concentrations of ozone to the chamber to generate more complex pools of peroxy radicals from the ozonolysis of alkenes highlighted that the PERCA instrument used in this work was very likely prone to an artifact due to the presence of O_3 in the chamber. Potential reasons such as (i) the formation and subsequent amplification of radicals from O_3-alkene reactions in the amplified channel of PERCA and (ii) the detection of NO_3 radicals and/or Criegee intermediates by PERCA have been ruled out. However, the origin of this artifact has not yet been identified. It is believed that this artifact was due to the use of long reaction tubes on the chemical amplifier during the intercomparison experiment since the use of this instrument in the laboratory with shorter reaction tubes did not lead to significant artifacts when ozone was sampled by the instrument. The cause of this artifact when long reaction tubes which are used need to be further investigated in the laboratory.

Box modeling was performed to gain additional insight into the experiments conducted in HELIOS and highlighted several issues which also need to be further investigated. In order to reproduce the HO_2+RO_2 mixing ratios measured by PERCA and SAMU during the two photolytic experiments involving oxalyl chloride, two different yields of chlorine atoms had to be implemented in the model while the operating conditions of the chamber were similar. This inconsistency between the two experiments is puzzling and requires further chamber experiments under various conditions to identify the reason. In addition, an unidentified source of organic peroxy radicals was observed during these experiments, which requires additional investigations to characterize it.

Simulating the two O_3-alkene experiments highlighted the inability of the base model to reproduce the measured mixing ratios of peroxy radicals, leading to an overestimation of HO_2+RO_2 and an underestimation of HO_2. It was shown that the model requires additional loss of organic peroxy radicals that converts them to HO_2, without further conversion into OH. It is speculated that this unnacounted loss may be due to unimolecular reactions of peroxy radicals that are not included in MCM. Additional simulations focusing on the implementation of unimolecular reactions of peroxy radicals in the model will be performed.

4.6 References

Ahmed, M., Blunt, D., Chen, D., Suits, A.G., 1997. UV photodissociation of oxalyl chloride yields four fragments from one photon absorption. The Journal of chemical physics 106, 7617–7624.

Amedro, D., Miyazaki, K., Parker, A., Schoemaecker, C., Fittschen, C., 2012. Atmospheric and kinetic studies of OH and HO2 by the FAGE technique. Journal of Environmental Sciences 24, 78–86. http://dx.doi.org/10.1016/S1001-0742(11)60723-7

Atkinson, R., Baulch, D.L., Cox, R.A., Crowley, J.N., Hampson, R.F., Hynes, R.G., Jenkin, M.E., Rossi, M.J., Troe, J., 2007. Evaluated kinetic and photochemical data for atmospheric chemistry: Volume III – gas phase reactions of inorganic halogens. Atmos. Chem. Phys. 7, 981–1191. https://doi.org/10.5194/acp-7-981-2007

Atkinson, Roger., Tuazon, E.C., Aschmann, S.M., 1995. Products of the Gas-Phase Reactions of O3 with Alkenes. Environ. Sci. Technol. 29, 1860–1866. https://doi.org/10.1021/es00007a025

Avzianova, E.V., Ariya, P.A., 2002. Temperature-dependent kinetic study for ozonolysis of selected tropospheric alkenes. International Journal of Chemical Kinetics 34, 678–684. https://doi.org/10.1002/kin.10093

Baklanov, A.V., Krasnoperov, L.N., 2001. Oxalyl Chloride A Clean Source of Chlorine Atoms for Kinetic Studies. The Journal of Physical Chemistry A 105, 97–103.

Burkert, J., Behmann, T., Andrés Hernández, M.D., Stöbener, D., Weißenmayer, M., Perner, D., Burrows, J.P., 2001. Measurements of peroxy radicals in a forested area of Portugal. Chemosphere - Global Change Science 3, 327–338. https://doi.org/10.1016/S1465-9972(01)00014-9

Duncianu, M., Olariu, R.I., Riffault, V., Visez, N., Tomas, A., Coddeville, P., 2012. Development of a New Flow Reactor for Kinetic Studies. Application to the Ozonolysis of a Series of Alkenes. J. Phys. Chem. A 116, 6169–6179. https://doi.org/10.1021/jp211480x

Fuchs, H., Brauers, T., Dorn, H.P., Harder, H., Häseler, R., Hofzumahaus, A., Holland, F., Kanaya, Y., Kajii, Y., Kubistin, D., Lou, S., Martinez, M., Miyamoto, K., Nishida, S., Rudolf, M., Schlosser, E., Wahner, A., Yoshino, A., Schurath, U., 2010. Technical Note: Formal blind intercomparison of HO_2 measurements in the atmosphere simulation chamber SAPHIR during the HOxComp campaign. Atmos. Chem. Phys. 10, 12233–12250. https://doi.org/10.5194/acp-10-12233-2010

Fuchs, H., Brauers, T., Häseler, R., Holland, F., Mihelcic, D., Müsgen, P., Rohrer, F., Wegener, R., Hofzumahaus, A., 2009. Intercomparison of peroxy radical measurements obtained at atmospheric conditions by laser-induced fluorescence and electron spin resonance spectroscopy. Atmos. Meas. Tech. 2, 55–64. https://doi.org/10.5194/amt-2-55-2009

Ghosh, B., Papanastasiou, D.K., Burkholder, J.B., 2012. Oxalyl chloride, ClC(O)C(O)Cl: UV/vis spectrum and Cl atom photolysis quantum yields at 193, 248, and 351 nm. The Journal of Chemical Physics 137, 164315. https://doi.org/10.1063/1.4755769

Hemmi, N., Suits, A.G., 1997. Photodissociation of oxalyl chloride at 193 nm probed via synchrotron radiation. The Journal of Physical Chemistry A 101, 6633–6637.

Horie, O., Moortgat, G.K., 1991. Decomposition pathways of the excited Criegee intermediates in the ozonolysis of simple alkenes. Atmospheric Environment. Part A. General Topics 25, 1881–1896. https://doi.org/10.1016/0960-1686(91)90271-8

Japar, S., Wu, C., Nikl, H., 1974. Rate constants for the reaction of ozone with olefins in the gas phase. The Journal of Physical Chemistry 78, 2318–2320.

Kanakidou, M., Seinfeld, J.H., Pandis, S.N., Barnes, I., Dentener, F.J., Facchini, M.C., Van Dingenen, R., Ervens, B., Nenes, A., Nielsen, C.J., Swietlicki, E., Putaud, J.P., Balkanski, Y., Fuzzi, S., Horth, J., Moortgat, G.K., Winterhalter, R., Myhre, C.E.L., Tsigaridis, K., Vignati, E., Stephanou, E.G., Wilson, J., 2005. Organic aerosol and global climate modelling: a review. Atmos. Chem. Phys. 5, 1053–1123. https://doi.org/10.5194/acp-5-1053-2005

Kukui, A., Ancellet, G., Le Bras, G., 2008. Chemical ionisation mass spectrometer for measurements of OH and Peroxy radical concentrations in moderately polluted atmospheres. Journal of Atmospheric Chemistry 61, 133–154. https://doi.org/10.1007/s10874-009-9130-9

Müller, M., Mikoviny, T., Jud, W., D'Anna, B., Wisthaler, A., 2013. A new software tool for the analysis of high resolution PTR-TOF mass spectra. Chemometrics and Intelligent Laboratory Systems 127, 158–165.

Nguyen, T.B., Tyndall, G.S., Crounse, J.D., Teng, A.P., Bates, K.H., Schwantes, R.H., Coggon, M.M., Zhang, L., Feiner, P., Millller, D.O., Skog, K.M., Rivera-Rios, J.C., Dorris, M., Olson, K.F., Koss, A., Wild, R.J., Brown, S.S., Goldstein, A.H., de Gouw, J.A., Brune, W.H., Keutsch, F.N., Seinfeld, J.H., Wennberg, P.O., 2016. Atmospheric fates of Criegee intermediates in the ozonolysis of isoprene. Phys. Chem. Chem. Phys. 18, 10241–10254. https://doi.org/10.1039/C6CP00053C

Onel, L., Brennan, A., Gianella, M., Ronnie, G., Lawry Aguila, A., Hancock, G., Whalley, L., Seakins, P.W., Ritchie, G.A.D., Heard, D.E., 2017a. An intercomparison of HO2 measurements by fluorescence assay by gas expansion and cavity ring-down spectroscopy within HIRAC (Highly Instrumented Reactor for Atmospheric Chemistry). Atmos. Meas. Tech. 10, 4877–4894. https://doi.org/10.5194/amt-10-4877-2017

Onel, L., Brennan, A., Seakins, P.W., Whalley, L., Heard, D.E., 2017b. A new method for atmospheric detection of the CH3O2 radical. Atmos. Meas. Tech. 10, 3985–4000. https://doi.org/10.5194/amt-10-3985-2017

Parker, A.E., Amédro, D., Schoemaecker, C., Fittschen, C., 2011. OH RADICAL REACTIVITY MEASUREMENTS BY FAGE. Environmental Engineering & Management Journal (EEMJ) 10.

Platt, U., Alicke, B., Dubois, R., Geyer, A., Hofzumahaus, A., Holland, F., Martinez, M., Mihelcic, D., Klüpfel, T., Lohrmann, B., Pätz, W., Perner, D., Rohrer, F., Schäfer, J., Stutz, J., 2002. Free Radicals and Fast Photochemistry during BERLIOZ. Journal of Atmospheric Chemistry 42, 359–394. https://doi.org/10.1023/A:1015707531660

Ren, X., Edwards, G.D., Cantrell, C.A., Lesher, R.L., Metcalf, A.R., Shirley, T., Brune, W.H., 2003. Intercomparison of peroxy radical measurements at a rural site using laser-induced fluorescence and Peroxy Radical Chemical Ionization Mass Spectrometer (PerCIMS) techniques. Journal of Geophysical Research: Atmospheres 108. https://doi.org/10.1029/2003JD003644

Ren, Y., Grosselin, B., Daële, V., Mellouki, A., 2017. Investigation of the reaction of ozone with isoprene, methacrolein and methyl vinyl ketone using the HELIOS chamber. Faraday Discuss. 200, 289–311. https://doi.org/10.1039/C7FD00014F

Schlosser, E., Brauers, T., Dorn, H.P., Fuchs, H., Häseler, R., Hofzumahaus, A., Holland, F., Wahner, A., Kanaya, Y., Kajii, Y., Miyamoto, K., Nishida, S., Watanabe, K., Yoshino, A., Kubistin, D., Martinez, M., Rudolf, M., Harder, H., Berresheim, H., Elste, T., Plass-Dülmer, C., Stange, G., Schurath, U., 2009. Technical Note: Formal blind intercomparison of OH measurements: results from the international campaign HOxComp. Atmos. Chem. Phys. 9, 7923–7948. https://doi.org/10.5194/acp-9-7923-2009

Xu, L., Møller, K.H., Crounse, J.D., Otkjær, R.V., Kjaergaard, H.G., Wennberg, P.O., 2019. Unimolecular Reactions of Peroxy Radicals Formed in the Oxidation of α-Pinene and β-Pinene by Hydroxyl Radicals. J. Phys. Chem. A 123, 1661–1674. https://doi.org/10.1021/acs.jpca.8b11726

Conclusions and Perspectives

Conclusions

The main objective of this work was to improve our understanding of peroxy radical measurements in the troposphere. It consisted in the assembling and characterization of two apparatus: a dual channel chemical amplifier at IMT Lille Douai (France), and a RO_xLIF system at Indiana University (US) using an existing FAGE instrument. In addition, the chemical amplifier developed in this work was compared to a FAGE instrument from the University of Lille (France) and a CIMS instrument from the University of Orléans (France) during an intercomparison exercise at the HELIOS atmospheric chamber.

The chemical amplifier developed for ground-based measurements was tested using two different approaches regarding the radical amplification chemistry, including the use of CO/NO (PERCA) and ethane/NO (ECHAMP). Optimum operating conditions for these two approaches were characterized together with the dependence of the amplifier chain length on reagent gases and humidity. In addition, the amplifier response was tested for different peroxy radicals, including HO_2 and a large range of RO_2 radicals, showing that the effective chain length can be derived from the calibrated HO_2 chain length and the known yields of organic nitrate and nitrite formation from RO_2 and RO radicals, respectively. Finally, ambient testing of this chemical amplifier using the PERCA approach showed that this instrument is capable of measuring ambient concentrations of HO_2+RO_2 at levels higher than 1-4 pptv under RH conditions up to 90% once the RH-dependence of the CL has been correctly characterized.

Chemical reactions occurring inside the amplification and background channels were modelled using the Master Chemical Mechanism (MCM) to test our understanding of the PERCA and ECHAMP amplification chemistries. The model/measurement comparison highlighted that the model overestimates the chain length by a factor of approximately 2 for both approaches. Additional simulations conducted to assess whether the formation of HNO_3 from HO_2+NO (not included in MCM) could impact the CL of chemical amplifiers highlighted that using the yield reported under dry conditions, and a 2-fold lower-than-reported water-dependence for this yield,

provides a reasonable description of the CL-dependence on reagent gases and RH for both PERCA and ECHAMP.

The RO_xLIF technique was implemented on an existing LIF-FAGE instrument at Indiana University to extend the measurement capability of this instrument to HO_2+RO_2. This work required to design the RO_2-to-HO_2 conversion flow-tube, couple it to FAGE and automate the measurement sequence and data acquisition. Operating conditions for the conversion flow-tube were optimized to maximize the instrument sensitivity towards HO_2 and RO_2 through both laboratory experiments and model simulations. Optimum conditions were identified by varying the addition of reagent gases (CO, NO), as well as the pressure and the residence time inside the flow-tube. The sensitivity of the instrument towards HO_2 and a few RO_2 radicals, including CH_3O_2, $C_2H_5O_2$ and $C_3H_7O_2$, was calibrated, showing that RO_2 sensitivity factors were 20-30% higher than for HO_2. Modeling results for isoprene-based and toluene-based peroxy radicals indicate that the sensitivity should be comparable between these RO_2 radicals and those tested in the laboratory (within 10%).

The Indiana University RO_xLIF apparatus was deployed in the field at the Indiana University Research and Teaching Preserve as part of the iRACE field campaign during summer 2019. Both ambient and indoor measurements of RO_2 and HO_2 were performed during this campaign, showing that this instrument is capable of measuring concentrations of peroxy radicals in contrasted environments. Ambient (outdoor) measurements of HO_2 and RO_2 were found to be in the range of previous measurements performed at this site and other forested sites in the world, providing confidence in this instrument. Indoor measurements showed that this instrument can also be successfully employed to investigate the fast variability of indoor radicals when different human activities such as cleaning take place.

Finally, an intercomparison experiment of peroxy radical measurements was performed at the ICARE institution in Orléans (France) to compare the chemical amplifier from IMT Lille Douai to a FAGE instrument from the University of Lille and a CIMS instrument from the University of Orléans. The comparison performed under various conditions in the HELIOS atmospheric chamber highlighted that the chemical amplifier using the PERCA approach was prone to an artifact due to the presence of O_3. It is believed that this artifact was due to the specific configuration used for this instrument during the intercomparison experiment, i.e. using long reaction tubes.

Box modeling of the kinetic experiments conducted in HELIOS also highlighted that the use of oxalyl chloride as a source of Cl atoms is not straightforwards. It was observed that different yields of chlorine atoms from oxalyl chloride photolysis had to be implemented in the model to reproduce the radical measurements performed on different days under similar conditions. In addition, O_3-alkene experiments performed in HELIOS also highlighted the inability of the MCM model to reproduce the measured mixing ratios of peroxy radicals, likely due to missing unimolecular reactions of peroxy radicals in the model.

Perspectives

For the chemical amplifier, the experiments and modeling conducted to characterize its response to peroxy radicals under various operating conditions highlighted that while the implementation of the $HO_2+NO \rightarrow HNO_3$ chemistry could lead to a reasonable agreement between the measured and simulated chain lengths (vs. NO, vs. CO, vs. RH) for both PERCA and ECHAMP approaches, the model overestimation of the ECHAMP CL and underestimation of the PERCA CL seems to indicate that our understanding of the amplification chemistry is still incomplete and deserves additional scrutiny.

In addition, several modifications could be tested to improve the sensitivity (higher CL) and to reduce the CL dependence on RH. For instance, interesting suggestions provided by Ezra Wood from Drexel University (US) would be to (i) run the chemical amplifier at a lower pressure to reduce the radical loss from RO+NO and RO_2+NO_2 reactions and (ii) dilute the air sample with dry oxygen to reduce RH in the reactors. Part of the loss in sensitivity due to the dilution effect would be balanced by favoring $RO+O_2 \rightarrow HO_2$ (radical propagation) compared to $RO+NO \rightarrow RONO$ (radical termination).

For the RO_xLIF apparatus, several aspects need to be straighten to increase our confidence in the measurements. Additional experiments and model simulations should be performed to investigate (1) why the radical loss may have changed inside the conversion flow-tube during the characterization experiments described in chapter 3, (2) the effect of pressure on the RO_xLIF sensitivity when the reagent gases are kept at the same concentration, (3) the RO_xLIF sensitivity towards a larger pool of RO_2 radicals, and (4) potential interferences from the thermal decomposition of unstable species in the conversion flow-tube (HO_2NO_2, $CH_3O_2NO_2$). In addition, future improvements for this instrument may involve (1) a longer and wider flow-tube to reduce

the surface to volume ratio, which in turn should lead to a decrease of HO_2 wall losses, (2) the use of different coating materials to further reduce radical wall losses, and (3) a shorter residence time in the flow-tube to increase the HO_2 signal detected from the conversion of RO_2.

The analysis of the intercomparison campaign presented in chapter 4 is only preliminary and needs to be further advanced to improve our understanding of peroxy radical measurements and to get more insights into potential issues associated to radical measurements. Additional box modeling should be performed to investigate the nature of the missing loss of peroxy radicals observed during the ozonolysis experiments.

Résumé

Les radicaux peroxyles (HO_2 et RO_2) sont des espèces clés en chimie atmosphérique. Avec le radical hydroxyl (OH), ils sont impliqués dans les mécanismes d'oxydation conduisant à la formation de polluants secondaires tels que l'ozone et les aérosols organiques. Comparer les mesures ambiantes de ces espèces à très courte durée de vie aux concentrations issues de modèles de boite permet d'évaluer la robustesse des mécanismes chimiques implémentés dans les modèles atmosphériques. Cependant, ces mesures ambiantes sont très difficiles à réaliser et quelques techniques seulement sont disponibles pour les mesures de terrain.

L'objectif principal de ce travail est d'améliorer nos connaissances sur deux de ces techniques : l'Amplification Chimique (CA) et la Fluorescence Induite par Laser des RO_x (RO_xLIF). La technique CA, simple et bon marché, permet la mesure de la somme HO_2+RO_2 et constitue une bonne solution pour le terrain. La technique RO_xLIF, plus complexe, permet de mesurer distinctement HO_2 et la somme des RO_2. Dans une première partie, un amplificateur à deux voies d'échantillonnage a été construit à l'IMT Lille Douai (France) et caractérisé pour deux chimies d'amplification : 1) au monoxyde de carbone (PERCA, PEroxy Radical Chemical Amplifier) et 2) à l'éthane (ECHAMP, Ethane CHemical AMPlifier). Dans une seconde partie, la technique RO_xLIF a été implémentée sur un instrument FAGE (Fluorescent Assay by Gas Expansion) à l'Université d'Indiana (USA). Les deux outils ont ensuite été testés lors de mesures ambiantes. Dans une dernière partie, PERCA et RO_xLIF ainsi qu'une troisième technique basée sur la spectrométrie de masse à ionisation chimique ont été comparés lors d'une campagne intensive à la chambre de simulation atmosphérique HELIOS à Orléans (France). Plusieurs expériences ont été menées afin d'évaluer la robustesse des mesures de radicaux peroxyles.

Mots clés : Radicaux peroxyles, techniques analytiques, atmosphère, campagne de mesure

Abstract

Peroxy radicals (HO_2 and RO_2) are key species in atmospheric chemistry, which together with the hydroxyl radical (OH), are involved in oxidation processes leading to the formation of secondary pollutants such as ozone and organic aerosols. Monitoring these short-lived species during intensive field campaigns and comparing the measured concentrations to box model simulations allow assessing the reliability of chemical mechanisms implemented in atmospheric models. However, ambient measurements of peroxy radicals are still considered challenging and only a few techniques have been used for field measurements.

The main objective of this work was to improve our knowledge on two measurement techniques: CA (Chemical Amplification) and RO_xLIF (RO_x Laser Induced Fluorescence). CA is a chemical technique for measuring the sum of peroxy radicals (HO_2+RO_2) whose simplicity and low cost makes it attractive for field measurements. ROxLIF is a laser-based technique allowing to speciate HO_2 and the sum of RO_2. In the first part of this thesis, a two-channel chemical amplifier was built at IMT Lille Douai (France) and characterized using 2 different amplification chemistries (PERCA, PEroxy Radical Chemical Amplifier, and ECHAMP, Ethane CHemical AMPlifier). In a second part, the RO_x-LIF technique was implemented on an existing FAGE (Fluorescent Assay by Gas Expansion) instrument at Indiana University (United States). Both the CA and RO_xLIF were tested for ambient measurements. In a last part, the CA using the PERCA approach, RO_xLIF and an additional technique based on chemical ionization mass spectrometry were intercompared at the HELIOS atmospheric chamber in Orleans (France). Several experiments were conducted to investigate the reliability of peroxy radical measurements.

Keywords: Peroxy radicals, analytical techniques, atmosphere, field measurements